Geometry, evolution and scaling of fault relay zones in 3D using detailed observations from outcrops and 3D seismic data

LONG, JONATHAN,JAMES

DEPARTMENT OF EARTH SCIENCES, DURHAM UNIVERSITY

Geometry, evolution and scaling of fault relay zones in 3D using detailed observations from outcrops and 3D seismic data

A Thesis Submitted to Durham University for
the Degree of Doctor of Philosophy in the
Faculty of Science.

Jonathan J. Long

March 2011

Abstract

A new surface attribute was developed during the course of the thesis, which enables fault-related deformation – specifically, the apparent dip of mapped horizons measured in a direction perpendicular to the average strike of a fault array (here termed “fault-normal rotation”, or “FNR”) – to be quantitatively analysed around imaged faults. The new utility can be applied to any 3D surface and was used to analyse centimetre-scale to kilometre-scale fault-arrays, interpreted from laser scan point clouds, digital elevation models, and 3D seismic datasets. In all studied examples, faults are surrounded by volumes of fault-related deformation that have variable widths, and which can consist of faults, fractures and continuous bed rotations (i.e. monoclines). The vertical component of displacement calculated from the areas of fault-related deformation on each horizon act to “fill-in” apparently missing displacements observed in fault throw profiles at fault overlaps. This result shows that complex 3D patterns of fault-related strain commonly develop during the geometrically coherent growth of a single fault-array. However, if the component of continuous deformation was not added to the throw profile, the fault-array could have been misinterpreted as a series of isolated fault segments with coincidental overlaps.

The FNR attribute allows the detailed, quantitative analysis of fault linkage geometries. It is shown that overlapping fault tip lines in relay zones can link simultaneously at multiple points, which results in a segmented branch line. Fault linkage in relay zones is shown to control the amount of rotation accommodated by relay ramps on individual horizons, with open relay ramps having accommodated by larger rotations than breached relay ramps in the same relay zone. Displacements are therefore communicated between horizons in order to maintain strain compatibility within the relay zone. This result is used to predict fault linkage in the subsurface, along slip-aligned branch lines, from the along-strike displacement distributions at the earth’s surface.

Relay zone aspect ratios (AR; overlap/separation) are documented to follow power-law scaling relationships over nine orders of magnitude with a mean AR of 4.2. Approximately one order of magnitude scatter in both separation and overlap exists at all scales. Up to half of this scatter can be attributed to the spread of measurements recorded from individual relay zones, which relates to the evolution of relay zone geometries as the displacements on the bounding faults increase. Mean relay AR is primarily controlled by the interactions between the stress field, of a nearby fault, and overlapping fault tips, rather than by the host rock lithology. At the Kilve and Lamberton study areas, mean ARs are 8.60 and 8.64 respectively, which are much higher than the global mean, 4.2. Scale-dependant factors, such as mechanical layering and heterogeneities at the fault tips are present at these locations, which modify how faults interact and produce relatively large overlap lengths for a given separation distance. Despite the modification to standard fault interaction models, these high AR relay zones are all geometrically coherent.

Table of contents

List of figures: Chapter 1

List of figures: Chapter 2

List of figures: Chapter 3

List of figures: Chapter 4

List of figures: Chapter 5

List of figures: Chapter 6

List of figures: Appendices

Acknowledgements

I am grateful for all the guidance given to me by my supervisors: R. Jones, R. Holdsworth, N. DePaola, and especially J. Imber. Other people I would like to acknowledge for their support and guidance during my studies are: M. van Noorden (Badley Geoscience Ltd), P. Griffiths (BG Group), B. Freeman (Badley Geoscience Ltd), R. Wightman (MVE), and my field assistant D. Sagi. I am particularly grateful to B. Freeman for coding the algorithm that enabled me to use TrapTester software to extract apparent dip data from horizon tri-meshes. Badley Geoscience Ltd. provided academic licenses and training for TrapTester. Schlumberger provided academic licenses for Petrel and Dynel2D. Geospatial Research Ltd. provided training for use of the laser scanner. D. Stevenson and G. Wilkinson provided invaluable IT support within the Department of Earth Sciences at Durham University. The Laminaria 3D Seismic data was provided by Geoscience Australia. And finally, I am very thankful for my funding, which was provided by a NERC Open CASE PhD studentship with BG Group (NE/F006586/1).

Declaration

No part of this thesis has previously been submitted for a degree at this or any other university. The work described in this thesis is entirely that of the author, except where reference is made to previously published or unpublished work.

Jonathan J. Long

Durham University

Department of Earth Science

March 2011

I dedicate this thesis to my wife. Without her love and support I would never have got this far.

Ella M. Long

Chapter 1. Introduction

The volume of rock within which faults overlap and transfer displacements is termed a relay ramp in map view and a relay zone in 3D. Peacock and Sanderson (1994) identified 4 stages of relay ramp evolution (**Fig. 1.1**): stage 1, fault segments do not overlap; stage 2, displacement is transferred through the strata between the overlapping faults producing a relay ramp; stage 3, linking faults and fractures begin to develop and cut across the ramp; and stage 4, occurs when the ramp is breached and a through going fault is formed.

Fault relay zone geometries are documented over a wide range of scales and follow power-law scaling relationships (Huggins et al., 1995; Acocella et al., 2000; Peacock, 2003; Soliva and Benedicto, 2004). In map view, relay zones can be approximated to rectangles with overlap lengths greater than their separation (**Fig. 1.2**). The overlap/separation ratio gives the aspect ratio (AR) of a relay ramp. The bounding

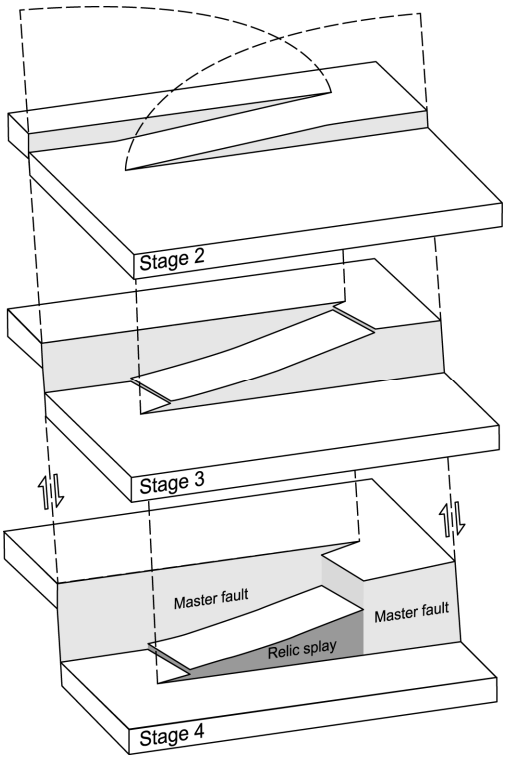

Fig. 1.1. A conceptual 3D diagram of a relay zone. Ramp rotations are towards the mutual hanging wall and are depicted to remain the same on each horizon, despite the progression in fault linkage stages with depth and increased displacement. A relict splay is formed when the ramp is breached by a through going master fault. Modified from (Peacock and Sanderson, 1994).

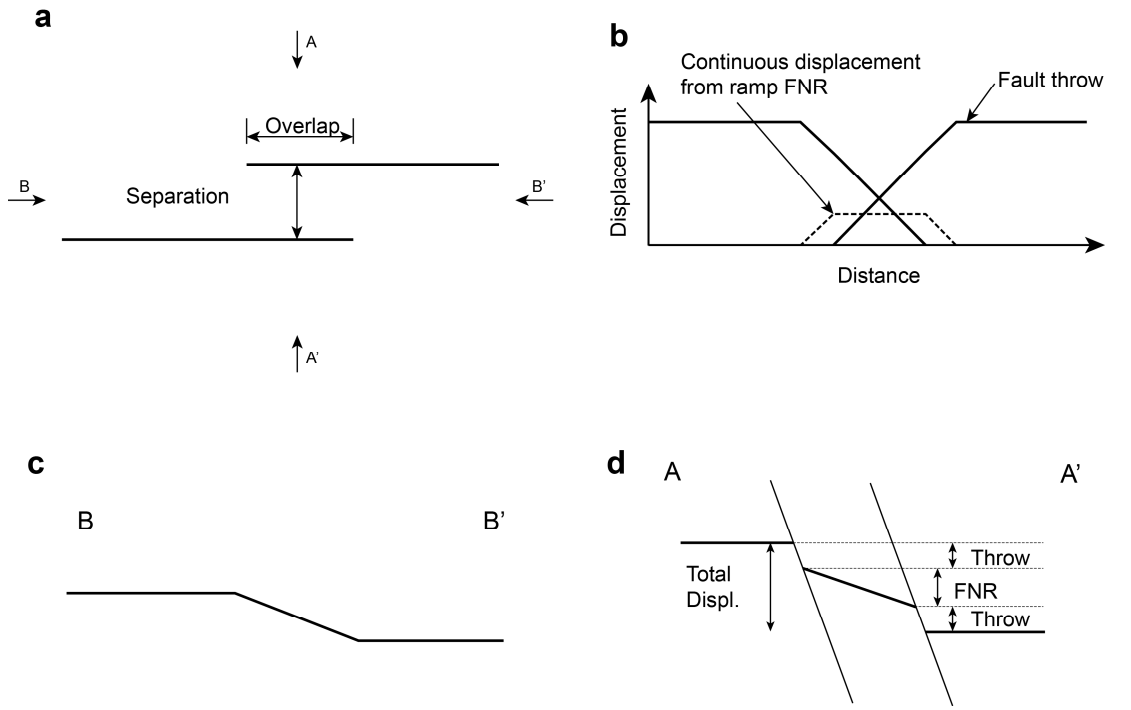

Fig. 1.2. (a) Schematic map view diagram of a relay ramp. (b) Displacement-distance (d-x) plot of the relay ramp in (a). (c) Cross-section through the ramp parallel to the strike of the bounding faults. (d) Cross-section normal to the strike of the bounding faults. Total displacement is composed of fault throw on both faults and a component of vertical displacement due to fault normal rotation (FNR) in the ramp, which is equivalent to fault normal shear in (Huggins et al., 1995).

faults that define and enclose a relay zone are likely to be non-planar and non-parallel (Huggins et al., 1995; Soliva and Benedicto, 2004; Kristensen et al., 2008). Relay zones are therefore rarely, if ever, likely to have the simple tabular geometries depicted by Peacock and Sanderson's (1994) idealised model (**Fig. 1.1**).

Fault-arrays comprise multiple fault segments (Peacock and Sanderson, 1991; Childs et al., 1995; Childs et al., 1996a; Willemse, 1997; Crider and Pollard, 1998b; Peacock, 2002). Fault segments within fault-arrays can be hard-linked by discrete faults (**Fig. 1.3**) or soft-linked by zones of continuous deformation (**Fig. 1.2** and **Fig. 1.3**) (Peacock and Sanderson, 1991; Walsh and Watterson, 1991; Trudgill and Cartwright, 1994; Childs et al., 1995; Walsh et al., 2003b). Fault linkage is a dynamic process that evolves with increased displacement (Peacock and Sanderson, 1994; Childs et al., 1995; Walsh et al., 1999; Kristensen et al., 2008). In 3D, fault linkage has been inferred to develop by the progressive replacement of the fault tip line with a branch line (BL), which is where two fault surfaces intersect and join (Walsh et al., 1999; Kristensen et al., 2008). (Walsh et al., 1999) propose an evolutionary model of fault linkage from a branch point

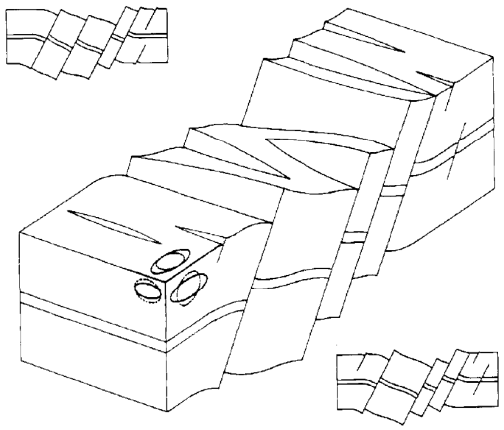

Fig. 1.3. Conceptual block diagram showing the principal features of geometric coherence. Faults can be soft-linked via a relay ramp or hard-linked by a branch line Insets show cross-sections on sides of the block. Strain ellipses on the sides of the block show the ductile strain, for the block as a whole, accommodated by structures which are too small to be represented on the diagram (unstrained circles shown with broken lines): the amount of strain shown is arbitrary (Walsh and Watterson, 1991).

(BP), to horizontal BL, to L-shaped BL, to U-shaped BL and finally to a fault bounded lens (**Fig. 1.4**). The basic building blocks of fault linkage are thus slip-aligned BL, slip-normal BL, and slip-oblique BL.

There are two end-member conceptual models of fault growth and linkage, the "isolated fault model" (Cartwright et al., 1996) and the "coherent fault model" (Walsh et al., 2003b) (**Fig. 1.5**). In the isolated fault model individual segments initially grew in isolation from other segments in the fault-array. In the coherent fault model individual fault segments initiate and grow as kinematically related components of the fault-array, which can be either hard-linked or soft-linked to each other (**Fig. 1.3** and **Fig. 1.5**). In the isolated fault model the total displacement distribution will have several local maxima, one located at the point of maximum displacement for each segment (**Fig. 1.5**b) (Cartwright et al., 1996). Whereas, in the coherent fault model the total displacement profile resembles that of a single isolated fault at all stages in the evolution of the fault-array (**Fig. 1.5**e) (Walsh et al., 2003b). Therefore, accurate measurements of the continuous, in addition to the discontinuous deformation, are vital to distinguish between these competing fault growth models (i.e. **Fig. 1.2**; b and d).Transfer of displacement between the bounding faults inevitably results in strain compatibility issues (i.e. the tendency to open voids or cause overlaps between

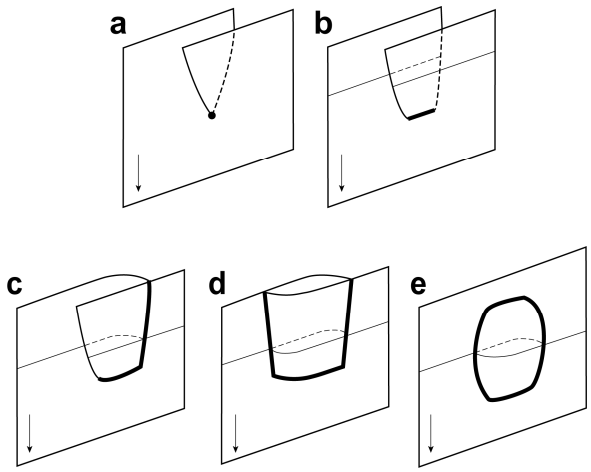

Fig. 1.4. A schematic diagram illustrating the 3D evolution stages of a branch line, arrows indicate the slip directions and fine lines are form lines. (a) Fault linkage initiates at a single unique BP. (b) A slip-normal BL initiates (bold). (c) Development of and L-shaped BL composing both a slip-aligned and slip-normal BL. (d) Both ends of the relay zone link forming a U-shaped BL. (e) And finally, a fault bounded lens. (c), (d) and (e) are all possible failed relay geometries, and (e) will only form if (c) and (d) are unstable. Taken from (Walsh et al., 1999).

adjacent rock volumes) within the relay zone. The main factors that influence the magnitude of strain incompatibility are: the BL orientations relative to the slip direction; the evolution of fault linkage in 3D; and the original locations, shapes, and orientations of the bounding faults (Walsh et al., 1999; Bonson et al., 2007). As a result of strain incompatibilities, sites of fault linkage are often associated with a wider and more developed damage zone (Davatzes et al., 2005; Fossen et al., 2005; Bonson et al., 2007). Damage zones can also develop due to fault propagation (Vermilye and Scholz, 1998) and growth (Shipton and Cowie, 2001). Conceptual models of fault zones depict a fault core, a relatively narrow zone of intense deformation on which displacement is localised, surrounded by a damage zone, a zone of diffuse and potentially interconnected fault/fracture network, both the fault core and damage zone can vary in space and time, as the fault evolves (See appendix 1: **Fig. A1** and **Table A1**) (Chester et al., 1993; Caine et al., 1996).

1.1 Primary aims of the thesis

1. To develop a new method for measuring and quantitatively analysing continuous deformations around faults.

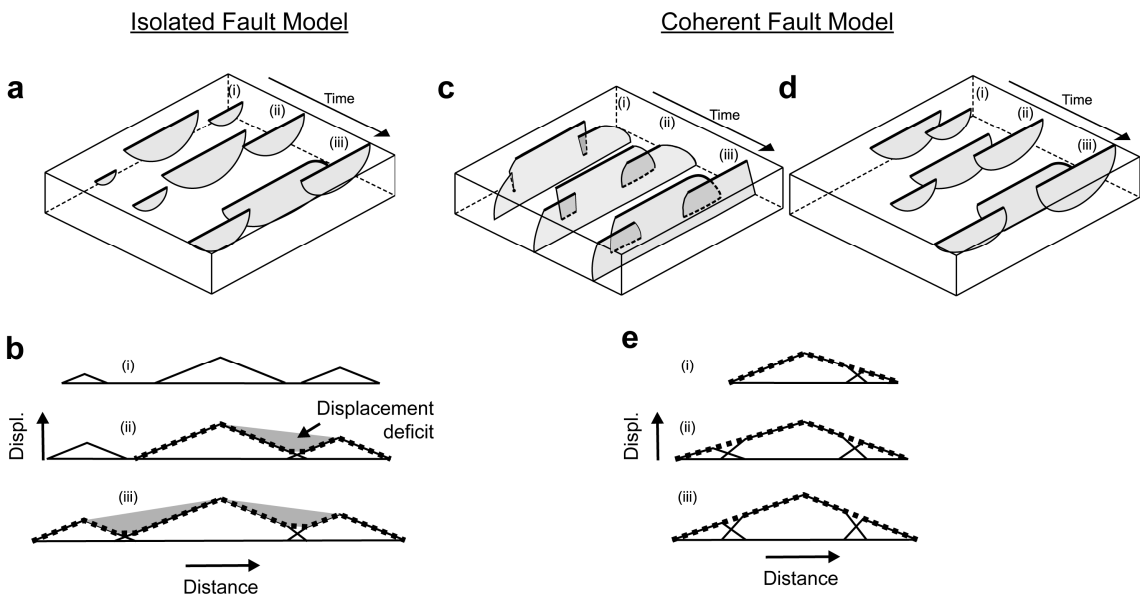

Fig. 1.5. Schematic illustrations of the two end-member models of formation of segmented fault-arrays. The block diagrams (a, c and d) each show three stages in the growth of a segmented fault-array (i–iii). The displacement-distance plots (b and e) are for the fault traces on the upper surfaces of the block diagrams (bold lines). The bold dashed lines in (c) indicate branch-lines. The coherent fault model is illustrated for segmented fault traces that are (c) hard-linked and formed by fault surface bifurcation and (d) soft-linked and formed by 3-D segmentation. The shaded areas in (b) indicate deficits in displacement between the adjacent fault segments, which are not due to not including vertical displacements from continuous deformation within relay zones. The aggregate displacement profiles (dashed lines) for the two models differ in that the points of maximum displacement are preserved where the faults were initially isolated (b) but a simple aggregate profile, that resembles that of an isolated fault, occurs at all stages of development in the coherent fault model (e). Modified from (Walsh et al., 2003b).

2. To determine if continuous deformation structures around mapped faults, such as fault propagation folds, monoclines and fault drag, are geometrically coherent parts of the overall fault-arrays.
3. To determine if faults grow and link as coherent fault-arrays (Walsh et al., 2003b) or by the coincidental overlap and linkage of originally isolated faults (Cartwright et al., 1996).
4. To investigate fault linkage geometries and strain compatibility issues in relay zones with slip-normal and slip-aligned branch lines.
5. To compile a database of relay zone aspect ratios (overlap/separation) from millimetre to kilometre-scales and refine power-law scaling relationships.
6. To determine what controls the global “ideal” aspect ratio of relay zones.
7. In regions that do not match the global relay zone aspect ratio, I aim to determine geological reasons for the observed shift in mean relay geometries.

1.2 Thesis outline and style

The content of chapters 2-7 are outlined individually below. The main result chapters (3-5) were submitted as standalone publications and as such, each contains a specific introduction, background, results, discussion, and conclusions. These chapters are recast, where appropriate, to fit consistently within the thesis. For the sake of consistency, pronouns referring to the author (myself) will appear in the plural form (i.e. we replaces I) throughout chapters 3-5 as an acknowledgement of co-authorship. The thesis only contains manuscripts for which I am the first author and was responsible for more than 90% of the data collection, interpretation and manuscript writing.

1.2.1 Chapter 2: Method

This chapter contains a detailed account of the theory and mechanisms behind the new utility developed during this thesis. The new surface attribute utility is applied to three different fault relay zones to demonstrate its ability to analyse faults at different scales and settings. The new utility is then contrasted to results from elastic dislocation models, as a means of confirming its validity for identifying fault-related strains. Criteria for identifying a coherent displacement profile are also outlined.

1.2.2 Chapter 3: Geometrically coherent continuous deformation in the volume surrounding a seismically imaged normal fault-array

Submitted as: Long, J.J., Imber, J., (2010). Geometrically coherent continuous deformation in the volume surrounding a seismically imaged normal fault-array. Journal of Structural Geology 32, 222-234.

This chapter is based on a detailed seismic study of the upper tip lines of a fault relay zone from the Inner Moray Firth. Detailed observations of both the discontinuous (i.e. faults) and continuous (i.e. monoclines) components of deformation are analysed, to give a new insight into the 3D distribution of fault-related strains surrounding a fault relay zone. This study is the first to conclusively show that seismic-scale monoclines are coherent parts of the fault-array.

1.2.3 Chapter 4: Strain compatibility and fault linkage evolution in relay zones on normal faults

Submitted as: Long, J.J., Imber, J., (2011). Strain compatibility and fault linkage evolution in relay zones on normal faults. Journal of Structural Geology (In review)

This chapter contains an in-depth study into 3D fault linkage geometries and evolution using seismic and outcrop studies. How strain compatibility is maintained within evolving non-tabular relay zones, is also investigated. Specific attention is applied to strain compatibility around slip-aligned and slip-normal branch lines.

1.2.4 Chapter 5: Fault relay zone scaling and the geological reasons for scatter in their geometries

Submitted as: Long, J.J., Imber, J., (2011). Fault relay zone scaling and the geological reasons for scatter in their geometries. Journal of Structural Geology (In review)

This chapter addresses the power-law scaling nature of relay zone aspect ratio (AR = overlap/separation), and what this implies about how faults interact at all scales. The geological reasons for higher than average outcrop-specific AR are investigated and modifications to fault interaction models are presented, which include the effect of mechanical layering and heterogeneities at fault tips.

1.2.5 Chapter 6: Discussion

This chapter contains discussion topics and wider applications relating to results obtained from preceding chapters. This chapter also presents possible future research topics that may be of importance to both scientific and industrial communities.

1.2.6 Chapter 7: Conclusions

This chapter summarises the main conclusions from chapters 3-5, and puts forth the main conclusions for the thesis.

Chapter 2. Method

A new method for analysing faults and fault-arrays was developed during the course of the thesis. The new method is based on the sampling of discontinuous and continuous geological structures (i.e. faults and normal drag/monoclines, respectively) from interpreted tri-mesh surfaces. In this chapter, I will give details on the creation of the digital tri-mesh surfaces, from both outcrop and seismic studies (Section 2.1), followed by how the new surface attribute was calculated (Section 2.2). I will then describe how geological information was extracted from 3D tri-mesh surfaces at centimetre, meter and kilometre-scales from laser scan, digital elevation models (DEM), and seismic data sources, respectively, to demonstrate the wide scope of locations and geological settings that can be analysed using the new surface attribute (Section 2.3). The new method is then compared to results from Elastic Dislocation (ED) models, which in theory should predict similar features (Section 2.4). And finally, I will show how the new method can be used to determine whether a fault-array is geometrically coherent (Section 2.5). For, identifying whether a fault-array is geometrically coherent is central to the rest of the thesis and underpins the results and interpretations (Chapters 3-5).

2.1 Surface building

2.1.1 Outcrop derived surfaces

2.1.1.1 Terrestrial laser scan data

In addition to traditional field work techniques, such as field mapping with a note book and compass, I used Terrestrial Laser Scanning (TLS) methods, also known as ground-based LiDAR, to collect digital 3D field data. This relatively new method of collecting geological data is briefly outlined and its advantages and limitations are noted, for details on TLS work flows see (Bellian et al., 2005; McCaffrey et al., 2005; Jones et al., 2009; Jones et al., In press).

The terrestrial laser scanner used was a Riegl Z420I with a mounted Nikon camera, which enables the collection of point-clouds coloured from the photos. Only surfaces

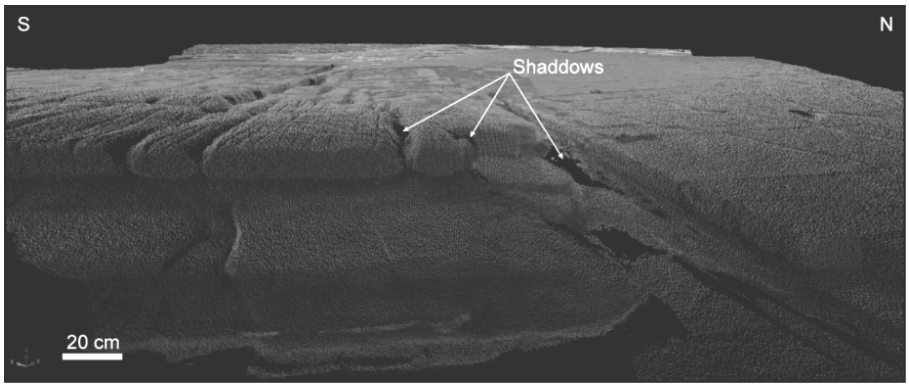

Fig. 2.1. A perspective view of a 3D point-cloud, acquired using TLS methods. The scan is of a faulted wave-cut-platform from Lilstock, Somerset, UK (See **Fig. 2.12**). Areas not in the direct line of sight of the scanner are left blank and shadows are cast over the outcrop. In this image multiple scan positions are combined to maximise data coverage.

in the line-of-sight of the scanner are recorded, as the laser does not penetrate the surface. Therefore, in highly textured outcrops data shadows can develop behind obstacles masking the target surface (**Fig. 2.1**). This limitation was overcome in part by using multiple tripod positions and merging the sequential scans. One of the main benefits of using TLS methods, and the main reason why it was used in this study, is that it can measure the detailed 3D shapes of exposed geological surfaces, such as bedding surfaces and fault surfaces (Jones et al., 2009). In this thesis, faulted, sub-horizontal, bedding surfaces were scanned at Kilve, Lilstock, and Lamberton (Chapter 5) (**Fig. 2.2**). In addition, TLS data from Moab was used to measure the geometries of a relay zone located above head height in a vertical road section (Chapter 4) (**Fig. 2.2**).

Before the point-cloud can be meshed to create a continuous surface, points from vegetation and non-target features, such as boulders/pebbles, must be removed. Depending on the size of the point-cloud and the processing power of your computer, the point-cloud must be down-sampled prior to meshing, for details of these post-processing steps see (Jones et al., 2009). When down-sampling was required care was taken to ensure the target geological feature, i.e. bedding surface, was not degraded. GoCad was used to mesh TLS point data with an average triangle size of 5 cm. The average triangle size was determined using a series of sensitivity studies, such as in (**Fig. 2.3**).

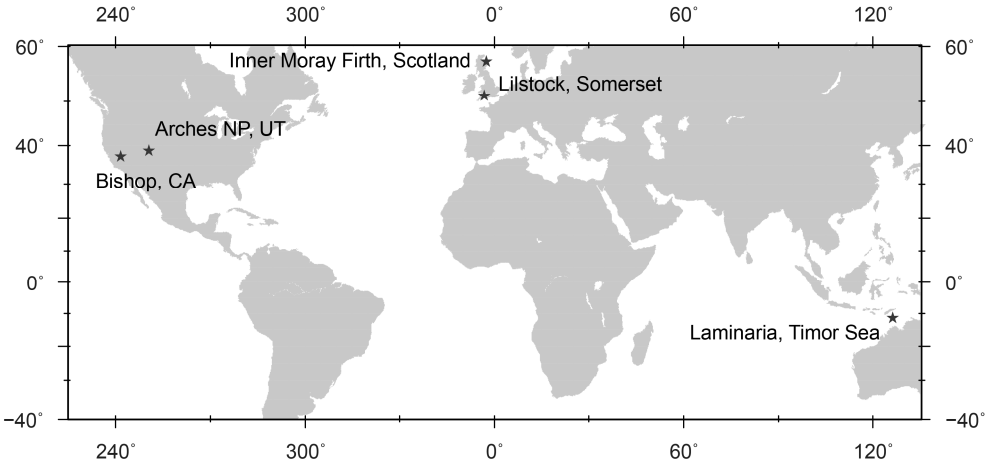

Fig. 2.2. A location map of the five case studies used to demonstrate the application of the FNR surface attribute to fault interpretation.

2.1.1.2 Digital elevation models

For outcrops with large (> 100 m) aerial extents terrestrial laser scanning was not possible, due to time and funding limitations. Therefore, freely available digital elevation models (DEM) were used to build surfaces for analysis. Where possible, the highest resolution DEM was obtained. From the DEM, continuously exposed faulted horizons were selected. These are mainly found in arid climates, such as south-eastern Utah, where vegetation cover is limited and erosion rates are low. As with TLS data, an optimum triangle size was established for each dataset and in general, an average triangle size of 10 m was used in the triangulation of DEM datasets.

2.1.2 3D Seismic derived surfaces

2.1.2.1 Interpretation of 3D seismic data

Unlike surfaces created from TLS and DEM data, which are digital surfaces fitted to outcrops that can be directly investigated in the field, surfaces derived from seismic reflection data need to be interpreted to extract geological features, and can only be sampled directly by well bores. Therefore, the methods used to interpret seismic horizons will affect the shape of the final surface.

To ensure the interpreted horizon surfaces accurately represent the seismic reflections the horizons were interpreted on closely spaced inline and crosslines (every 5th inline

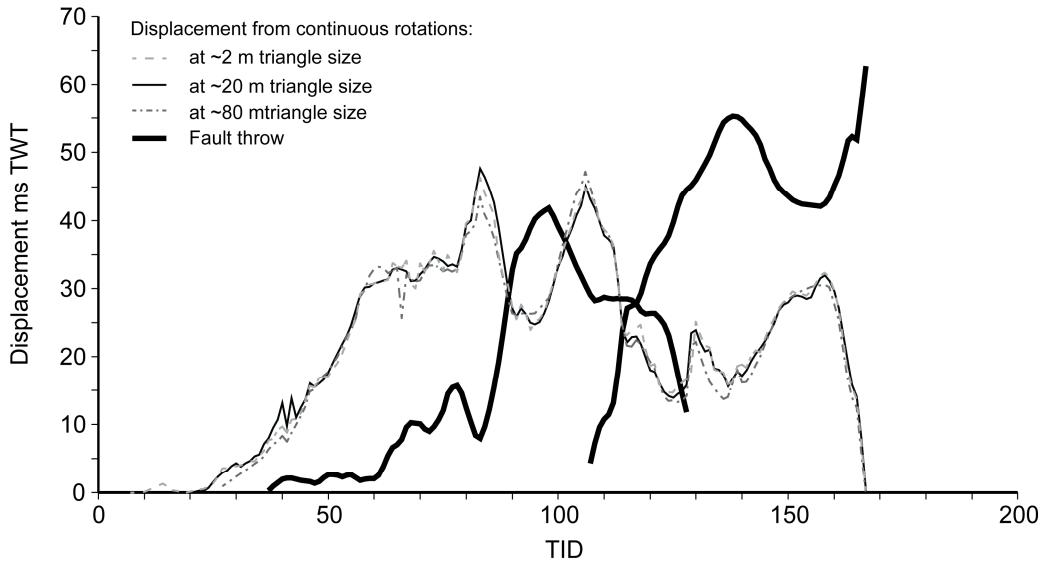

Fig. 2.3. An example of a sensitivity study to obtain the optimum triangle size for meshing raw data, such as point-clouds and seismic interpretations. In this example, from the Inner Moray Firth (IMF) seismic study (see chapter 3), the optimum average triangle size was selected to be 20 m, for it captures the along-strike changes in displacement, unlike the 80 m tri-mesh (red), and also filters out the noise observed in the 2 m tri-mesh (blue).

and crossline), and in areas of structural complexity, such as fault polygons and branch lines, the picking intensity increased to every inline and crossline. Automated picking was only used in areas of "tramline" reflections. All interpretations where checked to ensure they were geologically realistic and matched the seismic reflections. The software packages Petrel and TrapTester were used to interpret the seismic volumes used in this thesis.

Seismic data has inherent resolution limits and at depths similar to those studied for this thesis (>1.5–2 seconds TWT or approximately 2 km) only faults with throws greater than 20 m will typically have observable offsets (Townsend et al., 1998). Large sections of the fault surfaces with throws < 20 m are therefore not resolved through mapping of offset horizons (See appendix 1: **Fig. A2**b). However, by mapping the continuous deformation present beyond the seismically-resolved fault tips a greater proportion of the fault-related strain can be measured (**Fig. 2.4**a). This continuous (ductile) deformation, at the scale of observation, can be mapped with confidence due to the close spacing of the 3D seismic lines. The lateral resolution of seismic data depends on the width of the Fresnel zone, which is dependent on the wave-length of the seismic signal and the depth of the structure being imaged (Brown, 2004). The lateral

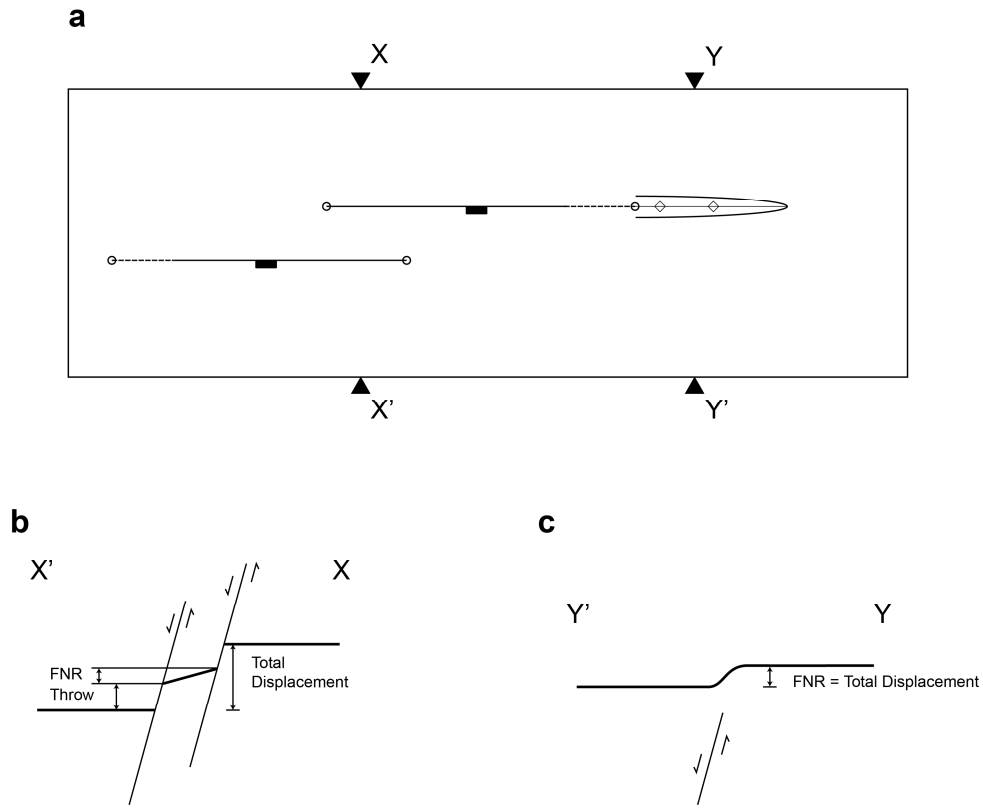

Fig. 2.4. (a) A schematic map view of two overlapping fault segments separated by a relay zone. The fault tips are circled. Along-strike of the fault tip, which is cut by cross-section Y, there is a monocline. (b) Cross-section orientated X-X', In the relay ramp beds are rotated towards the mutual hanging wall, here termed fault normal rotation FNR, which is equivalent to fault normal shear in (Cartwright et al., 1995; Huggins et al., 1995). The total amount of vertical displacement, across the fault-array, is composed of both fault throw and FNR. (c) Cross-section orientated Y-Y', across the monocline total vertical displacement equals FNR.

resolution thus decreases with depth. For the 3D seismic datasets used in this thesis, structures separated by a few tens of meters cannot be individually imaged. Therefore, the imaged locations of faults in seismic data are only ever approximations of their true locations, unless directly correlated by well data.

Velocity affects also need to be considered when interpreting seismic reflections in time. Sensitivity studies were conducted for all seismic datasets used in this thesis to determine if velocity structures altered the geometries of the studied faults. In all areas no lateral velocity anomalies, such as salt diapirs, existed, and the depth converted sections closely resembled the time sections (see each chapter for details). Therefore, to prevent the introduction of additional uncertainties, due to depth

converting the seismic volumes, the time-migrated volumes were used to analyse fault-related deformation.

2.1.2.2 Creating a surface from seismic interpretations

The next step was to mesh the interpreted seismic picks. Sensitivity studies were performed on selected horizon grids to determine the optimum triangle size. Large triangles produce smoother surfaces. Smaller triangles more closely match the picked horizon grid, but increase the potential for noise. In this case, "noise" refers to scatter due to natural variability in reflector dip that is not fault-related, miss-correlations of horizon grids across faults, and the inherent uncertainty associated with the sample interval of the seismic data (**Fig. 2.3**). For each dataset the triangle size varied, but for most seismic studies the average triangle size was 20 m, which ensured a representative reconstruction of the raw data for each location. The software package TrapTester was used to produce the tri-mesh surfaces for all seismic derived interpretations.

Workflow charts for building digital surfaces can be found in appendix 2: (**Fig. A3**. and **Fig. A4**).

2.2 Surface analysis

During the course of my thesis, I recognised the importance of being able to accurately and effectively sample areas of continuous horizon rotations in and around relay zones, for including vertical displacements across areas of continuous deformation can alter the shapes of displacement distance (d-x) plots (Huggins et al., 1995). With this brief, I developed a concept for a surface attribute that measures the location, intensity and vertical displacements in areas of continuous horizon rotation. Badley Geoscience Ltd. implemented my concept into TrapTester, on my behalf, and now a new utility exists that can quickly extract geological information from 3D tri-mesh surfaces. The surface attribute can be calculated from any tri-mesh from any scale. The new attribute records the variation of dip across a surface, measured along an arbitrary orientated transect line, which is equivalent to measuring the apparent dip of a surface. It also

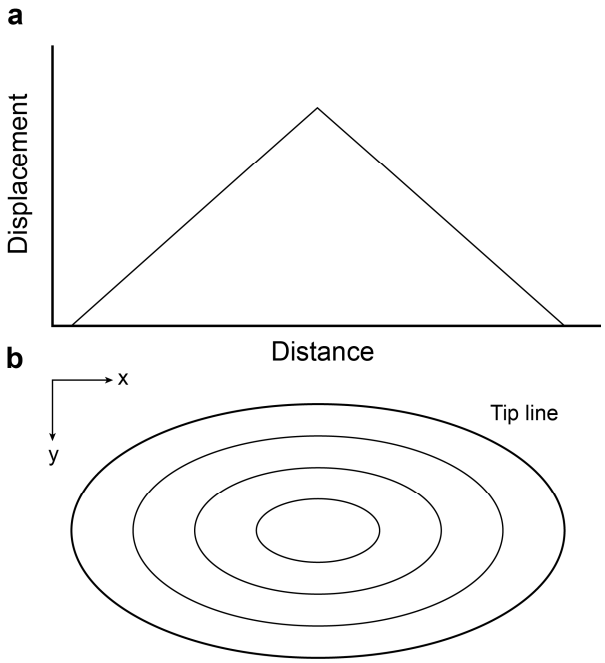

Fig. 2.5. (a) An "ideal" displacement distance (d-x) profile for an isolated fault. Displacement increases from zero at the tips to a maximum in the centre. (b) A strike projection of an "idealised" elliptical fault. Displacement decreased towards the centre of the fault surface in both x and y directions (Walsh et al., 2003b).

measures the vertical offset between points along a transect line, which can be used to construct displacement/distance plots. The attribute is termed FNR, which stands for Fault Normal Rotation (**Fig. 2.4**). In the following sections, I present details of how FNR was calculated, and in sections (2.3.1) to (2.3.3), three different relay zones, from a range of scales and data sources, are documented using the FNR surface attribute.

2.2.1 Theory behind the Fault Normal Rotation method

Fault-arrays at all scales consist of both discontinuous (i.e. faults) and continuous (i.e. monoclines or fault drag) deformation. It is common practice to record the vertical component of displacement (throw) between the hanging wall and footwall cut-offs, which defines the fault polygon. Previous studies have also noted the importance of continuous deformation, especially within relay ramps, in producing a geometrically coherent fault-array (Walsh and Watterson, 1991; Huggins et al., 1995). The FNR surface attribute builds on observations by Huggins et al., (1995) and automates the process of extracting fault normal shear measurements, which is equivalent to FNR, allowing the effective analysis on both the discontinuous and continuous deformation around mapped faults (**Fig. 2.4**). FNR measures both rotations synthetic to the faults,

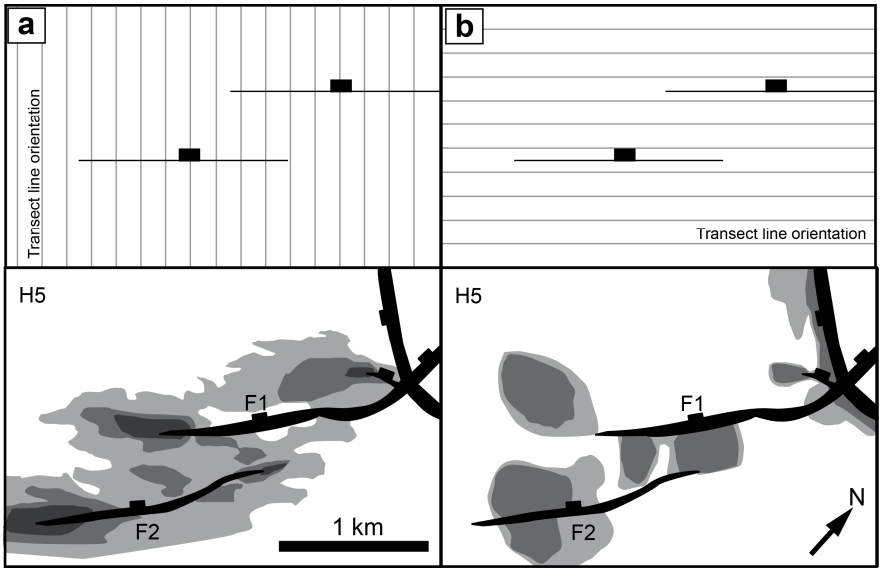

Fig. 2.6. (a) Top, a schematic illustration of the orientation of the sample lines relative to the studied faults. Bottom, FNR measured from strike normal transect lines are shown. Features such as monoclines are observed to extend along-strike of the mapped fault tips. The example comes from the IMF fault-array presented in chapter 3. (b) Top, transect lines are orientated parallel to the average strike of the fault-array. Bottom, the corresponding FNR map (technically these are not fault normal rotations, as they are recording rotations parallel to faults F1 and F2).

such as monoclines and fault drags, as well as reverse rotations, such as footwall uplift and hanging wall subsidence. For this thesis, only the synthetic shear/rotations are studied in the following chapters.

Faults formed under the same regional extension episode are assumed to have approximately sub-parallel strikes within a fault-array. This assumption allows the use of a single transect line orientation to sample multiple fault traces normal to their strike, which permits displacements between different strands of a fault-array to be compared.

It is hypothesised that by including the continuous deformation around mapped discontinuous fault traces will enable a greater proportion of the fault-related strains to be measured. Assuming fault-arrays are geometrically coherent and form due to a common regional extension direction, the total d-x profile, which includes vertical displacements from areas of continuous deformations, should more closely resemble a d-x profile of an isolated fault than the fault throw profiles alone (Walsh et al., 2003b). An idealised d-x profile, for an isolated fault, has zero displacement at the fault tips and displacement increases smoothly along a single gradient to a maximum at the

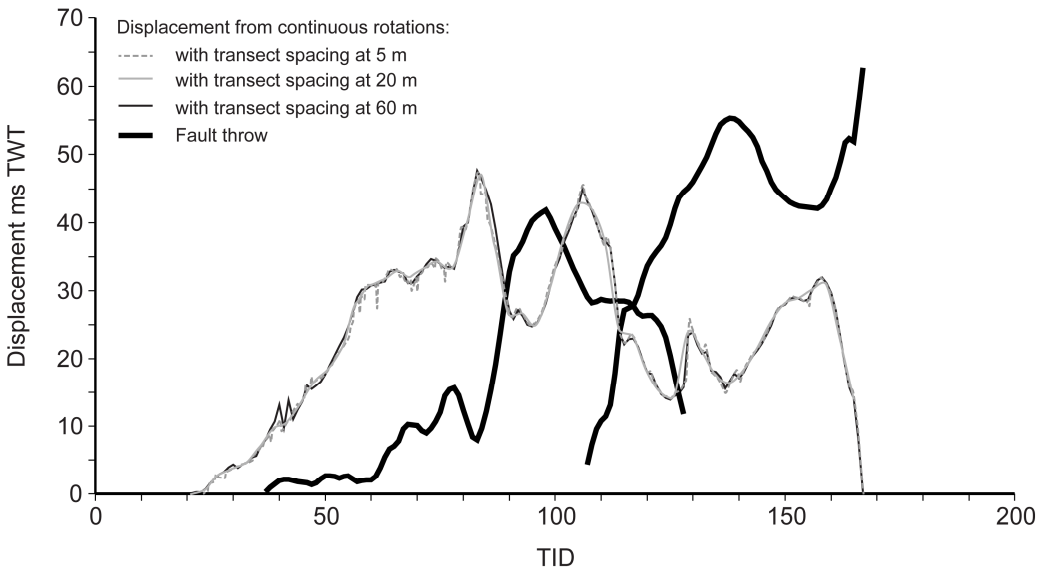

Fig. 2.7. An example of a sensitivity study to obtain the optimum transect line spacing for extracting displacements from continuous rotations (i.e. FNR) around the mapped fault-array. In this example, from the IMF seismic study (see chapter 3; horizon H6), an optimum transect line spacing of 20 m was selected, for it records the along-strike changes in displacement unlike the 60 m example (red), while removing the low level spikes observed in the 5 m example (blue).

centre of the fault (**Fig. 2.5**) (Walsh and Watterson, 1989; Peacock and Sanderson, 1991; Dawers and Anders, 1995).

2.2.2 Creating a sample gird

The sample grid consists of equally spaced transect lines, which are aligned perpendicular to the average strike of the studied fault-array (**Fig. 2.6**a). The spacing of the transect lines used in this study varies from 25 m at seismic-scales to 5 cm at outcrop-scales. Sensitivity studies were performed to ascertain the optimum transect line spacing for different datasets. Large transect spacing produces a smoothly varying displacement/length profile. Whereas, small transect spacing captures more of the along-strike variability (**Fig. 2.7**). The absolute minimum spacing is limited by the processing power of the computer. All faults in this thesis are assumed to be dip-slip (see relevant sections for details). The location of the sample grid was fixed, allowing comparison of displacements on different horizons. In addition, the orientation of the transect lines also acts as a filter and enhances structures that strike normal to them, and as a consequence also mask structures that strike parallel to the transect lines. For example (**Fig. 2.6**) shows the same horizon but with sample lines orientated perpendicular and parallel to the average fault strike. A disadvantage of using a fixed,

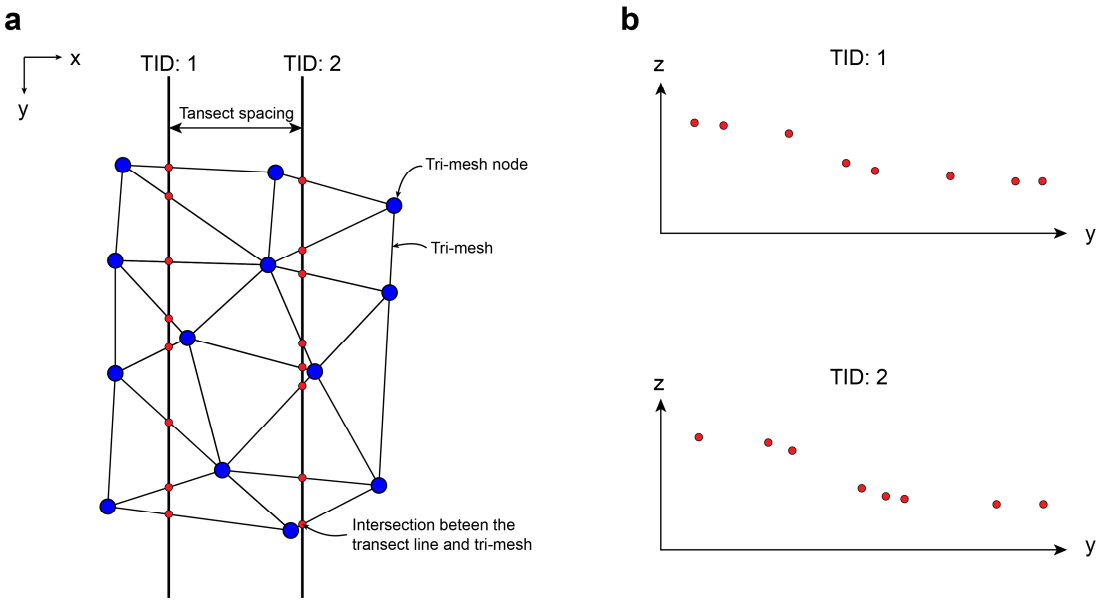

Fig. 2.8. (a) A schematic map view illustration of how FNR is calculated. Transect lines have a fixed orientation and separation. A data point is recorded at the intersection between the transect line (bold lines) and the edges of the triangles (thin lines) that make up the interpreted tri-mesh surface. Attributes collected at each intersection are; TID: transect ID number; XYZ coordinates; DIP: apparent dip between successive points; S: distance along a transect line; DS: distance between successive points along a transect line; and DZ: difference in depth between successive points along a transect line. (b) Profile plots of the transect lines in (a).

oriented sample grid arises when fault orientations varies along-strike, such as in areas of fault linkage. This geometric difference creates a miss-match between fault throw and adjacent continuous displacement, adding noise to the aggregate d-x profiles. In the majority of the studies, all faults are sub-parallel, so this effect was negligible.

2.2.3 Calculating FNR from tri-mesh surfaces

The FNR attribute was measured along orientated transect lines and is thus a measurement of the apparent dips across a surface in a pre-defined orientation. The measurements are taken at the intersections between the transect line and the edges of the triangles that compose the tri-mesh surface (**Fig. 2.8**). The apparent dip is measured between adjacent nodes. From the raw apparent dip maps areas of synthetic dip were selected, i.e. apparent dips that dip in the same direction as the nearby mapped faults. The next step was to distinguish apparent dips formed due to the continuous deformation of the volume surrounding the mapped fault-array, from dips caused by regional tilting of each horizon. The magnitude of regional tilt on each horizon was calculated in areas away from the mapped fault-array, and apparent dips

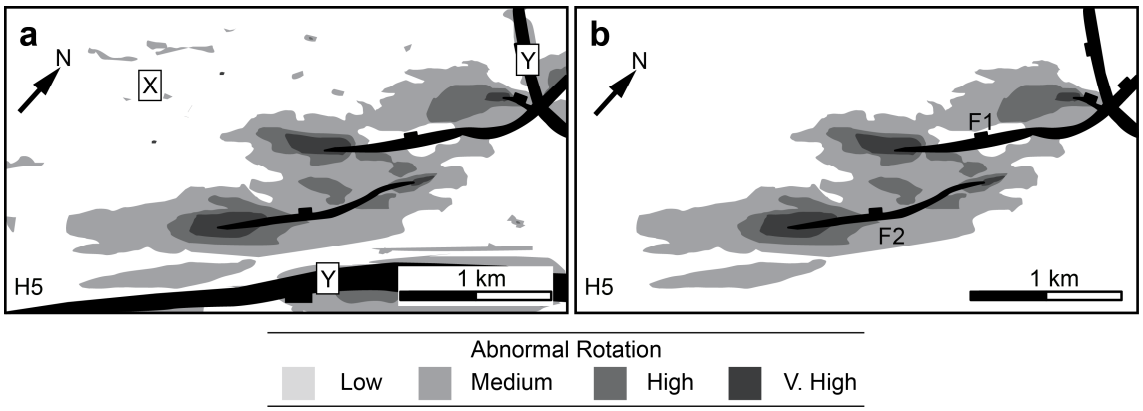

Fig. 2.9. (a) Areas of abnormal rotation where all apparent dips above the defined background regional values are selected, resulting in the selection of miss-picks and artefacts (X), and geometries on adjacent faults (Y). (b) Features, such as X and Y are removed to leave the abnormal rotations (FNR) attributed to the studied fault-array (F1 and F2).

less than or equal to the regional tilt were excluded from further analysis. Large apparent dips can also be caused by miss-ties in horizon grids between adjacent inlines or crosslines (**Fig. 2.9**a; point X) and/or by deformation related to other faults (**Fig. 2.9**a; point Y). These anomalies were removed by visual inspection and were also excluded from further analysis. The remaining areas of abnormal rotation were hypothesised to be fault-related continuous deformation in the volume surrounding the studied fault-array, hereafter termed "FNR" (**Fig. 2.9**b).

Finally, the vertical displacements attributed to FNR (i.e. continuous fault-related deformation) were summed along each sample line (**Fig. 2.10**), allowing direct comparison with fault throw measurements (**Fig. 2.4**).

2.2.4 Interpreting FNR maps and displacement profiles

The FNR surface attribute is only a tool to help the geologist/seismic interpreter and as such should be used in conjunction with existing interpretation techniques. Interpreting faults in seismic data is normally done on successive vertical seismic sections. However, FNR maps are horizon based and faults can equally be interpreted in map view, which captures more of the along-strike changes of fault-arrays (**Fig. 2.9**b). The raw data points, which coincide with the intersections between, the transect lines and tri-mesh edges, are gridded to aid interpretations, for details see appendix 2: **Fig. A5**. Interpretations from different horizons can be stacked to produce 3D fault surfaces surrounded by fault-related deformation (see Chapters 3 and 4 and figures therein).

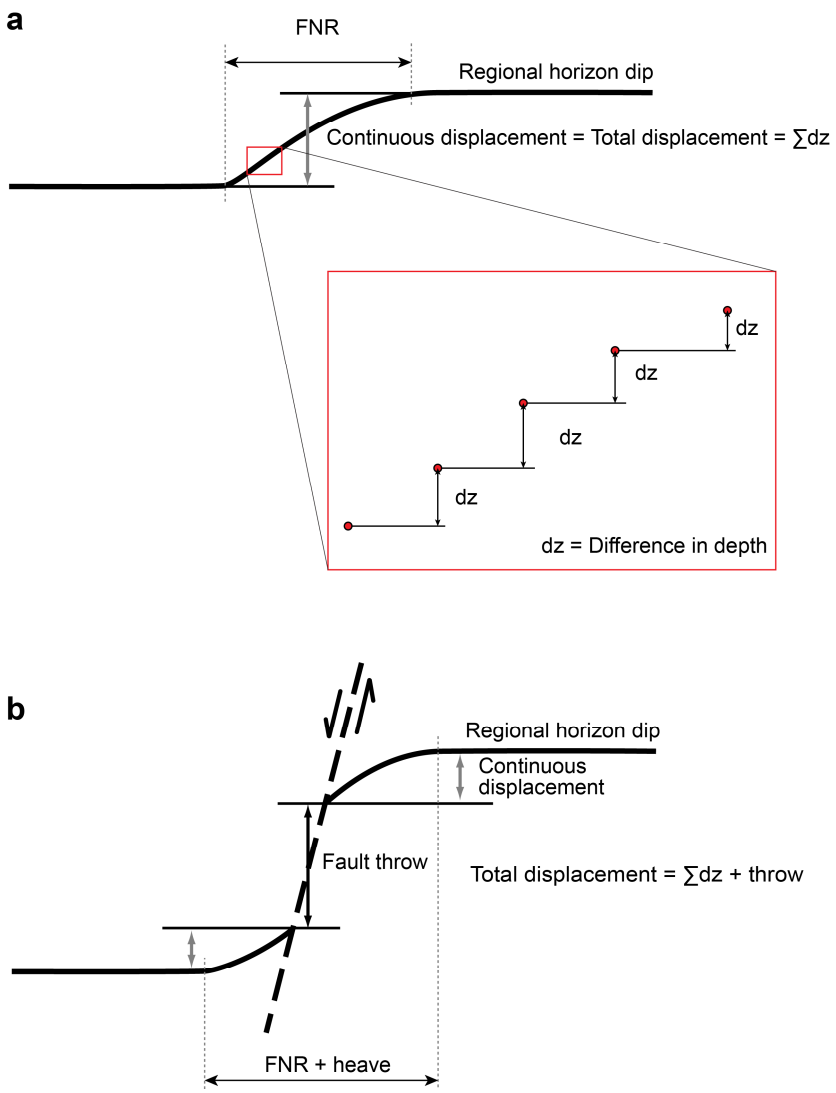

Fig. 2.10. Schematic illustrations of displacement measurements for two transect lines. The limits of abnormal rotation (i.e. FNR) are defined by the departure from the regional horizon dip. (a) The total vertical displacement is equal to the continuous displacement, which is the sum of the difference in depth measured between successive data points. Data points are located at the intersection between a transect line and the tri-mesh boundaries (**Fig. 2.8**). (b) Total displacement is a combination of fault throw and continuous displacement.

Three aspects of the FNR surface attribute can be used to interpret the location and properties of faults: the spatial distribution of FNR; the variation in intensity of apparent dip; and the vertical displacements calculated across the selected areas of interest. The location and intensity of apparent dips (gray scale images) can be interpreted by a geologist in similar ways to conventional faulted horizon dip maps (**Fig. 2.11**). Elongate bands of concentrated high FNR (dark greys to black points) are interpreted with confidence to be fault polygons (**Fig. 2.11**). In comparison, areas of diffuse low to medium FNR (light grey to grey points) that enclose the fault polygons are more difficult to interpret, as a range of geological structures can produce such

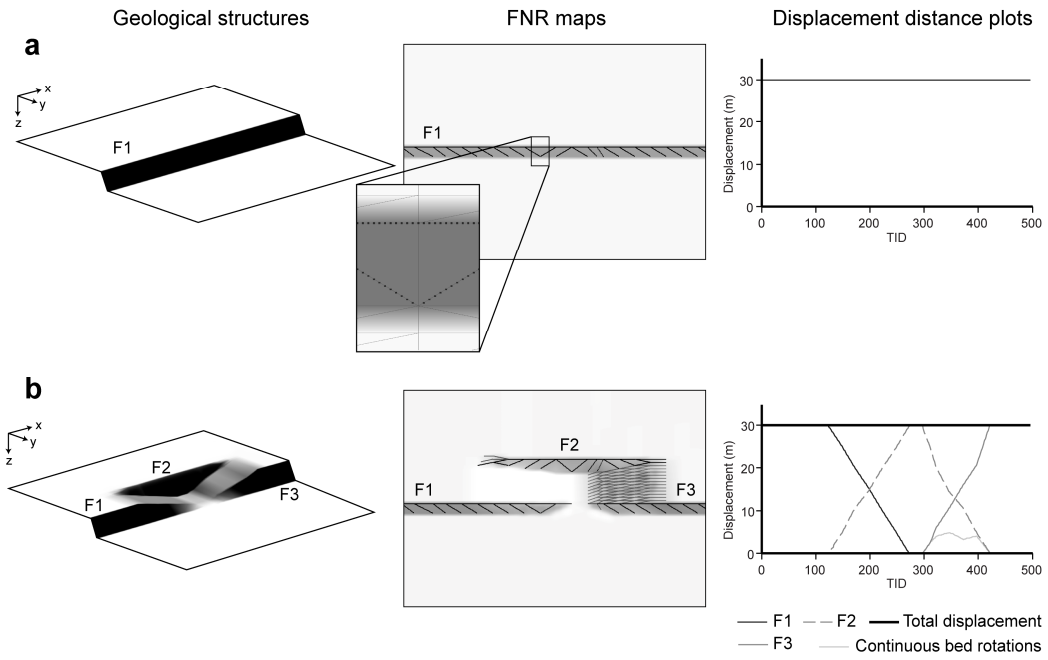

Fig. 2.11. Schematic models showing commonly observed relay ramp structures; a 3D view of the tri-mesh surface (left); the associated FNR map, consisting of the FNR point data overlaid on the shaded horizon surface, which appear as line at this scale (middle); and d-x profiles calculated from FNR point data (right). In each example transect lines run parallel to the y axis. (a) A simple fault scarp, FNR maps show a laterally continuous linear high (black points) and the d-x profile has a uniform total displacement. Inset, a close up image, the point data coincides with the edges of the tri-mesh. (b) A fault-array separated by two open relay ramps, one dips parallel to fault strike and the other has a component of dip towards the mutual hanging wall. In the relay ramp between F1 and F2, no FNR is present, as there is no variation in dip along the transect lines. The ramp between F2 and F3 has a component of dip normal to fault strike i.e. FNR (grey points). All structures sum to give a uniform total d-x profile.

rotations of seismic reflections (Steen et al., 1998; Townsend et al., 1998). At present, there are no seismic tools to image the unique distribution of geological structures in areas of diffuse continuous deformation around imaged fault polygons. Therefore, the FNR surface attribute only images changes in bulk deformation styles of the seismic horizon, from which faults and fault linkage are interpreted. The displacement from selected areas of FNR can also be plotted (**Fig. 2.11**: right), which graphically illustrate the along-strike changes in displacement on different structures. D-x profiles plotted from FNR data can be interpreted in similar ways to fault d-x plots (Ferrill and Morris, 2001). However, in FNR d-x profiles both continuous and discontinuous deformations are included.

In both seismic and outcrop derived data artefacts within the data need to be identified and discarded, such as river channels in seismic data and cover vegetation in

terrestrial laser scan data. In outcrop data non-tectonic features can be easily identify by visual inspection, whereas in seismic data more care is needed to recognise them. To help the reader to understand how to interpret FNR maps and d-x profiles, three examples from a range of scales and data types are presented in the next section. These examples also aim to demonstrate that the new FNR method, developed during my thesis, is a valid method for analysing geological structures at all scales.

2.3 Case studies from three different scales

2.3.1 A centimetre-scale example: Lilstock

Lilstock is situated on the Somerset coastline, UK, and contains world class exposures of centimetre-scale relay ramps (**Fig. 2.2**) (Peacock and Sanderson, 1991, 1994). The stratigraphy consists of alternating Lower Jurassic limestone and shale beds. The outcrops studied consist of a 12 cm thick limestone bed surrounded by a 69 cm thick shale bed above, and a 50 cm thick shale bed below (**Fig. 2.12**). Faults studied trend E-W and are probably related to the opening of the Bristol Channel basin during the Mesozoic (Peacock and Sanderson, 1994: and references therein). Faults are dip-slip with no signs of reactivation (**Fig. 2.12**). The relay ramp in (**Fig. 2.12** and **Fig. 2.13**) has a separation distance of 2.71 m and an average throw on the bounding faults of 20 cm. All bed rotations are towards the mutual hanging wall and are synthetic with the fault dips (**Fig. 2.13**). Veins form initially in the more competent limestone beds and do not continue into the shale beds (**Fig. 2.12**b: arrows). With continued extension faults grow within the veins forming pull-apart structures (Peacock and Sanderson, 1991, 1992). The veins at Kilve and Lilstock form prior to the faults (Crider and Peacock, 2004). The limestone bed rotates as rigid blocks bounded by veins and/or faults (**Fig. 2.12**b: location X).

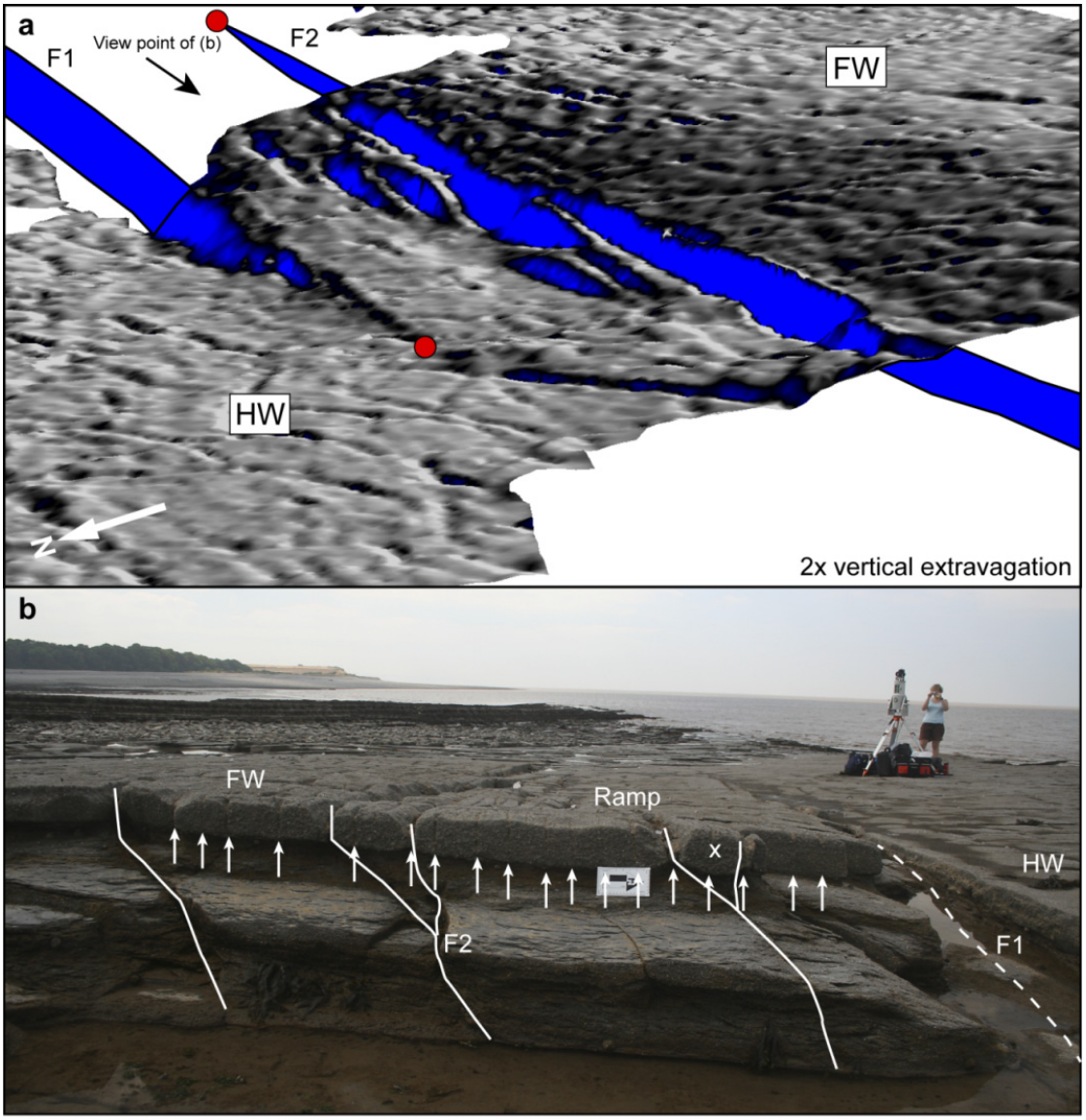

Fig. 2.12. (a) A perspective view of the Lilstock relay ramp (**Fig. 2.2**), looking SE, created from laser scan data (**Fig. 2.1**). The fault tips are located with circles. The surface is shaded for FNR (dip measured along transects orientated normal to the strike of faults F1 and F2). Light grey to white equal low FNR dips and blacks to dark grey high FNR dips. A wide zone of synthetic rotation towards the mutual hanging wall is located in the immediate footwall of F2. For a detailed FNR map see **Fig. 2.13**. (b) Photo cross-section of the ramp looking west. Faults are interpreted and veins within the limestone bed are located with arrows. Away from the relay zone there is limited veining. The limestone beds rotate as rigid fault bounded blocks within the surrounding shale layers, see (X).

Surfaces were created from 3D point data collected using TLS methods (Jones et al., 2009). Three scan positions encircled the relay ramp, of which only one is shown for brevity (**Fig. 2.12**b). The data was down-sampled to a point spacing of 5 cm and was meshed with triangles with an average size of 5 cm. Transect lines were orientated N-S, normal to the strike of the bounding faults, and transect spacing was 5 cm.

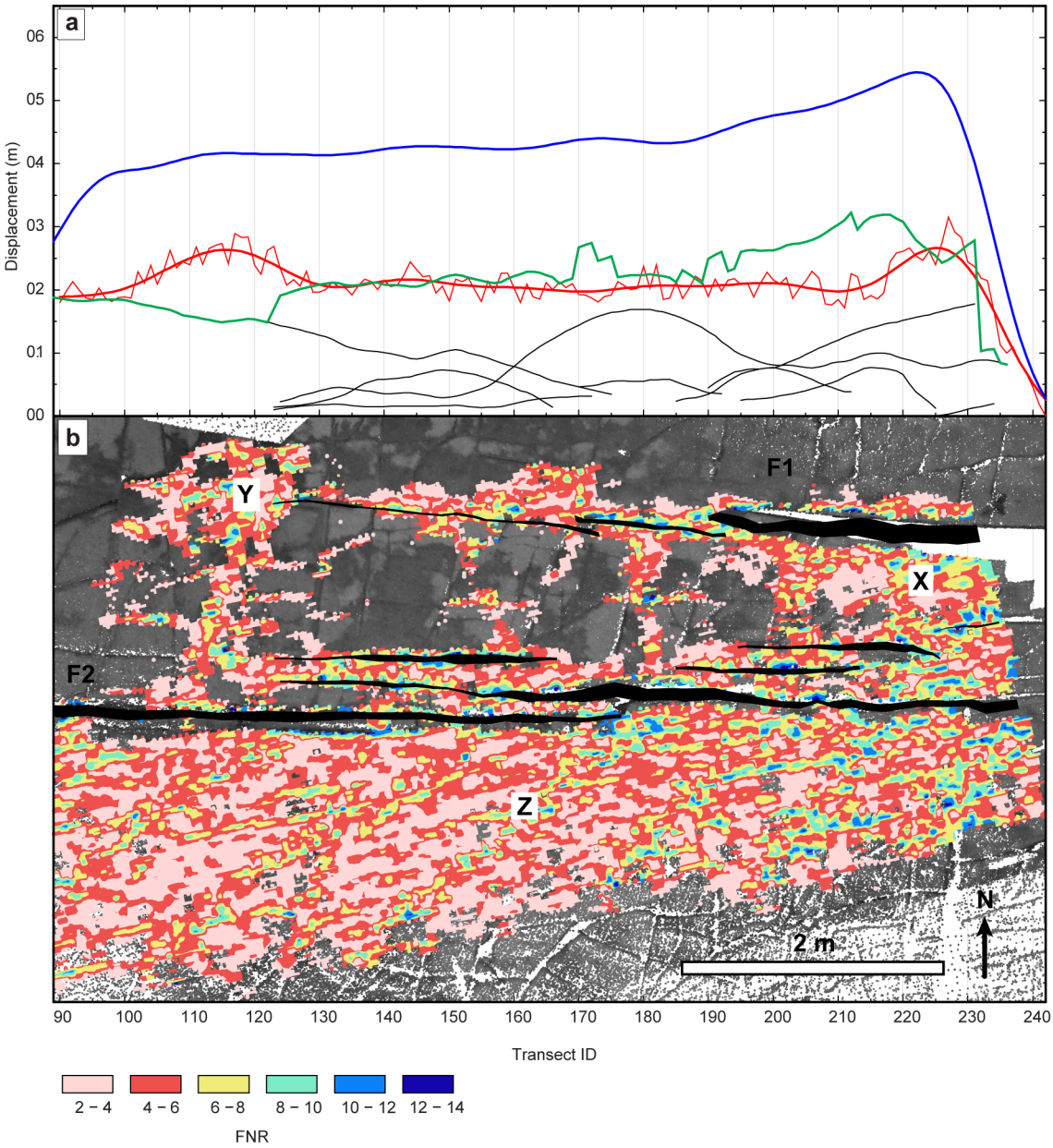

Fig. 2.13. (a) Displacement distance plot for the Lilstock relay ramp (**Fig. 2.12**). Black lines are throw profiles for the individual fault polygons in (b). The thin red line is the vertical displacement calculated from areas of FNR (b: pinks to blue). The green line is the aggregate displacement for all the fault polygons. The thick red line is a smoothed version of the thin red line, which removes the low level noise relating to erosion features and vegetation on the wave-cut-platform. (b) Map view of coloured laser scan data and overlying FNR maps. Faults F1 and F2 are parallel with near constant separation along-strike. Internal faulting forms en-echelon patterns between F2 and F1 and also trend parallel to the main bounding faults and vein orientations within the ramp. The mottled FNR map results from small (1-5 mm) undulations in the bedding surface due to the preferential erosion of veins and fractures. (X) The ramp has more rotations towards the mutual hanging wall in the east than the west. (Y) A zone of high FNR exist along-strike of the bounding fault F1. (Z) A ~2 m wide zone of high FNR stretches along the length of the relay ramp in the mutual footwall.

2.3.1.1 Results from Lilstock

The separation distance between the fault scarps remain approximately constant along-strike for each of the mapped bounding faults (**Fig. 2.13**: F1 and F2). The fault

spacing also coincides with the initial vein spacing (**Fig. 2.12**b) and the faults are observed to exploit these weaknesses and the fault tips pass laterally into veins.

The FNR maps record the distribution and intensity of the continuous deformation around the mapped faults. The patchy nature of the FNR map is due to erosion and the presence of low-relief vegetation and molluscs, which could not be removed from the TLS point-cloud (**Fig. 2.13**). These non-tectonic features also account for the spiky profile in (**Fig. 2.13**: thin red line). Within the ramp, there is a greater amount of continuous deformation (FNR) in the east (annotated X), which coincides with a series of en-echelon faults. In addition, the north bounding fault F1 has a zone of high FNR at its west tip (annotated Y). In the mutual footwall there is a ~2 m wide zone of FNR that dips towards the mutual hanging wall (annotated Z). The footwall deformation (Z) accounts for the majority of the observed FNR displacement (red line), despite it appearing to be a relatively minor feature in the outcrop photo (**Fig. 2.12**b). The total vertical displacements calculated from areas of FNR (red line) are greater than the throws measured on the fault scarps (**Fig. 2.13**a: black lines).

From Transect ID numbers 100 to 230, which removes sampling related edge effects, the total d-x profile decreases (blue line) towards the west. This is supported by field observations that indicate the fault-array decreases in displacement to the west (offshore).

2.3.1.2 Interpretation and discussion: Lilstock

The new method allows the relatively quick analysis of continuous deformation around a centimetre-scale relay zone, in terms of its distribution and contribution to the d-x plots (**Fig. 2.13**). The aggregate d-x profile for the fault polygons is irregular with variable displacement gradients along-strike (**Fig. 2.13**: green line). Whereas, including vertical displacements from areas of FNR has produced a total d-x profile that more closely resembles that of an isolated fault (**Fig. 2.13**: blue line). For displacements decrease steadily towards the west, which is comparable to one side of the idealised d-x profile in (**Fig. 2.5**a).

Continuous deformation, around faults in Lilstock, accounts for approximately half of the total displacement in the fault-array (**Fig. 2.13**). The limestone beds, at this scale, are able to rotate within the surrounding shale layers, as fault bounded blocks (**Fig. 2.12**: X). In mechanically layered sequences competent beds can rotate, as the weaker beds (i.e. shale) can accommodate volumetric strain by ductile movement (Ferrill and Morris, 2008). Therefore, the interbedded mechanical stratigraphy at Lilstock is proposed to facilitate the relatively high proportion of continuous deformation (**Fig. 2.13**). This is consistent with observations of monoclines on the wave-cut-platform from Kilve (located 2 km west of Lilstock), see chapter 5. Without the use of the FNR surface attribute the amount of displacement accommodated by areas of continuous bed rotations would have been difficult to ascertain.

2.3.1.3 Conclusions: Lilstock

1. The FNR surface attribute can be used to quantitatively interpret fault-related strains around mapped faults with centimetre-scale displacements at a resolution and accuracy not previously possible.
2. Fault throw and FNR displacements sum to give a total d-x profile that resembles that of a single isolated fault, which indicates the FNR maps highlight geometrically coherent areas of fault-related strain around mapped faults.
3. In detail, veins at Lilstock are initially confined within the mechanically strong limestone beds and faults subsequently form within the pre-existing veins.
4. And, at this scale, the limestone beds rotate as rigid fault bounded blocks and the amount of displacement calculated from areas of FNR are of equal magnitude to displacements on individual fault traces.

2.3.2 A meter-scale example: Delicate Arch relay ramp

Delicate Arch relay ramp is located in Arches National Park, Utah (**Fig. 2.2**). The relay ramp is 114 m wide and has an overlap length of 531 m (**Fig. 2.14**). The summed displacement across the two bounding faults is approximately 50 m (Rotevatn et al., 2007). The scale of the Delicate Arch relay ramp is comparable to the smallest resolvable relay ramps visible in most 3D seismic datasets. The bounding faults trend E-W and form in response to flexure of the hanging wall on the nearby larger offset fault, which bounds the southern margin of the Cache valley (Doelling, 2001). Faults in the Cache valley formed due to the collapse of an elongate salt dome in the Tertiary

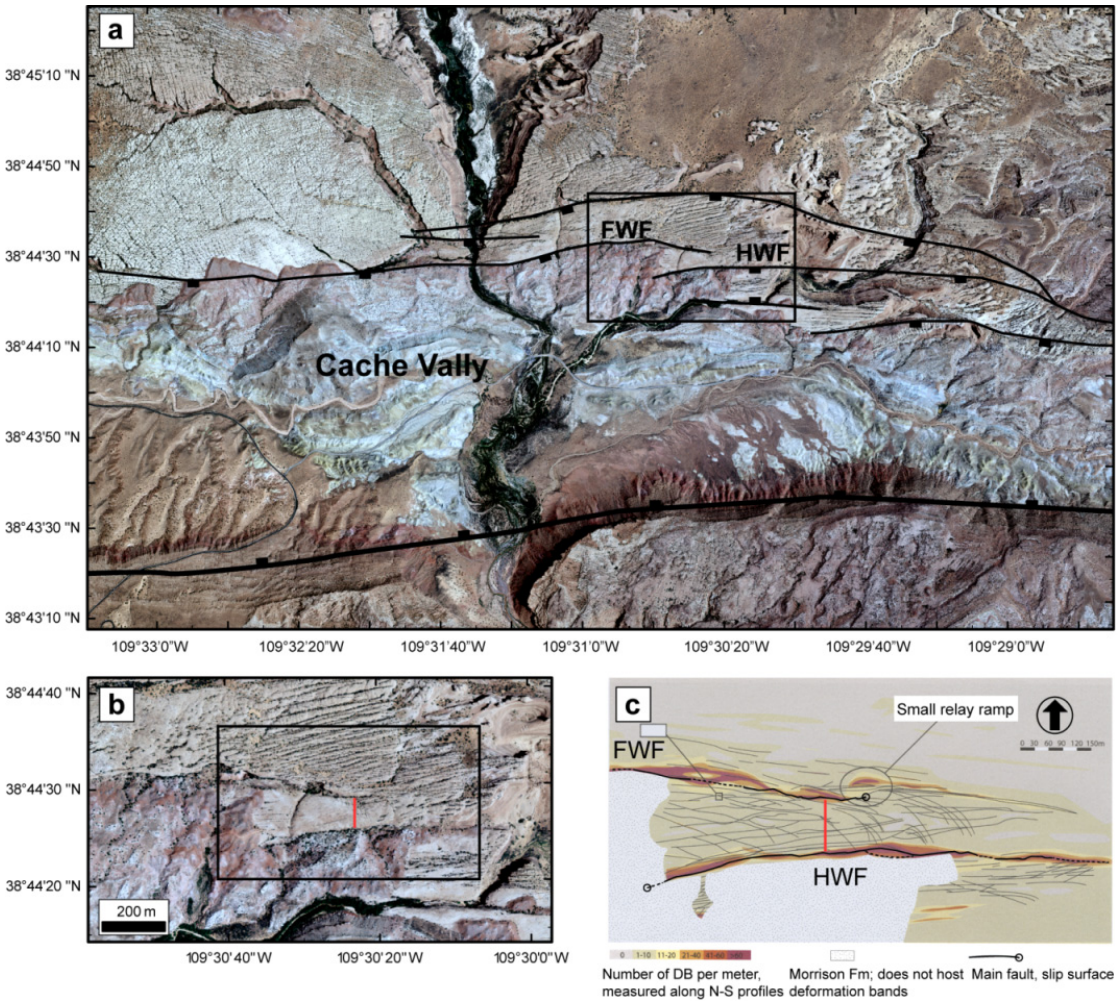

Fig. 2.14. (a) Aerial photo of the Cache Valley and Delicate Arch relay ramp. The main fault traces, visible in the aerial photo, are interpreted. The bounding faults of the Delicate Arch relay ramp (HWF and FWF) form in response to the handing wall roll over on the main valley bounding fault on the south flank of the Cache Valley (Rotevatn et al., 2007). (b) A close up on the Delicate Arch relay ramp. The location of field measurements taken during this study are located along a single transect line (red). (c) A map of deformation band density from (Rotevatn et al., 2007), in and around the Delicate Arch relay ramp, black box in (b).

(Doelling, 1988). At the surface the relay ramp is composed of the ~80 m thick Entrada sandstone Formation (Fm), which comprises 4-20 m thick, clean massive aeolian dune units (Rotevatn et al., 2007). The Morison Fm sits stratigraphically above the Entrada Fm (**Fig. 2.14**). For further details of the stratigraphy and tectonic history of SE Utah

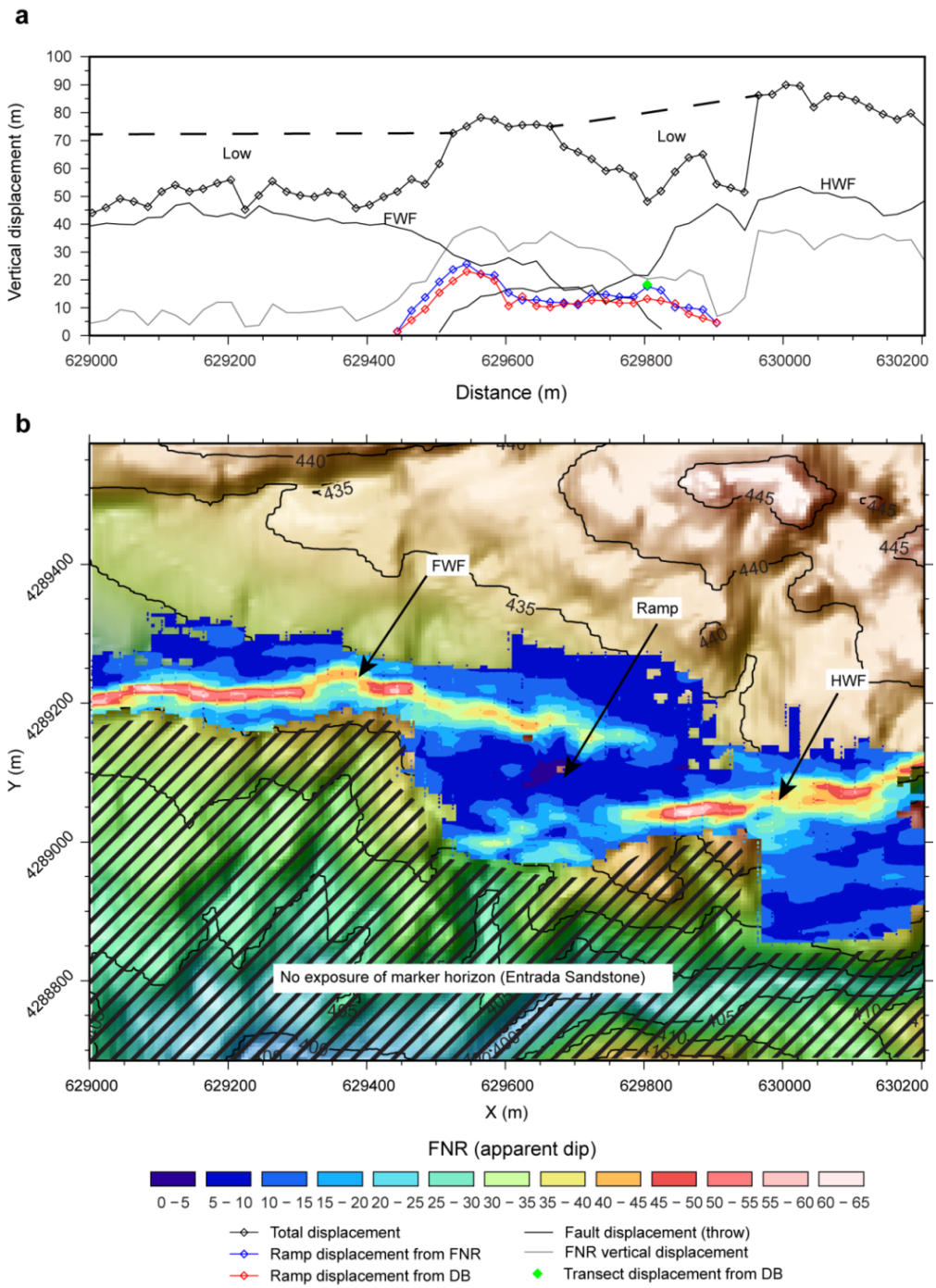

Fig. 2.15. (a) Displacement distance plot for Delicate Arch relay ramp, both displacements from FNR maps and calculated displacements from DB (red and green) are plotted. See text for explanation. (b) Map view of the contoured DEM surface, in meters. Overlaid is the FNR map (blue to pink). The FNR map picks up the segmented nature of the two bounding faults (**Fig. 2.14**). In the hanging wall the Morison Fm obstructs the marker horizon, resulting in lows in the total displacements profile (a).

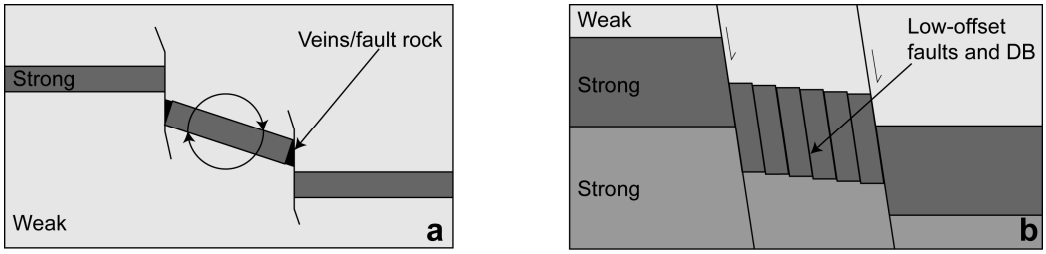

Fig. 2.16. (a) A strong mechanical layer confined within weak layers, such as Lilstock. The ramp is able to rotate as a rigid block between the two bounding faults, as the weak layers can deform ductilely. (b) Strong mechanical layers overlaid by a weaker layer, such as in Delicate Arch. The ramp rotations are accommodated by a net work of low offset shear surfaces, as the strong layer below cannot deform ductilely.

and Arches National Park see (Doelling, 1988, 2001).

The bounding faults of Arches relay ramp are themselves composed of smaller segments and at the tip of the footwall fault (FWF) a small relay is mapped with a separation distance of approximately 30 m (**Fig. 2.14**c) (Rotevatn et al., 2007). Internally the ramp has a high density of deformation bands (DB) when compared to the mutual hanging wall and footwall (**Fig. 2.14**). DB form from the collapse of pore structures in clean porous sandstone along shear surfaces (Fossen et al., 2007). DB, within the ramp, trend E-W, sub-parallel to the bounding faults, and in the east end of the ramp they also trend NW-SE (Rotevatn et al., 2007). Individual DBs are approximately 1 mm wide. A relationship exists between DB width and offset, which provides a means to estimate the accumulated offset produced by the DB from within the relay ramp (Fossen et al., 2007).

The tri-mesh surface was created from a digital elevation model (DEM) with a 10 m horizontal resolution. The average triangle size was 9 m. Structures with offsets below ~7 m are not visualised to have clear breaks in slope. Only the top of the Entrada Fm is used as a reference marker (**Fig. 2.14**: buff colour in a and b). The sample grid was oriented N-S, perpendicular to the average fault strike, and the transect lines were spaced every 20 m.

2.3.2.1 Results from Delicate Arch relay ramp

The along-strike bends, steps and segmented nature of the tips can be recognised in the FNR maps (**Fig. 2.15**b). The laterally continuous FNR highs (yellow-pink) correspond

with the mapped fault scarps, and wide areas of low FNR (blue-green) equate to areas of minor faulting and continuous bed rotations (**Fig. 2.14**b). Including the vertical displacements from the ramp and surrounding foot and handing walls, where exposed, has increased the total vertical offset across the fault-array from ~50 m to ~80 m. Despite the segmented nature of the bounding faults (**Fig. 2.15**b) the total d-x profile (black diamond) is fairly coherent. Notable lows are present in the total d-x profile, but these correspond to areas of no exposure of the Entrada Fm in the footwall, which are stratigraphically overlain by the Morison Fm (**Fig. 2.15**). Therefore, continuous deformations from areas of no exposure are missing from the total d-x profile (**Fig. 2.15**a: grey lines).

Within the ramp, vertical displacements, from areas of FNR, are plotted and compared to the calculated vertical displacements due to movement on all the mapped DB (**Fig. 2.15**). Both profiles closely resemble each other along their entire lengths. Fossen et al., (2005) relate DB width to displacement with displacement/width ratios ranging from 0.1 to 100. For this study, a displacement/width ratio of 10 is used to convert DB width to displacement, which best fits the data presented by (Fossen et al., 2005: their Fig. 13). The DB densities, used to calculate the displacements in (**Fig. 2.15**a: red diamonds) were taken from (Rotevatn et al., 2007), and a constant DB width of 1.5 mm was assumed, as it was the mean DB width recorded during a short field trip to Delicate Arch relay ramp (see digital appendix 5: DB table). In addition, during the field trip a single transect line orientated N-S was collected (**Fig. 2.14**), which measured the location and thickness of DB within the ramp (see digital appendix 5). The vertical displacements calculated from this transect line (**Fig. 2.15**: green diamond) matched those calculated from DB densities collected by (Rotevatn et al., 2007).

2.3.2.2 Interpretation and discussion: Delicate Arch relay ramp

The close relationship between FNR derived displacements and DB calculated displacement indicates that the observed rotation of the ramp towards the mutual hanging wall is primarily accommodated by the accumulated offsets on the multiple DB. This is different to Kilve, where the ramp rotates as intact rigid blocks (**Fig. 2.12**). The different styles of deformation are attributed to the different thickness of the

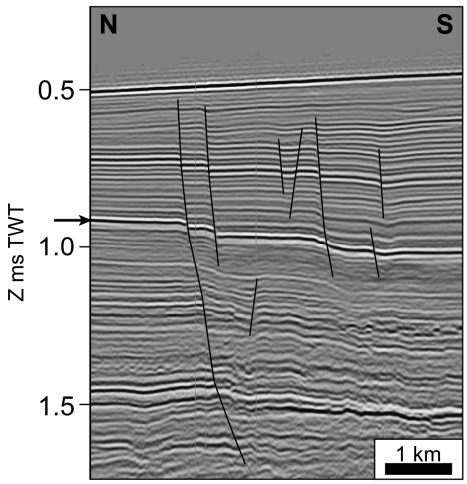

Fig. 2.17. A seismic section through the relay zone in (**Fig. 2.18**). The location of the horizon depicted in (**Fig. 2.18**) is shown by an arrow.

mechanical layers relative to fault offset within the ramp and the presence or lack of mechanically weak layers i.e. shale (**Fig. 2.16**). In the Delicate Arch example, the thickness of the Entrada sandstone (80 m thick) is greater than the offsets on the individual bounding faults (ca. 50 m), whereas the thickness of the limestone beds in Lilstock (12 cm) is smaller than the displacements on the bounding faults (ca. 20 cm). These limestone beds are also enclosed in weak shale layers. Therefore, the ramp at Delicate Arch is unable to rotate as a single block and to maintain strain compatibility the rotation of the ramp is accommodated by multiple low-offset DB (**Fig. 2.16**b).

2.3.2.3 Conclusions: Delicate Arch relay ramp

1. The FNR surface attribute can be used to quantitatively interpret fault-related strains around faults with meter-scale displacements derived from DEM data.
2. The FNR maps picks up the segmented nature of the bounding faults.
3. From field work and published data, the observed displacements calculated from FNR, within the relay ramp, can be accounted for by the summed offset on the deformation bands mapped within the ramp. Therefore, rather than a rigid block rotation of the relay ramp towards the mutual hanging wall, as observed in Lilstock, the ca. 80 m thick sandstone unit accommodates shear within the relay ramp by a network of low-offset deformation bands.

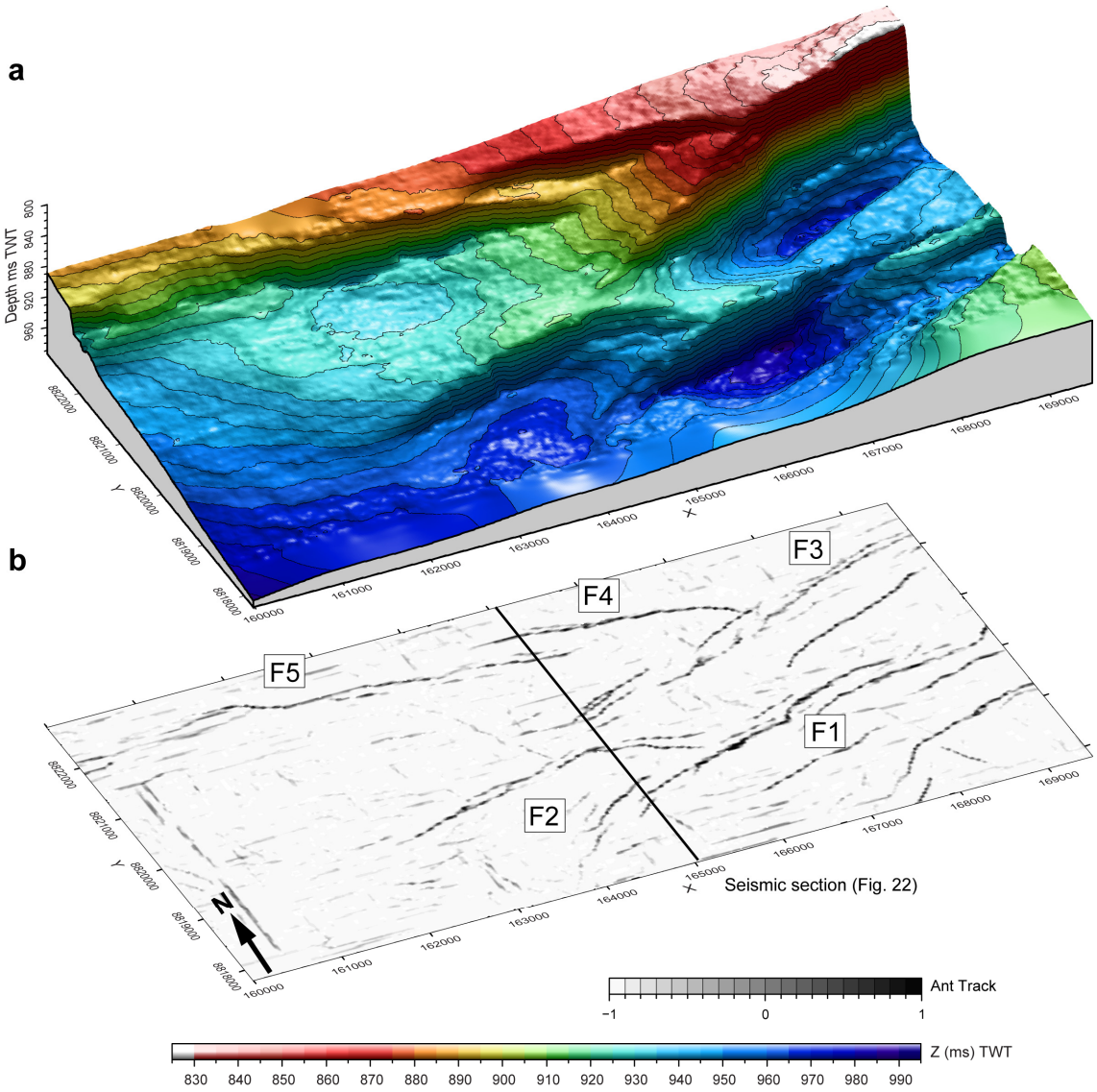

Fig. 2.18. (a) A 3D perspective view of a seismic horizon from Laminaria (**Fig. 2.2**), contoured for time. A relay zone is bound by five segments, which are themselves separated by smaller relays. (b) A perspective map view of the horizon in (a). The distributions of Ant-track attributes that intersect the horizon are plotted. Darker colours indicate a greater potential for a fault.

2.3.3 A kilometre-scale seismic example: Laminaria

Laminaria is located in the Timor Sea off the NW coast of Australia (**Fig. 2.2**). The study focuses on faults hosted in the top 1.5 seconds TWT of the carbonate-dominated stratigraphy (**Fig. 2.17**). The studied faults in Laminaria formed in the Mio-Pliocene due to the regional flexure of the Australian margin after collision with the SE Asian plate complex (De Ruig et al., 2000). The studied faults trend E-W and are highly segmented with relays zones ranging in separation from 70 to 1630 m (**Fig. 2.18**), for a detailed

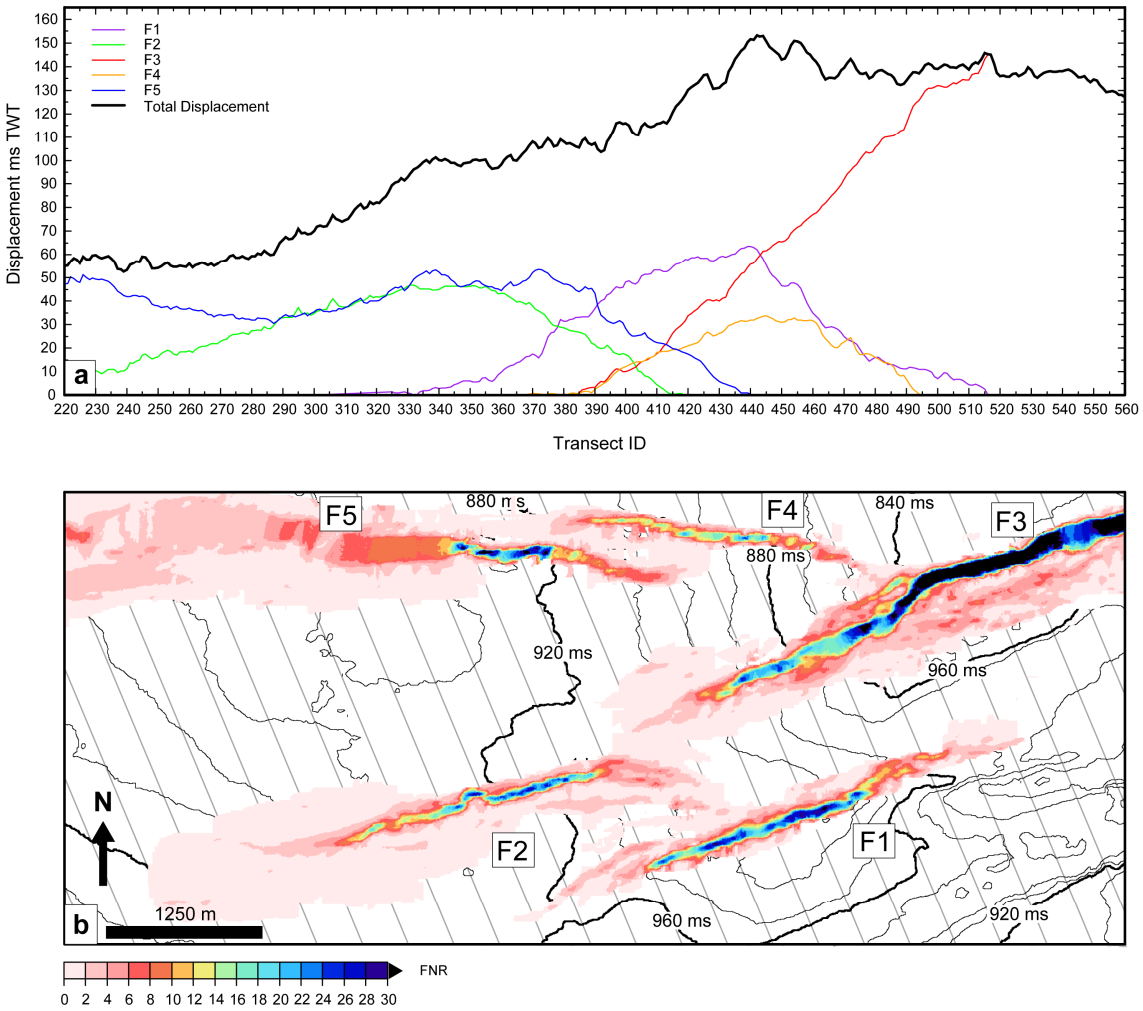

Fig. 2.19. (a) Displacement distance plot for Laminaria (**Fig. 2.18**). Total displacement decreases towards the east. (b) Map view of the time contoured horizon and FNR map (pink to blue). The orientation of the transect lines are shown in grey. The along-strike changes in displacement and FNR dip, observed in (**Fig. 2.18**), are fully captured in both (a) and (b), respectively.

location map see appendix 3: **Fig. A8**. Further details on the tectonic and sedimentary history can be found in chapter 4 and (De Ruig et al., 2000; Wightman et al., 2007).

An average triangle size of 10 m was used to mesh the interpreted horizons and sample lines were spaced every 25 m orientated normal (NW-SE) to the average strike of the fault-array (NW-SE) (**Fig. 2.18**). Away from areas of faulting the apparent dip (dip measured along the transect lines) of each horizons was calculated to be approximately zero (**Fig. 2.17**). Therefore, all rotations towards the mutual hanging wall were selected as potential areas of fault-related deformation.

2.3.3.1 Results and interpretation from Laminaria

The FNR map distributions of the relay zones in this seismic-scale example (**Fig. 2.18**) are comparable to those from centimetre (**Fig. 2.12**) and meter-scale relay zones (**Fig. 2.14**), both in terms of their aspect ratios (overlap/separation), and their segmented nature in map view. The five fault segments (F1-F5) and associated continuous deformation i.e. ramps and monoclines, all sum to produce a total d-x profile that decreases along a common displacement gradient towards the east (**Fig. 2.19**).

Traditional methods of picking faults are done in cross-section view (**Fig. 2.17**) and displacements on any one horizon are condensed on to a single fault pick. However, the new method (i.e. FNR maps) retains the horizontal distribution of deformation on every horizon (**Fig. 2.19**b). This allows all the detailed information contained on 3D seismic horizons to be incorporated in to the analysis of fault networks. For reference, FNR data can also be collapsed into a single displacement measurement, as is done in traditional fault stick interpretations. This allows displacement distributions on different horizons to be viewed together, for example see appendix 2: (**Fig. A6**). In addition, sub-sections of the fault-array, such as footwall deformation, can be potted on pseudo fault surfaces, so that vertical changes in fault-related deformation can be viewed in a single plot, for example see appendix 2: (**Fig. A6** and **Fig. A7**).

The increased amount of structural information contained in FNR maps allows fault geometries and fault interactions to be studied in great detail, especially for slip-aligned branch lines that are best captured in map view. See chapter 4 for more details on interpreting fault linkage geometries from FNR surface attributes.

2.3.3.2 Discussion: Laminaria

The self similarity between relay zones at all scales (**Fig. 2.12**, **Fig. 2.14**, and **Fig. 2.18**) support inferences that relay zones are scale invariant (Acocella et al., 2000; Gupta and Scholz, 2000; Peacock, 2003; Soliva and Benedicto, 2004). See chapter 5 for further details on the scaling of relay zones.

2.3.3.3 Conclusions: Laminaria

1. The FNR surface attribute can be used to analyse the distribution of discontinuous and continuous deformation on seismic horizons, which can be used in the interpretation of fault interaction and linkage geometries.
2. The newly developed FNR surface attribute is a useful tool for interpreting and analysing structural information from outcrop to seismic-scales.

2.4 A comparison of methods: FNR surface attribute and Elastic Dislocation (ED) modelling

In the previous section (2.3) I demonstrated that the FNR surface attribute method is a valid tool for analysing fault-related deformation. Elastic Dislocation modelling packages, such as FaultED, have also been used to predict the distribution of fault-

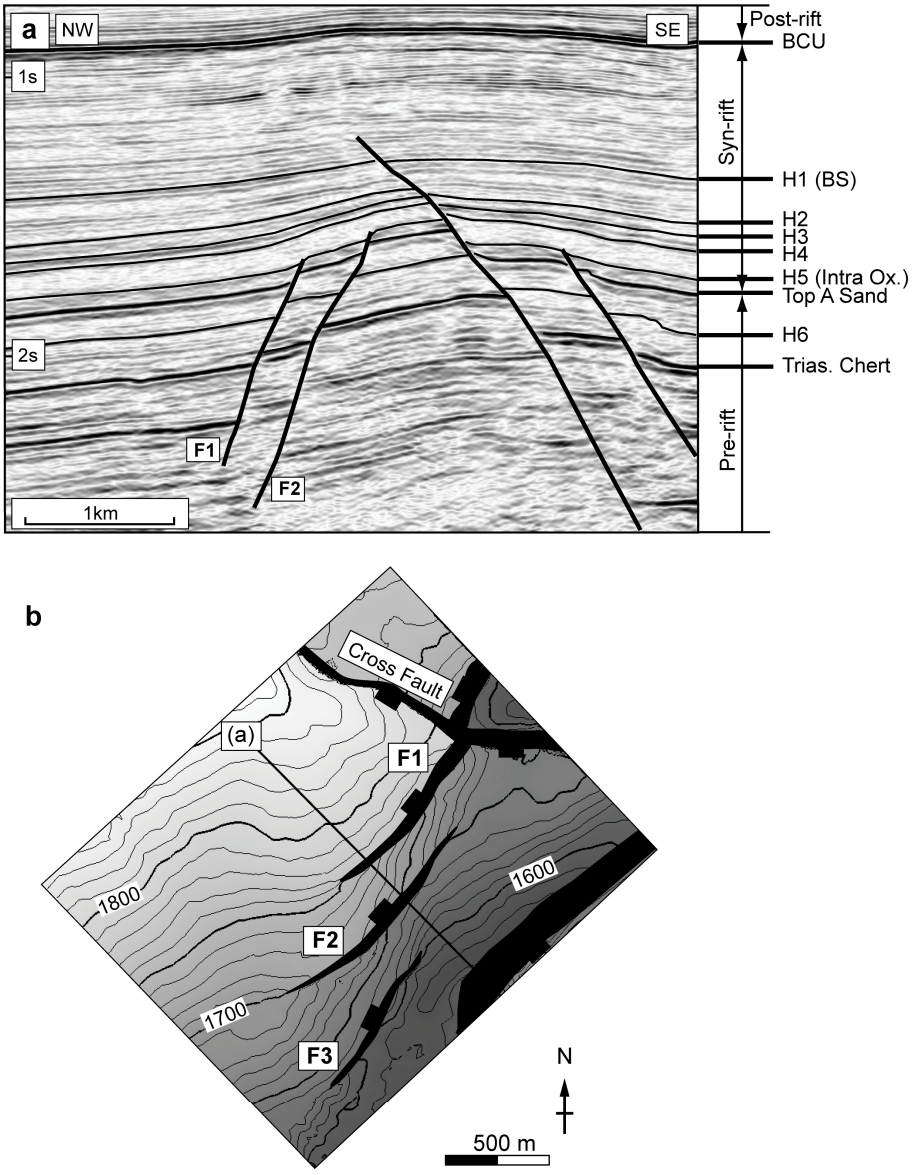

Fig. 2.20. (a) Seismic cross-section with horizon and fault interpretations from the IMF (**Fig. 2.2**). The location of the cross-section is shown in (b). The six mapped horizons used in this study are H1-H6 and regional marker horizons are also shown for context. (b) Time-structure map for horizon H6. The three faults in the study area display a left-stepping, en-echelon arrangement and are separated by relay ramps linking the footwall and hanging wall sediments. A later ENE-WSW trending cross fault, formed during minor post Cretaceous extension, cuts fault F1. Contour measurements are in ms two-way travel time.

related strains around seismic-scale faults (Maerten et al., 2002; Dee et al., 2007). These two methods both produce strain maps around faults, but do so in fundamentally different ways. For, the FNR surface attribute measures geometric features mapped/interpreted around faults. Whereas, ED modelling calculates strain distributions from the throw distributions and geometries of nearby faults, within a homogeneous elastic half space (Dee et al., 2007). For details of ED modelling see digital appendix 5: (Poster) and (Dee et al., 2007: and references therein). The aim of comparing the FNR and ED methods is to see if both predict similar distributions of fault-related strains providing additional confidence in the FNR method.

For the comparison I used a fault-array that consists of three NE–SW trending en-echelon segments separated by two relay zones, located in the Inner Moray Firth (IMF) (F1–F3; **Fig. 2.20**b). This is the same fault-array presented in detail in chapter 3, for details on the tectonic and sedimentary history see sections therein. In summary, F1 to F3 formed during the main phase of NW – SE extension during the Late Jurassic to Early Cretaceous (represented by the mapped interval H5–BCU; **Fig. 2.20**) (Underhill, 1991b; Thomson and Underhill, 1993). Aggregate displacement on the fault-array decreases towards the SW. The studied faults dip towards the NW, antithetic to nearby large-offset faults that dip towards the SE (**Fig. 2.20**).

The upper tip lines of faults F1-F3 are hosted within the shale dominated syn-rift sequence, while the lower tip lines are within the sandstone dominated pre-rift sequence (**Fig. 2.20**). It is worth noting upfront that ED modelling does not take into account variable lithology types or the evolution of the faults through time. FaultED assumes the sedimentary sequence was in place during the entire time the fault was active. Although, in growth strata the sediments are only in place for some of the time the faults were active. Therefore the growth strata in the IMF does not record deformation prior to its deposition, which means ED models will over predict the amount of fault-related strain in syn-tectonic sediments. Despite these assumptions, this study is proposed to be a useful first step toward cross validating the two methods.

2.4.1 FaultED Method

In order to make a direct comparison between observed FNR on a mapped horizon and the predicted response of an elastic medium to slip on the embedded faults the horizons need to be restored prior to the forward modelling (**Fig. 2.21**). The mapped horizons are used as the geological boundary conditions in the forward model and if they were not restored the model run would place the horizon in an incorrect location, and thus a direct comparison between the observed FNR and modelled strains would not be possible (**Fig. 2.21**b). In (**Fig. 2.21**d) the mapped horizons in the IMF are restored prior to the forward modelling. Therefore, the modelled strains are in the same spatial position as the observed FNR.

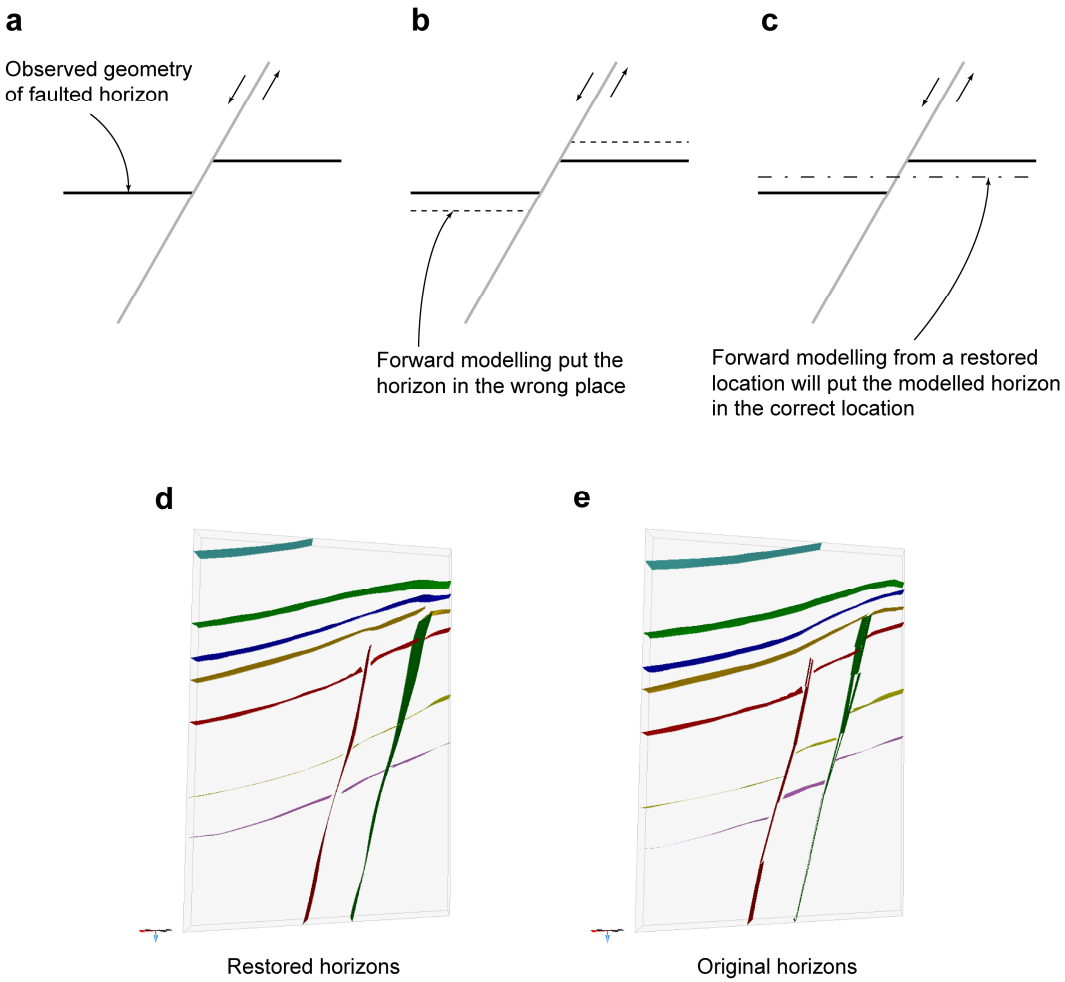

Fig. 2.21. (a) A schematic horizon and fault geometry. (b) The results of a forward model run with no restoration. The locations of the modelled strains no longer match the original horizon location (solid black line). (c) Restored the faulted horizon back to its undeformed state prior to forwards modelling will enable the properties observed on the original horizon to be directly compared to the predicted stresses and strains. (d) A cross section through the restored horizons in the IMF. (e) The same cross section as in (d) but with the horizons in their original locations.

2.4.2 Comparison of results

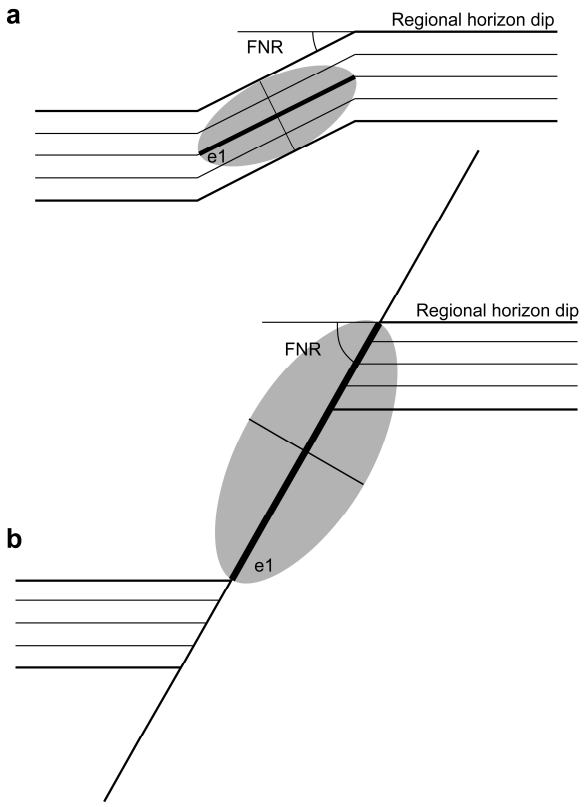

Fig. 2.22. Schematic diagrams illustrating the relationship between FNR and e1. (a) An area of continuous bed rotation with moderate displacement (throw and heave). FNR is the measure of apparent dip from the regional horizon dip. e1 is the longitudinal axis of a strain ellipse, which measures the change in shape (strain) of the area of bed rotation. (b) An area of faulting with relatively high displacement. In this example FNR increases and so does e1.

FNR or fault normal shear (Huggins et al., 1995) is a measurement of shear strain between and around faults (**Fig. 2.4**). To compare FNR to ED models a strain attribute was selected that best approximates the shear strains recorded by FNR. Longitudinal strain (e1) is a measurement of the maximum extension axis of a strain ellipse (**Fig. 2.22**). When a surface is deformed by extensional faults the surface is extended. In this study I relate an increase in FNR to equate to an increase in fault-related deformation, and thus an increase in extension and e1. In (**Fig. 2.22**) this relationship is illustrated with a monocline like structure (low FNR and low e1) and a fault (high FNR and high e1). Caution should be taken not to over interpret the results. For, seismic horizons have limited horizontal and vertical resolutions (Steen et al., 1998; Brown, 2004). And, despite their inferred similarities e1 and FNR are measuring different properties and are unlikely to match exactly. Therefore, only structures that are concordant over at least 100 m are compared.

In general the overall fit between the two methods is good. Highs in FNR and e1 are found in relay zones, at fault tips and encircling the mapped faults (**Fig. 2.24**). In detail, elongate highs are predicted by both methods past the lateral fault tips. Above the upper tip line both methods predict monocline-like features (H3-H1). And, on H6 both methods predict a low strain area in the hanging wall of fault F1. Although, the FNR method predicts a wide zone of low FNR encircling the faults on (H1-H5), this is not matched by the ED method, which predicts negligible strains in these regions (**Fig. 2.24**).

2.4.3 Discussion: FNR vs. ED

In regions where both methods predicted similar distributions of strains, i.e. above the mapped fault tip in areas of fault propagation folding (**Fig. 2.24**:H1-H4), we can have more confidence that both these methods are accurately identifying fault-related strains. Conversely, in areas where the correspondence between the different methods is poor, i.e. on horizons cut by the mapped faults (**Fig. 2.24**:H5-H6), the interpretations drawn from these regions should be checked. Three potential reasons for differences between the two methods are; one, FNR maps are picking up seismic artefacts, which is unlikely due to the careful interpretations undertaken. And two, ED models only describe a homogeneous medium and therefore layer based anisotropies, present in the IMF, are expected to accommodate strains heterogeneously, which are only averaged in the ED models. And finally, and probably the most important, ED theory implicitly models reverse drag around faults with the highest deflections of the hanging wall and foot wall occurring at the point of maximum displacement (**Fig. 2.23**). However, FNR maps the distribution of synthetic rotations. Therefore, on horizons cut by a fault surface the similarities between the two methods is likely to be less than on horizons not cut by a fault i.e. those above the fault tip (**Fig. 2.23**).

In the case of the IMF example only the top section of the fault-array, which lies above the mapped fault tip is compared with the ED model. In this areas ED theory does predict synthetic rotations. It is these synthetic rotations above the fault, i.e. fault propagation folds, which are compared. Therefore in this example from the IMF comparing ED and FNR strain distributions are valid on the horizons above the mapped

fault tips. As noted in (**Fig. 2.24**), on higher displacement horizons the similarities between the two methods decrease. For, in the IMF horizons cut by faults F1 and F2 (**Fig. 2.20**) display synthetic rotation that dip towards the mutual hanging wall, whereas the ED theory predicts reverse rotations on these horizons (**Fig. 2.23**).

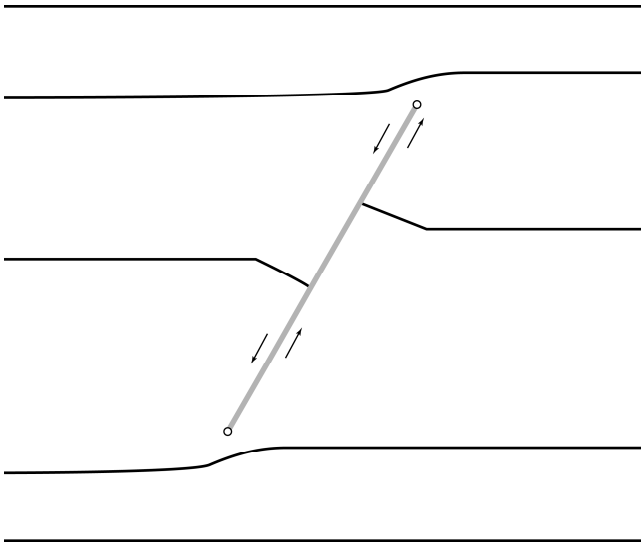

Fig. 2.23. A schematic illustration of the types of horizon geometries the ED theory will produce around a normal fault given originally horizontal horizons. Reverse rotations are implicitly modelled adjacent to the fault surface, as in (Barnett et al., 1987). Above the fault tip synthetic rotations are model, which are similar to the fault propagation folds in the IMF above faults F1 and F2 (**Fig. 2.20**).

2.4.4 Conclusions: FNR vs. ED

1. In general, the correspondence between the two methods is good above the map fault tips in areas of fault propagation folding. Whereas the correspondence between the methods on horizons cut by a mapped fault are relatively poor.
2. The positive correspondence is particularly pronounced in areas above and along-strike of the fault tips where the elastic displacements recreate the seismically-imaged monocline.
3. The presented correspondence suggests that both methods may indeed be appropriate for understanding strains in the volume surrounding seismically imaged faults.

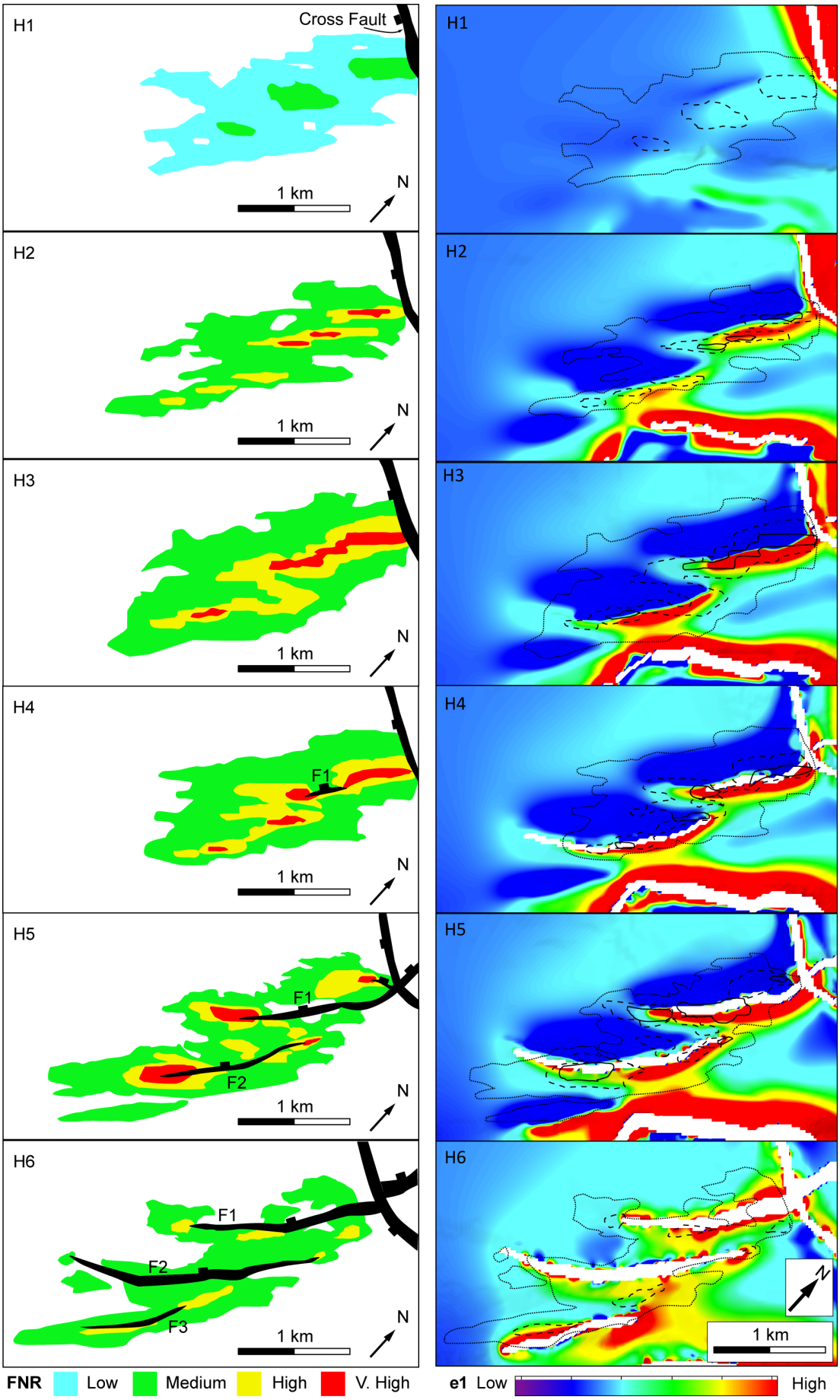
H1
Cross Fault
1 km
N
H2
1 km
N
H3
1 km
N
H4
F1
1 km
N
H5
F1
F2
1 km
N
H6
F1
F2
F3
1 km
N
FNR Low Medium High V. High
H1
H2
H3
H4
H5
H6
1 km
e1 Low High

Fig. 2.24. (Left) map-view distributions of abnormal rotation (FNR) for each horizon (**Fig. 2.20**: H1 to H6). White areas are not deformed by F1–F3. (Right) map-view distributions of longitudinal strains, e1. Overlaid are the outlines of abnormal rotations (FNR). For details on the FNR maps from the IMF see chapter 3. See text for a comparison.

2.5 Defining a geometric coherent fault-array: a field example from Bishop

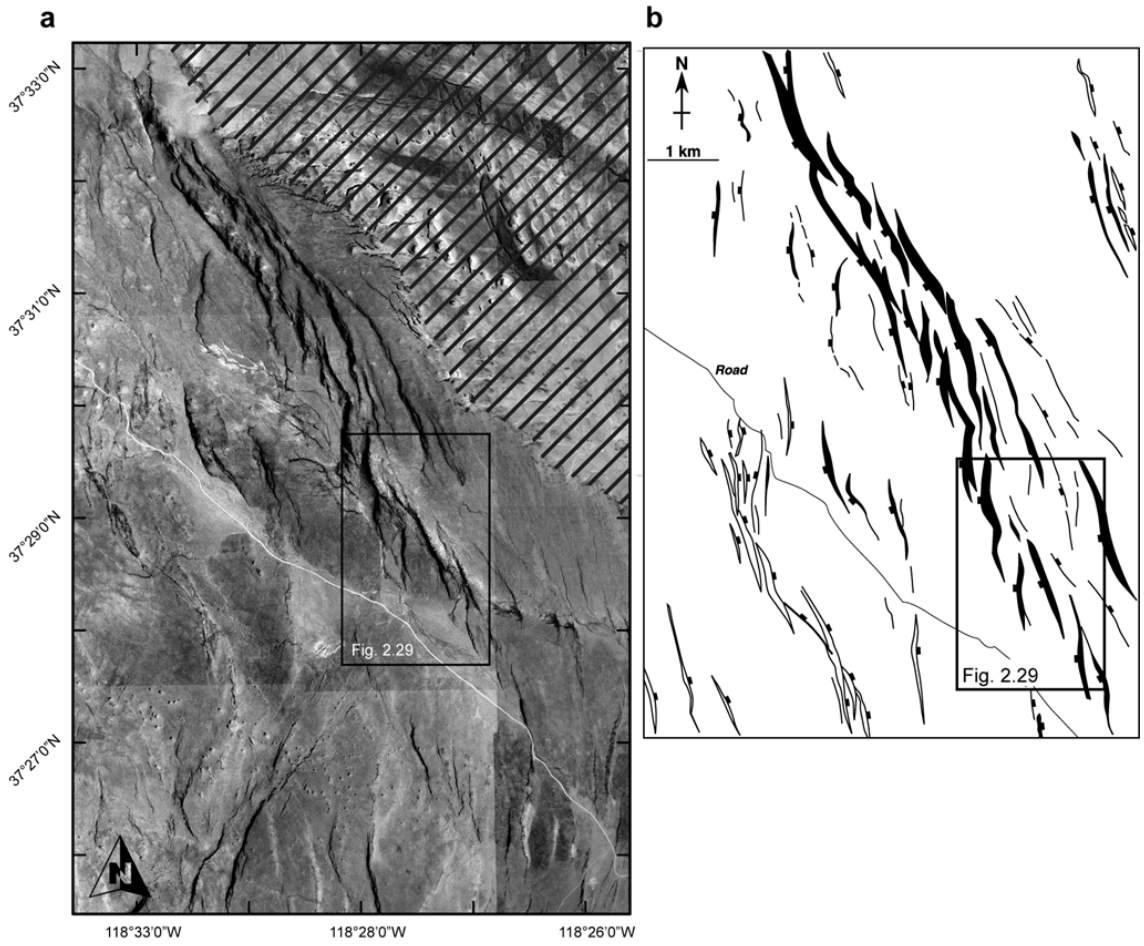

Fig. 2.25. (a) An aerial photo of a faulted volcanic tuff north of Bishop, CA (**Fig. 2.2**). Striped areas are heavily eroded and are not used in further studies. The fault-array trends NNW-SSE and individual segments trend more N-S. The fault-array decreases in displacement towards the south. (b) Fault interpretations, east dipping faults have a white fill and west dipping faults have a black fill, Modified from (McClay et al., 2002).

A geometrically coherent fault-array consists of a series of co-evolving overlapping fault segments and associated continuous bed rotations (Walsh and Watterson, 1991). In general, faults are sub-parallel and aligned normal to the regional extension direction. And, the total summed displacements across the fault-array should resemble that of an isolated fault (**Fig. 2.5**a) (Walsh and Watterson, 1991).

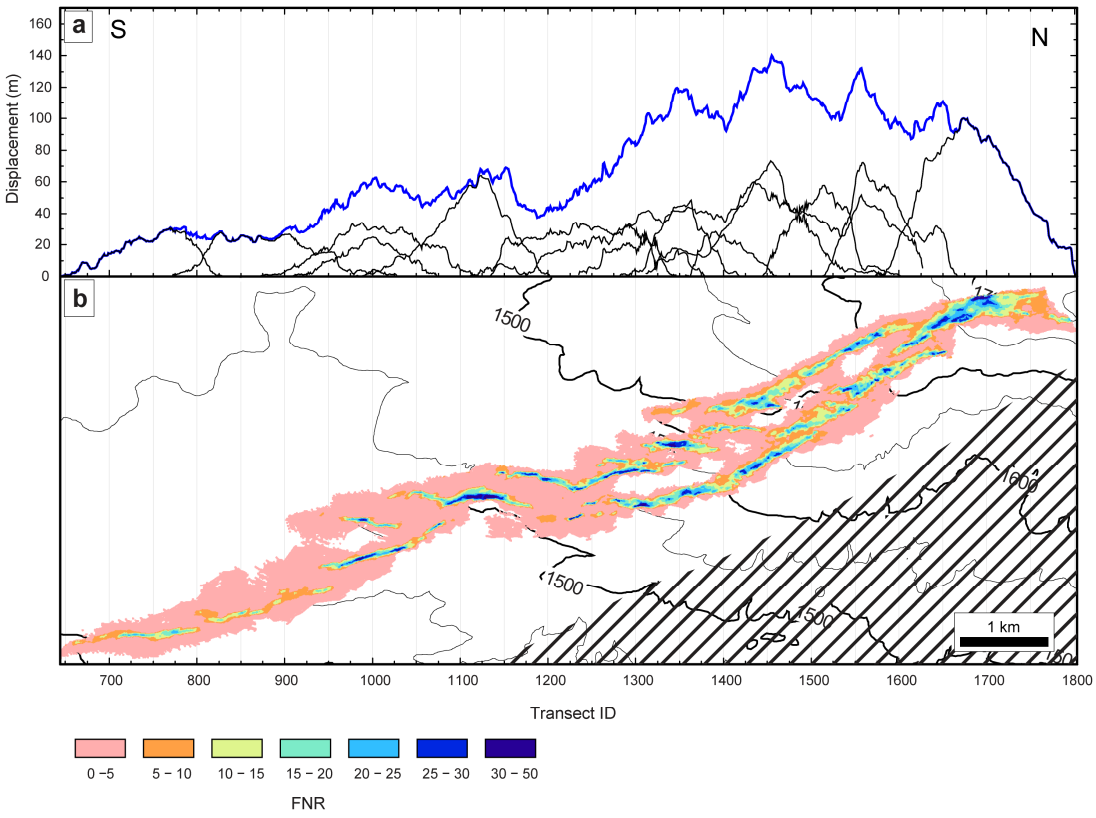

Fig. 2.26. (a) Displacement distance plot of a selection of fault segments from Bishop (**Fig. 2.25**). Transect line spacing is 10 m. Only segments that lie along-strike of each other are included in the fault-array. Black lines are the vertical displacement for the individual fault segments and associated FNR. The blue line is the total vertical displacement for all selected fault segments. Two peaks in the total d-x profile exist around Transect IDs 1100 and 1450. (b) Map view of the FNR map from which displacements were calculated. Striped areas depict the area of high erosion.

Knowing the ideal shape of a coherent fault-array is only the starting point. For, geometrically coherent fault systems can communicate displacements over horizontal separation distances of at least 6 km (Walsh and Watterson, 1991). Therefore, a question arises; at what point does one stop including fault-segments into a fault-array to achieve the "ideal" total d-x profile? In this section I aim to consider this question with examples from Bishop, California, and propose preliminary criteria for discerning which fault segments to include in a fault-array.

The fault-array trends NNW - SSE and is located north of Bishop, California, on the western margin of the Basin and Range province (**Fig. 2.2**). Individual segments trend roughly N-S and are arranged in left-stepping en-echelon arrays. The faults form within the 80 m thick volcanic tuff, which was deposited 764000 ± 5000 yrs ago (Izett and Obradovich, 1994). For details on the tectonic history of this region see (Pinter, 1995).

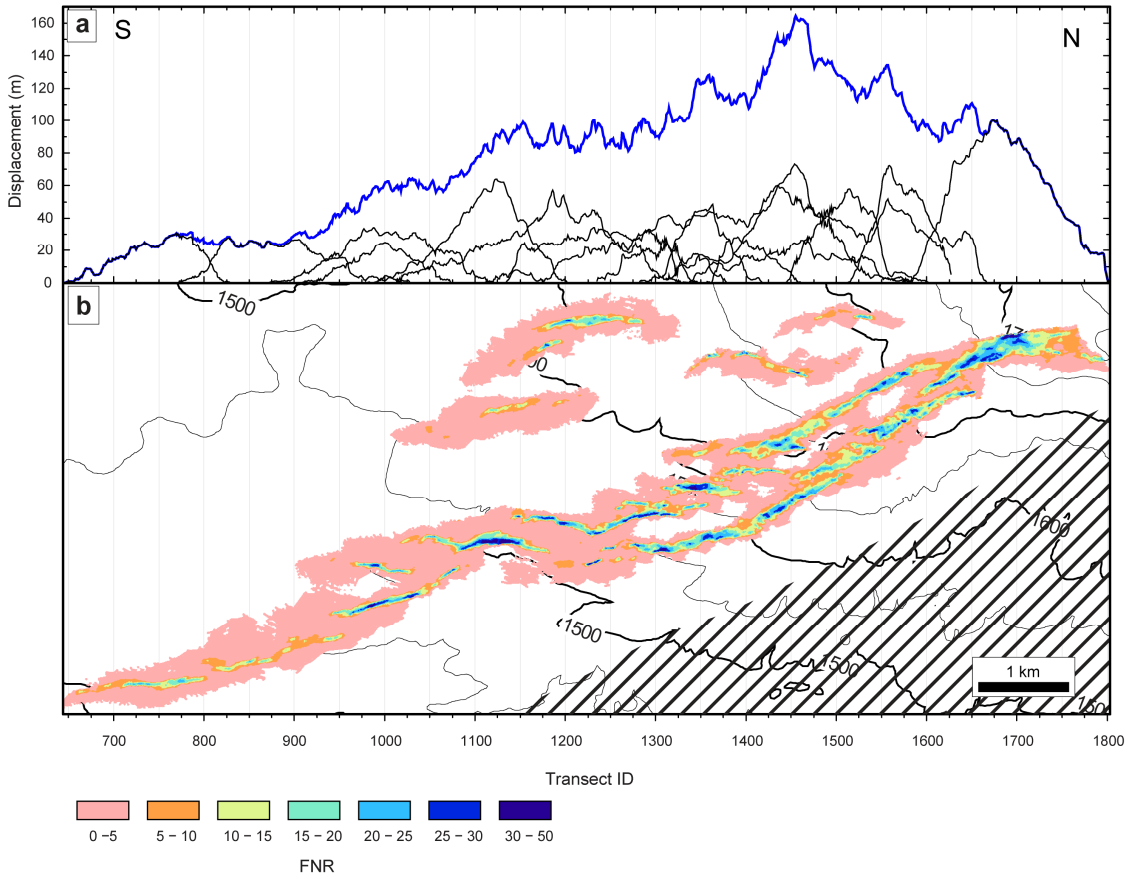

Fig. 2.27. (a) Displacement distance plot of a selection of fault segments from Bishop (**Fig. 2.25**). Transect line spacing is 10 m. Faults within the hanging wall are included in addition to those in (**Fig. 2.26**). The low between the two peaks in (**Fig. 2.26**a) is removed from the total d-x profile. Towards the south end of the fault-array displacements plateau out at about 35 m, which is not expected for an idealised d-x profile (**Fig. 2.5**a). (b) Map view of the FNR map from which displacements were calculated. Striped areas depict the area of high erosion.

In summary, faults in the Bishop Tuff record extension during the late Quaternary. Faults in the Bishop Tuff form due to the flexure of the upper crust in this section of the Owen Valley (Pinter, 1995). This accounts for the shallow depth at which faults nucleate (Dawers et al., 1993).

Most of the fault scarps are well preserved, although all show various degrees of degradation (Pinter, 1995). The Bishop Tuff has little vegetation cover and erosion is limited due to the arid climate. Therefore, the fault scarps can be clearly seen in the DEM and displacements are calculated from top of the Bishop Tuff (**Fig. 2.25**).

The surface was created from a DEM with a horizontal resolution of approximately 10 m (1/3 arc-second) and was meshed using an average triangle size of 10 m. Only the intact top bedding surface was used as a reference marker (**Fig. 2.25**). The sample grid

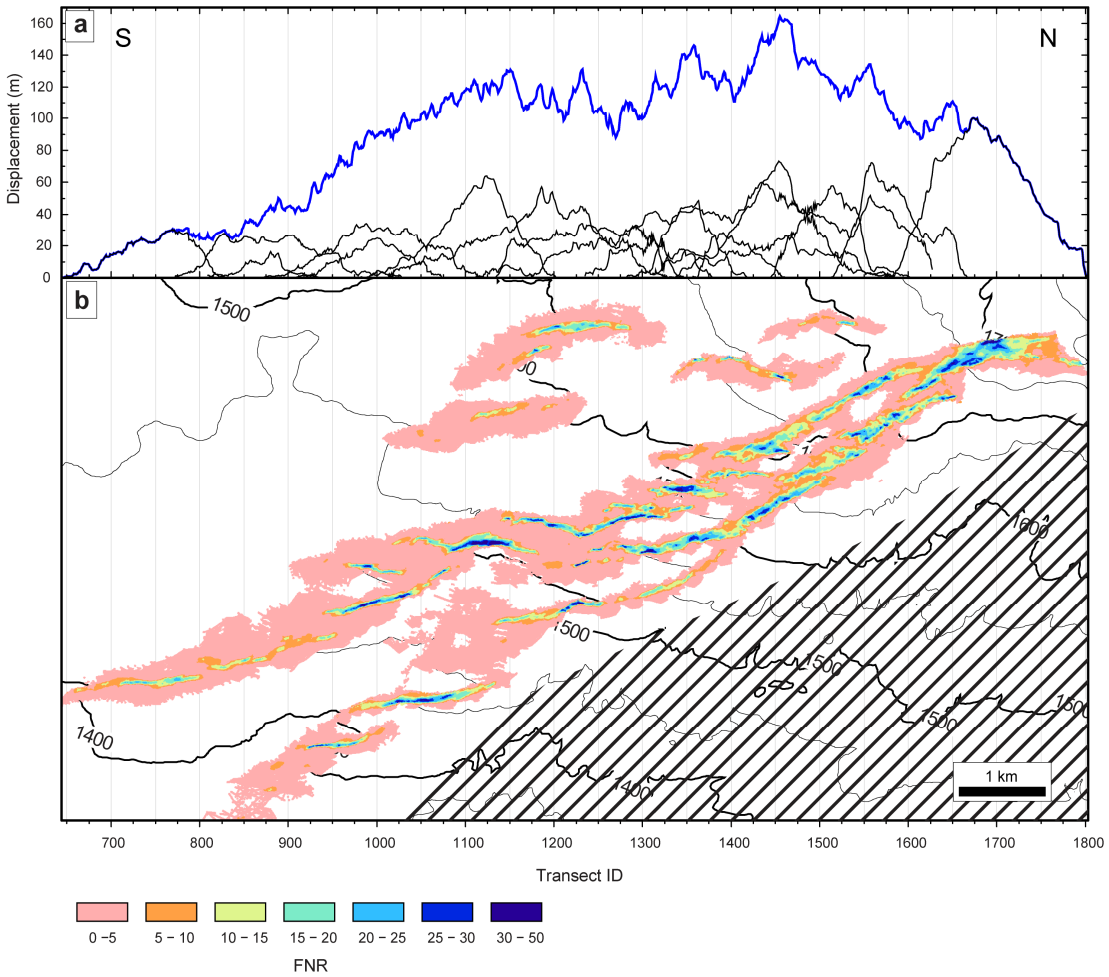

Fig. 2.28. (a) Displacement distance plot of a selection of fault segments from Bishop (**Fig. 2.25**). Transect line spacing is 10 m. Faults within the hanging wall and footwall are included in addition to those in (**Fig. 2.26**). The south end of the fault-array more closely resembles that of an idealised d-x profile (**Fig. 2.5**a), as displacement decrease steadily towards zero at the tip. The centre of the fault is missing displacement and this could relate to the missing fault segments in the area of erosion in the footwall (striped), see **Fig. 2.25**b. (b) Map view of the FNR map from which displacements were calculated. Striped areas depict the area of high erosion.

was oriented E-W normal to the strike of the individual fault segments. Sample line spacing was 10 m.

2.5.1 Results and interpretation: Bishop

The total d-x profiles in (**Fig. 2.26** to **Fig. 2.28**) all show a decrease in displacement towards the south. Depending on which fault segments are included in the fault-array there are different profiles shapes for the aggregate displacement, but on all profiles there are short wavelength (20-30 m) high amplitude spikes (5-10 m) along the entire length of the fault-array. These probably relate to erosion of the marker horizon and deposition of talus in the hanging wall, which distort underlying trends adding noise to

the d-x profiles. In an ideal setting we should observe a monotonic decrease in displacement from a maximum at the centre of the fault-array to a minimum at the tips. In this example the centre of the fault is inferred to be between TID 1450 to 1550 (**Fig. 2.26** to **Fig. 2.28**). The exact location is unknown due to an increased lack of exposure towards the north (**Fig. 2.25**). Therefore the total d-x profiles should peak near TIDs 1450 to 1550 and decrease towards the south with an inferred fault tip near transect identification (TID) 600 (**Fig. 2.26** to **Fig. 2.28**).

In (**Fig. 2.26** to **Fig. 2.28**) three different combinations of segments are included to make the fault-array. (**Fig. 2.26**) only includes fault segments that lie along-strike of each other in a ~1 km wide band, which is the most obvious selection of fault segments. The total d-x profile, which includes both fault throw and the vertical displacement from areas of continuous bed rotation, has pronounced undulations along-strike with two highs, one at TID 1450 and another around 1100. This resembles the isolated fault model prediction of d-x profiles (**Fig. 1.5**e). In (**Fig. 2.27**) and (**Fig. 2.28**) fault segments in the hanging wall and footwall are included in the fault-array. Each modifies the total d-x profile. Along-strike undulations in the total d-x profiles remain in (**Fig. 2.28**) and it is inferred that these relate to missing fault segments that have been eroded away and or other nearby synthetic and antithetic faults that should be included in the fault-array (**Fig. 2.25**).

In most studies, such as Laminaria (Section 2.3.3), only a sub-section of a larger fault-array is imaged. Therefore, it is important to determine whether the total d-x profile from a few overlapping segments give a representative picture of the large scale displacement distributions. The four fault segments in (**Fig. 2.29**a) were chosen as they resemble the fault geometries in (**Fig. 2.18**). The FNR map has reproduced the observed faults and fractures observed in the aerial photograph. However, the deposition of sediments in the hanging wall has decreased the scarp heights, which produce areas of wide continuous deformation (**Fig. 2.29**: X). Care is taken not to interpret these erosion and deposition features (**Fig. 2.29**: X and Y). Irrespective of these artefacts the displacements are still captured and included in the d-x profiles. Different fault segments, and their associated strains, can be selected and plotted individually on d-x plots (**Fig. 2.29**b). From now on a reference to a fault segment

includes continuous deformation surround the mapped fault scarps, unless fault throws and continuous deformations are directly referred to.

The summed displacements on the fault segments F1-F4 (**Fig. 2.29**: blue line), do not capture the true variations in displacements of the fault-array (**Fig. 2.29**: red line), which might be a typical selections of fault segments if the study area only included the regions in (**Fig. 2.29**a). Therefore, total d-x profiles are not fixed and can change shape depending on what fault segments are included (**Fig. 2.26** to **Fig. 2.29**). Therefore, when interpreting their shapes, i.e. do they resemble an isolated fault (Walsh et al., 2003b) or coincidental overlapping faults (Cartwright et al., 1996), care should be taken as their form is heavily dependent on the correct selection of fault segments that comprise the fault-array.

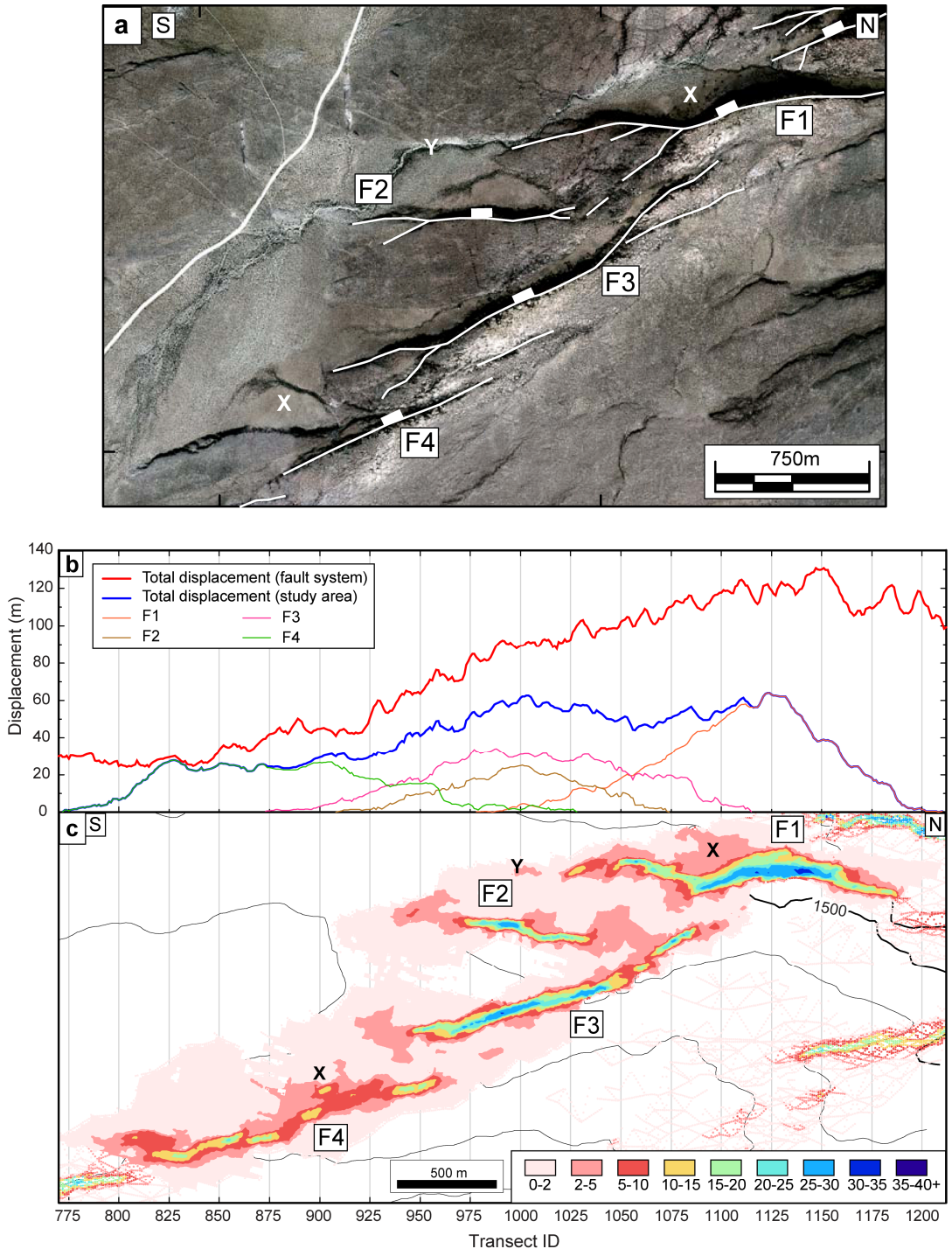

Fig. 2.29. (a) An aerial photo of a relay zone, from within the fault-array (**Fig. 2.25**: box). The geometry and scale of this relay zone is comparable to the relay zone from Laminaria (**Fig. 2.19**). Deposition of sand within the hanging walls (X), and erosion features, such as river channels (Y), give erroneous FNR readings and care should be taken not to miss interpret these non-tectonic features. (b) Displacement distance plot of a sub-selection of fault segments from Bishop. Transect line spacing is 10 m. The total displacement of the fault-array (red line) comes from (**Fig. 2.28**). The blue line represents the total d-x profile calculated from only fault F1 to F4. Not including all the nearby faults in the fault-array gives a false picture of the displacement distributions. (c) Map view of the FNR map from which displacements were calculated, contoured areas (pint to blue) are those of faults F1-F4 and point data (from which contours are made) are from the surrounding fault segments that make up the rest of the fault-array (**Fig. 2.28**). Non-tectonic features, from (a) are labelled X and Y.

2.5.2 Discussion: Bishop

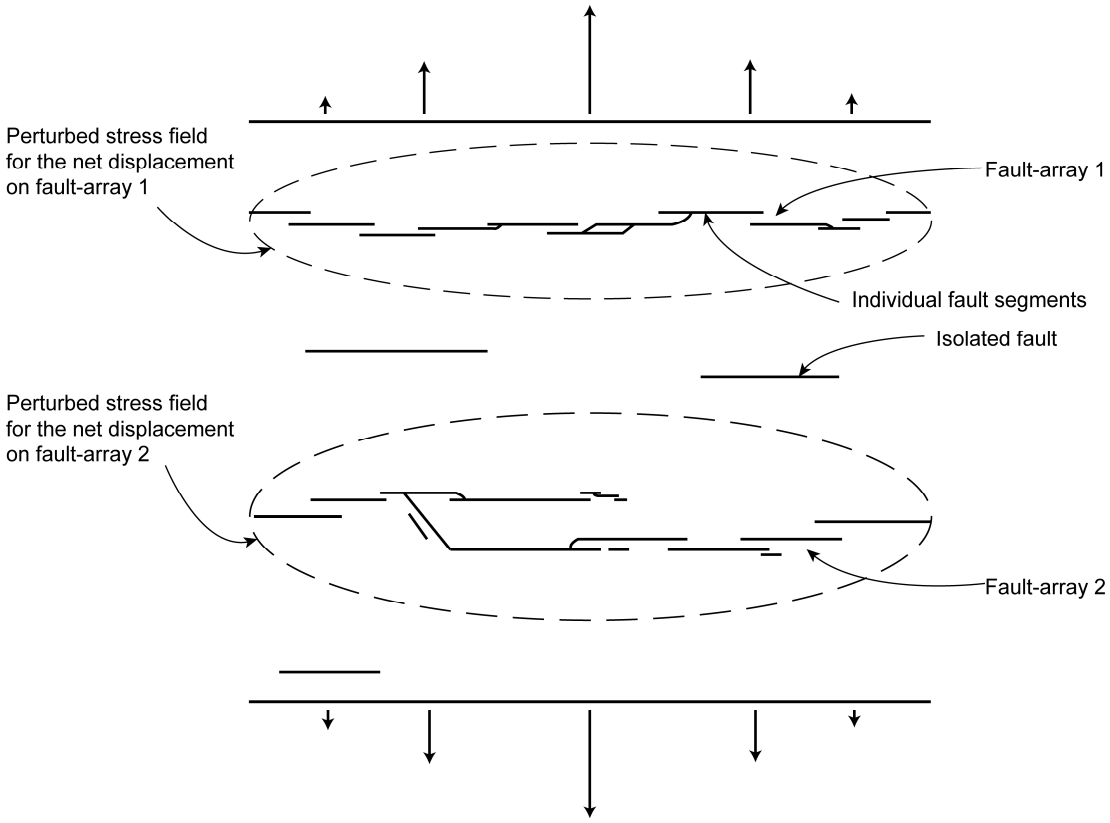

Fig. 2.30. A schematic model illustrating the means by which to determine if a fault segment should be included into a fault-array. Arrows on the boundaries indicate the amount of extension applied. Faults within the extensional terrain form parallel to the margin except in areas of fault linkage. The extents of the stress field around the fault-arrays are shown by the dashed line. Faults within the stress field appear as if one fault, when summed (**Fig. 2.5**). Faults outside of the dashed line are proposed to have d-x profiles that also resemble those in (**Fig. 2.5**). If all the faults and fault-arrays are summed they will equal the extension applied at the margins.

Including faults from the mutual footwall and hanging wall of the fault-array altered the total d-x profile and made it more like that of a d-x profile from an isolated fault (**Fig. 2.28**). Undulations in the total d-x profile do remain and some will relate to surface processes, such as erosion of the fault scarp and deposition of material in the hanging walls (**Fig. 2.29**). Other missing displacements may relate to nearby fault segments not included in the fault-array, such as the antithetic faults in the SW of the Bishop Tuff (**Fig. 2.25**b). The question is therefore, which faults make up a fault-array?

Identifying which faults comprise a fault-array must relate in part to how faults interact with each other. Faults are proposed to interact through their stress fields (Gupta and Scholz, 2000). The size of the stress field perturbation is controlled by the displacement on a fault. And, for fault-arrays the net displacement controls the

horizontal extent of a stress field (Gupta and Scholz, 2000). For details on how to calculate the stress field, and the critical stress drop contour, around a fault-array see chapter 5 and appendix 4. Therefore, faults with separation distances greater than the horizontal extent of the critical stress drop contour, which is located within the stress drop field of a nearby fault, are able to overlap unhindered, as if isolated from the nearby fault (**Fig. 2.30**). In contrast, when a fault propagates into the perturbed stress field of a nearby fault the two segments will become laterally pinned and form a relay zone (Gupta and Scholz, 2000). Therefore, it is proposed that faults that fall within the stress field produced by a fault-array will more strongly affect the d-x profile of that fault-array (**Fig. 2.30**). Whereas faults that are outside of the stress field will appear as if isolated from the nearby fault-arrays (**Fig. 2.30**). However, if all displacement from faults within a tectonic setting were summed the total displacement should match the extension applied at the margins and thus be geometrically coherent (**Fig. 2.30**) (Walsh and Watterson, 1991). Therefore, the greater the separation distance between faults/fault-arrays the more the individual faults/fault-arrays will resemble the d-x profiles of idealised isolated faults (**Fig. 2.5**a).

2.5.3 Conclusions: Bishop

1. The FNR surface attribute can be used to interpret a fault-array comprising of many individual segments and allows displacements to be compared between regions of interest.
2. A fault-array consists of fault segments that sum together to form a coherent fault-array, which resembles that of an isolated fault. The collection of fault segments that comprise a fault-array all interact through their stress fields and form due to the same extensional mechanisms.
3. The greater the separation distance between faults/fault-arrays the more the individual faults/fault-arrays will resemble the d-x profiles of idealised isolated faults.

Chapter 3. Geometrically coherent continuous deformation in the volume surrounding a seismically imaged normal fault-array

Abstract

We calculated an apparent dip attribute, which was used to ascertain the spatial distribution of fault-related continuous deformation. The vertical component of displacement calculated from the continuous deformation acts to "fill-in" missing displacement in the fault-throw profile. This result shows that apparently complex 3D patterns of continuous strain in the volumes surrounding the fault-array developed as part of a single, geometrically coherent fault-array. However, if this component of continuous deformation was not added to the throw profile, the fault-array could have been misinterpreted as a series of isolated fault segments with coincidental overlaps. This technique permits the analysis of continuous deformation structures, which are up to an order of magnitude smaller than previously described. In the study area, these structures are interpreted as small fault-propagation folds, forming in a shale-dominated cover sequence. The fault-propagation folds above the upper tip line of the mapped fault-array bifurcate upwards from the fault surface into three coherent lobes and resemble secondary fault segments. The near-constant along-strike length of the region of continuous deformation throughout the syn-rift sequence implies that the length of the fault-array was established at an early stage in its growth, prior to the establishment of a seismically-visible fault surface.

3.1 Introduction

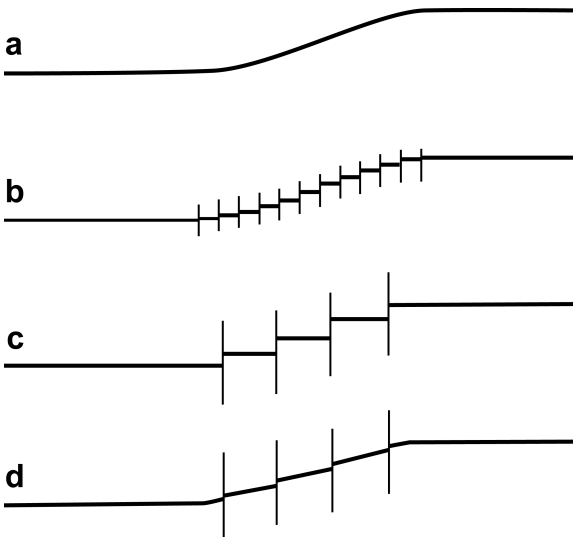

Fig. 3.1. Schematic representation structural geometries that produce the appearance of continuous deformation at the scale of observation for a seismic reflection profile. (a) Rotation of the seismic horizon. (b-c) Different arrangements of sub-seismic scale faults. (d) Horizon rotation and sub-seismic scale faults. Taken from (Steen et al., 1998).

Fault-arrays comprise multiple fault segments (Peacock and Sanderson, 1991; Childs et al., 1995; Childs et al., 1996a; Willemse, 1997; Crider and Pollard, 1998b; Peacock, 2002) that typically grow as geometrically coherent structures (Walsh and Watterson, 1991; Childs et al., 1995; Walsh et al., 2003b). Fault segments within these arrays can be hard-linked by discrete faults or soft-linked by zones of continuous deformation (Peacock and Sanderson, 1991; Trudgill and Cartwright, 1994; Childs et al., 1995; Walsh et al., 2003b). In seismic reflection profiles, continuous deformation is commonly expressed as the rotation, thickening or thinning of strata within the deformed volume between soft-linked faults (Walsh et al., 1996). Continuous strains result from any combination of plastic deformation and/or small-scale faults or fractures below the resolvable limits of seismic data, e.g. (**Fig. 3.1**) (Steen et al., 1998; Townsend et al., 1998). The specific limits at which structures can be resolved depend on the depth of the feature and the quality of the seismic data.

Geometric coherence is the concept that faults and fault-related strain maintain regular and systematic geometries and relationships throughout the evolution of a

fault-array. The throws due to faults and associated continuous deformation should together produce smoothly varying d-x profiles, which resemble that of a single fault (Walsh et al., 2003b). If a fault-array has maintained geometric coherence this must suggest kinematic coherence, which is the systematic and linked accumulation of displacement across the fault-array (Walsh and Watterson, 1991). The fault-propagation model of Marchal et al. (1998) predicts that fault-arrays evolve by the coherent growth and linkage of secondary faults, which are small faults that form at the propagating tips of a primary fault segment. Secondary faults can form as separate fault segments soft-linked to the primary fault via relay zones, or as hard-linked structures that bifurcate from the main fault surface. This fault growth model can be applied to both horizontal and vertical tip lines (see appendix 1: **Fig. A2**) (Marchal et al., 1998; Marchal et al., 2003). Fault-propagation will ultimately result in segmented fault tip lines, as shown by observations of naturally occurring faults (McGrath and Davison, 1995; Childs et al., 1996b; Marchal et al., 2003; Kristensen et al., 2008)

Fault-propagation folds are manifestations of fault-related continuous deformation that develop ahead of a propagating tip line and which deform the free surface (Withjack et al., 1990; Corfield and Sharp, 2000; Sharp et al., 2000; Gawthorpe et al., 2003; Finch et al., 2004; Jackson et al., 2006; White and Crider, 2006; Ford et al., 2007). In the case of synsedimentary normal faults, fault-propagation folds are expressed as monoclines whose axes lie parallel to the strike of the fault-array. The development of a synsedimentary monocline results in the main depocentre being offset into the hanging wall, in comparison with emergent synsedimentary normal faults where the depocentre is located in the immediate hanging wall of the fault (Sharp et al., 2000; Gawthorpe et al., 2003). Scaled analogue and numerical models of extensional fault-propagation folds above rigid basement fault blocks have shown that the amplitudes and wavelengths of monoclines are controlled by the dip of the basement fault and by the rheology of the overlying strata. These models also show that the mechanical stratigraphy controls whether fault-arrays within the cover are isolated or hard-linked to the basement fault (Withjack and Callaway, 2000; Finch et al., 2004).

The aim of this chapter is to describe the three dimensional (3D) geometry of the brittle and continuous deformation at and beyond the upper tips of a synsedimentary normal fault-array in the Inner Moray Firth basin (IMF). However, the method and applications are not limited to synsedimentary settings, or to the IMF. We use interpretations of 3D seismic reflection data to test the idea that deformation at

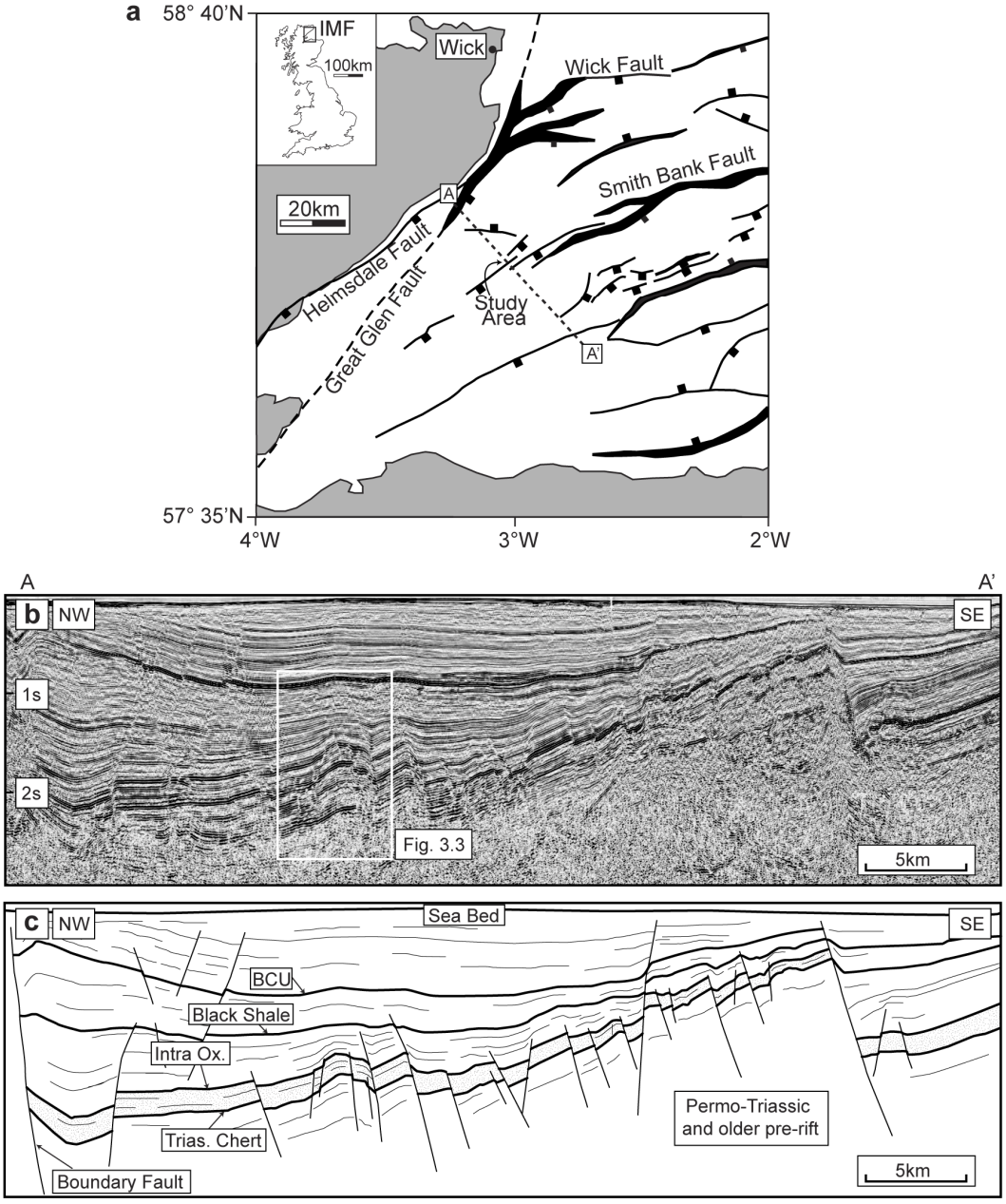

Fig. 3.2. (a) Regional 2D seismic section across the Inner Moray Firth (IMF) basin. (b) Interpretation of (a) showing the main marker horizons. (See Figure 4 for detailed stratigraphy). The IMF is an extensional half graben with the maximum subsidence against the Helmsdale–Wick basin-bounding fault systems to the NW. (c) Schematic structural geometry of the IMF for the regional base syn-rift stratigraphic horizon (see **Fig. 3.4**). BCU is the Base Cretaceous Unconformity; Intra Ox. is an Intra Oxfordian reflector that marks the base of the syn-rift sequence in the study area.

seismically imaged fault tips, including continuous deformation, is geometrically coherent. The methodology described here allows us to make inferences about the complex geometric arrangement of secondary faults, on which the offsets are below the resolution of the seismic data and are therefore manifest, at least in part, as continuous deformation at the scale of observation. The scale of structures studied in this chapter (maximum throw ca. 115 ms) is greater than those described by (Kristensen et al., 2008), but less than those of (Corfield and Sharp, 2000).

3.2 Geological setting

The study area is located in the Inner Moray Firth basin (**Fig. 3.2**). The main phase of NW-SE extension occurred during the Late Jurassic to Early Cretaceous (represented by the mapped H5 to BCU interval; **Fig. 3.3** and **Fig. 3.4**). There is little evidence for active extension during the Triassic to Mid-Oxfordian, which is represented by the mapped Triassic chert to Horizon H5 interval (**Fig. 3.3** and **Fig. 3.4**). This extension produced the regional NE-SW trending normal fault set (**Fig. 3.2**c) (Underhill, 1991b; Thomson and Underhill, 1993) and associated half-graben basin fill (**Fig. 3.2**) (Underhill, 1991b). Sediment packages thicken towards the NW along the Helmsdale–Wick boundary fault systems (**Fig. 3.2**). Subsequent Cretaceous sedimentation records gentle regional subsidence. Post-Cretaceous reactivation of some large-offset faults has occurred in the IMF. Faults that offset the BCU are recognised as being reactivated, but no evidence is found for post-Cretaceous deformation having reactivated faults in the immediate study area.

The study focuses on deformation within the Middle to Upper Jurassic succession, which encompasses the uppermost part of the pre-rift and lowermost syn-rift sequences (**Fig. 3.3** and **Fig. 3.4**). Regionally, the onset of syn-rift sedimentation was marked by deposition of the H5 horizon (Intra Oxfordian reflector). Correlation of seismic reflectors with nearby wells shows that the mapped syn-rift sequence (H5-H1) is shale-dominated and overlies a sandstone-dominated pre-rift sequence, which includes Horizon H6 (**Fig. 3.4**).

The mapped fault-array consists of three NE-SW trending en-echelon segments (F1-F3; **Fig. 3.3**) separated by two relay zones. Aggregate displacements on the fault array decreases towards the mapped lateral tips. The studied faults dip towards the NW, antithetic to nearby large offset faults that dip towards the SE (**Fig. 3.3**).

The mapped H1-H5 sequence thickens from footwall to hanging wall across F1, F2 and F3 (**Fig. 3.3**). Fault scarps in the IMF show no evidence for footwall erosion, which suggests that F1, F2, and F3 were either blind faults, or were synsedimentary faults that were blanketed with sediments during deposition of the Late Jurassic to Early Cretaceous syn-rift sequence (Underhill, 1991b, a; Nicol et al., 1997; Childs et al., 2003). Analysis of throws on the mapped faults show that F1, F2 and F3 have vertical displacement gradients greater then ca. 0.16 (**Fig. 3.5**). This value is consistent with vertical displacement gradients calculated for synsedimentary faults in other areas (Nicol et al., 1996; Nicol et al., 1997; Cartwright et al., 1998; Walsh et al., 2003a). Furthermore, the boundaries between sub-horizontal and sub-vertical throw contours, which separate pre- and syn-faulting parts of the fault surface (Childs et al., 2003), coincide with the base of the regional syn-rift sequence (TopA horizon; **Fig. 3.5**). These observations suggest that faults F1, F2, and F3 were active during the deposition of the Upper Jurassic syn-rift sequences (**Fig. 3.3** and **Fig. 3.4**; H5-H1). This inference is consistent with previous studies that have also shown similar faults in the IMF to be synsedimentary in origin (Underhill, 1991a, b; Nicol et al., 1997; Childs et al., 2003; Walsh et al., 2003a). Together, our observations suggest that sedimentation rates generally outpaced fault displacement rates throughout Late Jurassic to Early Cretaceous extension (Childs et al., 2003). Importantly, the synsedimentary character of these faults enabled them to interact with the free surface, facilitating the development of fault-propagation folds (Sharp et al., 2000; Gawthorpe et al., 2003).

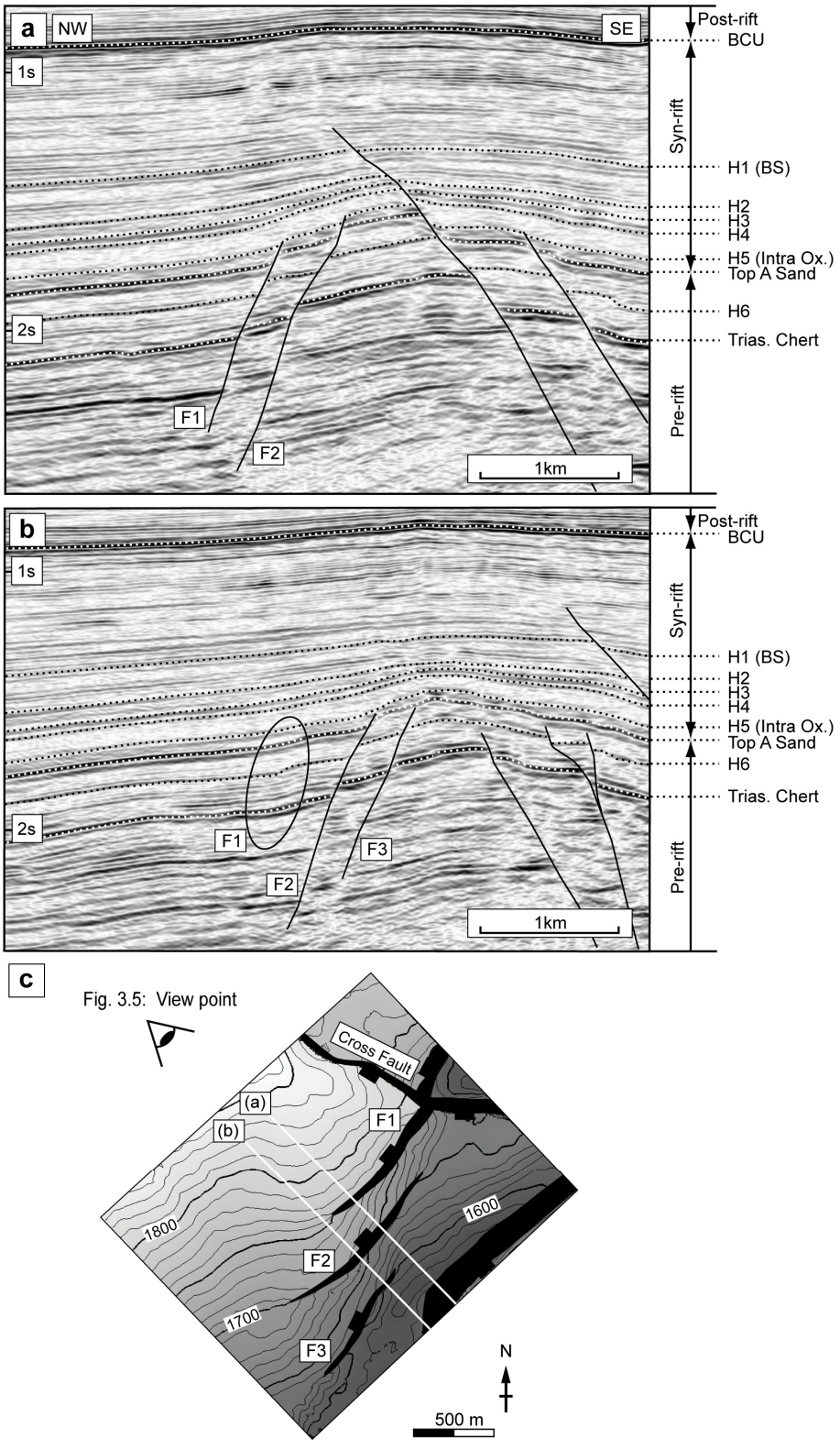

Fig. 3.3. (a-b) Adjacent seismic profiles aligned normal to the strike of the mapped fault-array. The six mapped horizons used in this study are H1-H6 and regional marker horizons are also shown for context. (b) Rotated horizons past the SW tip of fault F1, circled. (c) Time-structure map for horizon H6. The three faults in the study area display a left-stepping, en-echelon arrangement and are separated by relay ramps linking the footwall and hanging wall sediments. A later ENE-WSW trending cross fault, formed during minor post Cretaceous extension, cuts fault F1. Contour measurements are in ms two-way travel time.

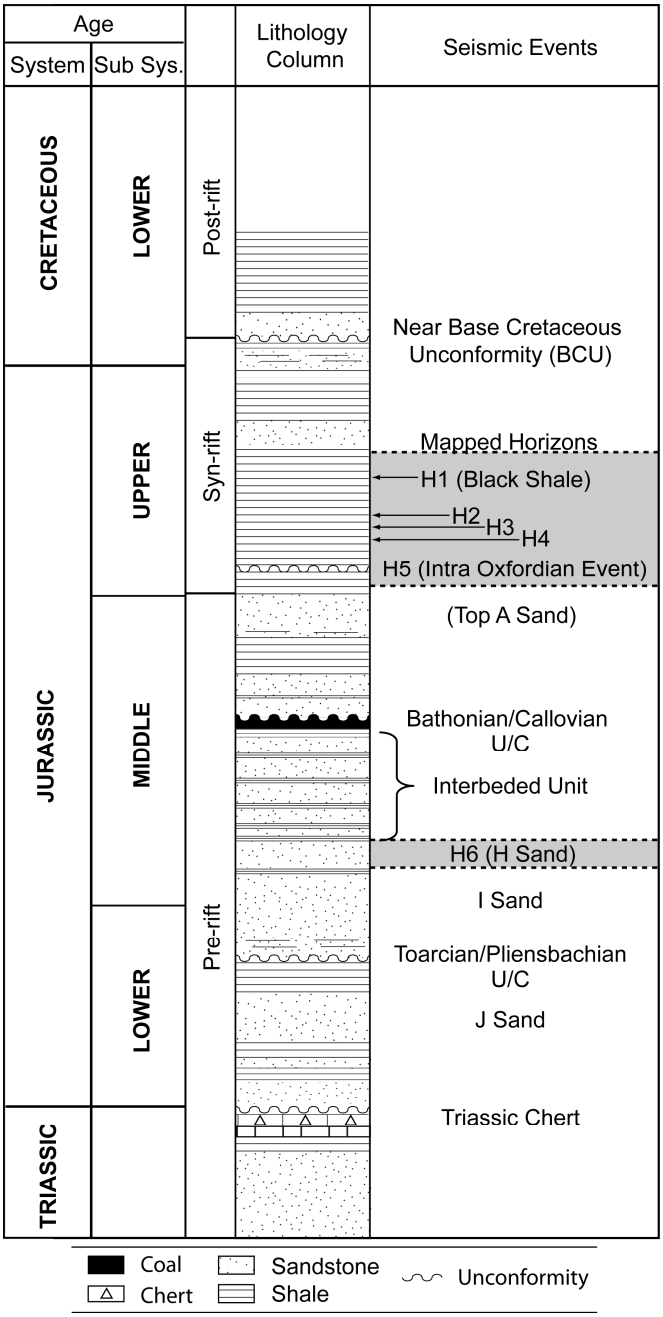

Fig. 3.4. Lithological units from the study area (Beatrice Field), adapted from (Stevens, 1991). Horizons used in this study are highlighted (grey). H1-H5 are in the syn-rift sequence, while H6 is in the pre-rift section.

3.3 Method

3.3.1 3D seismic interpretation

The 3D seismic survey used in this study is located over the Beatrice oil field within the central IMF (**Fig. 3.2**). The seismic survey has a 12.5 m by 12.5 m inline and crossline spacing. The aerial extent of the study area within the survey is 3 km by 2 km. Velocity

information from nearby wells was used to depth convert a seismic section. The velocity data are consistent with a uniform overburden lacking lateral velocity variations (**Fig. 3.6**). Therefore, the depth conversion process had a minimal effect on the overall geometries observed, apart from a uniform vertical expansion of the entire section. Relative changes of the fault geometries are negligible between the depth and time sections (**Fig. 3.6**). Consequently, to prevent the introduction of additional uncertainties due to depth converting the data, the time-migrated volume was used to analyse fault-related deformation.

Six horizons (H1-H6) that are either cut by or located above the upper tip line of the mapped fault-array were picked on every fifth inline and crossline. Areas of structural complexity were interpreted on every second inline and crossline (25 m spacing).

3.3.2 Quantifying continuous and discontinuous deformation

A detailed account of the method used in this chapter/paper can be found in chapter 2 of this thesis. For reference, the terminology Abnormal Rotation, used in this chapter, is equivalent to Fault Normal Rotation (FNR), which is used in other chapters in the thesis.

3.3.2.1 Discontinuous deformation (fault throw)

Fault throw is defined as the vertical component of displacement measured between mapped horizon cut-offs (Needham et al., 1996). Throw was measured along sample lines orientated perpendicular to the average strike of the studied faults. Sample line spacing was 20 m. All faults were assumed to have dip-slip displacements (Underhill, 1991b) and the location of the sample grid was fixed, allowing comparison of displacements on different horizons. A disadvantage of using a fixed, oriented sample grid arises when individual faults are not parallel to the average fault strike for the sample volume. This geometric difference creates a miss-match between fault throw and adjacent continuous displacement, adding noise to the aggregate d-x profiles. In this study, all faults are sub-parallel so the effect is negligible.

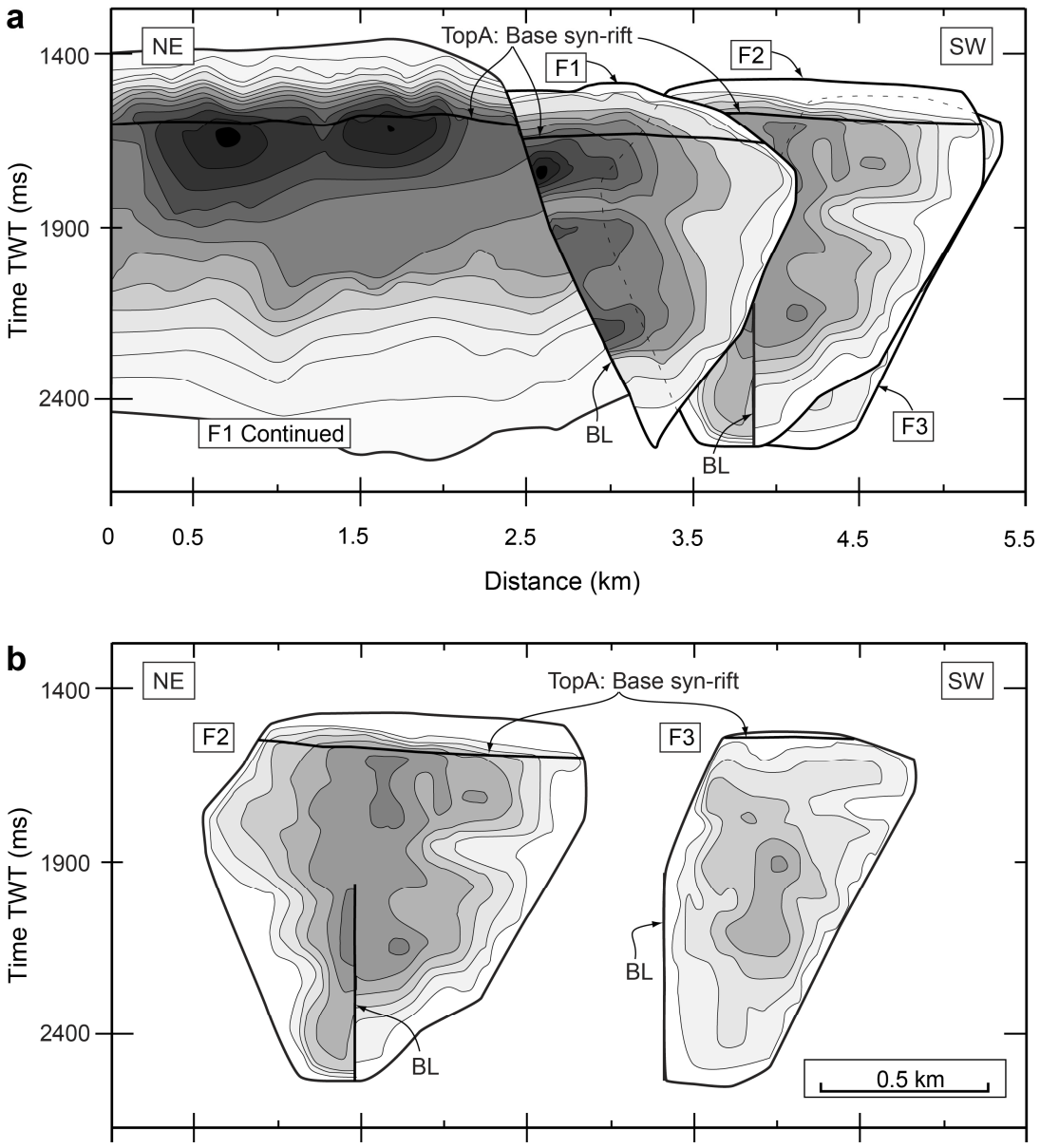

Fig. 3.5. Plots of fault throw with contour interval of 10 ms TWT. Throw values go up to 120 ms TWT (darkest colour). The hanging wall cut-off for horizon TopA (Top A Sand, **Fig. 3.4**) is marked on the plots and represents the base of the syn-rift sequence. (a) Composite fault image viewed in strike projection, showing the spatial relationship of faults F1, F2 and F3 (See **Fig. 3.3**c for context). F1 is cut by a later cross fault and continues off the edge of the seismic data to the NE. (b) Throw plots for faults F2 and F3. F2 and F3 are partially linked along a branch line (BL). Vertical throw gradients are measured for each fault from the point of maximum displacement to the upper tip line. Vertical throw gradients are 0.5, 1.3, 0.34 and 0.18 for faults F1, F1 continued, F2 and F3 respectively.

The maximum uncertainty associated with the positions of mapped cut-offs is estimated to be 6 ms TWT. Of this, 4 ms TWT arises from the sampling interval of the seismic data. The remaining uncertainty is associated with errors in correlating the interpreted horizon picks across faults. In areas where the seismic horizons are well imaged, the uncertainty due to errors in correlation approach zero.

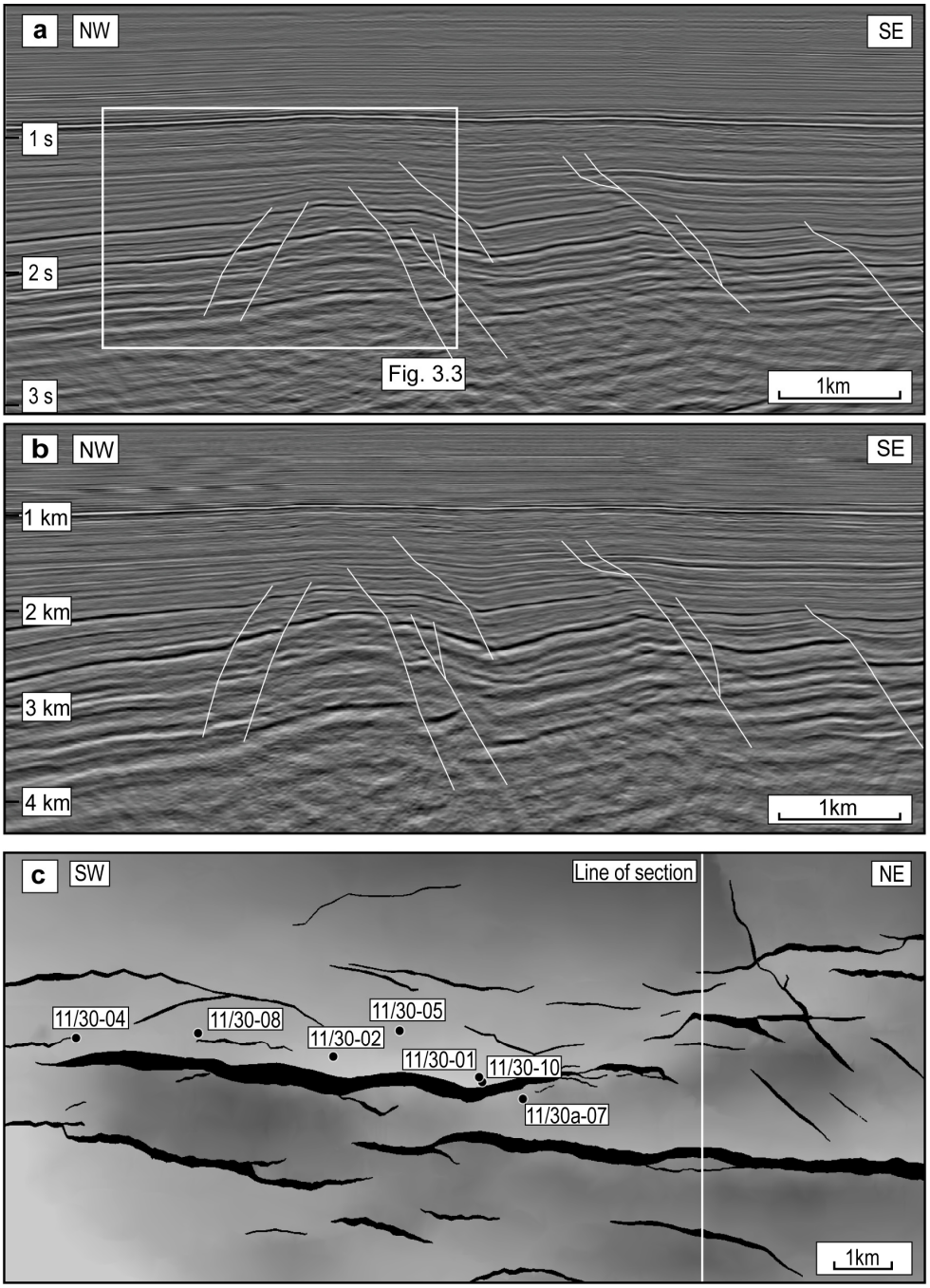

Fig. 3.6. Seismic sections through the study area. (a) Time section. (b) Depth-converted section using velocity information from nearby wells (c). (c) A time-structure map for regional horizon TopA, showing the location of the section and nearby wells. The map is coloured for two-way travel time (TWT), and dark colours equal largest TWT.

The ability to interpret fault offsets in seismic data is controlled by the vertical resolution of the data. At depths similar to those in this study (>1.5–2 seconds TWT or approximately 2 km) only faults with throws greater than 20 m will typically have observable offsets (Townsend et al., 1998). Large sections of the fault surfaces with smaller throws are therefore not resolved through mapping of offset horizons.

However, by studying the continuous deformation present beyond the mapped fault tips a greater proportion of the fault-related strain can be measured. This continuous deformation at the scale of observation can be mapped with confidence due to the close spacing of the 3D seismic lines and by minimizing miss-ties on horizon grids.

3.3.2.2 Continuous deformation (apparent dip)

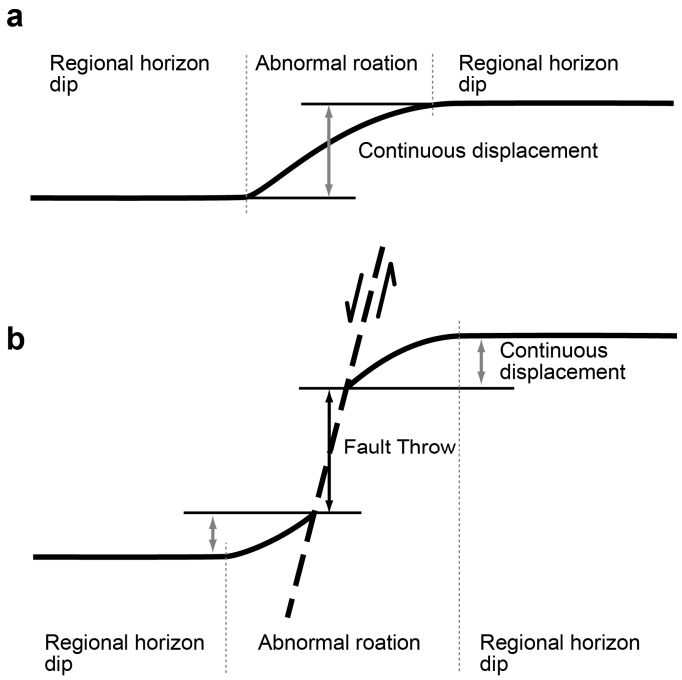

Fig. 3.7. Schematic illustration of displacement measurement for examples of abnormal rotation. The limits of abnormal rotation are defined by the departure from the regional horizon dip. The vertical displacement or throw is calculated for a monoclinal fold.

The vertical component of displacement due to continuous deformation in the volume surrounding the mapped faults was calculated from the apparent dip of triangulated horizon grids. Apparent dip was measured along the same set of sample lines used to calculate fault throw, thus allowing direct comparison with fault throw (**Fig. 3.7**). Sensitivity studies were performed on selected horizon grids to determine the optimum triangle size. Large triangles produce smoother surfaces. Smaller triangles more closely match the picked horizon grid, but increase the potential for noise (see **Fig. 2.3**). In this case, “noise” refers to scatter due to natural variability in reflector dip that is not fault-related, miss-correlations of horizon grids across faults and the inherent uncertainty associated with the sample interval of the seismic data. An

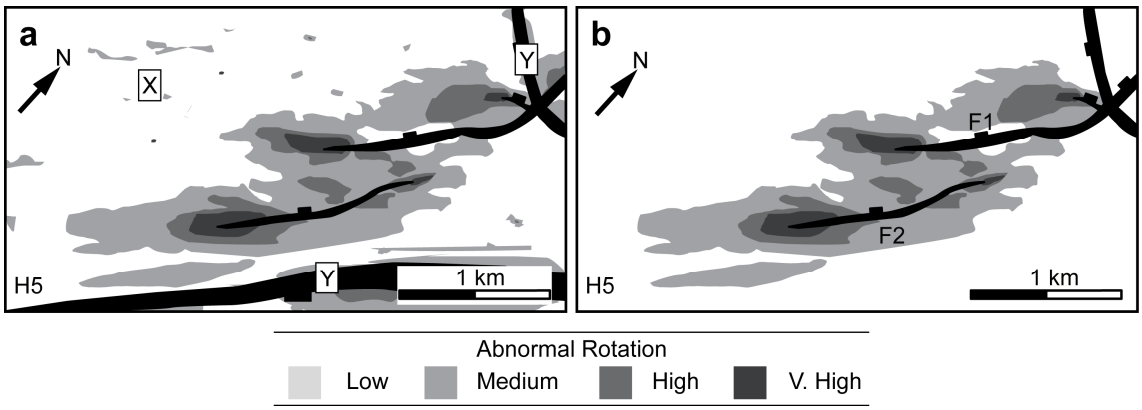

Fig. 3.8. (a) Areas of abnormal rotation where all apparent dips above the defined background regional values are selected, resulting in the selection of miss-picks and artefacts (X), and geometries on adjacent faults (Y). (b) These features are removed to leave the abnormal rotations attributed to the studied fault-array.

average triangle size of 20 m was used to ensure a representative reconstruction of the raw data.

The next step was to distinguish apparent dips due to continuous deformation in the volume surrounding the mapped fault-array (here termed "abnormal rotations") from dips caused by regional tilting of each horizon. The half-graben geometry of the IMF means that reflectors display a regional tilt towards the NW (**Fig. 3.2**). Some of the tilt is also likely to result from flexure in the footwall of a major fault located immediately SE of the studied fault-array (**Fig. 3.2** and **Fig. 3.3**) (Barnett et al., 1987). The magnitude of regional tilt on each horizon was calculated in areas away from the mapped fault-array, and apparent dips less than or equal to the regional tilt were excluded from further analysis. Large apparent dips can also be caused by miss-ties in horizon grids between adjacent inlines or crosslines (**Fig. 3.8**a: point X) and/or by deformation related to other faults (**Fig. 3.8**a: point Y). These anomalies were removed by visual inspection and were also excluded from further analysis. The remaining areas of abnormal rotation were hypothesised to be fault-related continuous deformation in the volume surrounding the studied fault-array (**Fig. 3.8**b).

Maps showing the distribution of abnormal rotation around the mapped fault-array were contoured for "low" (≤ 2°), "medium" (2°-4°), "high" (4°-12°), and "very high" (> 12° excluding fault polygons) values of abnormal rotation. As shown previously, depth conversion results in vertical expansion of seismic sections (**Fig. 3.6**), allowing comparison of abnormal rotations on different horizons.

Finally, the vertical displacements attributed to continuous fault-related deformation were summed along each sample line, allowing direct comparison with fault-throw measurements (**Fig. 2.10** and **Fig. 3.9**).

Fig. 3.9. (Next page) Left, map-view distributions of abnormal rotation for each horizon. Each map uses a grey-scale for the magnitude of abnormal rotation (see **Fig. 3.8** and main text). White areas are not deformed by F1-F3. Right, displacement distance (d-x) profiles for each horizon. The geographic position of the maps is fixed for each horizon. The graphs record the amount of vertical displacement due to abnormal rotation (shaded areas on maps) and the throws of seismically imaged faults. Graphs (H1 – H6) all show displacement gradually decreasing to the SW. Solid black lines are for continuous deformation, light gray lines are for fault throws, thin black lines are for total fault throw and dashed lines are for the total vertical component of the deformation.

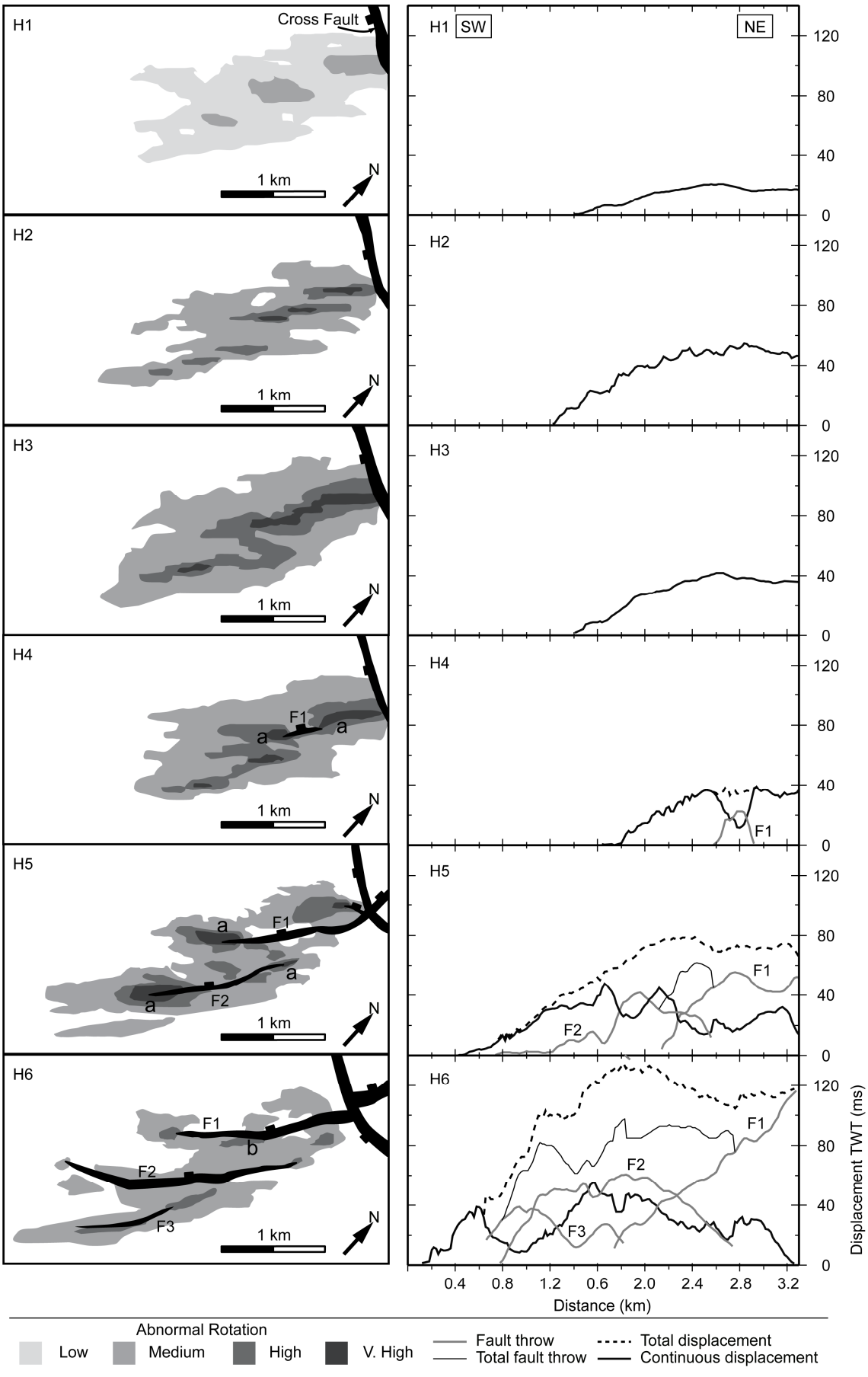
H1
Cross Fault
1 km
N
H1 SW
NE
120
80
40
0
H2
H3
H4
F1
a
H5
F2
b
H6
F3
0.4
0.8
1.2
0.6
2.0
2.4
2.8
3.2
Distance (km)
Displacement TWT (ms)
Abnormal Rotation
Low
Medium
High
V. High
Fault throw
Total fault throw
Total displacement
Continuous displacement

3.4 Results

3.4.1 Reflector geometries

Horizons H1 to H3 are located above the seismically imaged upper tip line of the fault-array. Horizons H4 to H6 are cut and offset by one or more of the mapped fault segments, F1, F2 and F3 (**Fig. 3.3**). Vertical seismic sections oriented approximately perpendicular to fault strike show that the youngest H1 – H3 sequence (and, where it is not faulted, the older H3 – H5 sequence), change in thickness across the underlying fault-array. The points at which younger H1 – H3 sequences achieve their maximum thicknesses are not immediately adjacent to the upward projection of the underlying fault plane, but are located up to 200 m to the NW, towards the mutual hanging wall of the fault-array (**Fig. 3.3**). In contrast, the oldest H5 – H6 sequence is commonly thicker in the immediate hanging walls of the mapped faults (e.g. **Fig. 3.3**b, adjacent to fault F1).

Reflector dips vary around the seismically imaged fault tips. Dip values typically increase within regions tens to hundreds of metres wide situated either side of and/or above mapped upper tip points (**Fig. 3.3** and **Fig. 3.9**). The steepest horizon dips occur in narrow zones above fault tips (e.g. **Fig. 3.9**: left hand side). Steep dips also occur along-strike from the lateral tips of seismically imaged faults. These anomalous rotations occur within both pre- and syn-faulting sequences (e.g. **Fig. 3.9**b: Horizon H6). In all cases, the anomalous rotations occur in strata that dip towards the mutual hanging wall of the fault-array, giving rise to broad monoclines and sharper kinks (**Fig. 3.3**).

3.4.2 Spatial distribution of continuous deformation

In map view, the patterns of abnormal rotation observed on horizons H1 – H4 are not uniformly distributed above faults F1 and F2, but rather occur as patchy areas of high and low abnormal rotations (**Fig. 3.9**: left hand side). Regions of high and very high rotation occur above the seismically imaged tip lines of F1 and F2, expressed as discrete en-echelon bands (dark grey) surrounded by wider zones of more gentle

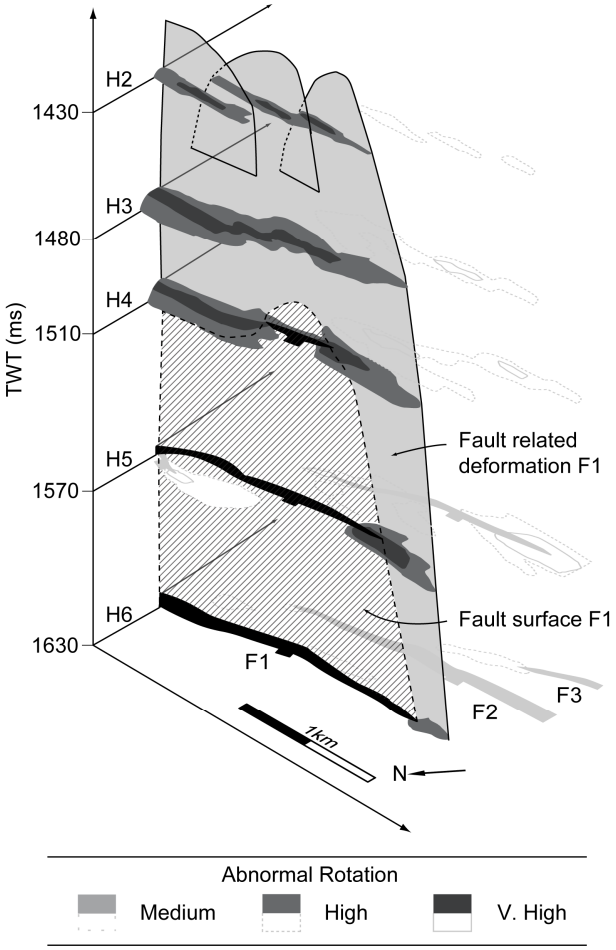

Fig. 3.10. A composite 3D view showing the distribution of the high and very high levels of abnormal rotation in the volume surrounding the mapped F1 fault segment. The cross-hatched area represents the mapped F1 fault surface. A variable thickness zone of fault-related deformation encircles fault F1, grey area.

abnormal rotation (light grey) (**Fig. 3.9**: horizons H1 – H4). The en-echelon bands of high to very high rotation vary in width between 60 and 300 m and coincide with the projected locations of the seismically imaged faults from below (**Fig. 3.10**). The steep limbs of these monoclinal bands are located over the projected hanging wall blocks (**Fig. 3.3**).

Horizon H1 is the youngest horizon to have been affected by faults F1 and F2 and marks the uppermost boundary of continuous deformation that can be imaged in the seismic volume. Starting at horizon H1 and working downward toward the mapped upper tip line, the distribution and magnitude of abnormal rotation changes noticeably (**Fig. 3.9**). Horizon H1 is characterised by a 750 m wide zone of low abnormal rotations,

which trends NNE–SSW and contains patches of medium abnormal rotation (darker grey) that are arranged in a left-stepping en-echelon pattern.

On Horizon H2, an 800 m wide zone of fault-related continuous deformation follows the same NNE – SSW trend as horizon H1. Within this wide zone are three approximately 90 m-wide bands of high to very high abnormal rotations, which trend NE – SW and again have a left-stepping, en-echelon arrangement. The NNE – SSW trend persists for Horizon H3, where the wider zone of continuous deformation contains a continuous band of parallel, NE – SW trending, left-stepping segments that merge to define the overall NNE – SSW trend.

Horizon H4 is also characterised by a general NNE – SSW trending zone of continuous deformation. Fault F1 intersects H4 (**Fig. 3.9**: Horizon H4). The magnitude of continuous deformation is noticeably reduced in the immediate hanging wall of the mapped fault trace (**Fig. 3.9**: Horizon H4, graph). The greatest magnitude of continuous deformation for this horizon occurs at the fault tips (i.e. directly above the trace of F1 on H5) and above the projected location of F2 (**Fig. 3.9** and **Fig. 3.10**).

Two seismically imaged fault segments cut horizon H5 (**Fig. 3.9**). Fault F1 has a maximum throw of approximately 50 ms at this level. The distribution and amount of continuous deformation on horizon H5 is markedly different as compared to the overlying horizons. The high levels of continuous deformation present on the younger horizons (H2 – H4) are reduced in the immediate foot and hanging walls of F1 and F2 (**Fig. 3.9**). However, high levels of continuous deformation extend beyond the mapped south-western tip of fault F1 to a distance approximately equal to the length of the fault trace seen on the underlying horizon H6 (**Fig. 3.9**, Horizons H5 – H6, point a). In addition, NE-SW and E-W trending bands showing high levels of continuous deformation occur, respectively, at the tips of F2 and within the relay zone between F1 and F2.

Horizon H6 is cut by three seismically imaged fault segments, and displays minimal continuous deformation in the hanging wall of fault F1. The SW tip of fault F1 also displays smaller magnitudes of continuous deformation compared to the same region

on H5. Horizon H6 contains the maximum along-strike extent of fault F1 hence there are no (seismically imaged) fault tip lines that lie directly beneath the mapped tip of F1 (**Fig. 3.5**). The immediate footwall of fault F1 is characterised by a band of continuous deformation adjacent to a prominent right-stepping bend in the fault trace (**Fig. 3.9**: Horizon H6, point b). This band of anomalous dips follows the same trend as the fault trace immediately to the NE of the right-stepping bend.

3.4.3 Displacement distance profiles

The displacement distance (d-x) profiles (**Fig. 3.9**: right hand side) show the vertical offsets (throws) on faults F1, F2 and F3 together with the vertical component of continuous displacement calculated from the areas of abnormal rotations (**Fig. 3.9**: left hand side). The d-x plots are therefore a graphical representation of the discontinuous and continuous displacements for each horizon. All following measurements of throw/ vertical displacement are in two way travel time.

The maximum aggregate vertical component of displacement decreases from approximately 140 ms on H6 to about 80 ms on the overlying H5 horizon, but has an approximately constant value of between 40 and 50 ms on horizons H2 to H4. The maximum aggregate component on H1 is about 20 ms. The along-strike extent of the region affected by faulting and/or continuous deformation displays a similar pattern. The south-western “tip point” of the deformation zone is situated about 300 m further towards the NE on horizon H5 compared with H6, and by about 1200 m in the same direction on H4 compared with H5. By contrast, the tip of the deformation zone maintains an approximately constant position for horizons H1 – H4.

Continuous displacement accounts for a significant proportion of the total deformation observed on each horizon. Horizons H6-H5 have approximately equal amounts of displacement partitioned between continuous deformation and mappable fault offsets (**Fig. 3.9**). Horizons H1-H3 are entirely deformed by continuous deformation while horizon H4 is nearly all continuous deformation.

On each horizon, the total displacement curve (dashed line) resembles that of a single fault more than either the fault displacement or continuous displacement curves alone

(**Fig. 3.9**). Close inspection of the d-x plots shows striking inverse correlations between the observed magnitudes of continuous and discontinuous displacement (**Fig. 3.9**). For example, abrupt increases in the magnitude of continuous displacement occur at the NE tip of F2 and SW tip of F1 on horizon H5, which helps to "smooth out" the total d-x profile (**Fig. 3.9**: H5). Similarly, midway along the strike of F2 a low in fault displacement is matched by an increase in continuous displacement (**Fig. 3.9**: H5). These relationships maintain an aggregate profile that resembles one for a single fault. Similar relationships can be observed on the other horizons (**Fig. 3.9**: H4-H6). The d-x profiles derived solely from continuous displacement on horizons H1 – H3 are also seen to resemble that of a single coherent fault. Thus, d-x profiles resembling that of a single coherent fault are present at all levels within the sequence.

3.4.4 Description of fault F1

Fault F1 has a maximum throw of 115 ms TWT decreasing towards the mapped SW tip. Fault F1 displays its maximum lateral extent on horizon H6 and decreases in length upwards to horizon H4 (**Fig. 3.9** and **Fig. 3.10**). Horizon H6 is characterized by a zone of abnormal rotation that extends 100 m beyond the mapped fault, but the horizontal extent of the region of abnormal deformation increases upwards between horizons H6 – H4 (**Fig. 3.10**). The tip line of fault F1 directly underlies Horizons H5 and H4. Therefore, a correlation exists between an increase in the extent of abnormal rotation beyond the mapped fault tip and the presence of a seismically imaged fault plane immediately beneath those horizons. The transition from the sandstone-dominated pre-rift strata to the shale-dominated syn-rift sequence occurs at horizon H5 (**Fig. 3.3**). This transition also marks an increase in the ratio of continuous deformation to fault displacement, and the appearance of a wide zone of low to medium rotation, measured normal to strike (**Fig. 3.9**). Above fault F1 (H4-H1) is a zone of strong abnormal rotation. This zone splits into three distinct linear bands on horizon H2. These zones of abnormal rotation trend NW-SE matching the mapped fault below.

3.5 Interpretation and discussion

3.5.1 Geometric coherence

A consequence of syntectonic sedimentation, such as that inferred in the study area, is the development of different sediment thicknesses in the hanging wall and footwall of mapped faults. Therefore, it is important to consider the role of differential compaction in producing rotated seismic reflectors and apparent monoclinal geometries, as reported by Thomson and Underhill (1993) elsewhere in the IMF basin. Compactional drapes are likely to be greatest within depocentres containing the thickest syn-faulting sequences. This situation will occur towards the centres of faults, that is, closest to the point of maximum throw. However, our observations show that continuous rotations of seismic reflectors are likely to be greatest at fault tips, not within the hanging walls of seismically imaged fault traces. Similarly, rotated reflectors can also be seen within the pre-growth (pre-H5) sequence, which was presumably well-compacted prior to the onset of faulting. Some compactional drapes interpreted by Thomson and Underhill (1993, their Fig. 5) are related to faults with marked convex-upward geometries, whereas the faults in the present study area are sub-planar (**Fig. 3.3**c). We conclude that the observed abnormal rotations were primarily a response to fault growth and propagation, rather than differential compaction. However, differential compaction may have subsequently exaggerated stratal dips and monoclinal geometries.

Our results show that the continuous deformation in the volume surrounding the upper part of the mapped normal fault-array is characterised by rotations of seismic reflectors, resulting in increased dips towards the mutual hanging wall. These “abnormal rotations” give rise to broad monoclines and sharper kinks. In map view, regions of continuous deformation appear to be patchily but systematically distributed, with the greatest magnitudes of abnormal rotation occurring above or along-strike from mapped upper and lateral fault tip points, adjacent to bends in fault traces, and within relay zones (**Fig. 3.9**). The vertical component of displacement calculated from the continuous deformation acts to “fill-in” missing displacement in the throw profile for the aggregate fault-array (**Fig. 3.9**). The aggregate d-x profile more closely

resembles that of a single fault than either the fault throw or continuous d-x profiles alone (Huggins et al., 1995; Walsh et al., 2003b). The mapped structures therefore appear to have developed as part of a single, coherent fault-array.

3.5.2 Fault-propagation folding and the influence of mechanical stratigraphy

In detail, the youngest syn-rift horizon (H1) shows the development of broad monoclines (**Fig. 3.9**). Older syn-rift horizons display sharp, NE-SW trending "kinks" (areas of high abnormal rotation) that are situated directly above mapped fault tip lines (**Fig. 3.9** and **Fig. 3.10**) within broad regions of more gentle rotation. The kinks become more pronounced and better interconnected on older horizons (**Fig. 3.9**: H2 – H5). Trading space for time, we interpret these observations to mean that the broad, low-amplitude folds developed at an early stage of fault propagation but were subsequently deformed by sharper kinks situated directly above propagating tip lines.

This interpretation is consistent with the results of analogue and numerical models that simulate faulting and fault-propagation folding in the sedimentary cover above a predefined "basement" fault (Withjack et al., 1990; Finch et al., 2004). Numerical models show that deformation of a weak cover sequence is initially characterised by the development of a broad monocline above the basement fault. With increasing slip, deformation becomes more localised above the propagating fault, giving rise to tight fault-propagation folds within the broad monocline (Withjack et al., 1990; Finch et al., 2004). As deformation continues, the limbs of the sharp, kink-like fault-propagation fold steepen until they are finally breached by the propagating fault. By contrast, the presence of a strong cover sequence results in a narrower monocline and more rapid propagation of the basement fault into the cover. These models show that the mechanical strength of the cover sequence is an important control on the development of fault-propagation folds.

The inherent limit in seismic resolution means that it is impossible to quantify the proportion of continuous displacement accommodated by plastic deformation vs. sub-seismic scale faulting, without direct sampling by drilling (see appendix 1: **Fig. A2**). Nevertheless, it is important to point out that the fault-propagation folds described in

this study have vertical extents (amplitudes) of approximately 40 ms (**Fig. 3.9**), which is more than an order of magnitude smaller than comparable seismic examples of fault-propagation folds on the Halten Terrace, offshore Norway (vertical extents between 500 – 1000 ms) (Withjack et al., 1990; Corfield and Sharp, 2000). Here, fault propagation folds developed in a shale-dominated syn-rift sequence overlying pre-rift red beds and evaporites (Marsh et al., 2009). The overall scale of fault-propagation folding is controlled by the size of the underlying faults, but it appears that the geometry and evolution of the folds is controlled by the mechanical properties of the overburden sequence (Withjack et al., 1990).

3.5.3 Growth of the mapped fault-array

The total d-x profiles (fault throw plus continuous deformation; **Fig. 3.9**) show that the along-strike extent of the region affected by fault-related deformation on F1, F2 and F3 is less from the H6 (pre-rift) and H4 (syn-rift) stratigraphic level, but is approximately constant within the overlying syn-rift horizons. Similarly, maximum aggregate displacements are less between horizons H6 to H4, but are nearly constant for H4 to H2 before decreasing again for H1. The near-constant width and along-strike extent of the region affected by fault-related deformation suggests that the volume of continuous deformation surrounding the mapped faults is enclosed by a steeply-plunging (sub-vertical) lateral tip line. The observation of near-constant along-strike length throughout the syn-rift sequence is interpreted to imply that the lateral length of the fault-array was established at an early stage in its growth. This inference is consistent with a previous study that suggests that fault lateral lengths may be near-constant from early fault system development (Walsh et al., 2002).

The small changes in aggregate displacement upward through the H4 to H2 syn-rift succession are consistent with a small vertical displacement gradient above horizon H5 (**Fig. 3.9**: right hand side). The near-constant aggregate displacement for these horizons, followed by a decrease in displacement for the youngest syn-rift horizon, H1, could be interpreted as evidence for fault reactivation following a period of stasis during the deposition of H4 to H2, e.g. (Cartwright et al., 1998). However, our preferred interpretation, which requires only a single phase of rifting, is that the small

vertical displacement gradients resulted from an increase in the sedimentation rate relative to the displacement rate on the evolving fault-array. This increase in the ratio of sedimentation to fault displacement could have occurred due to an absolute increase in the sedimentation rate, or due to a temporary decrease in fault-slip rate in this part of the IMF basin, cf. (Jackson, 1999), or a combination of both mechanisms. In any case, blanketing of the fault scarps facilitated the development of fault-propagation folds in the overburden.

3.5.4 Geometry and evolution of fault F1

The lateral tip line of fault F1 in the study area plunges steeply towards the SW (**Fig. 3.10**). The north-eastern upper tip line is sub-horizontal beneath H4, but south-westward it curves up and penetrates H4. The lateral "tip line" or boundary of the continuously deformed region around F1 has a similar geometry to the lateral fault tip line, plunging steeply south-westward. The 3D reconstruction clearly shows that regions of high continuous strain, i.e. monoclines, on horizons H4 – H6 directly overlie the lateral tip line of F1. Monoclines observed at fault tips, similar to those seen here, are often recorded in outcrop data (Cartwright and Mansfield, 1998; Jackson et al., 2006; Ferrill et al., 2007). Our results therefore confirm White and Crider's (2006) suggestion, which was based on outcrop data and linear-elastic boundary-element method modelling, that monoclinal folds are likely to develop above the blind, lateral extents of surface-breaking, synsedimentary faults.

The reflectors above the mapped upper tip line of fault F1 are deformed by three en-echelon, left-stepping monoclines (fault-propagation folds). The internal structure of the monoclines is below the resolution of the seismic data, but the analysis of the aggregate d-x profiles show that the folds developed as a coherent part of the fault-array. The simplest model to explain the en-echelon arrangement of the monoclines is that the upper tip line of fault F1 bifurcated (split) as it propagated upwards from horizon H5, forming three en-echelon, left-stepping lobes. On H4, the central lobe is visible as the mapped trace of F1 (**Fig. 3.9**). This interpretation is consistent with previous models for the coherent growth of segmented fault-arrays (Childs et al., 1996b; Marchal et al., 2003; Walsh et al., 2003b). Importantly, our findings show that

the distribution of continuous deformation can be mapped and visualised using 3D seismic data, providing a method to study the interactions between primary and secondary fault segments even where the aggregate throw is only a few tens of milliseconds TWT (**Fig. 3.10**).

Analysis of seismic data alone cannot, however, explain all of the observed relationships. In particular, it is not clear as to why anomalous dips are commonly observed to be low or absent in the immediate hanging walls of mapped faults (e.g., **Fig. 3.9**). It could be because stratal dips are very high within narrow zones immediately adjacent to the fault traces, hence are not imaged in seismic data. This hypothesis would suggest that reflector dips increase with increasing displacement on adjacent faults. This concept is consistent with continuous deformation originating due to, or being modified by, frictional drag. Alternatively, the absence of continuous deformation may suggest that some segments that propagated upwards and broke the surface more rapidly than in adjacent regions (Ford et al., 2007).

3.5.5 Practical applications

Our results show that areas with abnormal rotations can be used to identify regions of fault-related deformation in 3D seismic data. Correct identification of small-scale fault-related deformation has implications for modelling fluid flow (hydrocarbons, ground water, CO_2) in the subsurface. The method proposed here is versatile and can be used in any tectonic setting and complements existing techniques used to sample fault throw. Previous studies (e.g. Steen et al., 1998; Townsend et al., 1998) have suggested that dip anomalies can be used to identify areas of small (sub-seismic) scale faulting in 3D seismic volumes. For example, (**Fig. 3.9**) highlights areas of anomalous rotations within the relay ramp between F1 and F2 on horizon H5, and adjacent to the right-stepping bend in the trace of F2 on H6. The map-view geometries suggest that these areas of continuous deformation may be associated with, respectively, an incipient breaching fault cutting obliquely across the relay ramp and a footwall splay fault associated with a breached relay on F2. The coherency of the aggregate d-x profiles is consistent with these inferences. The key point is that the techniques described here allow rigorous geological analysis of these anomalies, enabling us to investigate

possible implications if they are treated as faults or fault-related fracture systems, such as investigating the geometry and evolution of fault linkage in relay zones (Chapter 4).

3.6 Conclusions

1. We have calculated the apparent dips for six horizons within a 3D seismic volume, measured along sample lines oriented perpendicular to the average strike of a mapped fault-array. This dip attribute is used to derive the spatial distribution of fault-related continuous deformation, from which we calculated the vertical component of displacement due to continuous deformation. This measure of continuous displacement is directly comparable to fault throw.
2. This technique permits the analysis of continuous deformation structures (fault-propagation folds) that are up to an order of magnitude smaller than previously described.
3. Our study supports previous work, which demonstrated that fault-arrays and associated volumes of continuous deformation surrounding them are geometrically coherent and are likely to have been kinematically coherent throughout their evolution (Walsh and Watterson, 1991; Walsh et al., 2003b).
4. The observation that a fault-array remains coherent as it propagates is not unexpected, if we assume a coherent growth model (Marchal et al., 1998; Walsh et al., 2003b). However, without inclusion of the continuous deformation, the d-x profile for this fault-array could have been miss-interpreted as representing three isolated fault segments with coincidental overlaps.
5. The along-strike extent of the volume of continuous deformation above the upper tip line of the mapped fault-array is approximately constant upwards through the growth sequence, implying that the length of the fault-array was established at an early (small displacement) stage in its development.
6. Analysis of the continuous deformation in the volume above one of the mapped fault segments (F1) reveals a pattern of deformation that is consistent

with the distribution of secondary faults expected to develop during tip line bifurcation (Childs et al., 1996b; Marchal et al., 2003). The techniques described in this study can therefore be used to infer the 3D distribution of fault-related strain ahead of propagating fault surface if space is traded for time in the analysis.

7. Our results also confirm previous model predictions that monoclinal folds are likely to develop above the blind, lateral extents of surface-breaking faults (White and Crider, 2006).

8. The analysis of continuous deformation can potentially be used to postulate the existence of sub-seismic scale faults and fracture systems, (e.g., at fault bends and within relay ramps) for the purpose of considering their effects on rock properties and fluid behaviour if the structures were present.

Chapter 4. Strain compatibility and fault linkage evolution in relay zones on normal faults

Abstract

Detailed interpretations of 3D seismic and field data show that relay-bounding faults link simultaneously at multiple points along overlapping tip lines, resulting in segmented branch lines. To maintain strain compatibility between the linked and open ramps at different depths within a relay zone, displacements on the bounding faults and rotations within the ramps are communicated up and down dip, irrespective of whether the relay is breached or open at that level. This imparts an apparently linked displacement-length profile shape onto un-linked horizons, and allows relict splays to continue accommodating displacement on linked horizons until the relay zone is fully breached. Slip-normal fault linkage can enhance fault curvature normal to the slip direction, which impedes continued slip. The removal of these slip-normal bends can modify fault linkage geometries and while restraining bends remain, slip on both arms of the relay can occur. Slip-normal fault linkage also encloses the base of relay zones with fault surfaces and with continued rotation of the overlying horizons towards the mutual hanging wall volumetric strains may develop in the base of the ramp to maintain strain compatibility. Despite complex fault linkage geometries and strain compatibility issues all horizons within the relay zones remained geometrically coherent.

4.1 Introduction

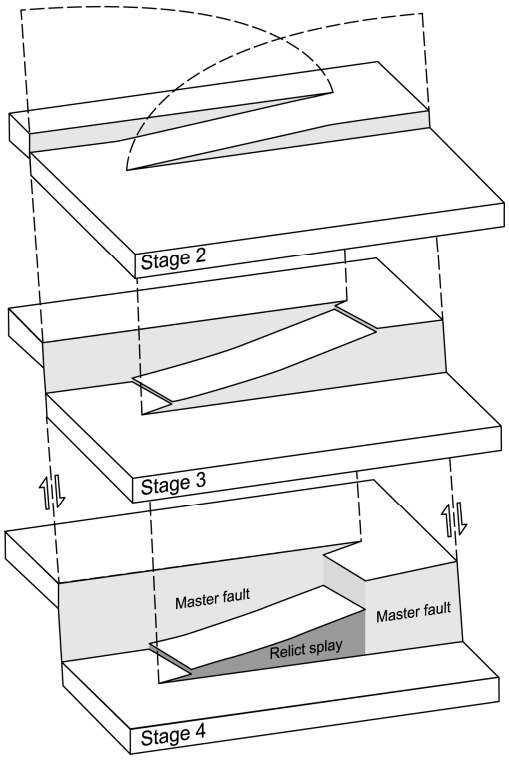

Fig. 4.1. A conceptual 3D diagram of a relay zone. Ramp rotations towards the mutual hanging wall are depicted to remain the same on each horizon despite the progression in fault linkage stages with depth and increased displacement. A relict splay is formed when the ramp is breached by a through going master fault. Modified from (Peacock and Sanderson, 1994).

Faults grow by the propagation of the fault tip lines (Cowie and Scholz, 1992; Cowie and Shipton, 1998) and by fault segment linkage, at all scales (Cartwright et al., 1996; Childs et al., 1996a; Marchal et al., 1998; Peacock, 2002; Walsh et al., 2002). Fault linkage can occur between initially physically separate segments or between fault lobes that have bifurcated from the primary slip surface but are physically attached to it, e.g. Appendix 1: (**Fig. A2**) (Marchal et al., 2003; Walsh et al., 2003b). Fault linkage is a dynamic process that evolves with increased displacement (Peacock and Sanderson, 1994; Childs et al., 1995; Walsh et al., 1999) .

The volume of rock within which faults overlap and transfer displacements is termed a relay ramp in map view and a relay zone in 3D. Peacock and Sanderson (1994) identified 4 stages of relay ramp evolution (**Fig. 4.1**): stage 1, fault segments do not overlap; stage 2, displacement is transferred through the strata between the overlapping faults producing a relay ramp; stage 3, linking faults and fractures begin to

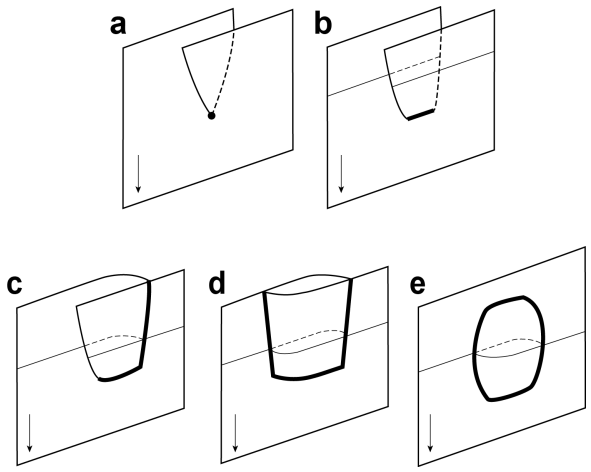

Fig. 4.2. A schematic diagram illustrating the 3D evolution stages of a branch line, arrows indicate the slip directions and fine lines are form lines. (a) Fault linkage initiates at a single unique BP. (b) A slip-normal BL initiates (bold). (c) Development of and L-shaped BL composing both a slip-aligned and slip-normal BL. (d) Both ends of the relay zone link forming a U-shaped BL. (e) And finally, a fault bounded lens. (c), (d) and (e) are all possible failed relay geometries, and (e) will only form if (c) and (d) are unstable. Taken from (Walsh et al., 1999).

develop and cut across the ramp; and stage 4, which occurs when the ramp is breached and a through going fault is formed. In 3D, fault linkage has been inferred to develop by the progressive replacement of the fault tip line with a branch line (BL), which is where two fault surfaces intersect and join (Walsh et al., 1999; Kristensen et al., 2008). Walsh et al., (1999) propose an evolutionary model of fault linkage from a branch point (BP), to horizontal BL, to L-shaped BL, to U-shaped BL and finally to a fault bounded lens (**Fig. 4.2**). The basic building blocks of fault linkage are thus slip-aligned BL, slip-normal BL, and slip-oblique BL.

The bounding faults that define and enclose a relay zone are likely to be non-planar and non-parallel. Relay zones are therefore rarely, if ever, likely to have the simple tabular geometries depicted by Peacock and Sanderson's (1994) idealised model (**Fig. 4.1**). Transfer of displacement between the bounding faults inevitably results in strain compatibility issues within the relay zone (i.e. the tendency to open voids or cause overlaps between adjacent rock volumes). The main factors that influence the magnitude of strain incompatibility are: the BL orientations relative to the slip direction; the evolution of fault linkage in 3D; and the original locations, shapes and orientations of the bounding faults. We do not comment further on the compatibility issues arising from variations in the orientations and shapes of the bounding faults, for details see (Bonson et al., 2007). Despite these strain compatibility issues, sites of fault

linkage are inferred to be geometrically coherent (Walsh and Watterson, 1991; Childs et al., 1995; Walsh et al., 2003b; Long and Imber, 2010). Geometric coherence is the concept that faults and fault-related strains maintain regular and systematic distributions throughout their evolution. Fault throws and associated continuous deformation should sum to produce total d-x profiles that resemble the displacement distributions of a single fault (Walsh and Watterson, 1991; Walsh et al., 2003b). If a fault-array has maintained geometric coherence it suggest kinematic coherence, which is the systematic and linked accumulation of displacement across the fault-array (Walsh and Watterson, 1991).

Fault bends are intimately associated with BL on normal faults (**Fig. 4.1** and **Fig. 4.2**) (Walsh et al., 1999; Bonson et al., 2007). Slip-aligned BL produce bends with axis parallel to the direction of continued slip, and are thus kinematical concordant (Walsh et al., 1999) and are termed neutral bends (Peacock and Sanderson, 1991). Relay zones with slip-normal fault linkage generate bends normal to the continued slip direction (**Fig. 4.2**b) and are termed releasing or restraining bends (Walsh et al., 1999). The main differences between slip-aligned and slip-normal BL is that slip-aligned BL maintain compatibility via simple shear strains, whereas restraining and releasing bends deform by pure shear strains (Walsh et al., 1999). Both slip-aligned and slip-normal BL can occur within a single relay zone (**Fig. 4.2**) and intermediate structures are also possible, but only the end members are considered further.

To maintain strain compatibility, BL are often associated with varying complexities of minor fault, veins, ductile deformation of incompetent layers, and enlarged zones of heavily deformed fault rock (Davatzes et al., 2005; Bonson et al., 2007). These detailed studies were based on outcrop observations. Outcrops typically provide limited information on the 3D geometries of branch lines and associated relay zones, although more recent studies have begun to investigate the 3D complexity of BL, by analysing closely-spaced serial sections through faults with centimetre-scale throws (Kristensen et al., 2008). In contrast, 3D seismic data can be used to study the gross geometries of fault-arrays and BL geometries, from which Walsh et al., (1999) developed their model of BL geometries (**Fig. 4.2**). However, the discrete geometries of low offset structures

around BL are not always imaged in 3D seismic data because of its inherent resolution limits (Steen et al., 1998; Townsend et al., 1998).

Seismic studies permit us to investigate BL development and linkage in 3D whereas outcrop studies, of slip-aligned and slip-normal BL, allow us to investigate the mechanisms by which strain compatibility is maintained. The novelty of this study is that we use a technique that allows us to image both discontinuous (i.e. breaks in seismic reflections) and continuous deformation (i.e. unbroken reflections) in 3D seismic data (Long and Imber, 2010), i.e. chapter 3. By including continuous deformation structures in our interpretations we are able to image more of the fault-related deformation around faults than has been previously possible, in seismic data, in areas of fault linkage.

For this study, 3D seismic data comes from the carbonate dominated Laminaria High, off the NW Australia margin. An example of a slip-aligned BL comes from an interbedded carbonate shale sequence at Lilstock, Somerset, UK. The slip-normal BL example is located within a siltstone and sandstone sequence from Moab, Utah, USA. Due to the limited exposure of BL in outcrops we use examples from different lithologies. It is assumed that the general strain compatibility issues will be similar regardless of lithology. However, the mechanisms by which the compatibility issues are accommodated may be different, e.g. dissolution in carbonates verses brecciation in sandstones.

From these detailed outcrop and 3D seismic studies, we aim to document the strain compatibility issues around slip-aligned and slip-normal BL, and in doing so better constrain the evolution of fault linkage in 3D.

4.2 Geological background: Laminaria High, Bonaparte Basin, NW Australia

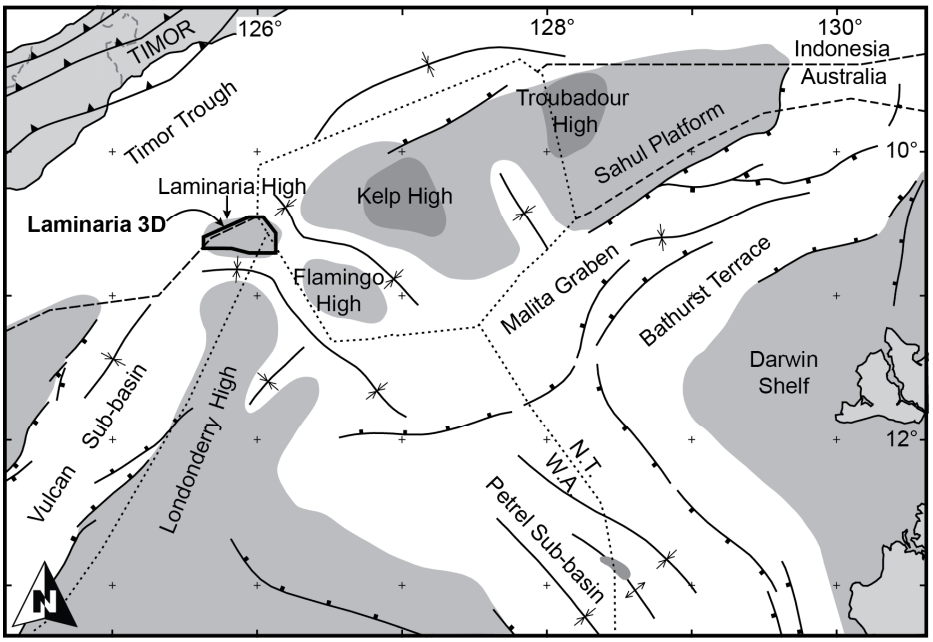

Fig. 4.3. Geological setting and Late Jurassic structural elements of the NW Australian shelf. The location of the Laminaria 3D seismic survey is annotated.

The Laminaria High is located within the Northern Bonaparte basin on the NW continental margin of Australia (**Fig. 4.3**) (Whittam et al., 1996; De Ruig et al., 2000). For a detailed location map see appendix 3: **Fig. A8**. In this chapter, faults in the top 2.5 km of sediment have been analysed using a high quality 3D seismic reflection dataset (**Fig. 4.4**). The density of the carbonate dominated sedimentary sequence does not vary greatly with depth, apart from around horizon H9, which is characterised by elevated acoustic impedance and a peak in corrected density (**Fig. 4.4**c: DRHO). The sediments above horizon H4 are syn-tectonic and thicken across the studied faults into the hanging wall (**Fig. 4.5**), which all show apparent normal offsets, as also noted by (De Ruig et al., 2000: their Fig. 11). Syn-tectonic mass transport complexes and channel features are present and where they cross the studied faults no signs of strike-slip movement are recorded.

The faults formed due to the flexural loading of the Australian margin in the Mio-Pliocene, caused by the collision of the Australian margin with the SE Asian plate complex. The Mio-Pliocene faults initiated in the overburden (Tertiary sediments) and

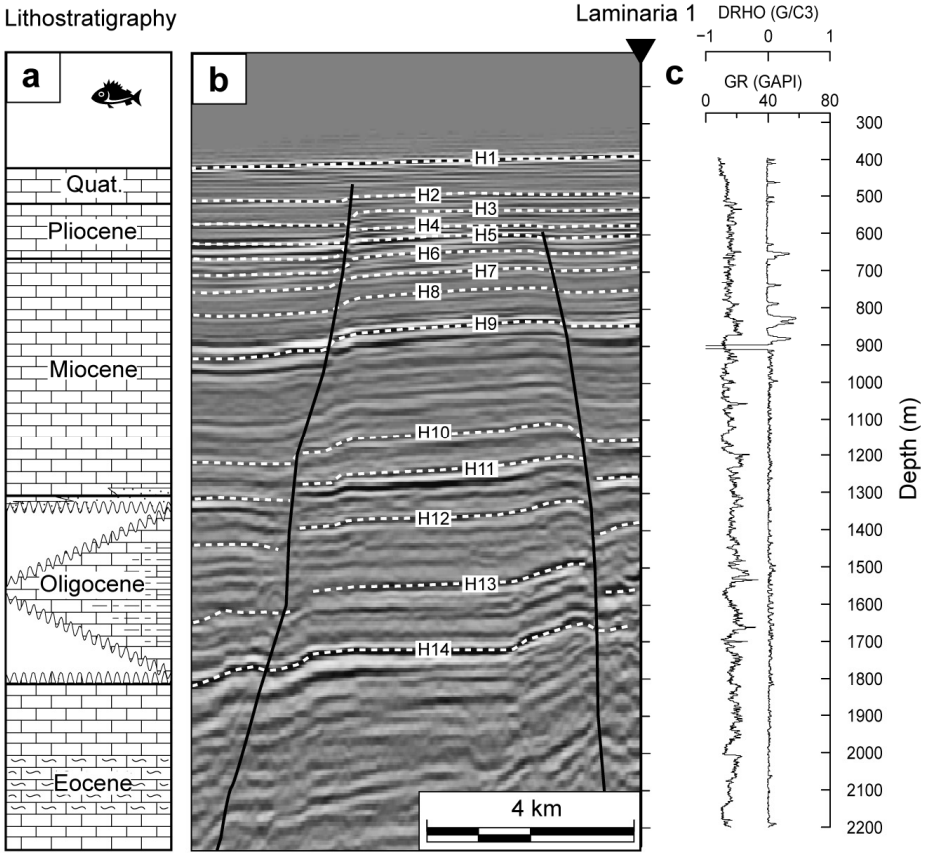

Fig. 4.4. (a) Lithostratigraphic column for the Laminaria High based on the Laminaria 1 well and regional studies by (De Ruig et al., 2000). (b) Laminaria 1 well intersection seismic line, in depth. The well location is marked by an arrow and the fourteen interpreted horizons are shown. (c) Corrected density (DRHO) (right curve) and gammer ray (GR) logs (left curve).

propagated downwards towards the reactivated E-W trending Mesozoic faults (De Ruig et al., 2000). Faults within the overburden also trend E-W and are highly segmented. Seismically-resolvable fault separations (the horizontal distance between overlapping fault segments, measured perpendicular to fault traces) range from approximately 70 to 1630 m (**Fig. 4.6**). The upper tip lines interact with the Quaternary growth sequence indicating continued fault movement until recent geological times (**Fig. 4.4** and **Fig. 4.5**).

Two relay zones have been studied in detail, referred to as Laminaria R1 and R2 (**Fig. 4.5** and **Fig. 4.6**). Both relays are located on the same laterally continuous fault-array (**Fig. 4.6**). Relay R1 comprises segments F2 and F3, and relay R2 segments F3 and F4. The fault-enhancing attribute Ant-Tracking highlights the locations of breaks in seismic

reflections (Pedersen et al., 2005), confirming that the faults are indeed segmented (**Fig. 4.6**b).

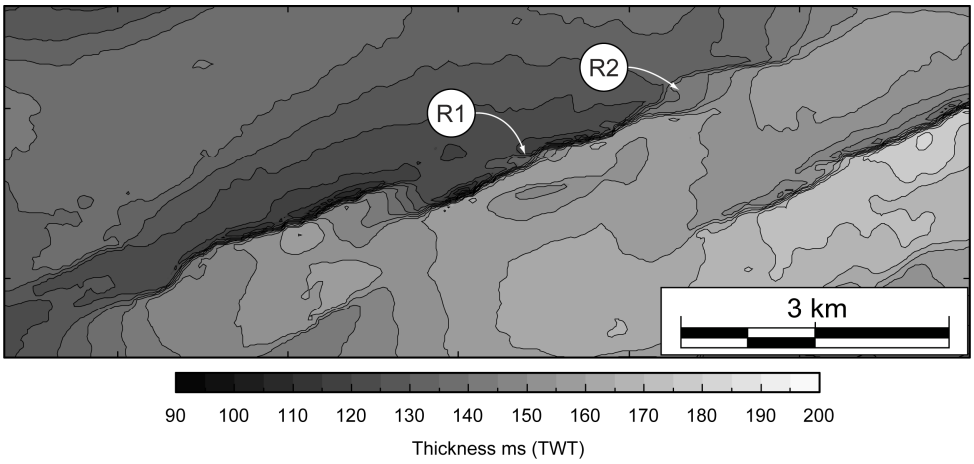

Fig. 4.5. An isochron map for the growth packages from horizon H4 to horizon H2, which are intersected by the studied faults. Horizon H4 is the base of the syn-sedimentary sequence (**Fig. 4.4**). The changes in accommodation space delimit the location of active faulting at the time of deposition. Relay ramps R1 and R2 are labelled. All fault segments on the NE-SW trending fault-array are active during the same time.

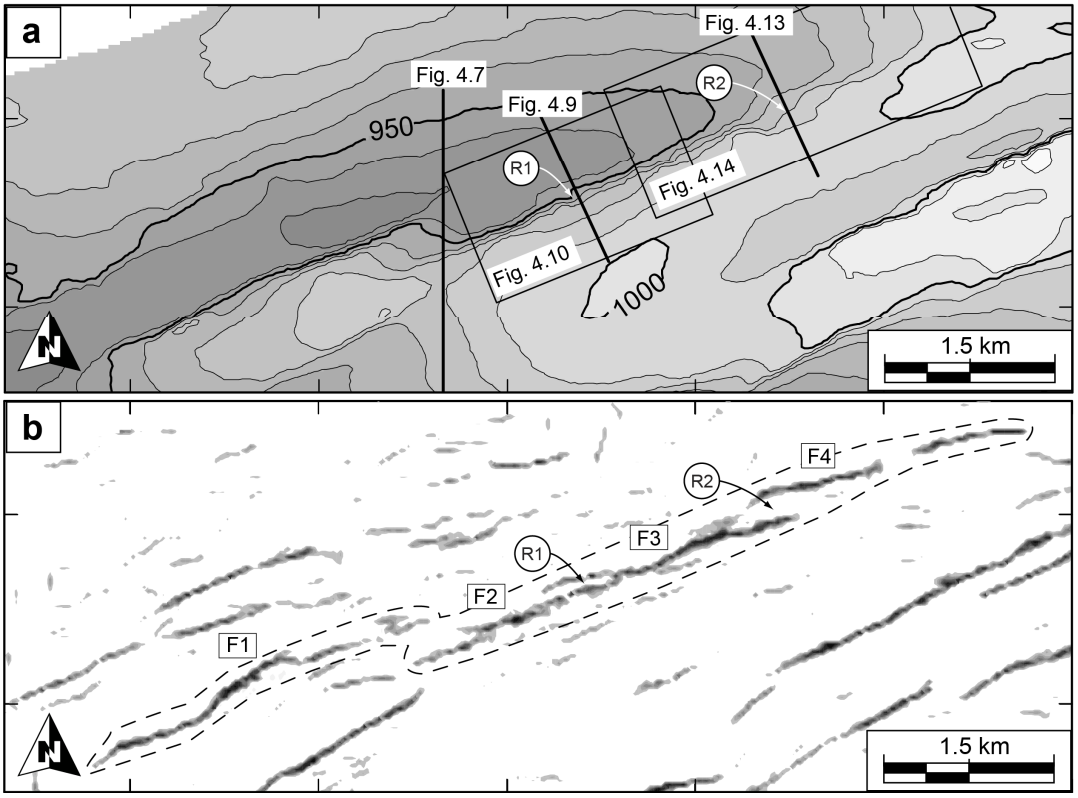

Fig. 4.6. (a) Time structure map of horizon H8 contours in ms TWT. Relays R1 and R2 are indicated along with seismic sections. Fault polygons can be identified by closely spaced contours. Relays R1 and R2 belong to a single fault-array trending NE – SW. (b) A fault enhanced attribute map (Ant-Tracking) for horizon H8, from the same area as in (a). Dark greys indicate a stronger discontinuity within the seismic volume (i.e. faults). The fault segments used in this chapter are circled and named for reference.

4.3 Method

A detailed account of the methods used in this chapter can be found in chapter 2.

4.3.1 3D seismic interpretation

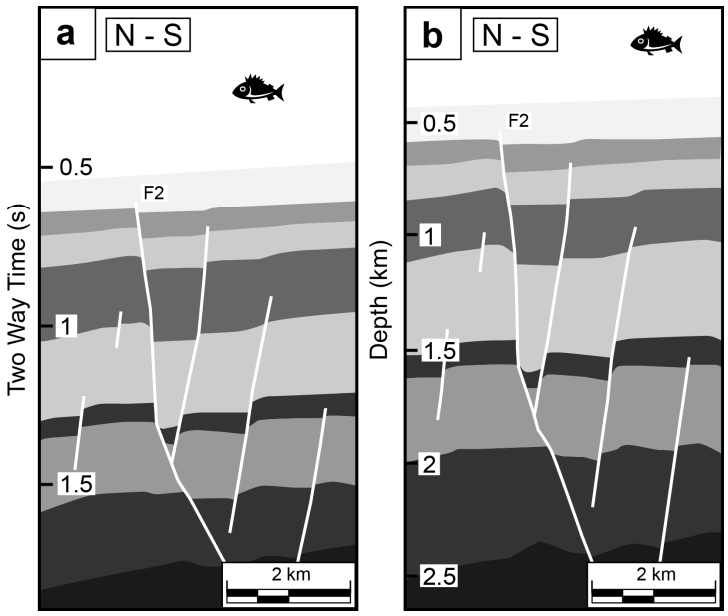

Fig. 4.7. (a) An interpreted time section through the study area, see (**Fig. 4.6**) for its location. (b) Depth converted seismic line, using velocity information from surrounding wells.

The 3D seismic survey covers the Laminaria High and has an area of approximately 760 km^2 (**Fig. 4.3**). It was collected in 1995 in an E-W direction with asymmetric binning (12.5 x 25 m) and is a time-migrated volume.

Velocity information from nearby wells (**Fig. A8**) was used to depth convert a seismic section (**Fig. 4.7**). The velocity data is consistent with a uniform overburden lacking lateral velocity variations. Therefore, the depth conversion process had a minimal effect on the overall geometries observed. Relative changes of the fault geometries are negligible between the depth and time sections (**Fig. 4.7**). Consequently, to avoid the introduction of additional uncertainties due to depth converting the data, the time-migrated volume was used to analyse fault relay zone geometries.

Horizons were interpreted on bright, laterally continuous reflections (**Fig. 4.4**) from only the top 1.8 seconds TWT (~2.5 km). Interpretations were checked to ensure all

potential seismic artefacts were correctly identified and that the picked horizons follow the seismic signal, especially in areas of structural complexity.

4.3.2 Quantifying continuous deformation: Fault Normal Rotations (FNR)

We calculated the apparent dip of each mapped horizon surface along transects orientated perpendicular to the average strike of the faults. This apparent dip attribute allowed us to quantify the discontinuous (i.e. faults) and the continuous deformation on each horizon, as described in (Long and Imber, 2010), i.e. chapters 2 and 3. Transect line spacing was 25 m. The transect lines record the continuous deformation around mapped faults as Fault Normal Rotations (FNR), which is equivalent to fault normal shear in (Huggins et al., 1995). From selected areas of FNR we calculate the vertical component of displacement.

Regions of fault-related continuous deformation surrounding the mapped faults were identified as areas in which the apparent dip deviates from the regional dip of the horizon. In Laminaria the regional dip is nearly horizontal to gently dipping to the NE (**Fig. 4.6**). Faults not relating to the studied relay zones and seismic artefacts, such as miss-ties are removed by visual inspection and are excluded from further analysis (Long and Imber, 2010), i.e. chapters 2 and 3.

The angle between the transect line and the geological structures will govern the apparent dip. For instance a transect line orientated parallel to a fault scarp, along which there is no change in dip, will give a blank FNR map. When faults are sampled normal to strike, FNR maps enhance linear sub-parallel structures, such as faults formed by the same regional extension (**Fig. 4.8**: FNR maps).

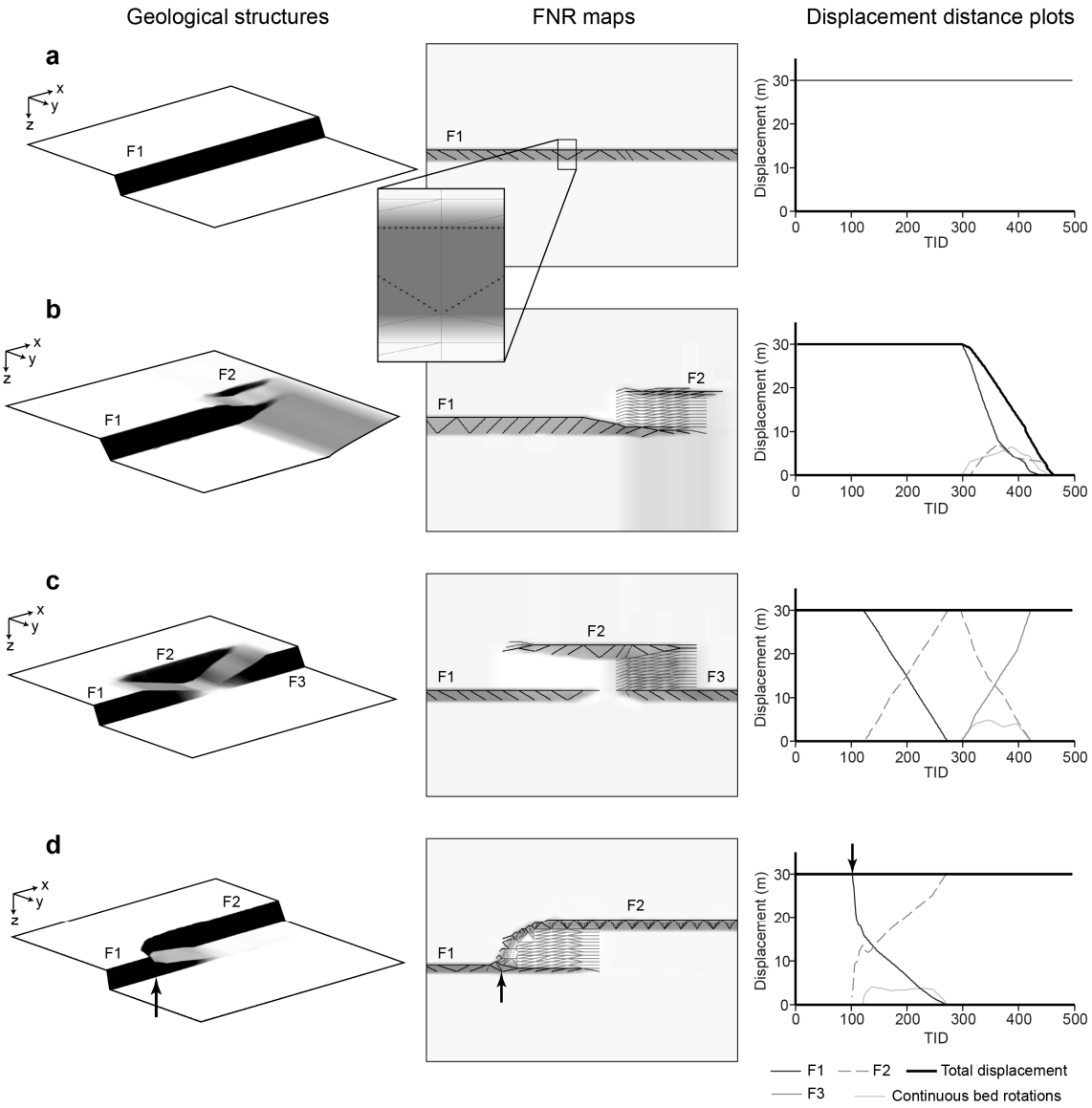

Fig. 4.8. (a - c) Schematic models showing commonly observed relay ramp structures; a 3D view of the tri-mesh surface (left); the associated FNR map, consisting of the FNR point data overlaid on the shaded horizon surface, which appear as lines at this scale (middle); and d-x profiles calculated from FNR point data (right). In each example transect lines run parallel to the y axis. (a) A simple fault scarp, FNR maps show a laterally continuous linear high (black points) and the d-x profile has a uniform total displacement. Inset, a close up image, the point data coincides with the edges of the tri-mesh. (b) The termination of a fault-array with a segmented fault tip separated by a small relay ramp that dips towards the mutual hanging wall. FNR maps depict two laterally continuous FNR highs (black points) separated by a zone of rotation towards the hanging wall (grey points). Total displacement decreases along-strike and the d-x profiles for each structure within the fault-array are plotted. (c) A fault scarp separated by two open relay ramps, one dips parallel to fault strike and the other has a component of dip towards the mutual hanging wall. In the relay ramp between F1 and F2 no FNR is present as there is no variation in dip along the transect lines, which are orientated parallel to the strike of the ramp. The ramp between F2 and F3 however, has a component of dip normal to fault strike i.e. FNR. All structures sum to give a uniform total d-x profile. (d) A breached relay ramp with a through going FWF (F2) leaving a relict splay along-strike of the HWF (F1). In each panel the branch point is located with an arrow. The ramp has a component of dip towards the mutual hanging wall. The fault linkage is identified as the point where the two laterally continuous FNR highs coalesce. Note the change in FNR on the fault surface (black points to grey points) as F2 swings into parallelism with the transect lines. Fault linkage is accompanied by an abrupt along-strike drop in displacement on fault F1.

4.3.2.1 Interpreting FNR

The FNR surface attribute is only one of several tools that can be used to help the geologist/seismic interpreter and, as such, should be used in conjunction with existing seismic interpretation tools (e.g. Ant-tracking). The challenges associated with correctly interpreting fault linkage geometries in seismic data are not unique to this study. For example, Walsh et al., (1999) infer fault linkage geometries from the coalescence of mapped fault polygons, which are interpreted from 3D seismic data. However, in this chapter we use the FNR surface attributes to facilitate the interpretation of geological structures, which enables us to interpret fault linkage geometries in greater detailed than those in published studies of faults with total offsets of 10s to 100s m.

Three aspects of the FNR surface attribute can be used to interpret fault linkage: the spatial distribution of FNR; the variation in intensity of apparent dip; and the vertical displacements calculated across the selected areas of interest (Long and Imber, 2010) i.e. chapters 2 and 3. The location and intensity of apparent dips (represented throughout this chapter as gray scale images) can be interpreted by a geologist in similar ways to conventional faulted horizon dip maps. Elongate bands of concentrated high FNR (dark greys to black points) are interpreted with confidence to be equivalent to fault polygons produced by conventional fault and horizon mapping techniques (**Fig. 4.8**a). In comparison, areas of diffuse low to medium FNR (light grey to grey points) that enclose the fault polygons are more difficult to interpret, as a range of geological structures can produce such rotations of seismic reflections (Steen et al., 1998; Townsend et al., 1998). At present, there are no seismic tools to image the unique distribution of geological structures in areas of diffuse continuous deformation around imaged fault polygons. Therefore, the FNR surface attribute only images changes in bulk deformation of the seismic horizon, from which fault linkage is interpreted. The displacement distribution from selected areas of FNR can also be plotted (**Fig. 4.8**: right), which graphically illustrate the along-strike changes in displacement on different structures. Abrupt along-strike drops in displacement (**Fig. 4.8**d: F1) are often associated with fault linkage (Maerten et al., 1999), for more details on how fault linkage is interpreted see the next section (4.3.2.2).

4.3.2.2 Interpreting fault linkage from FNR maps

We interpret fault linkage geometries using vertical seismic sections and by analysing the changes in deformation styles of seismic horizons imaged at different levels within a relay zone. The ability to measure fault linkage in map view gives us a better control on the location of vertical BL, whereas seismic sections favour identification of horizontal BL. The key characteristics used to identify areas of fault linkage are the shapes of the d-x profiles and the visual distributions of FNR (**Fig. 4.8**).

In (**Fig. 4.8**) a series of schematic faulted horizon surfaces have been constructed that represent commonly observed relay ramp geometries. From these surfaces the FNR attribute is calculated to illustrate their distributions to aid identifying such structures in real datasets. The FNR data is displayed as point data in (**Fig. 4.8**) however, for clarity, in the main results FNR is contoured. Abrupt along-strike changes in displacement are indicative of BP, for at a BP displacement is transferred onto the through-going fault leaving a portion of the fault segment with low displacements, termed a relict splay (**Fig. 4.8**d). Fault linkage in FNR maps is interpreted in comparable ways to outcrop exposures, assuming that linear bands of high FNR equate to fault polygons, i.e. (**Fig. 4.8**a). If so, linkage occurs when two linear FNR highs coalesce (**Fig. 4.8**d: FNR map). Linear FNR highs, separated by relatively wide zones of low to medium FNR, are interpreted as relay ramps (**Fig. 4.8**: b and c). The irregular displacements near the BP on fault F2 in (**Fig. 4.8**d) relate to sampling errors that occur when the fault trace rotates into parallelism with the transect lines (Long and Imber, 2010), i.e. chapters 2 and 3.

4.3.2.3 Errors in calculated vertical displacement from FNR

To build confidence in our interpretations we address possible errors associated with FNR maps and subsequent calculated vertical displacements. The largest potential sources of error come from incorrectly including vertical discontinuities arising from either non-tectonic structures, such as river channels and seismic velocity artefacts, or from including faults that form due to earlier or later tectonic events. In Laminaria care

was taken to select only co-evolved faults from the same fault-array (**Fig. 4.5** and **Fig. 4.6**); no large seismic velocity artefacts are observed in the study areas (**Fig. 4.7**).

Geometric coherence and hence kinematic coherence has been demonstrated between faults up to 6 km apart, measured normal to fault strike (Walsh and Watterson, 1991), which means faults outside the study area (**Fig. 4.6**) could affect the d-x profiles of faults F1 to F3. This can account for undulating or skewed total d-x profiles; alternatively total d-x profiles with multiple maximum peaks could result from the coincidental overlap of isolated faults (**Fig. 1.5**) (Trudgill and Cartwright, 1994; Cartwright et al., 1995; Cartwright et al., 1996). Finally, the mismatch between fault strike and the orientation of the transect lines, along which displacement is calculated, will lead to the potential under-sampling or over-sampling of fault displacements, which can add low level noise to d-x profiles (Long and Imber, 2010), i.e. chapters 2 and 3.

4.4 Slip-aligned fault linkage examples

4.4.1 3D seismic data: Laminaria R1

4.4.1.1 Fault geometries

In map view, the footwall fault (FWF) F3 trends obliquely to the hanging wall fault (HWF) F2 and increases in separation towards the SW (**Fig. 4.9**). The Ant-Track attribute can be seen to coalesce at the NE end of the ramp indicating fault linkage. In cross-section, faults F3 and F2 are characterised by "tramline" geometries with depth, with seismically-resolvable faults within the relay zone. The horizons within the ramp dip towards the mutual hanging wall, as observed in many other relay zones (Huggins et al., 1995). The average thickness between the pre-tectonic horizons H4 and H9 outside of the relay zone is 241 ms TWT, whereas the thickness between the same

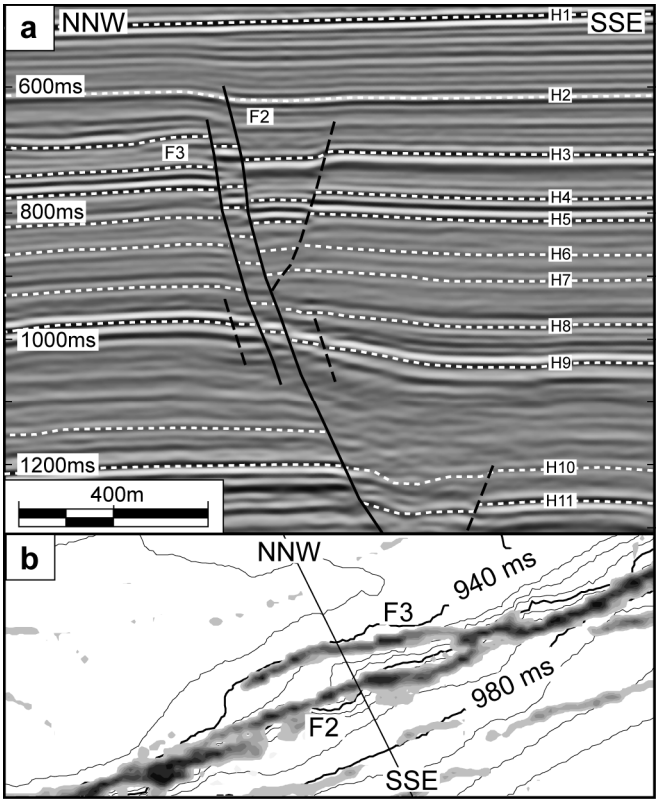

Fig. 4.9. (a) Seismic profile through relay R1 (**Fig. 4.6**). The separation distance between faults F2 and F3 remains constant with depth. On horizon H9 the ramp has elevated rotations toward the mutual hanging wall and minor faults in the hanging wall and footwall. The upper tip line of F2 terminates at H2 whereas F3 terminates lower in the sequence mid-way between H3 and H2. (b) The distributions of Ant-Track fault attributes for horizon H8. From the time depth contours the ramp can be seen to dip towards the SE and the Ant-Track attributes are observed to coalesce at the NE end of the ramp. The location of the seismic profile is shown.

markers within the relay zone is lower at 235 ms TWT, which suggests tectonic volume loss within the ramp. There is no indication that the F3 fault links at depth with the through going F2 fault. Minor faults occur in the volume adjacent to the relay zone, with an increase in secondary faulting on horizon H9 (**Fig. 4.9**: dashed lines). The total throw across faults F2 and F3 is approximately 60 ms TWT.

The upper tip points of F2 and F3 terminate within the growth strata and sediments thicken into the hanging wall. The tip point of F2 lies above horizon H2, whereas F3 stops midway between H3 and H2 (**Fig. 4.9**). This observation suggests that fault F2 continued to move after F3, which supports the inference that F3 is a relict splay formed when the faults linked in the NE corner of the ramp along a slip-aligned BL.

It is at this point that most published studies of fault linkage would stop (Walsh et al., 1999), but we continue our analysis and now present detailed observations of 3D fault interaction and linkage.

4.4.1.2 Spatial distribution of continuous deformation

We have analysed FNR on six representative horizons that contain structures associated with relay R1 (**Fig. 4.9** and **Fig. 4.10**). In map view, areas of high FNR (> 8° of apparent dip) form elongate bands that we interpret to be the locations of imaged fault polygons surrounded by variable widths of low FNR (< 7° of apparent dip). On each horizon the pattern of FNR is different with a marked change in the distribution of FNR on horizons H8 and H9 (**Fig. 4.9** and **Fig. 4.10**).

Starting at the shallowest horizon (H2) and working down through the relay zone, key features on each horizon in (**Fig. 4.10**) are noted. On horizon H2 the tips of F2 and F3 approach each other and overlap is approximately 125 m (**Fig. 4.10**). The two fault segments are bridged by a band of elevated FNR (4° - 6° apparent dip). Overall, the FNR map pattern resembles that of a fault with an along-strike bend.

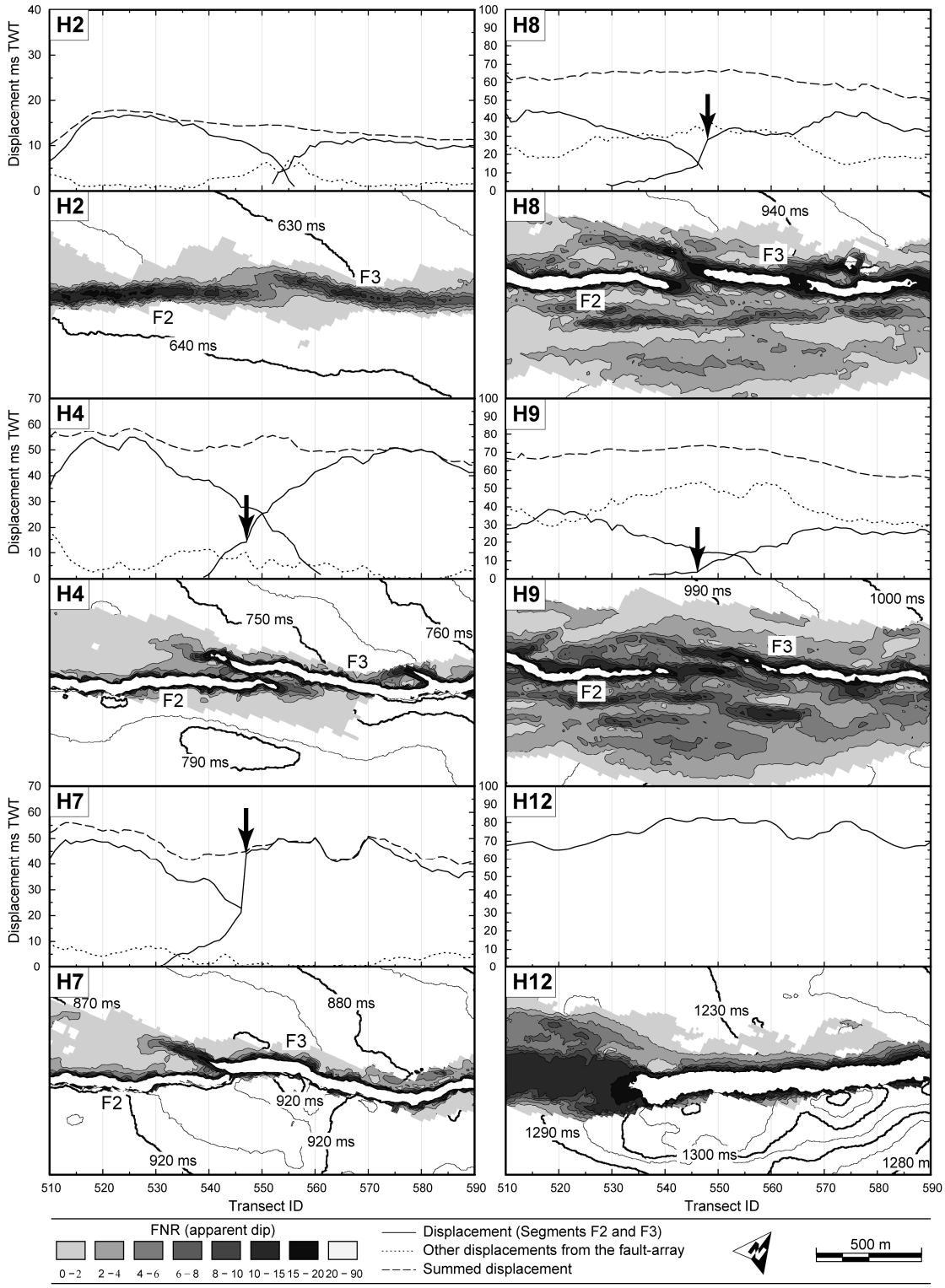

Fig. 4.10. A selection of six mapped horizons that intersect relay R1 (**Fig. 4.9**). For each horizon there is a detailed map view image showing the distribution of continuous deformation (FNR). Above which are the corresponding displacement distance profiles, which show the amount of displacement occurring across the areas depicted in map view (shaded areas). Displacement is split into the vertical offsets on fault scarps F2, F3, and all other structures, which can include both rotated horizons and minor faults in the footwall and hanging wall. At all levels within the relay zone the displacement distance profiles are geometrically coherent. See text for detailed descriptions of each horizon.

On horizon H4 faults F2 and F3 now overlap by 625 m. The internal ramp rotations are towards the hanging wall and the magnitude varies along-strike (2° - 8° apparent dip). The ramp is open at both ends but the separation distance between the F3 and F2 decreases around transect line 550 (**Fig. 4.10**). The total width of the fault-array, measured at the centre of Laminaria R1 and including the surrounding zone of low FNR, is 310 m.

Horizon H7 records a change in style of FNR distributions. Fault F2 coalesces with the imaged F3 fault scarp near transect line 545 (**Fig. 4.10**), similar to (**Fig. 4.9**b). The portion of fault F3 from 545 to 530, which overlaps F2, has low FNR compared to the adjacent F2 fault trace. The internal ramp rotations are low (0° - 2° apparent dip) when compared to H4. Low FNR is asymmetrically distributed about the relay ramp with little to no measured FNR in the mutual hanging wall.

The general ramp geometries on horizon H8 are similar to H7 with the NE tip of fault F2 coalescing with F3 near transect line 545 (**Fig. 4.10**). The relatively low FNR value for the BP is an artefact of the rotation of the linking fault into parallelism with the transect line orientation. Internal ramp rotations are patchy and low. The distribution of FNR around the relay zone is markedly different compared with horizons H2 to H7. The width of the deformed region, measured at the centre of Laminaria R1, has increased from 275 m on H7 to 770 m on H8. Minor fault traces in the mutual hanging wall are observed to follow the NE-SW trend of faults F2 and F3 (**Fig. 4.9** and **Fig. 4.10**).

The width of the fault-array on horizon H9 (885 m) is similar to H8 and also has low-offset NE-SW trending faults in the mutual hanging wall and footwall. However, in detail, the two fault polygons of F2 and F3 do not coalesce, as on H7 and H8. This deformation pattern is most simply interpreted as representing an open relay ramp (**Fig. 4.8**c). The distribution of FNR in the relay zone more closely resembles those of H4 than the nearby horizon H8 (**Fig. 4.10**). The internal ramp rotations are patchy but high (4° - 8° apparent dip), when compared to H7 and H8.

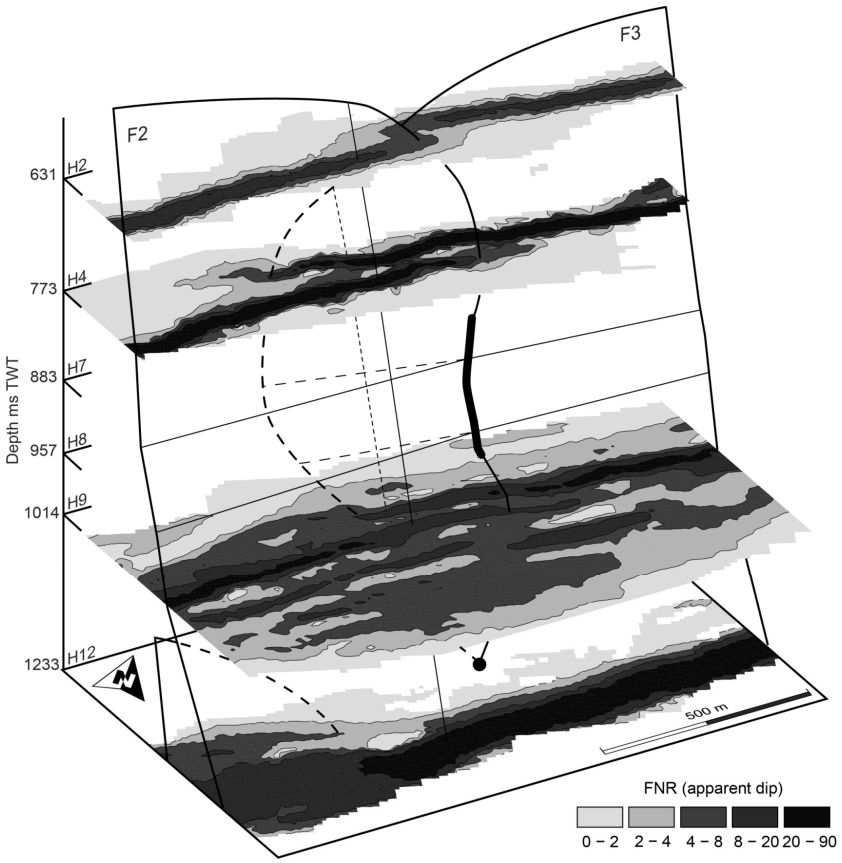

Fig. 4.11. A composite 3D view of relay R1, showing the distribution of FNR. Horizons H7 and H8 are removed for clarity, their interpreted locations are shown, see (**Fig. 4.10**) for detail. Solid black lines indicate the location of the interpreted fault tip lines. Dashed lines indicate where a fault tip line is hidden by a fault surface in the foreground. Bold lines indicate branch lines and the branch point is circled. The thin sub-vertical lines on the fault surfaces represent the location and intersection of the seismic profile in (**Fig. 4.9**). See text for detail.

A continuous NE-SW trending band of high FNR cuts horizon H12 (**Fig. 4.10**), and is the down-dip continuation of both F2 and F3 (**Fig. 4.9**). The drop in apparent dip (white to mid grey) between transects 510 to 535 results from the increased width of the fault polygon. A BP or slip-normal BL is not directly imaged in vertical seismic sections (**Fig. 4.9**), although a BP/slip-normal BL must exist where faults F2 and F3 merge into the continuous fault trace observed on horizon H12.

The 3D geometry of the faults, branch lines and associated continuous deformation has been inferred based on interpretations of the FNR maps (**Fig. 4.11**). The relay zone geometry varies from an open ramp on H2 to H4, to a breached ramp on H7 to H8, then returning to open ramp geometry on H9, and finally terminating at a BP (or slip-normal BL) between H9 and H12 (**Fig. 4.11**). Published models of 3D fault linkage would predict a continuous BL propagating outwards from the BP (**Fig. 4.2**) (Walsh et

al., 1999; Kristensen et al., 2008). The interpreted open ramp geometries on horizon H9 are more complex than implied by this evolutionary model, which suggest an alternative or modification is required.

4.4.1.3 Displacement distance profiles

The displacement distance (d-x) profiles for Laminaria R1 show the vertical offsets (throws) on fault polygons F1 and F2, together with the vertical component of continuous displacement calculated from the surrounding areas of FNR, which includes both rotated horizons and minor faults within the footwall and hanging wall (**Fig. 4.10**). The fault tips are taken at the point at which displacement on the laterally continuous FNR highs decreases to zero. On each horizon, the total displacement curve (dashed line) resembles that of a single continuous fault, such as on H12.

On close inspection of the individual d-x profiles, horizons H2 displays approximately symmetrical changes in displacement gradients on the overlapping faults F2 and F3 (**Fig. 4.10**). In contrast, horizons H7 to H8 show abrupt drops in displacement on fault F3 at the transition from the through going fault to the relict splay across the interpreted BP, near transect line 545 (**Fig. 4.10**: arrows). On horizons H4 and H9 a small, but noticeably abrupt drop in displacement is also observed near transect line 545 on fault F3 (**Fig. 4.10**: arrows).

4.4.2 Outcrop studies of slip-aligned fault linkage: Lilstock

The horizons within Laminaria R1 all dip towards the mutual hanging wall but on horizons H4 and H9 that are interpreted as having open (unlinked) relay ramps, the magnitudes of FNR within the relay zone is elevated compared to those observed on horizons H7 and H8, which appear to be cut by a through-going fault (**Fig. 4.10**). The change in ramp dip within a relay zone implies strain compatibility (space) problems between horizons. The outcrop example at Lilstock further illustrates the relationship between fault linkage and changes in bed rotation at different levels within a relay

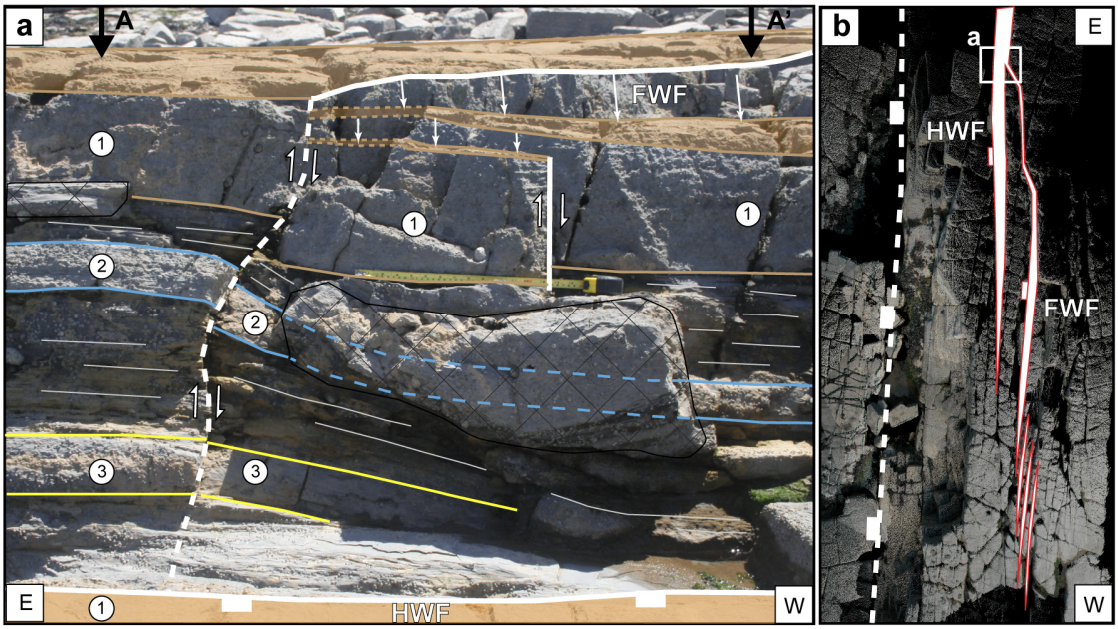

Fig. 4.12. Lilstock relay ramp and slip-aligned BL, Somerset, UK. (a) An interpreted field photo of an exposed BL (dashed white line) and surrounding deformation, sketch lines follow bedding surfaces and depict lateral changes in bed dip. White arrows indicate areas of fault offset and sense of movement. (b) Map view of terrestrial laser scan data depicting the geometries of the overlapping faults. The location of the BL is at the east end of the relay ramp, white box. Three limestone beds are cut by the BL and are exposed on the fault scarp of the HWF where bed (1) is offset by 68 cm (a). West of the BL, within the relay ramp (b), beds dip varies with depth (a). See text for measurements of vertical offsets between locations (A) and (A'), black arrows, and for bed dips. Hashed areas are fault rock smeared down the fault surface.

zone close to a slip-aligned BL. We also study how strain compatibility is maintained between beds.

The outcrop at Lilstock is located on a wave-cut platform in northern Somerset, UK. For a detailed location map see appendix 3: **Fig. A10**. The stratigraphy consists of moderately dipping, interbedded Lower Jurassic limestone and shale beds. Limestone bed thicknesses range on average from 5 cm to 1 m and shale beds from 5 cm to 5 m. Faults used in this study trend E-W and display normal, dip-slip displacement, with no signs of strike-slip or reverse reactivation. The faults are believed to have nucleated in the more competent limestone beds (Peacock and Sanderson, 1991, 1992). A slip-aligned BL is exposed on a 68 cm high fault surface (**Fig. 4.12**). In combination with detailed outcrop studies, fault geometries and detailed bed rotations where measured using a high resolution Terrestrial Laser Scanner (TLS).

The relay ramp in (**Fig. 4.12**b) has a separation distance of 90 cm and maximum offset on the boundary faults of 68 cm. The change in deformation style at different depths

within the relay zone can be observed. The slip-aligned BL is visible on the exposed fault surface of the hanging wall fault (HWF) and is the intersection between the footwall fault (FWF) tip and the HWF surface (**Fig. 4.12**). The relay zone is breached by the propagation of the FWF through the ramp (**Fig. 4.12**b).

Three limestone beds are exposed on the fault scarp (**Fig. 4.12**a). Bed (1) is 21 cm thick, and is offset by 9 cm across the BL. It is oriented 123/14°SW adjacent to the BL and 121/9°SW measured 1 m to the west of the BL. Bed (2) is 8.5 cm thick, is offset by 3.5 cm across the BL, and dips 126/55°SW adjacent to the BL and 124/13°SW measured 1 m to the west of the BL. Finally, bed (3) is also 8.5 cm thick, is offset by 0.5 cm across the BL, and dips 128/25°SW adjacent to the BL and 123/14°SW measured 1 m west from the BL (**Fig. 4.12**).

The intervening shale beds change in thickness as they approach the BL to accommodate the different dips of the competent limestone beds (**Fig. 4.12**: beds 1-3), thus maintaining strain compatibility within the relay zone. Moving west away from the slip-aligned BL, beds (2) and (3) become sub-parallel with bed (1). The total vertical offsets measured across beds (2) and (3) at locations A and A' are equal to that of bed (1) measured over the same distance (**Fig. 4.12**a). The along-strike change in displacement observed on the three limestone beds are accommodated by different structures close to the BL. Bed (1) accommodates the majority of the deformation by slip across the BL, whereas beds (2) and (3) have minimal slip on the BL and the offsets are accommodated mainly by continuous rotations of the beds within the relay ramps, as beds (2) and (3) steepen towards the BL. Bed (1), west of the BL, would display relatively uniform, low magnitudes of FNR, which is equivalent to horizon H8 in Laminaria R1 (**Fig. 4.10**). Beds (2) and (3) would display elevated FNR adjacent to the slip-aligned BL, with FNR on these beds decreasing to that measured on bed (1) at location A' west of the BL (**Fig. 4.12**). This is equivalent to horizon H7 in Laminaria R1, which has low FNR within the majority of the relay ramp but displays elevated FNR close to the interpreted slip-aligned BL. Horizons H4 and H9 resemble parts of beds (2) and (3) in that they have elevated FNR but, unlike Beds (2) and (3), high FNR is observed over the entire ramp.

Mechanical layering can influence the propagation of fault tips resulting in “fringed” tip lines in mechanically layered sequences, where the fault is laterally more advanced in the competent layers (i.e. carbonates) than in the incompetent layers (i.e. shales) (Schöpfer et al., 2006: their Fig. 13). The thicker more competent bed (1) is inferred to be more favourable for fault propagation, allowing early linkage of the relay ramp at this level. In contrast, the relay ramp on beds (2) and (3) remained open (unlinked) for longer. Once linked, bed (1) preferentially accommodated offset by increased slip on the breaching fault, whereas beds (2) and (3) accommodated strains by the continued rotation of the beds in the relay ramp, facilitated by thickness changes within the surrounding shale beds, until strains were eventually localised onto a breaching fault. Fault linkage evolution therefore controls the internal ramp geometries, which at Lilstock, is influenced by the mechanical layering.

4.5 Slip-normal fault linkage examples

4.5.1 Laminaria R2

4.5.1.1 Fault geometries

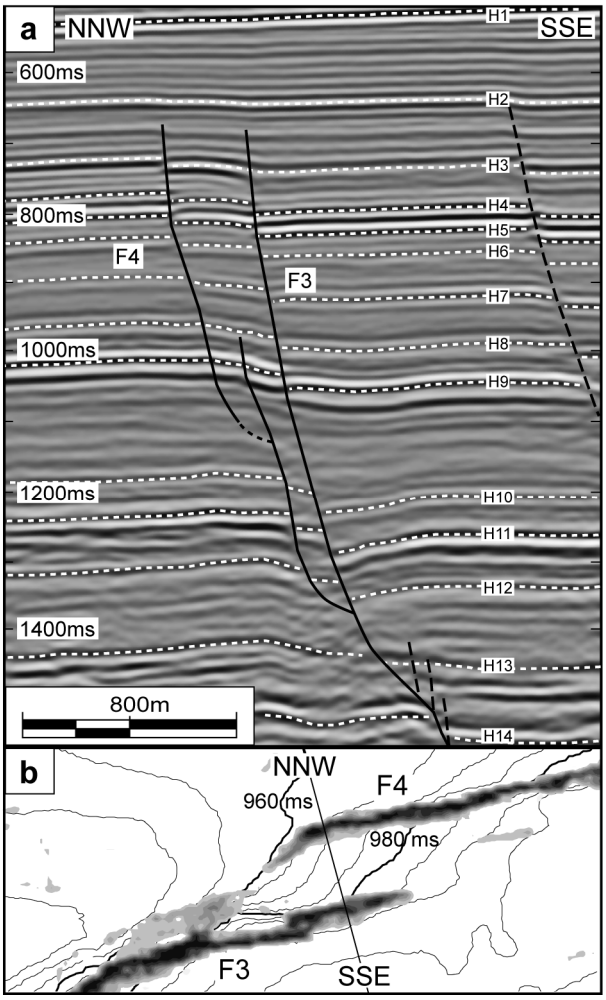

Fig. 4.13. (a) A seismic profile through Laminaria R2 (**Fig. 4.6**). The separation distances between faults F3 and F4 decreases at 1100 ms TWT and is associated with a shallowing of the fault dip. F4 links at depth with F3 bellow H12. The amount by which the ramp is rotated towards the mutual hanging wall varies on each horizon. Both fault tips terminate at the same level within the growth sequence. (b) Map view distribution of fault enhanced Ant-Track attributes. The SW tip of F4 has rotated and is shown to cross the ramp. Time depth contours display the internal form of the ramp, which dips towards the SE.

In cross-section, fault segment F3 is approximately planar with depth whereas F4 has a pronounced concave-upward bend at 1100ms TWT and again at 1400 ms TWT (**Fig. 4.13**). These down-dip bends reduce the separation distance with depth from 280 m on horizon H4 to 130 m on H11. The internal ramp reflections all dip towards the mutual hanging wall but dip varies with depth. Below H7, ramp rotations increase with

depth until H11, where shallow dips similar to those above H7 are observed. The average thickness of the pre-faulting H4-H9 interval outside of the relay zone is 241 ms TWT. Within the relay zone the thickness varies from 235 ms TWT adjacent to the FWF and 246 ms TWT adjacent to the HWF. The majority of this internal thickness variation occurs between H6 and H7, which increases in thickness towards the mutual hanging wall. As with relay R1, these thickness changes are postulated to be tectonic in origin, for they do not coincide with the growth strata above horizon H4. An internal fault is present within the relay zone and is associated with the vertical bend at 1100 ms TWT. The continuous rotations towards the mutual hanging wall increase around this fault. Both F3 and F4 upper fault tips terminate into the growth sequence midway between H3 and H2, indicating that both segments were active until shortly before deposition of H2.

In map view, on horizon H8, the Ant-Track attribute that corresponds to F4 is observed to rotate at its SW end and cross the ramp towards fault segment F3 (**Fig. 4.13**b). From this section of the relay zone, the HWF H4 appears to be the through-going fault (**Fig. 4.1**: stage 4). The combination of slip-aligned fault linkage (**Fig. 4.13**b) and slip-normal fault linkage (**Fig. 4.13**a) produce bounding fault geometries with both along-strike and down-dip bends. These fault geometries, caused by fault linkage, produce strain compatibility issues within the ramp. These are now studied in detail within the R2 relay zone (Section 4.5.1.2) and using a complementary outcrop example from the Moab Fault (Section 4.5.2).

4.5.1.2 Spatial distribution of continuous deformation

Starting at the shallowest horizon (H2) and working down through relay R2, key features on six representative horizons are noted (**Fig. 4.14**). Horizon H2 displays up to 5 ms TWT of recorded total offset across a 430 m wide band of low FNR (0° – 6°), measured at the centre of the relay zone on transect 612. These en-echelon bands of FNR are aligned NE-SW. The SW end of the overlap zone is connected by an area of low FNR (0° – 2°).

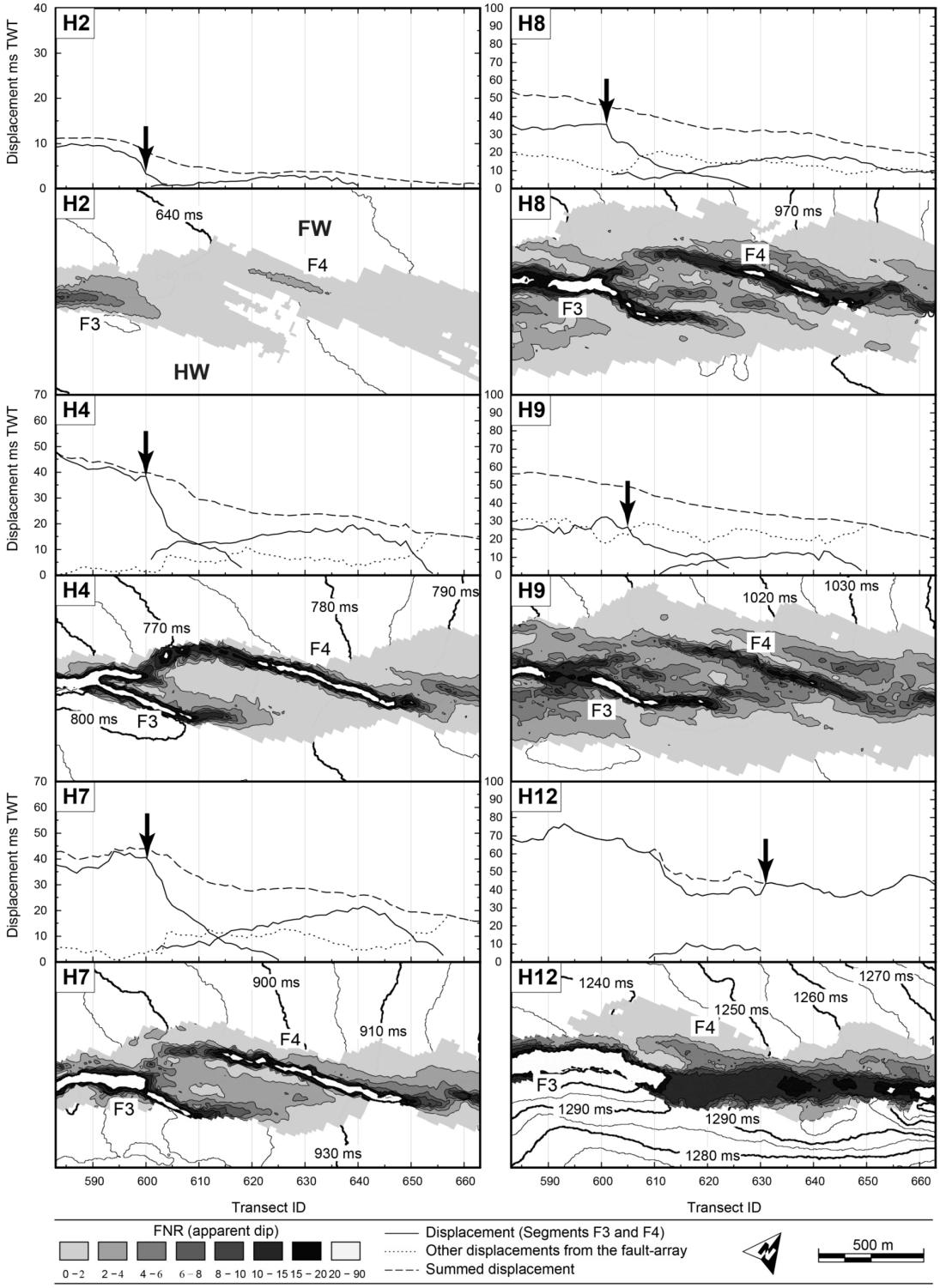

Fig. 4.14. A selection of six mapped horizons that intersect relay R2 (**Fig. 4.13**). For each horizon there is the map view distribution of FNR and the corresponding displacement distance profiles. Displacement is split into the vertical offsets on fault scarps F3, F4, and all other structures, which can include both rotated horizons and minor faults in the footwall, hanging wall, and relay ramp. As with Laminaria R1, Laminaria R2 remains geometrically coherent on every horizon. See text for a detailed description of each horizon.

Elongate FNR highs (> 8° of apparent dip) are well established on horizon H4, with displacements up to 50 ms TWT. These are interpreted as fault polygons which trend NE-SW. Fault F4 rotates nearly ninety degrees before merging with fault F3. This occurs at the SW end of the relay zone (transect line 600). The internal ramp rotations are low (0° – 2°) and uniform across the ramp. The mutual hanging wall and footwall of the relay display zero FNR. A 325 m long linear band of high FNR protrudes out into the ramp from the BP between F3 and F4 (**Fig. 4.14**).

The general distributions of FNR on horizon H7 are similar to those on H4. The apparent lows in FNR at the BP (near transect line 600) between F3 and F4 at the SW end of the ramp is an artefact of the fault striking parallel to the transect lines. When horizon H7 is viewed in 3D there is a clearly visible fault scarp connecting the HWF F4 to the FWF F3 (**Fig. A9**). The internal ramp rotations have increased (2° – 4°) when compared to those on H4 (0° – 2°) (**Fig. 4.14**).

Within the relay ramp on horizon H8 there are two linear bands of high FNR 375 to 200 m long, respectively, which trend NE-SW. The boundary faults F3 and F4 have similar geometries to horizons H4 and H7. As on horizon H7 there is a sampling artefact (anomalously low FNR), at the SW end of the relay ramp, at transect line 605. In 3D a fault scarp is image crossing the ramp, but it is less pronounced than that observed on H7 (**Fig. 4.14** and **Fig. A9**).

On horizon H9 two linear FNR high are aligned NE-SW. Unlike on previous horizons there is no observed N-S trending FNR high at the west tip of fault F4, between transect lines 600 to 610. Instead, an area of diffuse, low to medium FNR separates the two overlapping faults F3 and F4. In 3D no fault scarp is visualised cutting the ramp, as in H7 and H8 (**Fig. A9**). This horizon is therefore inferred to contain an open relay ramp. Internally, the ramp contains two 200 m long linear FNR highs similar to those on H8 (**Fig. 4.14**).

Horizon H12 is dominated by a large laterally continuous FNR high with an along-strike bend at transect 605, which underlies the BP identified on overlying horizons H2 to H9. In the footwall of this large fault scarp there is a low offset FNR high that trends sub-

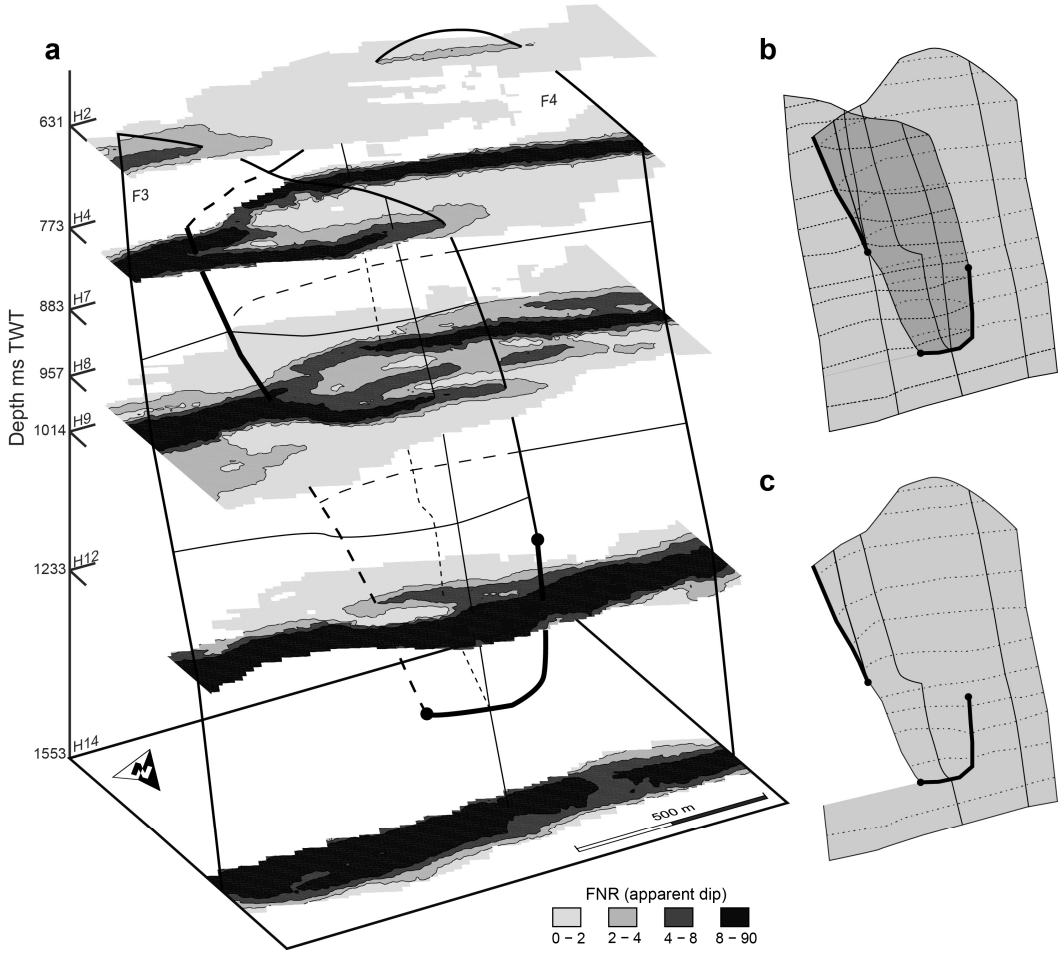

Fig. 4.15. (a) A composite 3D view of relay R2. Horizons H7 and H9 are removed for clarity, their interpreted locations are shown, see (**Fig. 4.14**) for details. Solid black lines indicate the location of interpreted fault tip lines. Dashed lines indicate where a fault tip line is hidden by a fault surface in the foreground. Bold lines indicate branch lines and the branch points are circled. The thin sub-vertical lines on the fault surfaces represent the location and intersection of the seismic profile in (**Fig. 4.14**). (b) A simplified sketch of the interpreted fault surfaces and BL geometries in (a). (c) Only the through going FWF F4 is shown. The fault has a series of scoops (vertical and horizontal bends) relating to the location of the slip-aligned and slip-normal fault linkages. See text for further details.

parallel to the main fault trace. This structure coalesces with the main fault to the NE at transect 625, and is open to the SW at transect 605 (**Fig. 4.14**). When viewed in cross-section, this minor structure is related to fault segment F4 (**Fig. 4.13**).

The relationship between the different horizons and the down-dip changes in linkage geometries can be more easily appreciated in 3D (**Fig. 4.15**). Horizons H2 to H8 are broadly similar and link along a slip-aligned BL in the SW end of the relay zone. A transition occurs on horizon H9 and both ends of the relay ramp are interpreted as open. Below H9 the sense of linkage swaps and linkage occurs along the NE end of the ramp. From cross-section the relay zone is also interpreted to link along a slip-normal

BL below H12. The resultant BL is discontinuous (**Fig. 4.15**). Faults F3 and F4 eventually merge into a single laterally continuous fault, below horizon H12. Fault linkage has created a series of "scoops" (vertical and horizontal fault bends) on the through going FWF F4 (**Fig. 4.15**c). These features developed when fault F4 linked to the overlapping HWF F3 along both slip-normal and slip-aligned BL.

As with Laminaria R1, these observations are more complex than published evolutionary models of fault linkage geometries (**Fig. 4.2**). If we were to follow the model proposed by (Walsh et al., 1999) then Laminaria R2 would probably be interpreted as a relay zone with an L-shaped or U-shaped BL originating from a single BP.

4.5.1.3 Displacement distance profiles

As observed in Laminaria R1, which is located along-strike on the same fault-array (**Fig. 4.6**), the total displacement curve (dashed line) for each faulted horizon resembles that of a single continuous fault (**Fig. 4.14**). Total displacement decreases towards the NE on all horizons.

For horizons H2 to H8 the d-x profiles for the HWF F3 displays the characteristic abrupt drop in throw across the interpreted BP (**Fig. 4.8**d), near transect line 600, at which the SW tip of the FWF F4 also terminates (**Fig. 4.14**, arrowed). On horizon H9 the displacement at the SW tip of FWF F4 decreases gradually to zero and terminates near transect line 610. A drop in throw on the HWF F3 is also observed around transect line 605. This corresponds spatially to the location of the BP on horizons H4 to H8. Horizon H12 is cut by a low offset structure in the footwall of the dominant fault, which relates to fault F4 on above horizons. Offset on this minor structure increases to the NE where it coalesces with the main fault trace. As observed in Laminaria R1, horizons H8 and H9 have a large proportion of continuous deformation, which in some locations is equal to the offsets on the fault polygons (**Fig. 4.10** and **Fig. 4.14**).

4.5.2 Moab splay relay

The bounding faults of the Laminaria R2 relay zone are linked by a slip-normal BL at depth. Horizons within the relay zone also display variable inclinations towards the mutual hanging wall. The combination of enclosing fault geometries and a deforming ramp creates strain compatibility (space) problems at the base of the ramp where sediments are confined by the fault surfaces. To better understand these space problems and the structures needed to maintain strain compatibility in these regions we study the Moab splay relay zone, which has similar cross-sectional geometries to the Laminaria R2 relay zone (**Fig. 4.13** and **Fig. 4.16**). For an overview of the Moab study area see appendix 3: (**Fig. A11**).

The faults studied are located within the Upper Carboniferous Honaker Trail Formation of the Paradox Basin, Utah. The sediments consist of shallow marine to near shelf sandstones and siltstones (Doelling et al., 2002). In this outcrop, the porous sandstone beds are fine grained and range in thickness from 7.5 m to 8.1 m, while siltstone beds range in thickness from 0.59 m to 6.4 m, measured using a terrestrial laser scanner (TLS).

The outcrop is located in the footwall of the NW-SE trending Moab fault. The Moab fault movement is dated to occur between 60 and 43 Ma (Tertiary) and is related to salt movement (Davatzes et al., 2005). Faulting either occurred at the maximum burial depth (2000 – 2500 m) of the Middle Jurassic Entrada sandstone (Garden et al., 2001), which sits 301-2457 m stratigraphically above the Honaker Trail Formation, or during the subsidence immediately before maximum burial (Nuccio and Condon, 1996).

The studied fault-array trends NW-SE and most of the faults dip towards the SW. Faults F1 and F2 (**Fig. 4.16**) splay off the Moab fault and continue for approximately 500 m into its footwall (Doelling et al., 2002). They probably formed synchronously with the Moab fault. Lineations on the fault surfaces indicate dip-slip movement. In cross-section, Faults F1 and F2 link down-dip at a BP. The maximum aggregate throw on the studied faults is 8.5 m (**Fig. 4.16** and **Fig. 4.17**); in comparison, the throw on the nearby Moab fault is 732 m (Doelling et al., 2002).

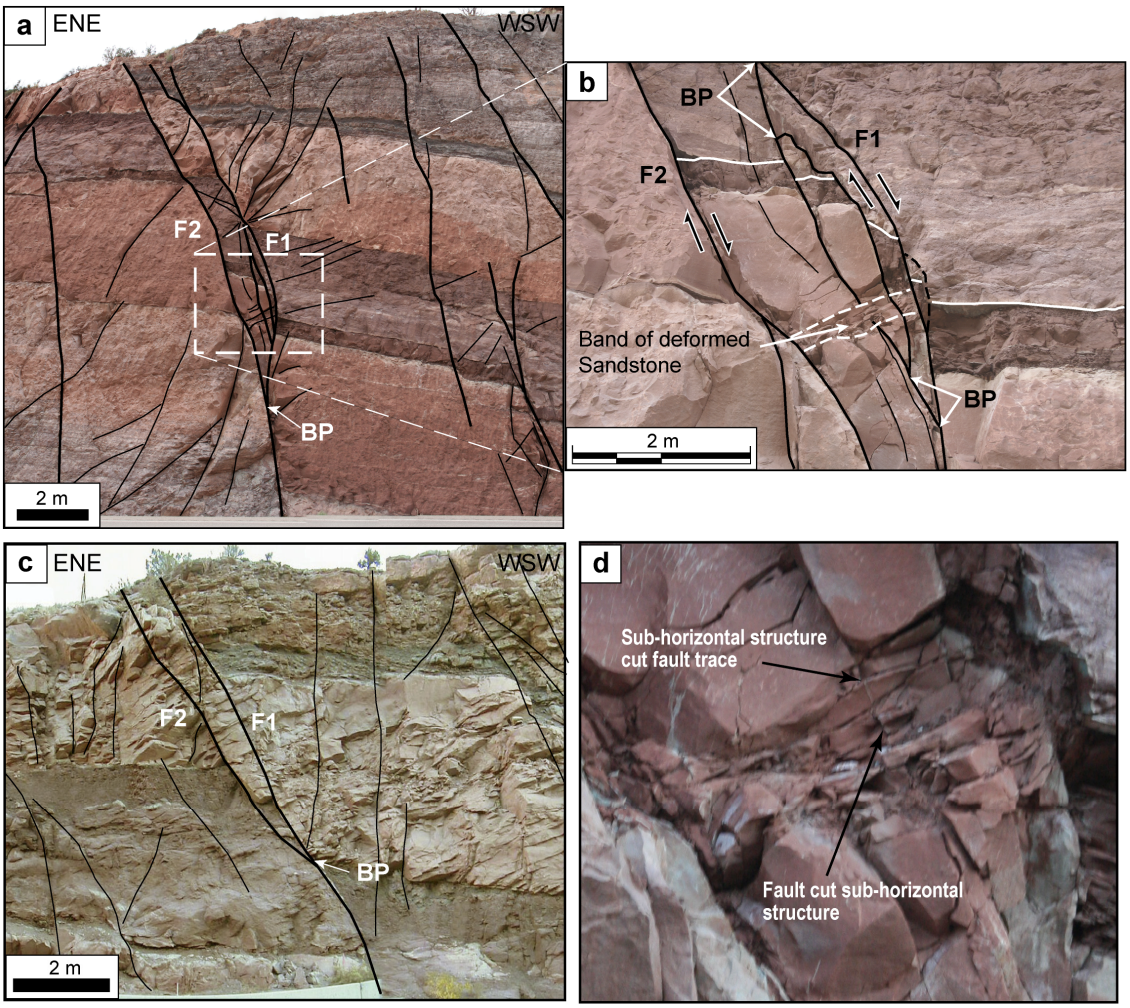

Fig. 4.16. Moab splay relay zone and slip-normal BL, Utah, USA. (a) An interpreted field photo of two overlapping dip-slip normal faults (F1 and F2), linking down-dip at a BP. (b) Close-up on the base of the ramp, white box in (a). A series of secondary faults cut back into the ramp and link to the main bounding faults, labelled BP. A sub-horizontal band of deformed sandstone crosses the ramp. The siltstone bed (dark red) also thickens across the ramp. (c) A previous section through the fault approximately 10m to the NW. The faults can be traced between the two sections and fault F1 has a straighter profile that in (a). (d) A close up of the sub-horizontal band of deformation. A cross cutting relationship exists whereby both the horizontal and sub-vertical tectonic features cross cut one another. No signs of lateral shearing are present along the sub-horizontal structure. Photo (c) courtesy of Russell K. Davies of Rock Deformation Research USA Inc., taken in 2003.

The outcrop has a vertical face that trends NNE – SSW. For a detailed photo mosaic of the relay zone see appendix 3: (**Fig. A12**). Fault and bed geometries above what could be reached from ground level were measured using a TLS. Prior to widening of the nearby road, another section through the faults was exposed approximately 10 m to the NW. The faults can be traced between both sections and in both F1 and F2 link down dip forming a slip-normal BL (**Fig. 4.16**: a and c).

4.5.2.1 Fault geometries

The Moab splay relay zone consists of two overlapping, NW-SE trending dip-slip normal faults. In cross-section, the HWF F1 increases in dip downwards and coalesces with the FWF F2 at a BP. This reduces the separation of the overlapping faults from a fairly consistent 2.5 m to a 31 cm wide fault zone over a distance of 3.9 m above the BP. A slip-normal BL is inferred to connect the two BP observed in sequential cross-sections through the Moab splay relay zone (**Fig. 4.16**: a and c). The sediments in the base of the relay zone are thus completely enclosed by the boundary faults F1 and F2 (**Fig. 4.16**).

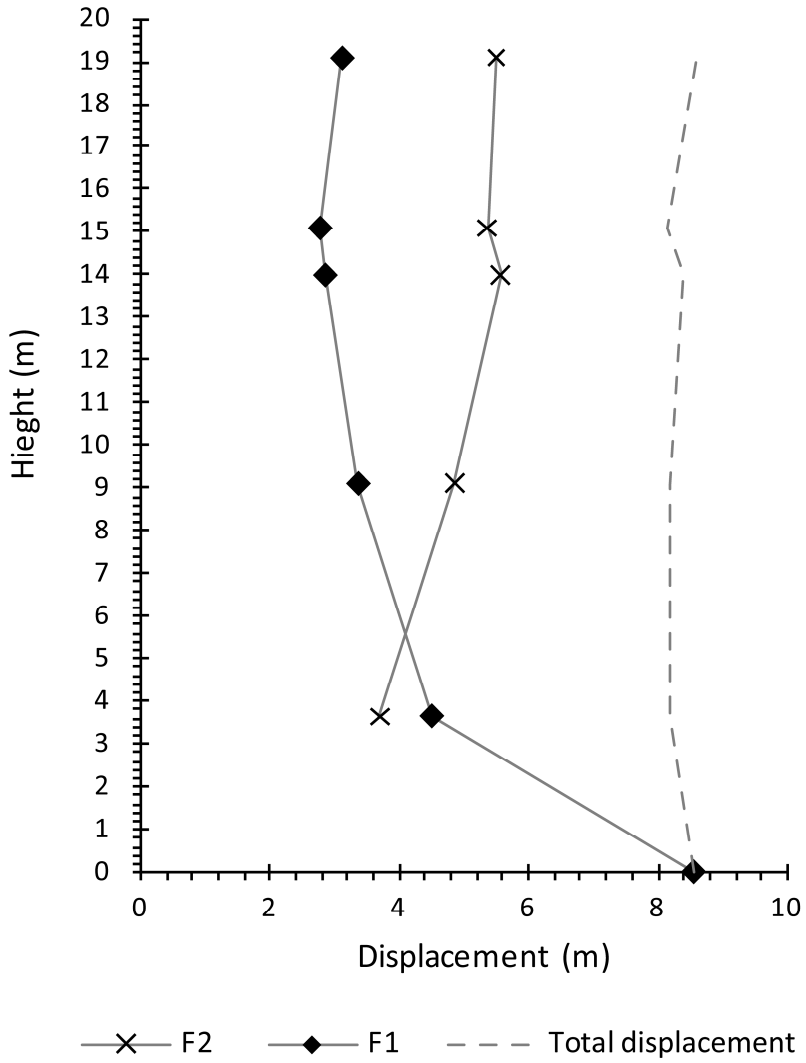

Fig. 4.17. Vertical displacement profiles for the Moab splay relay zone. Fault F2 decrease is vertical displacement towards the BP (**Fig. 4.16**). Vertical displacement on F1 increases towards the BP and becomes the through going fault at depth represented by the jump in displacement. At all levels the total displacement remains relatively constant.

In detail, the convex-upward bend in the HWF F1 is cut by minor faults that step back into the ramp (**Fig. 4.16**b). The net effect of these faults is to produce a straighter profile, which is more favourable for slip. Within the ramp a 43 cm wide sub-horizontal band of deformed sandstone crosses the entire width of the relay zone. This is located 3.9 m above the BP at the point where separation distance begins to decrease (**Fig. 4.16**a). The band of deformed sandstone does not correspond to a bedding surface. On close inspection, the sub-horizontal tectonic structures are cross-cut by minor faults and fractures that cut back into the ramp. In addition, these minor faults and fractures, which are oriented parallel to the main bounding faults, are themselves cross cut by some of the sub-horizontal tectonic bands, which indicates both structures are forming together (**Fig. 4.16** and **Fig. A12**). There is no visible evidence of lateral movement across the sub-horizontal structures.

The less competent siltstone beds (dark grey) change in thickness within the relay zone, from 59 cm near F2 to 98 cm next to F1. This suggests tectonically induced volume change within the weaker layers, which has accommodated strain within the relay zone, as is also observed at Lilstock within the incompetent shale beds (**Fig. 4.12**).

The vertical displacement profiles for the two overlapping faults F1 and F2 (**Fig. 4.16**) are presented in (**Fig. 4.17**). The throws are measured from a detail 3D point cloud collected using a TLS, which enabled us to measure detailed displacement data from portions of the outcrop above head height.

Fault F1 has lower total throws above the BP when compared to F2 (**Fig. 4.17**: > 3.4 m). However, below the BP (**Fig. 4.17**: < 3.4 m), where only one fault (F1) is present, the throw on the through going fault F1 jumps to maintain a nearly constant vertical displacement profile (**Fig. 4.17**: dashed line). This confirms that faults F1 and F2 do form a relay zone.

To check our interpretations of fault linkage, i.e. which fault is the through going slip surface, and to map the distributions of strain within a down-dip confined relay zone,

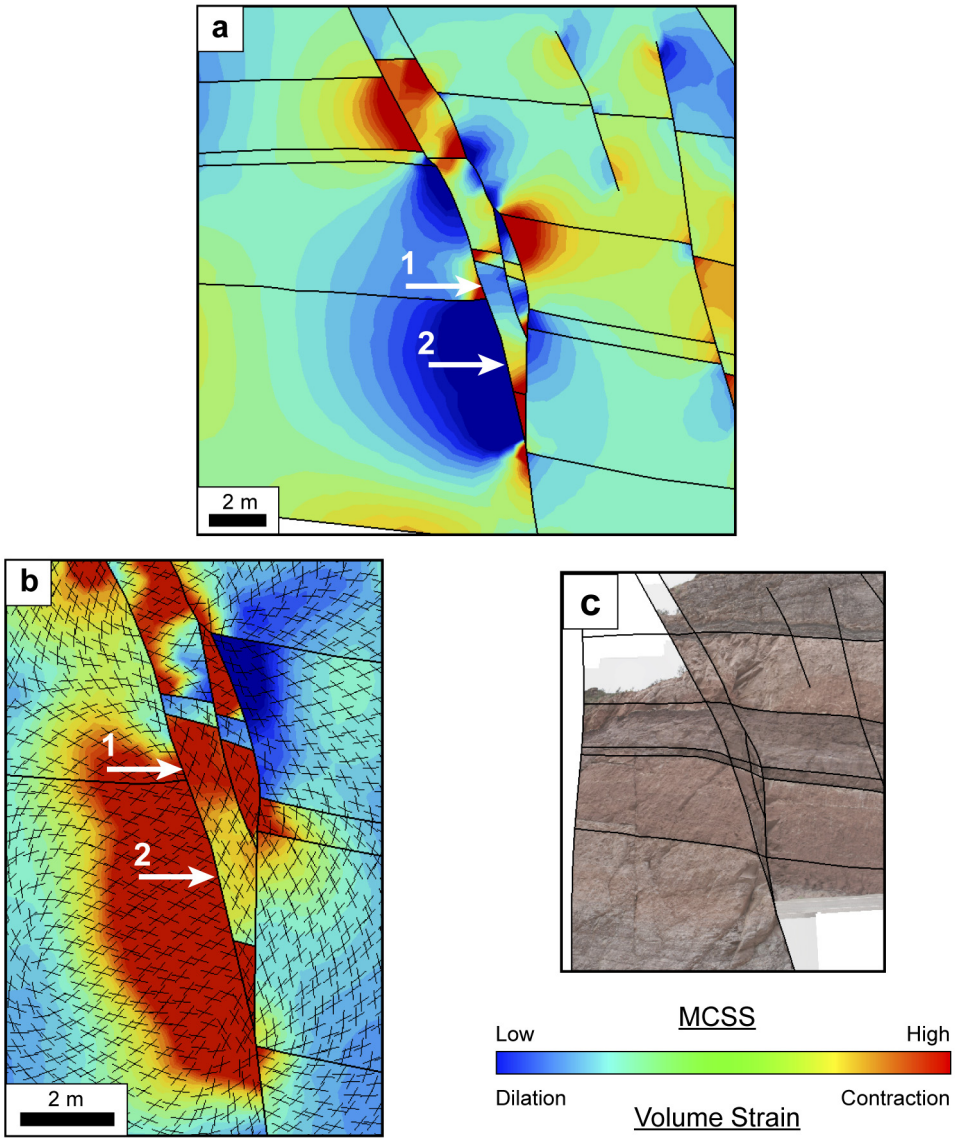

Fig. 4.18. Restoration results from Dynel2D for fault geometries observed in (**Fig. 4.16**a). (a) Volume strains distributions, an area of dilation occurs at arrow (1) within the relay zone and area of contraction near the base of the relay at arrow (2). (b) Maximum coulomb shear stress (MCSS) distributions and predicted fault orientations. High MCSS are observed at arrow (1) and medium values at arrow (2). Predicted fault orientations closely resemble those observed in (**Fig. 4.16**). (c) The restored section.

we restored the mapped faults using the geomechanical restoration package Dynel2D (Maerten and Maerten, 2006).

4.5.2.2 Restoration results

Two fault linkage geometries were restored, one with F2 as the through going fault, and another with F1 as the main through going fault. The second restoration gave the closest match between modelled results and observed geometries (**Fig. 4.18**). This

linkage configuration is supported by observations from the outcrop itself. Firstly, the previous section (before road widening) through this relay zone depicts fault F1 to have the more ideal shape for slip, i.e. straight (**Fig. 4.16**c). Secondly, the curvature produced by the fault linkage on fault F1 has partially been removed by continued fault movement. For, if F1 was inactive after it linked with F2 the ramp and F1 would be passively moved in the mutual hanging wall as a relict structure. However, this is not the case, thus implying continued slip on F1 post-linkage (**Fig. 4.16**).

Focusing within the relay zone, high maximum coulomb shear stress (MCSS) indicate areas that are likely to have shear fracture and faults in the predicted orientations (**Fig. 4.18**b). These match well with observed fractures and faults (**Fig. 4.16**). For example, at arrow (1) the predicted fault orientations are sub-parallel to the main bounding faults F1 and F2. In the outcrop (**Fig. 4.16**b) this area is observed to have multiple normal faults that cut back into the ramp. In addition, this area is also predicted to be an area of dilation (**Fig. 4.18**a), indicative of extension. Below this area, in the base of the ramp, at arrow (2) (**Fig. 4.18**a), volume strains indicate an area of contraction, which relates in outcrop to the approximate position of a sub-horizontal band of deformed sandstone (**Fig. 4.16**b). This band is orientated perpendicular to the maximum compressive stress direction, as indicated by the orientation of the predicted Andersonian fault patterns (**Fig. 4.18**b).

4.5.2.3 Moab interpretations

The band of sub-horizontal deformation located within the footwall of F1 and that sits totally within the relay zone (**Fig. 4.16**) could be due to a series of geological processes. Unfortunately this part of the outcrop is above head height and was not viewed directly. Two possible explanations to its origin are as follows: one, a shear stress develops within the ramps either due to the rotation of beds towards the hanging wall (i.e. bed parallel slip), or undulations in the footwall fault (F2) could create a sub-horizontal shear band within the ramp, as material is translated down the uneven fault surface; two, the porous sandstone undergoes tectonic compaction due to imposed compressive stress within a fault bounded wedge (i.e. a relay ramp). The lack of lateral offset across the sub-horizontal bands, as indicated by the cross cutting relationships

(**Fig. 4.16** and **Fig. A12**) suggest that explanation one is potentially incorrect. In addition, the tectonic structure is not located on a bedding surface ruling out bed parallel slip. We therefore favour the second option whereby the sub-horizontal zone of deformation formed in response to increased compressional stresses within a structurally confined relay ramp. Other evidence that supports the inference for compression in the base of the ramp comes from the geomechanical modelling, which directly models volume loss and thus compression (**Fig. 4.18**a: arrow two).

It is inferred from this outcrop that the Moab splay relay zone continued to deform after linkage of the bounding faults, F1 and F2, by rotation of the beds towards the mutual hanging wall (**Fig. 4.16**). It is this continued rotation of beds above the slip-aligned BL that causes the space problem to develop in the base of the ramp and thus the resultant compression. The strain compatibility issue flagged by this outcrop will apply to seismic scale relay zones that exhibit enclosing fault geometries within relay zones that continue to deform post linkage, which is the case for Laminaria R2 (**Fig. 4.15**b).

4.6 Discussion

4.6.1 Geometrically coherent fault linkage

Our results show that the continuous deformation within the rock volume surrounding seismically imaged normal faults is characterised by the rotation of seismic reflectors towards the mutual hanging wall. These “highs” in FNR are aligned into a series of overlapping elongate bands surrounded by regions of low FNR that display variable widths (**Fig. 4.10** and **Fig. 4.14**). In detail, the pattern of FNR associated with relay zones varies substantially on each horizon and between horizons. However, aggregate d-x profiles resemble those of single fault more so than either of the fault segments alone (Huggins et al., 1995; Walsh et al., 2003b). This indicates that the mapped structures are all geometrically coherent, and thus developed as part of a single coherent fault-array, despite complex distributions of FNR and strain compatibility issues within each relay zone.

4.6.2 Slip-aligned fault linkage evolution

Fault linkage in Laminaria R1 is shown to pass downward from linked (**Fig. 4.10**: H7 to H8), to open (**Fig. 4.10**: H9), and finally linked again at a BP above horizon H12 (**Fig. 4.11**). This interpretation of a discontinuous slip-aligned BL does not correspond to current models of BL evolution, as we do not observe a sequential propagation of fault linkage outwards from a single BP (Walsh et al., 1999; Kristensen et al., 2008). We agree that fault linkage can initiate from a BP, but we postulate that fault linkage can initiate simultaneously at multiple points within a relay zone. This multi-point linkage could be facilitated by non-uniform fault tip line propagation within a layered sedimentary sequence (Schöpfer et al., 2006), as inferred to explain vertical displacement distribution within the Lilstock relay zone (**Fig. 4.12**).

4.6.2.1 Fault linkage evolution and variable relay ramp geometries

In Laminaria R1 and R2, the relay ramps are interpreted as being open (intact) on horizon H9. This horizon is characterised by elevated rotations towards the mutual hanging wall, compared to the breached relay ramps on horizons H8 to H7 (**Fig. 4.10**). Observations from Lilstock also show that relay ramps can have different dips at different levels within the same relay zone. Again, this variability relates to fault linkage evolution (**Fig. 4.12**). In addition, 3D distinct element models of relay growth and breaching by Imber et al., (2004) also predict increased ramp dips within open relay ramps compared with breached ramps within the same relay zone (Imber et al., 2004: their Fig. 8).

Relay ramps continue to rotate unhindered until they are linked, afterwards they continue to rotate by a reduced amount until the relay zone is fully breached in 3D (Imber et al., 2004; Hus et al., 2006). When linked and open ramps coexist at different depths within a single relay zone, open relay ramps accommodate strains by increased ramp rotations, whereas in linked relay ramps deformation is localised onto the through going fault. Therefore, the evolution of fault linkage will result in a relay zone with different degrees of ramp rotations. This results in strain compatibility problems between horizons with variable ramp rotations. In Lilstock (**Fig. 4.12**) this space

problem is accommodated by ductile shale movement. In Laminaria R1 a 6 ms TWT decrease in thickness is observed within the relay zone compared to un-deformed sections, measured between the same marker horizons (**Fig. 4.9**). From the well logs (**Fig. 4.4**), the carbonate-dominated sequence of the Laminaria High does not appear to contain weak layers (e.g. shale). Therefore, other mechanisms than those implied in Lilstock are needed to accommodate the variations in horizon geometries within the relay zone, such as secondary faulting and/or dissolution.

Peacock and Sanderson's (1994) idealised model of a relay zone does not take into account strain compatibility issues between horizons, because all dip uniformly towards the mutual hanging wall. We therefore propose that ramp geometries will vary depending on the fault linkage history and the ability of the host sequence to accommodate the volumetric strains required to maintain compatibility between horizons. An implication of this is that tectonically-induced thickness changes observed within relay zones in seismic data, such as in Laminaria R1 and R2 (**Fig. 4.9** and **Fig. 4.13**), will be associated with elevated deformation within those layers.

In the Lilstock example (**Fig. 4.12**), where offset of the individual beds are small compared to the thickness of the ductile shale beds, the shale beds are able to dissipate the potential strain incompatibilities between beds 1, 2, and 3. However, within sequences that do not have interbedded weak layers, such as Laminaria, variations in ramp dip, within a relay zone, are not dissipated between horizons and therefore movement (displacement) on one horizon has the potential to influence the geometries of other horizons, for movement must be conserved i.e. strain compatibility must be maintained between horizons. In the next section, we address the implications of fault linkage within a relay zone and what affect it has on strain distributions on nearby (i.e. under-/overlying) un-linked horizons.

4.6.2.2 Implications of strain compatibility between open and linked horizons within a single relay zone

In this chapter we observe that when overlapping faults link at a particular stratigraphic level, displacement become localised onto a through going fault.

Therefore, parts of the overlapping fault surfaces may become bypassed by continued slip, termed relict splays (**Fig. 4.1**: stage 4) (Childs et al., 1995; Cartwright et al., 1996; Walsh et al., 1999). On a d-x profile, the presence of a relict splay is characterised by an abrupt drop in displacement on the through-going fault at the point of linkage (**Fig. 4.8**d). Such drops in displacement have been observed on horizons H7 and H8 in Laminaria R1, and on horizons H4, H7 and H8 in Laminaria R2 (**Fig. 4.10** and **Fig. 4.14**: arrows). However, moderate drops in displacement are also observed on horizon H9 in Laminaria R2, and on horizons H4 and H9 in Laminaria R1 at equivalent locations to those on the under-/overlying linked horizons (**Fig. 4.10** and **Fig. 4.14**: arrows). The relay ramps on horizons H9 in R2 and H4 and H9 in R1 are however, interpreted as being open (**Fig. 4.11** and **Fig. 4.15**).

Two possible reasons for the similarity between d-x profiles on linked and open horizons, from within the same relay zone, are: 1, faults link below the resolution of the seismic data and the absence of linkage on open horizons is incorrectly interpreted; and/or 2, to maintain strain compatibility between the open ramps and linked relay ramps above/below, regions of the fault surface bypassed by continued slip (i.e. relict splay) on the linked horizons, lead to restricted (lower than normal) displacements on the entire fault segment that contains the relict splay, assuming that no weak layer dissipates displacements between horizons. Both these possibilities would impart an apparently linked d-x profile shape onto un-linked horizons within the same relay zone. Our results from horizons H9 Laminaria R1 and R2 do not however indicate the presence of a single continuous linking fault crossing the ramp. In addition, well logs from the Laminaria High indicate the lack of mechanically weak layers (e.g. thick shales) that could dissipate vertical strain gradients (**Fig. 4.4**). From these observations we favour the second explanation for the similarity between d-x profiles. However, it is noted that tectonic mechanisms, such as dissolution or secondary faulting could also accommodate vertical strain gradients between linked and intact relay ramps on under-/overlying horizons.

In detail, to conserve motion and maintain strain compatibility between horizons a reduction in slip at one level, such as on a relict splay, will lead to a reduction in slip up and down-dip of that location. We therefore propose that the breaching of a relay

ramp, by slip-aligned linkage, and the subsequent partitioning of displacement on to the through going fault will lead to reduced slip on the bypassed fault at *all* levels within the relay zone (**Fig. 4.19**). The flip side of this inference also accounts for the continued movement on relict splays and continued rotation of ramps on linked relays within relay zones that contain open relay ramps, i.e. are not fully breached (Imber et al., 2004). In addition, to maintain a geometrically coherent total d-x profile on the open horizons the rotations within the ramp must increase to balance the drop in displacement of the restricted fault segment (**Fig. 4.19**c), which is observed (**Fig. 4.10** and **Fig. 4.14**).

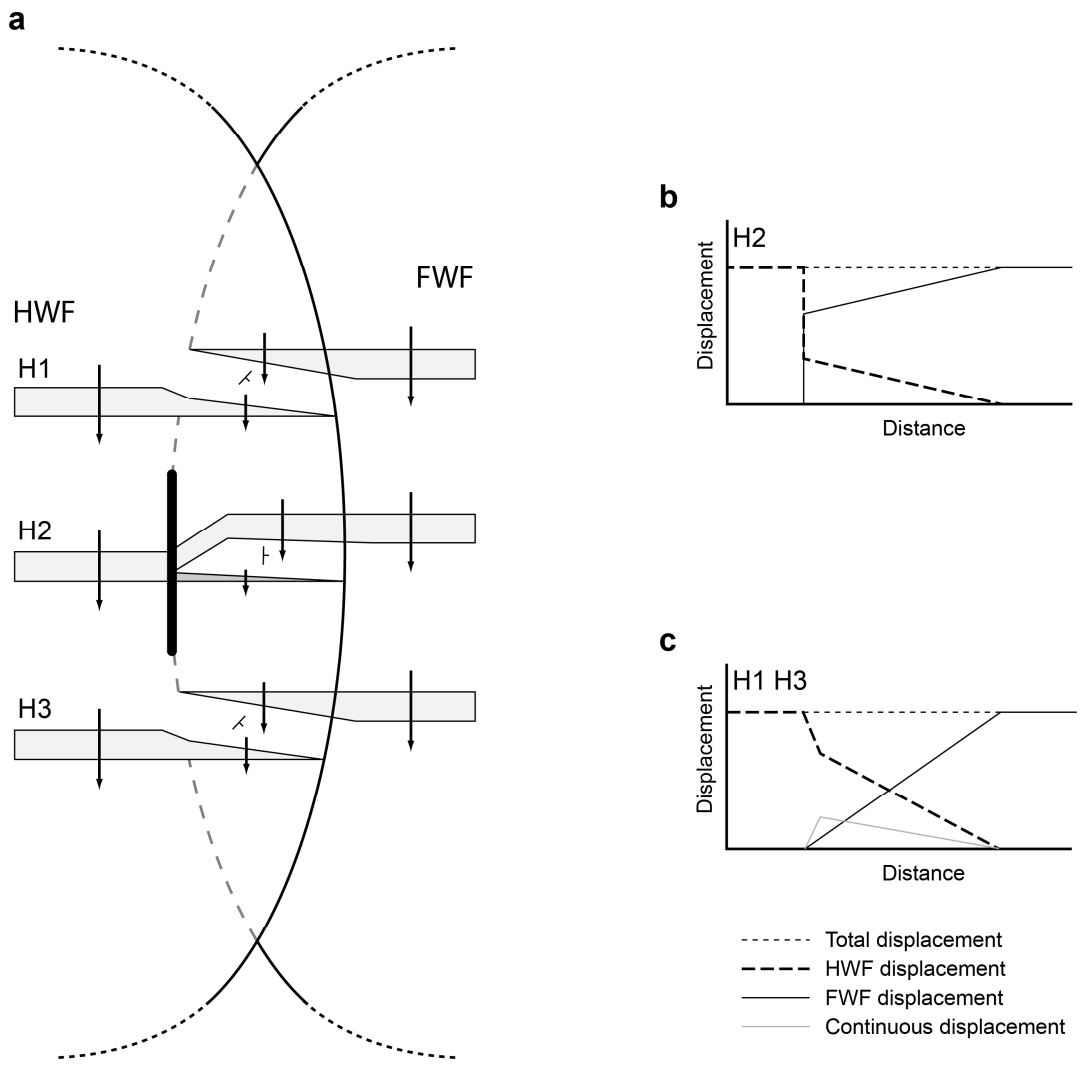

Fig. 4.19. A schematic model illustrating the effect of slip-aligned fault linkage on open relay ramps from within the same relay zone. (a) Horizons H1 and H3 are open and H2 is linked along a slip-aligned BL (bold). A through going fault connects the HWF and FWF on H2 with a relict splay (dark grey) along-strike of the HWF. Arrows indicate the proportion of slip taken up on different sections of the overlapping faults. Fault movement on the HWF is partially restricted due to the bypass of deformation from the relict splay onto the through going fault, H2. To maintain strain compatibility between horizons restricted movement due to fault linkage on H2 will be communicated up and down dip onto H1 and H3. Likewise, movement on the HWF on H1 and H3 will be communicated onto the relict splay. (b) d-x profiles for H2, displacement drops across the BL. (c) The d-x profiles on H1 and H3, for the HWF (dashed line), display an along-strike drops in displacement at sites that correspond to the location of linkage on H2. To maintain a coherent total d-x profile (thin dashed line) the amount of rotation within the ramps on H1 and H3 increase (grey line) to compensate the low displacements on the overlapping sections of the HWF.

The precise mechanism by which strains are transferred up and down dip is unknown due to limitations in the resolution of the seismic and well log data. However, in Lilstock changes in bed geometries, and thus displacements, are accommodated by intervening mechanically weak shale layers (**Fig. 4.12**). Therefore, it is postulated that strain transfer between open and linked relay ramps within the same relay zone will be

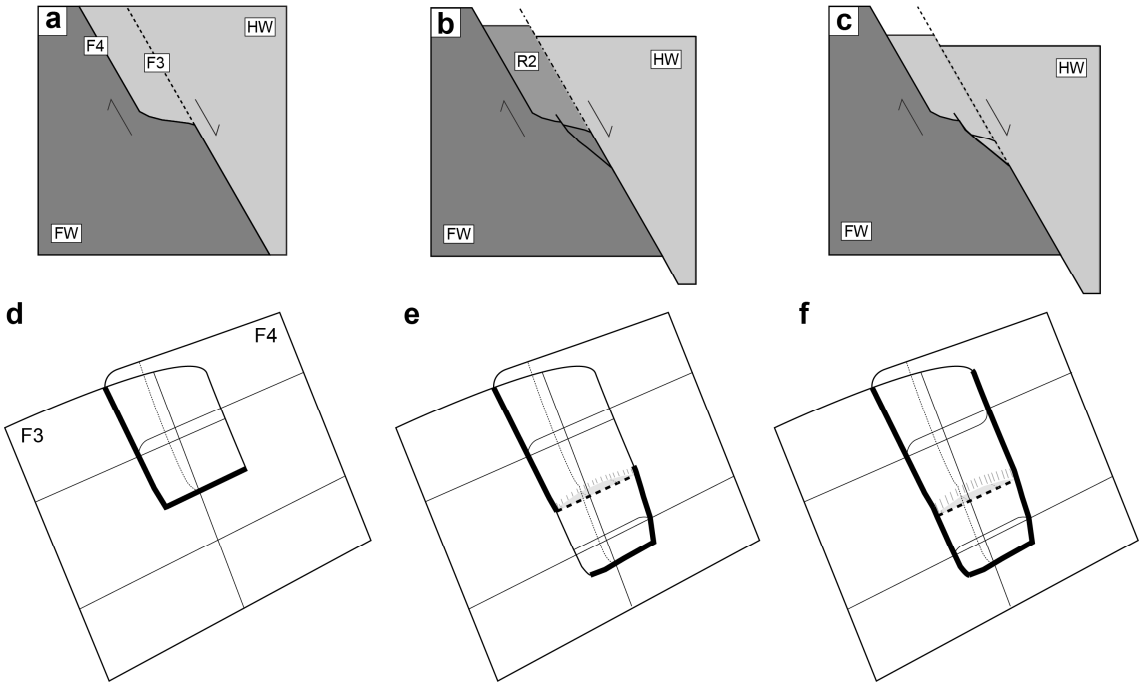

Fig. 4.20. A schematic model illustrating slip-normal fault linkage and resultant strain compatibility issues. (a) F4 links down-dip to F3 producing a through going fault and a restraining bend in the footwall. (b) Movement of the hanging wall material past the bend in the F4 is restricted which caused an increase in damage within the footwall and continued movement on what would be the relict fault splay, F3. (c) The restraining bend is sheared off producing a fault surface that can better accommodate the slip on the through going fault. (d) Perspective view of (a). (e) Perspective view of (b). The BL geometry is complicated when the younger secondary fault interacts and links with the existing fault surface. This results in a discontinuous BL. (f) Perspective view of (c). As deformation continues the relay zone will become fully breached. Horizontal thin lines in (d to f) are form lines, vertical thin lines are the location of cross-sections (a-c), and shaded areas are portions of the sheared off fault surface. Bold lines represent BL.

generally accommodated by weak mechanical layers and sub-seismic scale structures (e.g. stylolites).

It is therefore proposed that the shape of a d-x profile from an outcrop example of an open relay ramp could thus be used to predict if the relay zone is breach along a slip-aligned BL in the subsurface (**Fig. 4.19**). This inference is similar to that of Soliva et al., (2008) who infers slip-normal fault linkage from the asymmetric displacement distributions on overlapping faults. These two models combined can potentially be used to predict the locations of linked fault segments in the subsurface. (See chapter 6 for a discussion of wider implications).

4.6.3 Slip-normal BL and fault curvature

Relay zones with slip-normal fault linkage and thus down-dip fault bends (i.e. releasing or restraining bends) are well documented structures and are implied in evolutionary models of BL (**Fig. 4.2**) (Walsh et al., 1999; Kristensen et al., 2008). "Scoops" or depressions can form along the bounding faults, such as those seen along the footwall fault in Laminaria R2, when faults link by both slip-normal and slip-aligned BL (**Fig. 4.15**c). Such irregularities on the fault surface create asperities in the fault zone, which impede fault movement. With continued displacement, these asperities are removed to produce smooth slip surface (**Fig. 4.20**) (Bonson et al., 2007; Childs et al., 2009). For instance, along the Moab splay fault, removal of asperities is manifested by successive secondary faults that cut back into the ramp, straightening out the down-dip bend in the through going HWF (**Fig. 4.16**). Likewise, in Laminaria R2 secondary faults cut back into the footwall of the through going FWF, which extends the ramp in the direction of slip and reduces the curvature of the through going fault (**Fig. 4.20**a-c). Therefore, slip-normal fault linkage can cause secondary faults to develop in the base of ramps, at sites of enhanced fault curvature, and hence complicate fault linkage geometries as these secondary faults interact and link with existing fault surfaces (**Fig. 4.20**d-f). Consequently, a relay zone may appear fully breached in 3D but will continue to deform internally until all asperities are removed (**Fig. 4.20**).

4.6.4 Slip-normal fault linkage and strain compatibility

In Moab and Laminaria R2 the ramp rotates towards the mutual hanging wall between two coevolving faults, with ramp rotations increasing towards the slip-normal branch line at the base of the relay zone (**Fig. 4.13** and **Fig. 4.16**). Ramp rotation is the result of shear stresses that develop between overlapping faults and is a critical element of deformation to be considered in a coherent fault-array (Walsh and Watterson, 1991; Ferrill and Morris, 2001).

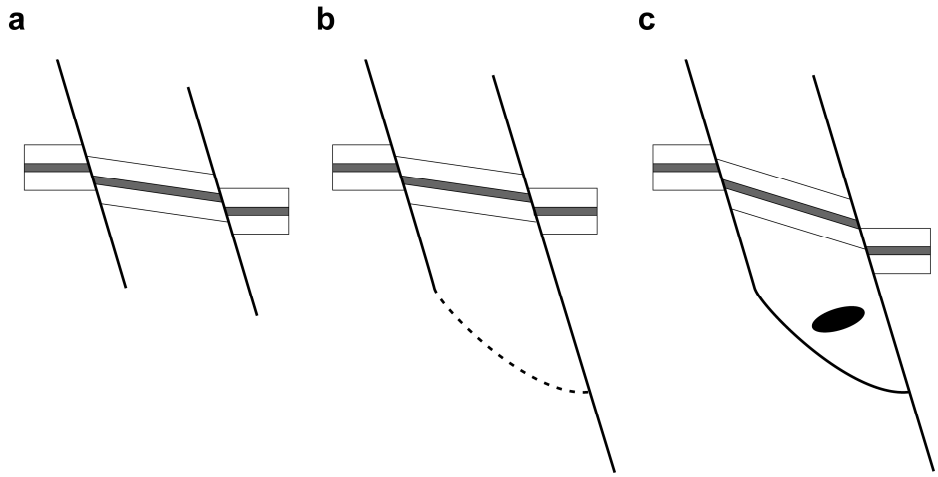

Fig. 4.21. (a) A schematic relay zone with bed rotations towards the mutual hanging wall. (b) The relay links along a slip-normal BL, the black circle represents the initial un-deformed state of the ramp, at the point prior to down-dip fault linkage. (c) With continued rotation of the ramp a space problem is created in the base of the structure against the enclosed fault surfaces. This leads to compression and volume loss in the base of the ramp, as indicated by the deformed black ellipse (i.e. strain ellipse). With continued displacement the restraining fault geometries will be sheared off, as shown in (**Fig. 4.20**).

In Laminaria R2, displacements on the FWF F4 decreases towards the slip-normal BL (**Fig. 4.13** and **Fig. 4.14**: d-x profiles). To maintain a geometric coherent total d-x profile, the proportion of displacement accommodated within the ramp must increase to counteract the reduction in displacement on the bounding fault, as is observed on H7 to H9 (**Fig. 4.14** and **Fig. A7**d). The reduction of slip on the FWF F4 is interpreted to result from the presence of a restraining fault bend at depth on the FWF (**Fig. 4.13**a and **Fig. 4.15**c), for the FWF surface is not favourable aligned for continued slip, as demonstrated numerically (Soliva et al., 2008). In Moab we can directly observe how strains are accommodated in relay ramps that display both rotation of beds towards the mutual hanging wall and are completely enclosed by fault surfaces, due to slip-normal fault linkage (**Fig. 4.16**).

In (**Fig. 4.16**) strains within the ramp are taken up by minor normal faults, which dissect the ramp enhancing bed rotations toward the mutual hanging wall and by an inferred zone of sub-horizontal tectonic compaction. The restoration of the Moab relay zone indicates areas of volume loss and high shear stress within the base of the relay ramp, which relate to the location of inferred compaction structures (**Fig. 4.16**b and **Fig. 4.18**). The deformation within the base of the relay ramp, at Moab (**Fig. 4.16** and **Fig. 4.18**), is interpreted to accommodate the space problems created by the rotation

of beds within a structurally confined relay zone (**Fig. 4.21**). For instance in (**Fig. 4.21**), slip-normal fault linkage encloses the base of the ramp with fault surfaces (**Fig. 4.21**b), and continued rotation/shearing of the overlaying beds compresses strata against the bounding faults, which results in volumetric strains (**Fig. 4.21**c). This implies that the relay zone was active and the ramp was accommodating rotations while linked along a slip-normal branch line. This inference is possible if the relay zone was not fully breached in 3D (Imber et al., 2004). An assumption of this model is that faults are fixed structures that are not bent by subsequent slip and thus act as mechanical boundaries, which results in strains becoming concentrated on one side of the fault rather than being dissipated within the surrounding wall rock, as is predicted to occur around isolated faults (Barnett et al., 1987).

Insights gained from the Moab outcrop can be used to help interpret Laminaria R2, which displays similar ramp rotations towards the mutual hanging wall and enclosed bounding faults. The vertical thicknesses, of pre-tectonic strata, within the ramp (R2) are reduced when compared to strata thicknesses away from the fault-array, which indicates volume loss (in cross-section) (**Fig. 4.13**). However, the type of structures likely to form In Laminaria will differ to those in Moab due to the differences in lithology. In the carbonate dominated Laminaria sequence it is postulated that dissolution structures would form normal to the imposed compressive stress direction. Therefore, in general, the base of relay zones, enclosed by fault surfaces, should be characterised by a high density of volumetric deformation (**Fig. 4.16** and **Fig. 4.21**c). To apply observations from outcrops to seismic-scales we need understand how fault and in particular fault relay zones scale, which is covered in chapter 5.

4.7 Conclusions

1. Relay zones remain geometrically coherent at all levels despite the different distributions of FNR on each horizon and the variable stages of fault linkage.
2. Fault linkage, in relay zones, does not exclusively evolve from a branch point but has been shown to link simultaneously at multiple points along overlapping fault tip lines. As a result, branch lines can be segmented. Multiple points of

fault linkage and segmented BL could result from the overlap and linkage of fringed tip lines (Schöpfer et al., 2006).

3. Fault linkage controls the amount and location of ramp rotations within a relay zone. For, on open levels ramps rotate freely whereas on linked horizons strains are localised onto the through going fault. This will lead to relay zones with variable amount of ramp rotation within a single structure, controlled by fault linkage evolution.

4. On linked relay ramps, displacements are mainly accommodated by slip on the breaching fault, with limited slip along the relict splay. In comparison open ramps above or below a linked horizon accommodate displacements by slip on both the bounding faults and ramp rotations. Therefore, to maintain strain compatibility between the linked and open ramps, within a relay zone, displacement is restricted on the entire bounding fault segment that contains the relict splay, assuming that no weak layer dissipates vertical displacements gradients between horizons. This imparts an apparently linked d-x profile shape onto un-linked horizons within the same relay zone and also allows relict splays to continue accommodating displacement on linked horizons (**Fig. 4.19**). This continues until the relay zone if fully breached. The shape of d-x profiles from open relay ramps could therefore be used to identify areas of slip-aligned fault linkage in the subsurface.

5. Slip-normal fault linkage can enhance fault curvature normal to the slip direction, such as in Laminaria R2 and the Moab relay. Fault curvature at BL can acts as an asperity impeding slip on the through going fault. With continued deformation these asperities are removed by secondary faults, which modify the geometry of the through going fault making it more favourable for continued slip. The removal of asperity also modifies fault linkage geometries (**Fig. 4.20**). While restraining bends remains on the through going fault slip on both arms of the relay can occur. Without a full appreciation of the 3D fault linkage geometry it is difficult to predict when a relay zone is fully breached.

6. Relay zones that have slip-normal fault linkage enclose the base of relay zones with fault surfaces. Therefore, continued rotation of the overlying ramps

develops high compressive stresses and volume strains develop within the base of the relay zone. For, bed rotations in the base of the relay zone are confined against the bounding fault surfaces and branch line. Therefore, to maintain strain compatibility volume loss must occur by increased compaction normal to the maximum compressive stress direction (**Fig. 4.21**).

Chapter 5. Fault relay zone scaling and the geological reasons for scatter in their geometries

Abstract:

The overlap and separation of relay zones follow a power-law scaling relationship over nine orders of magnitude. Approximately one order of magnitude scatter in both separation and overlap exists at all scales. Up to half of this scatter can be attributed to the spread of measurements recorded from individual relay zones, which relates to the evolution of relay zone geometry as the displacements on the bounding faults increase. Relay aspect ratio (AR; defined as overlap/separation) is primarily controlled by the stress interaction between the overlapping fault tips, rather than by host rock lithology. At the Kilve and Lamberton study areas, mean ARs are 8.60 and 8.64 respectively, which are much higher than the global mean, 4.2. Both outcrops are mechanically layered and faults were initially confined within competent layers, resulting in low displacement/length ratios and thus relatively small perturbations of the stress field. Lateral propagation of overlapping faults was therefore unhindered until the faults breached through the mechanical layer and the stress perturbation expanded. At Kilve, fault tips are also associated with veins, which change the material properties at the tips and are mechanical heterogeneities the propagating fault can exploit, which facilitates greater overlap lengths.

5.1 Introduction

Fault-arrays comprise multiple fault segments at all scales (Peacock and Sanderson, 1991; Childs et al., 1995; Childs et al., 1996a; Willemse, 1997; Crider and Pollard, 1998a; Peacock, 2002). As the fault-array grows these segments overlap to form relay zones (**Fig. 5.1**a), which are dynamic structures that evolve with increased displacement (Peacock and Sanderson, 1994; Childs et al., 1995; Walsh et al., 1999). The linkage of fault segment at relay zones is a fundamental process by which faults grow (Cartwright et al., 1996; Walsh et al., 2003b). In map view, stages in the evolution of relay ramps have been recognised with relay ramps starting as open structures with a continuous relay ramp linking the footwall and hanging wall (**Fig. 5.2**a) (Peacock and Sanderson, 1994). As displacement on the bounding faults increases, the ramp continues to rotate (i.e. to accommodate shear strains) and linking faults begin to grow (**Fig. 5.2**b). Finally, a through going fault is formed producing a breached relay ramp (**Fig. 5.2**c). Within a single relay zone it is inferred that different stages of relay ramp evolution can coexist (Peacock and Sanderson, 1994).

Fault relay zone geometries are documented over a wide range of scales and follow power-law scaling relationships (Huggins et al., 1995; Acocella et al., 2000; Peacock, 2003; Soliva and Benedicto, 2004). In map view, relay zones can be approximated to rectangles with overlap lengths greater than their separation (**Fig. 5.1**). The overlap/separation ratio gives the aspect ratio (AR) of a relay ramp. These geometric properties are easily obtained in map view. The variation of AR on different horizons, within a single relay zone, is governed by the tip line geometries of the boundary faults. Relay zone AR can be used to study the interaction between overlapping faults, which helps us to understand how faults interact and link (Crider and Pollard, 1998a; Acocella et al., 2000; Gupta and Scholz, 2000; Soliva and Benedicto, 2004).

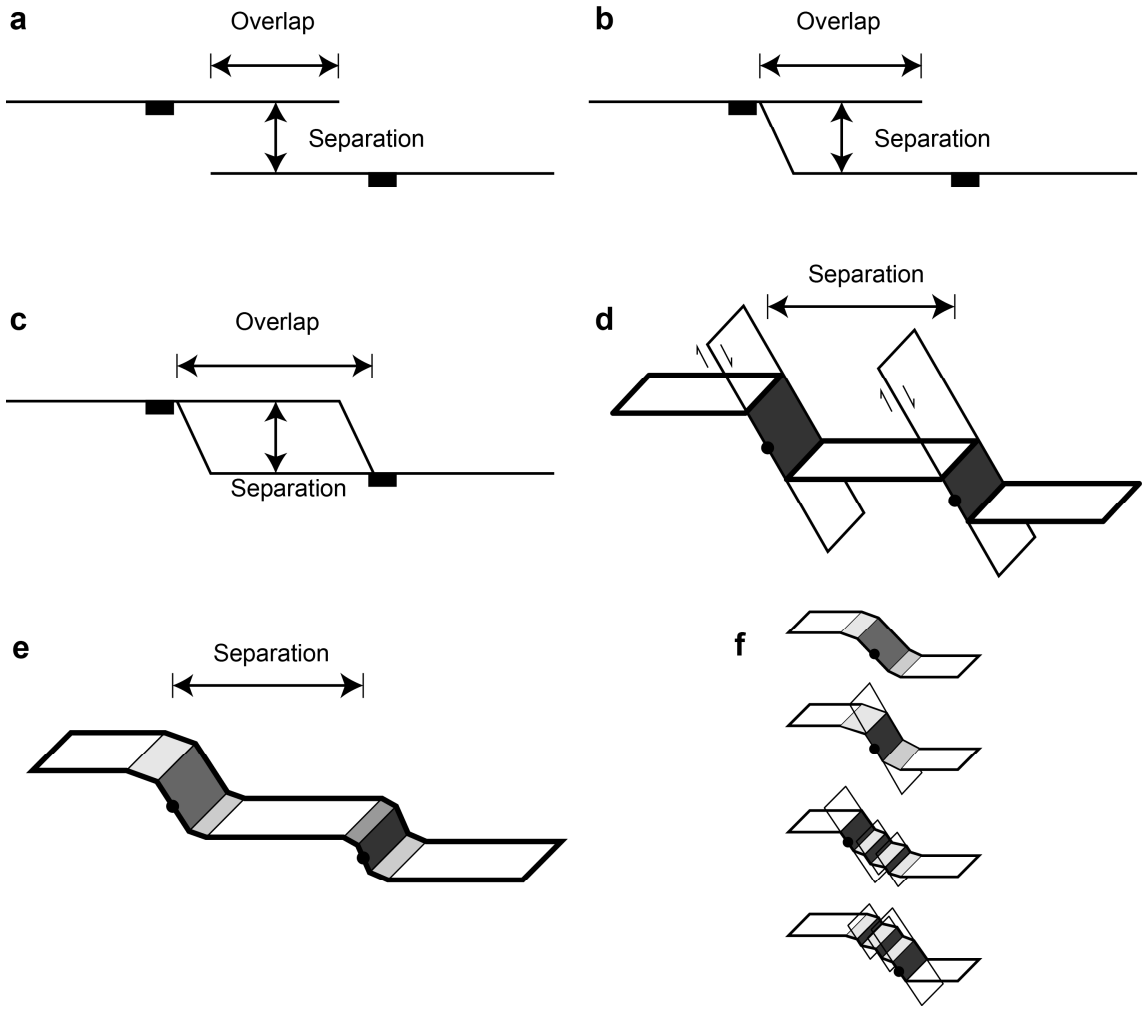

Fig. 5.1. (a) A schematic depiction of a relay ramp in map view. Fault overlap is measured between the two overlapping fault tips and separation is the distance between the two fault segments measured from the centre of the relay ramp. Relay zone Aspect Ratio (AR) = Overlap/Separation. (b) A linked relay ramp (**Fig. 5.2**b). Overlap length is measured between the BP and the fault tip. (c) A fully breached relay ramp (**Fig. 5.2**c). Overlap length is measured between the two BP. (d) In detail, faults have a component of heave and the separation distance is thus measured from the centre of the fault polygons. (e) When a relay ramp consists of two laterally continuous FNR highs (i.e. monoclines) the separation distance is measured to the centre of the laterally continuous FNR with the largest measured offset. (f) Laterally continuous FNR highs from seismic data for a single fault segments could results from any of the presented interpretations, each with a different location to which separation should be measured (black circle).

Fault tip line geometries and thus relay zone geometries can be modified by the stratigraphy in which they form, and especially by mechanical boundaries between lithological layers (Nicol et al., 1996; Wilkins and Gross, 2002). In mechanically layered sequences, faults often initiate within the more competent layer (Peacock and Sanderson, 1991; Schöpfer et al., 2006). Faults can be confined within mechanical layers leading to faults with low displacement-length ratios (Benedicto et al., 2003; Soliva et al., 2005).

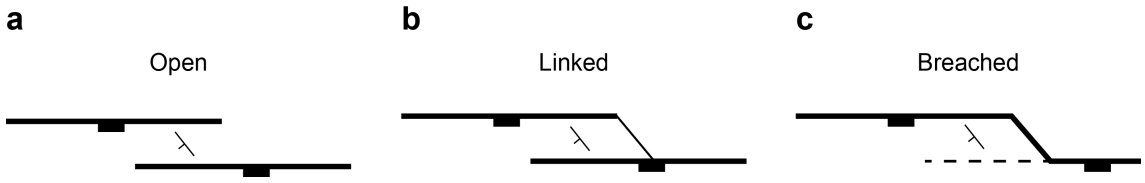

Fig. 5.2. Schematic diagrams of relay ramps illustrating the different stages of their evolution. (a) Open relay ramps are composed of overlapping segments that transfer strains through a relay ramp. (b) Faults propagate across the ramp as strains are built up between the overlapping faults. These linking faults normally initiate at fault tip but can form midway through the ramp. (c) Breached relay ramps develop when a through going slip surface is formed leaving a relict fault segments within the hanging wall or footwall.

Soliva and Benedicto, (2004) noted an increase in AR from open through linked to breached relays. However, AR alone provides little information on the stage of interaction between overlapping faults (Aydin and Schultz, 1990; Huggins et al., 1995; Gupta and Scholz, 2000; Soliva and Benedicto, 2004). Combining displacement distributions with AR measurements is a better indicator of fault interaction (Gupta and Scholz, 2000; Soliva and Benedicto, 2004). A linkage criterion was developed by Soliva and Benedicto, (2004), which states that for a given relay separation (**Fig. 5.1**) increased displacement will lead to more evolved linkage geometries (**Fig. 5.2**). A model of fault interactions was proposed by Gupta and Scholz, (2000), which is based on the interaction between a fault tip with and the stress drop region around a nearby fault (**Fig. 5.3**). This model of fault interaction gives a mechanism for producing the self-similar relay ramp AR observed from outcrop to seismic-scales (Soliva et al., 2006; Soliva et al., 2008; Favreau and Wolf, 2009). For, the horizontal extent of the stress drop region around a fault increases with increased displacement, which, in general, increases proportionally with fault length (Walsh and Watterson, 1988; Cowie and Scholz, 1992; Gillespie et al., 1992; Dawers et al., 1993; Schlische et al., 1996; Walsh et al., 2002), except when confined within mechanical layers (Ackermann et al., 2001; Benedicto et al., 2003). See section 5.1.1 for details of Gupta and Scholz, (2000) fault interaction model.

In this chapter we aim to build an accurate database of fault relay zone measurements (AR) spanning at least six orders of magnitude from detailed outcrop studies, digital elevation models (DEM) and 3D seismic datasets. Also, where relevant, data from the literature is included (The complied relay data can be found in digital appendix 5: relay tables). Data collection errors and uncertainties will be fully discussed and we aim to

refine the database (i.e. remove scatter) to produce a representative scaling factor that characterises relay zone geometries (AR) over the studied scale range. We also aim to investigate the change in relay zone geometries with increase displacement and identify key stages in their geometric evolution. Finally, from the detailed analysis of relay zones, from different outcrop locations, we aim to build on the fault interaction model of Gupta and Scholz, (2000) by suggesting possible modifications, which can account for outcrop-specific variations in mean relay zone geometries.

5.1.1 Gupta and Scholz's (2000) fault interaction model

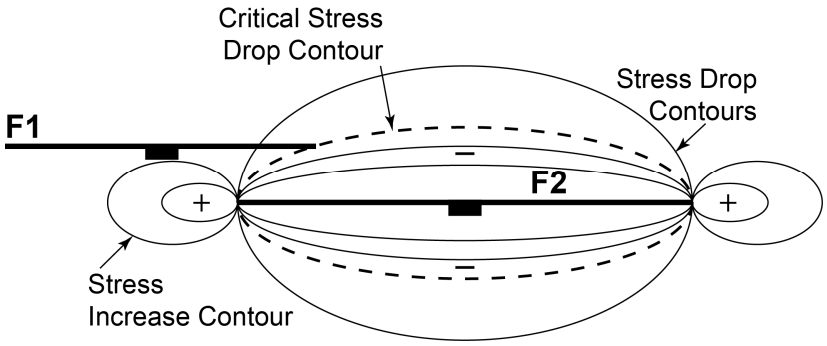

Fig. 5.3. Map view of the stress field around fault F2 and its interaction with the propagating tip of F1. The stress field for F2 is modelled as if an isolated fault, which is taken to be a first order approximation of the stress field for the relay zone. Each fault is surrounded by a region of stress drop and stress increase near the tips. Taken from (Gupta and Scholz 2000).

When faults slip they modify the local stress field, giving rise to shear stress drops adjacent to the centres of fault segments and stress increases at their tips (**Fig. 5.3**) (Willemse et al., 1996). The distance over which the local stress field is modified is related to fault displacement, with larger displacement faults modifying the local stress field over greater distances (Gupta and Scholz, 2000). For a summary of the fault interaction model and the maths behind it, see appendix 4.

To calculate the shear stress drop region around a fault Gupta and Scholz, (2000) assume an elastic displacement field to exist at the time of faulting. This is supported by observations of stress shadow zones around faults, which are equated to displacement fields, into which faults do not propagate or nucleate (Ackermann and Schlische, 1997). The stress shadow is also demonstrated by elastic boundary element models (Gupta and Scholz, 1998). Both of these supporting studies are based on the same faults in the Solite Quarry used by Gupta and Scholz, (2000) to develop their

model of fault interaction. Gupta and Scholz, (2000) used an elastic model with a vertical dislocation to calculate displacement fields around faults. It is assumed that the elastic stresses do not relax between periods of fault growth, despite the large strains and time scales associated with faulting, and therefore, from the net displacement on a fault segment they calculated net static stress drop.

Gupta and Scholz, (2000) used the two-dimensional (2D) solution for a deflected horizontal surface due to a vertical screw dislocation from Contreras et al., (1997), modified to incorporate changes in slip and depth. Fault planes are represented as rectangles with uniform d-x distributions with depth, however true slip distributions on faults do vary with depth and are better represented by a elliptical fault with displacement approaching zero at their tips (Barnett et al., 1987). Therefore, to counteract the overestimate of the stress field the inputted fault height is half the actual value. From the deflected horizontal surface the shear strain is calculated and combined with the shear modules of that surface, from which the stress drop region can be calculated. Gupta and Scholz, (2000) assumes the stress distributions around an isolated fault to be a first-order approximations of the stress fields around two interacting faults (**Fig. 5.3**), even though the stress fields can be quite perturbed around relay zones (Segall and Pollard, 1980; Crider and Pollard, 1998a). They also only consider the shear stress changes induced on a fault (F1) by slip on a nearby fault (F2) (**Fig. 5.3**).

The fault propagation and interaction model of Gupta and Scholz, (2000) is summarised by the propagation criterion:

$$\sigma_{p(F1)} = \sigma_y + \Delta\sigma_{(F2)} \qquad \textbf{(Eq.1)}$$

Where $\sigma_{p(F1)}$ is the peak stress for fault F1 (**Fig. 5.3**), σ_y is the material yield strength and $\Delta\sigma_{(F2)}$ is the induced shear stress drop caused by fault F2 (**Fig. 5.3**). Therefore, for a mode III fault tip to propagate within a region of low shear stress (**Fig. 5.3**), the stress concentrations at the tip must increase to balance the stress drop and the material yield strength (Gupta and Scholz, 2000). At a crack tip material deforms plastically, while ahead of the tip material deforms elastically. Gupta and Scholz, (2000) note that

for an isolated fault the elastic-plastic Dugdale model requires the stress concentrations at a fault tip to equal the yield stress (Cowie and Scholz, 1992). For details see appendix 4.

Fault propagation is therefore enhanced or hindered by the stress fields of nearby faults, as observed by (Aydin and Schultz, 1990). According to (**Eq. 1**), fault tips within the stress increase region will grow towards each other facilitating fault overlap. In contrast, fault tip propagation within the stress drop region will be hindered. In order that fault F1 continues to propagate within the stress drop region (**Fig. 5.3**), stress concentrations at the fault tip need to increase, which can be achieved by increasing fault displacement gradients, which are commonly observed on overlapping faults in relay zones (Walsh and Watterson, 1989; Huggins et al., 1995; Nicol et al., 1996; Ferrill and Morris, 2001). For a given fault separation, fault segment size, and material properties of the host rock, there is a critical stress drop contour, located within the stress drop region of the adjacent fault (**Fig. 5.3**), through which an overlapping fault does not propagate (Gupta and Scholz, 2000). The location of the critical stress drop contour also coincides with the boundary of the stress shadow region outlined in (Ackermann and Schlische, 1997). The interaction between the propagating fault tip and the critical stress drop contour limits the overlap length of the relay zone thus controlling their aspect ratio (AR). Once a relay zone is laterally pinned continued displacement increases strains within the ramp and linking faults begin to form (**Fig. 5.2**).

5.2 Background geology

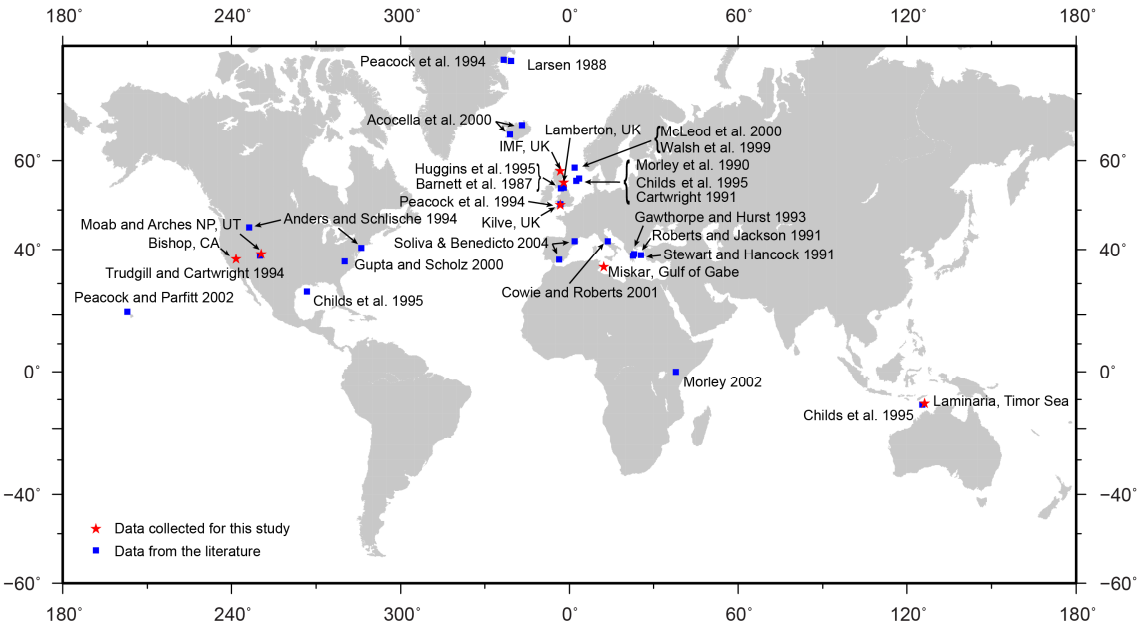

Fig. 5.4. Location map of all data sources used in this study. All the data comes from extensional terrains and are recorded in the digital appendix 5: relay tables: 1 and 2.

In this chapter, data from original research locations are combined with studies from previous chapters and literature examples (**Fig. 5.4**). Background information on locations already mentioned in this thesis can be found in the original chapter where they were first presented. For datasets not previously mentioned a brief geological overview is given.

5.2.1 Kilve and Lilstock, Somerset, UK

Kilve and Lilstock are located on a 7 km long stretch of the Somerset coast (**Fig. 5.5**). For a detailed location map see appendix 3: (**Fig. A10** and **Fig. A13**). The lithologies and tectonic histories for each location are similar due to their close proximity. The stratigraphy consists of alternating Lower Jurassic limestone and shale beds, with the thicknesses of the limestone beds ranging from 5 cm to 1 m and the shale beds from 5 cm to 5 m (**Fig. 5.6**). Faults studied trend E-W and are probably related to the opening of the Bristol Channel basin during the Mesozoic (Peacock and Sanderson, 1994: and references therein). Reverse and strike-slip reactivation of structures in the Bristol Channel occurred during the Late Cretaceous or Tertiary (Brooks et al., 1988; Peacock

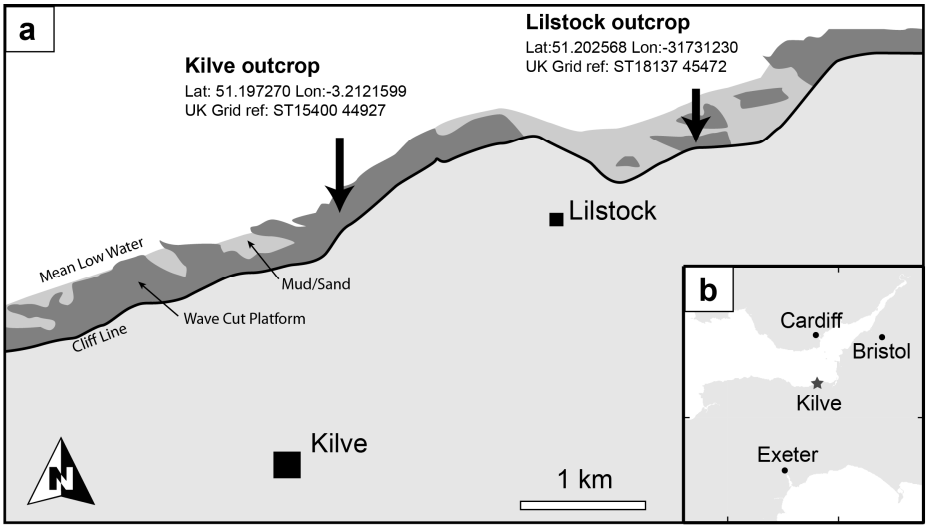

Fig. 5.5. (a) Outcrop locations from Kilve and Lilstock. (b) Location of Kilve in the UK.

and Sanderson, 1992). However, none of the faults used in this study show signs of strike-slip or reverse reactivation. The average separation distance of fault relay ramps is 43 cm (Digital appendix 5: Relay table 1), and the studied faults have an average throw/displacement of 20 cm. Published displacement/length ratios from Kilve approximate range from 0.01 to 0.1 (Peacock and Sanderson, 1991).

The mechanical layering at Kilve and Lilstock has a strong affect on the distribution of deformation (**Fig. 5.6**). Veins form initially in the more competent limestone beds and with continued extension faults grow within the veins forming pull-apart structures (Peacock and Sanderson, 1991, 1992). Fault tips are observed to terminate along-strike into veins that trend E-W, with the veins forming prior to the faulting (see appendix 3: **Fig. A14**) (Crider and Peacock, 2004). Fault tip lines propagating through a mechanically layered sequence can be pinned below a relatively weak layer, such as shale, which can lead to the development of fault propagation folding (Ferrill et al., 2007; Ferrill and Morris, 2008). In (**Fig. 5.6**) directly below the thick shale layers (Shale: A), the limestone bed (1) displays greater continuous rotations compared to bed (2 – 3) with similar offsets. Therefore, depending on the interaction between faults and the different mechanical layers, the distribution of deformation, on a single fault, can change markedly over relatively short vertical distances (**Fig. 5.6**).

The data was collected using traditional field techniques and Terrestrial Laser Scanning (TLS) methods. From the detailed TLS point cloud high resolution horizon surfaces

where created, from which the Fault Normal Rotation (FNR) can be calculated (See Chapter: 2 for details on data collection methods).

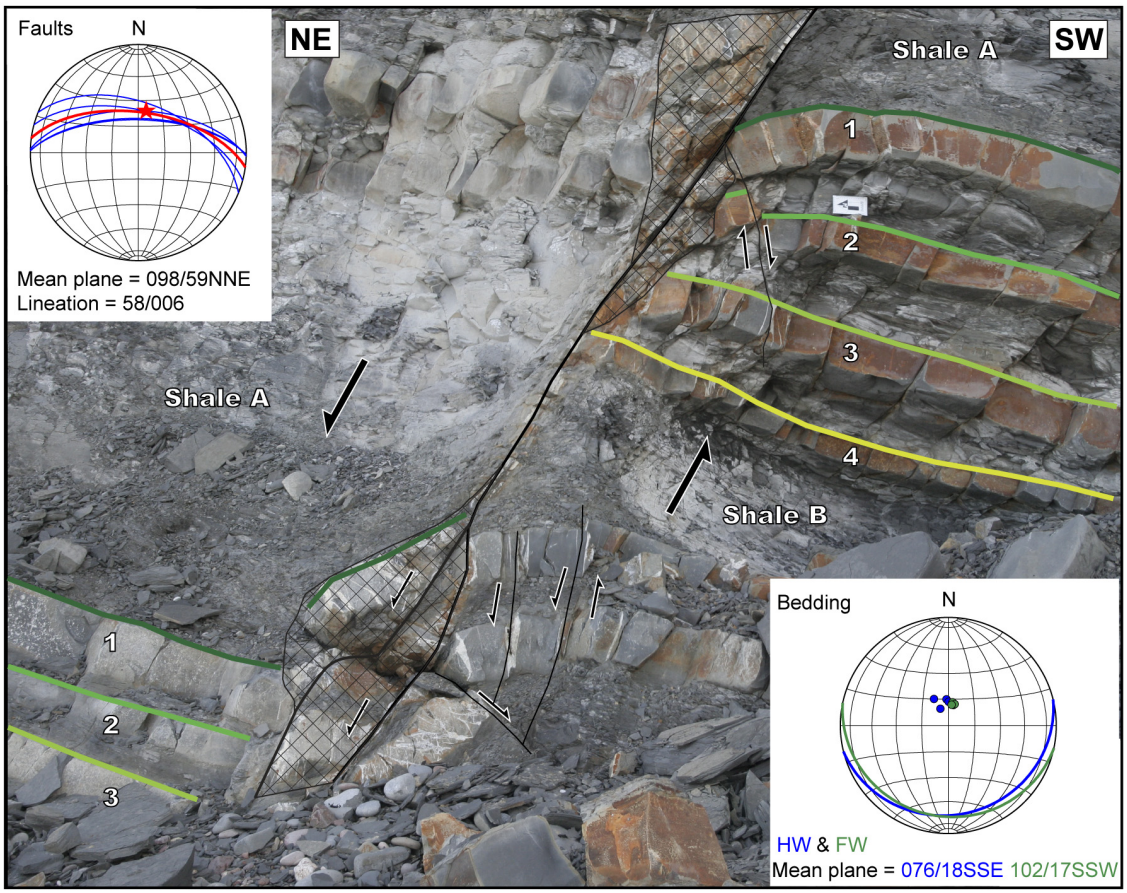

Fig. 5.6. Photographic cross-section of a fault from Kilve. Inset top left, fault are orientated approximately E-W dipping 59 degrees to the north. Offset across the fault is approximately 2.4 meters. Hatch areas are zones of intense deformation close to the fault. Deformation in the footwall is variable down-dip. Bed (1) has rotation towards the hanging wall, while bed (4) has no fault-related bed rotations. In the hanging wall there is little bed rotations on beds (1-3) and bed (4) is not observed. The stratigraphy consists of alternating limestone and shale beds. Inset bottom right, bedding data from the footwall and hanging wall measured ~1 m away from the fault.

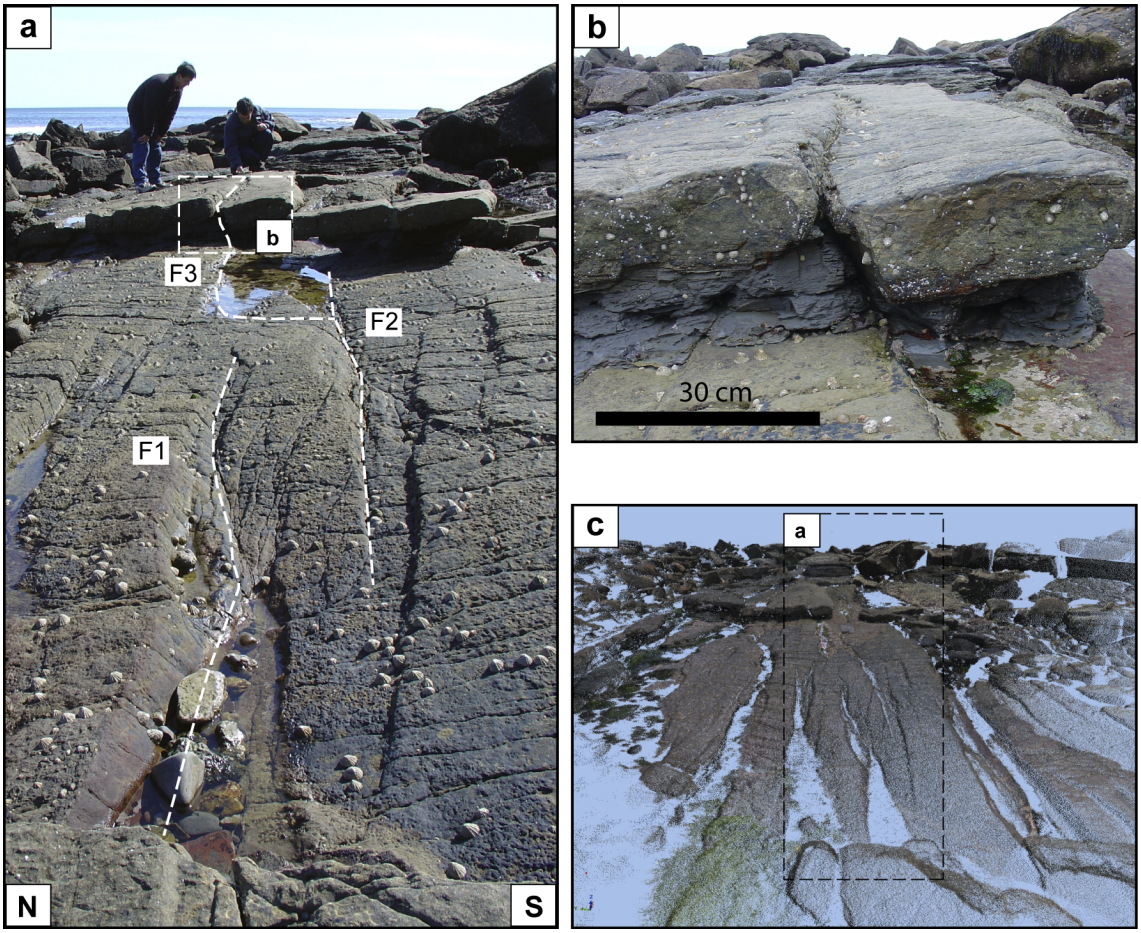

Fig. 5.7. (a) Overview photo of the Lamberton wave-cut-platform looking along-strike of the main fault trend. Faults and relay ramps are recorded in the exposed sandstone beds. Faults F1-F3 are the same as in (**Fig. 5.8**). (b) Cross-section through the faulted sandstone shale sequence. (c) Laser scan image of the Lamberton foreshore used to create detailed elevation surfaces in (**Fig. 5.8**).

5.2.2 Lamberton, Berwickshire, Scotland

The study area is located on the shallowly-dipping east limb of the N-S trending Berwick monocline (Shiells, 1964). Normal faults cut both limbs of the kilometre-scale monocline and are either synchronous with or post date the folding. The studied faults strike E-W and are exposed on a series of flat-lying sandstone beds with offsets less than 20 cm (**Fig. 5.7** and **Fig. 5.8**). For a detailed location map with nearby geological structures for context, see appendix 3: **Fig. A15**. The faults have not been reactivated and all the faults are dip-slip. The average separation distance of fault relay ramps is 12 cm (Digital appendix 5: Relay table 1) and faults have an average throw/displacement of 10 cm (**Fig. 5.8**). The stratigraphy consists of Carboniferous age, interbedded sandstone and shale beds. The faults terminate upwards into a thick shale sequence that overlies the studied stratigraphic section (**Fig. 5.9**). The faults initiate within the

more competent sandstone beds and have a mean displacement/length ratios of 0.07, which is fairly low when compared to global datasets that range from 0.01 to 1 (Kim and Sanderson, 2005). Similar to Kilve and Lilstock, the data was collected using traditional field techniques and detailed TLS workflows (**Fig. 5.7**c) (Jones et al., 2008).

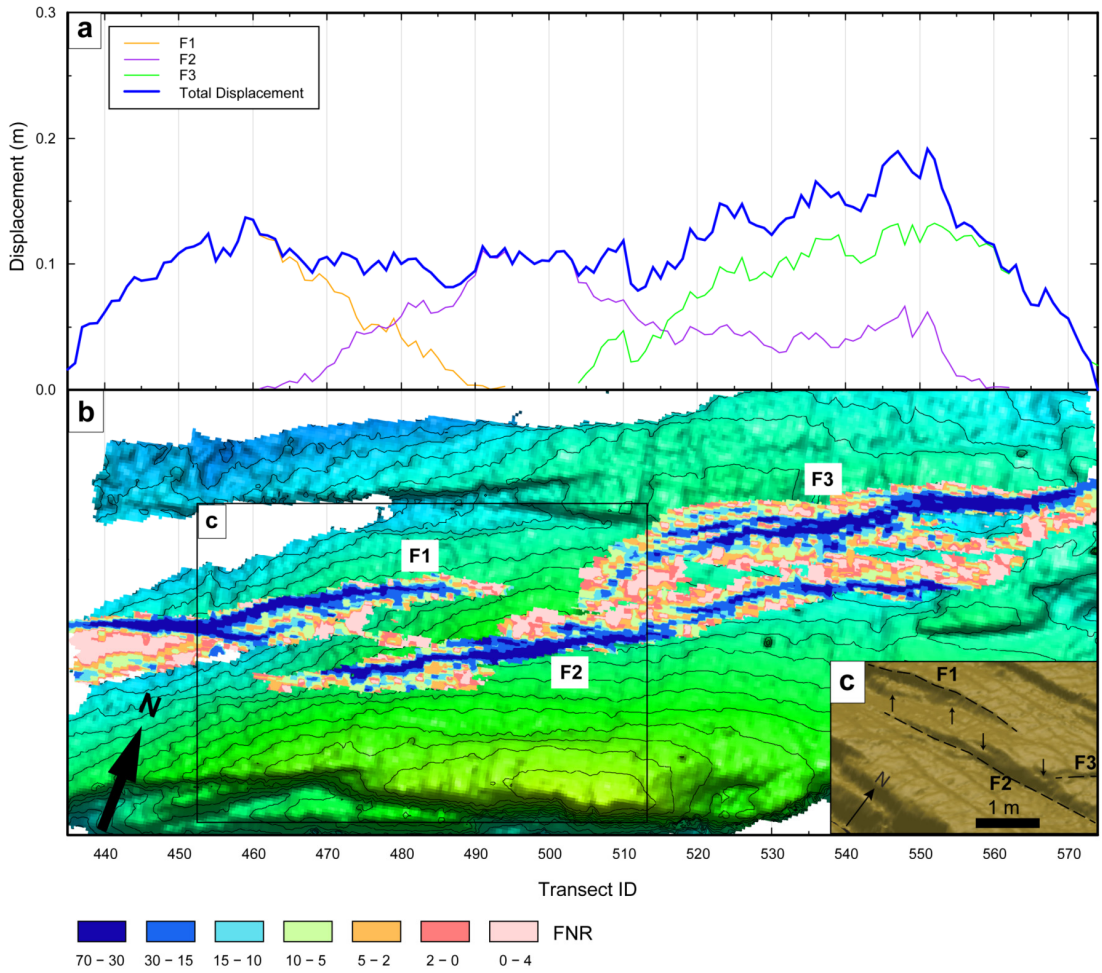

Fig. 5.8. (a) Displacement distance plot from regions of contoured FNR, located in map view on (b). The total d-x profile resembles that of a single fault, it includes areas of continuous bed rotations around the mapped faults and along-strike of mapped fault tips. Low wavelength spike in the d-x profiles relate to erosion features and organic material on the wave-cut-platform (See **Fig. 5.7**). (b) A contoured elevation surface of sandstone bed (C) from Lamberton (See **Fig. 5.7**). Two relatively large relay ramps are selected between faults F1-F2 and F2-F3. Relay ramp F1-F2 is open and relay ramp F2-F3 is linked at the E to SE end. (c) The main fault traces F1-F3 (dashed lines) are composed of many smaller relay ramps (arrows).

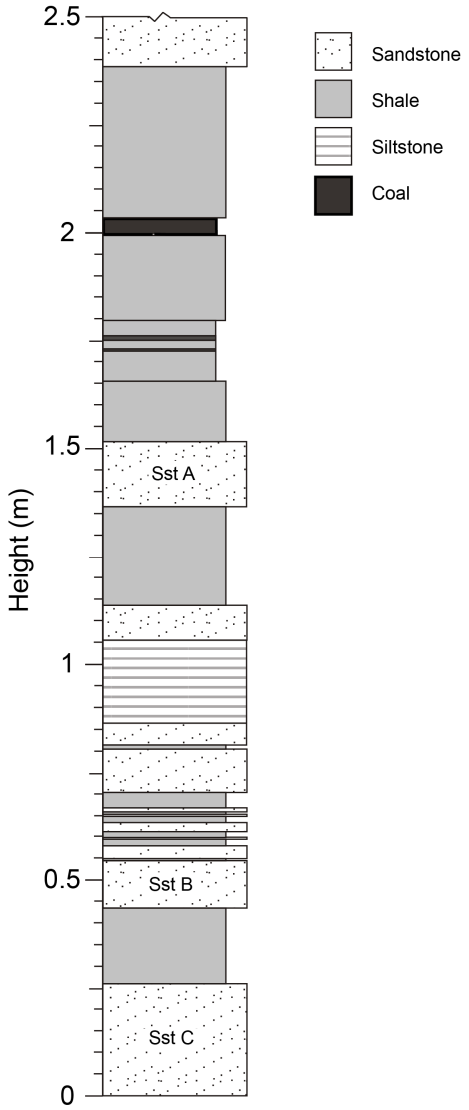

Fig. 5.9. Stratigraphic log from Lamberton, UK. Faulting is locally capped by the thick shale sequence above bed (A).

5.3 Sampling related errors

Relay zones are commonly described in terms of their overlap and separation (**Fig. 5.1**a-c) (Aydin and Schultz, 1990; Huggins et al., 1995; Acocella et al., 2000; Gupta and Scholz, 2000; Soliva and Benedicto, 2004). We now aim to outline and discuss sources of error and uncertainties pertaining to the measurement of fault overlap length and fault separation. In the context of this chapter, uncertainty in the data occurs when multiple interpretations can be drawn from the same data and the correct interpretation cannot be ascertained. Erroneous relay zone measurements are those that incorrectly record a relay zone AR due to sampling related inaccuracies. For, errors

due to the incorrect or biased sampling of the population tell us nothing about fault relay zones and only act to obscure any underlying geological trends, which are the primary interest of this chapter.

5.3.1 Measuring fault overlap length

Fault relay zone overlap is defined as the length between the two overlapping fault tips and is effectively measuring the length of the relay ramp (**Fig. 5.1**a). In linked relay ramps overlap length is measured from the branch point (BP) to the fault tip (**Fig. 5.1**b), or BP to BP (**Fig. 5.1**c). Measuring overlap length is thus dependant on correctly locating fault tips and BP. BP are the intersections between two faults and in comparison to fault tips are relatively easy to locate. For, displacements at BP are relatively high compared to fault tips, which taper out to zero. Therefore, in datasets which have limited vertical and horizontal resolutions, such as 3D seismic data, the errors in locating the fault tips will be greater than those for locating the BP. We thus concentrate further discussion on correctly identifying the location of the fault tips. The errors and uncertainties associated with defining fault tips will vary depending on what technique is used to image the bounding faults. For, in outcrops fault tips can be studied unhindered by errors linked to imaging resolution, whereas in seismic data there is an inherent resolution limit below which discrete fault geometries cannot be visualised (Steen et al., 1998; Townsend et al., 1998). Therefore, outcrop data is used to develop criteria for identifying the location of fault tips, which can then be applied to seismic interpretations.

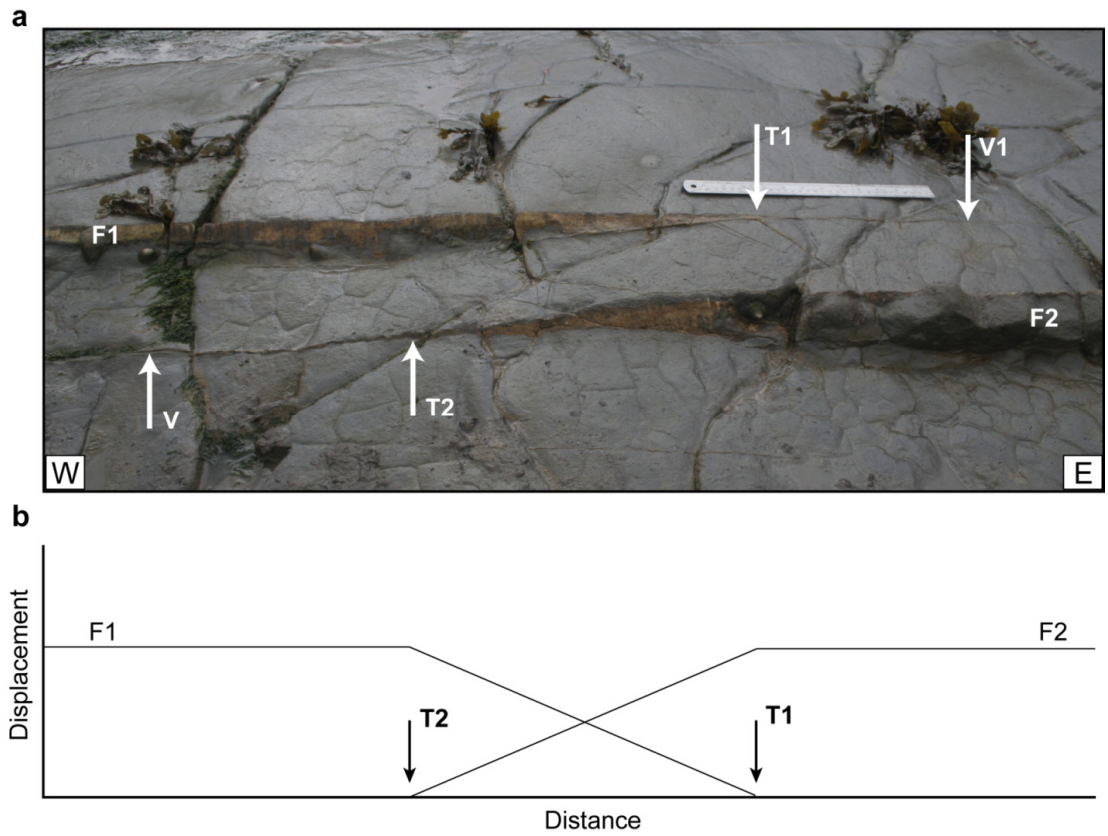

Fig. 5.10. A field photo from Kilve of a "*simple*" relay ramp that resembles the schematic depiction of a relay ramp in (**Fig. 5.1**a). Fault tips for faults F1 and F2 are annotated. Veins are located along-strike of the fault tips, annotated V. (b) A schematic displacement-distance plot for faults F1 and F2 (a). Fault tips are located at the point where displacement of the fault decreases to zero.

5.3.1.1 Criteria for locating the fault tip

A *simple* relay zone (i.e. a relay zone that resembles basic schematic models, see **Fig. 5.1**a) consists of two planar overlapping fault segments with fault tips located at the points at which throw on the faults reaches zero (**Fig. 5.10**). However, as faults increase in size their fault tips are observed to be composed of multiple segments and/or zones of wide spread continuous rotation, i.e. monoclines (**Fig. 5.11** and **Fig. 2.14**) (Cartwright and Mansfield, 1998).

Fault tip regions can have markedly different geometries between faults in the same outcrop (**Fig. 5.10**, **Fig. 5.11**, and **Fig. 2.12**), and even more so, between faults from different outcrops and scales (**Fig. 2.12**, **Fig. 2.14**, and **Fig. 2.18**) (Cartwright and Mansfield, 1998). For that reason, a fault tip is located using the total d-x profile and is

the point at which displacement decreases to zero (**Fig. 2.15**). Along-strike variations in total vertical displacement (including fault normal rotation) can be measured in both seismic and outcrop data, which allows consistency in locating fault tips at different locations and scales. Total d-x profiles are the sum of all offsets on structures associated to that fault-array and include both continuous and discontinuous deformation structures. At the centre of a fault segment displacement is typically localised on a single connected slip surface. In contrast, at low displacements sections of a geometrically coherent fault-array, such as fault tips, displacement can be taken up on multiples soft-linked fault segments and/or monoclines. The amount of continuous deformation at a fault tip will depend on many factor such as, the size of the fault, the relative location of the fault tip line (see chapter 3 and discussion therein), and the interaction between a propagating fault and different mechanical layers (**Fig. 5.6**) (Ferrill and Morris, 2008).

An example of an outcrop-scale fault termination is shown in (**Fig. 5.11**). The fault trends E-W dipping to the north and intersects the cliff line at (**Fig. 5.6**), with a maximum observed offset of 2.5 m (**Fig. 5.12**). In cross-section (**Fig. 5.6**), in the footwall, the distribution of deformation changes from beds (1 to 4). Bed (1), which is below a 2 m thick shale layer, has an 80 cm wide zone of continuous rotation stretching back into the footwall. Bed (2) displays similar continuous rotations as bed (1) but is faulted close to the main fault trace. Beds (3) and (4) have little to no continuous rotations but have a high density of factures and veins within 80 cm of the main fault trace. In comparison, the hanging wall beds are relatively flat lying close to the fault (**Fig. 5.6**). In map view (**Fig. 5.11** and **Fig. 5.12**), the fault passes laterally into a monocline. Bed rotations are facilitated by surrounding shale layers and wedge shaped veins (**Fig. 5.11**b). Veining becomes wider as rotations increase towards the centre of the fault, i.e. eastwards (**Fig. 5.11**c-e). Despite the presence of a monocline at the fault tip the total vertical displacement (throw) calculated from the monocline displays a monotonic decrease towards the west (**Fig. 5.12**c), indicating it is a coherent part of the fault trace. From the cliff section (**Fig. 5.6**), it is inferred that the along-strike termination of the fault on beds (3) or (4) would not be characterised by a monocline,

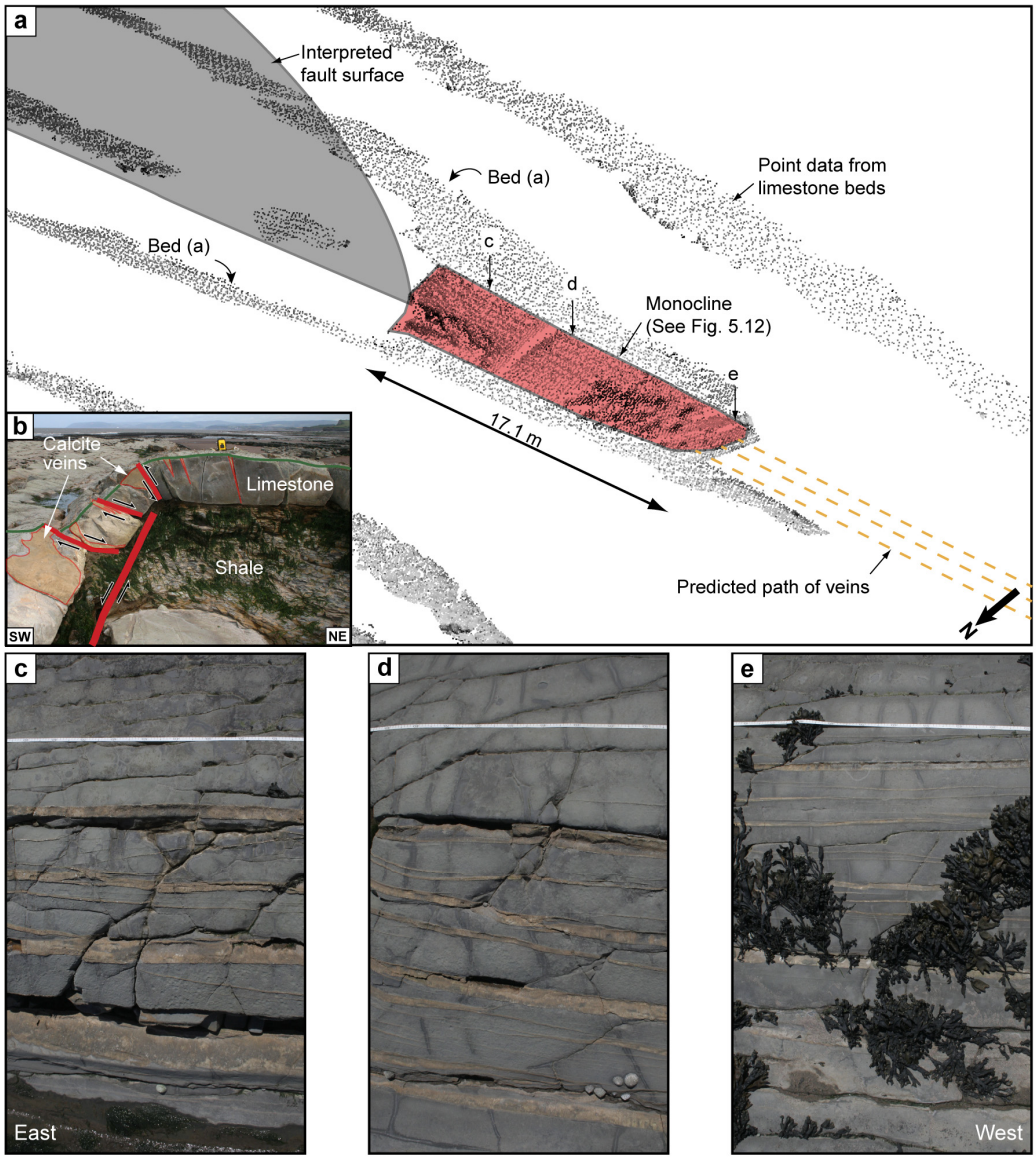

Fig. 5.11. (a) An overview of a fault termination from the wave-cut-platform at Kilve. Point data from the limestone bed tops are shown. A cross-section through this fault is in (**Fig. 5.6**). The interpreted fault surface changes laterally into an area of continuous bed rotation 17.1 m long, i.e. a monocline. (b) A cross-section through a different monocline at Kilve which illustrate how bed rotations are accommodated by wedge shaped veins and minor faults. (c-e) A series of photos of the monocline looking vertically downwards, their relative locations are annotated in (a). All photos are about 1 m wide. (c) Veins have relatively large heaves compared to (e) and offsets are visible in the north of the monocline. (d) No offsets are visible and rotations are accommodated by vein heave. (e) Rotations across the monocline are minimal and the veins are narrow but laterally continuous. The veins are predicted to continue along-strike into areas of no exposure, yellow lines in (a).

due to the lack of an overlying mechanically weak layer to facilitate the development of a fault propagation fold (i.e. a monocline).

Another example of a structurally complex fault tip comes from the Arches relay ramp, which is a seismic-scale structure (**Fig. 2.15**). The bounding faults are hosted within a

thick sandstone unit and have a maximum observed throw of around 50 m. The exposed fault tip on F1 is characterised by a ~100 m wide zone of deformation consisting of low offset secondary faults, deformation bands and continuous bed rotations toward the mutual hanging wall. As with the previous example (**Fig. 5.12**), when the vertical component of displacement is summed across all structures, at the fault terminations, the d-x profile resemble that of isolated faults whereby displacements decrease gradually to zero (**Fig. 2.15**). Therefore, including continuous deformation in the volumes surrounding discrete faults result in d-x profiles that better resemble those of single idealised faults where displacements decrease to zero at the fault tips (**Fig. 5.10**b). This indicates that continuous deformation and/or secondary fault segments located at the termination of a fault are geometrically coherent parts of the fault-array and should be included in the measurement of fault overlap length.

5.3.1.2 Measuring fault length in field data

The errors associated with measuring relay ramps in outcrop are related to the tools used to measure them and the accuracy and precision of that tool. Most traditional field measurements are based on 1D analysis i.e. measuring throws between the hanging wall and footwall in cross-section using a ruler. However, this type of analysis does not allow accurate measurements of continuous bed rotations, i.e. FNR. For, even at outcrop-scales there are continuous rotations around faults in the form of monoclines and fault drag, which are necessary to accommodate the displacement field around faults (Barnett et al., 1987). To record these continuous rotations we used a Terrestrial Laser Scanner (TLS) (See chapter: 2). Using high resolution scan data enabled greater detail to be observed at fault tips, thus increasing the measured fault length (**Fig. 5.12**). However, laser scanning can only be applied in certain settings (See Chapter 2). In areas with no TLS data, where possible, the continuous deformation around fault tips was included in measurements of fault length by visual inspection of bed rotations. (See digital appendix 5: Relay table 1, column “Data Type”).

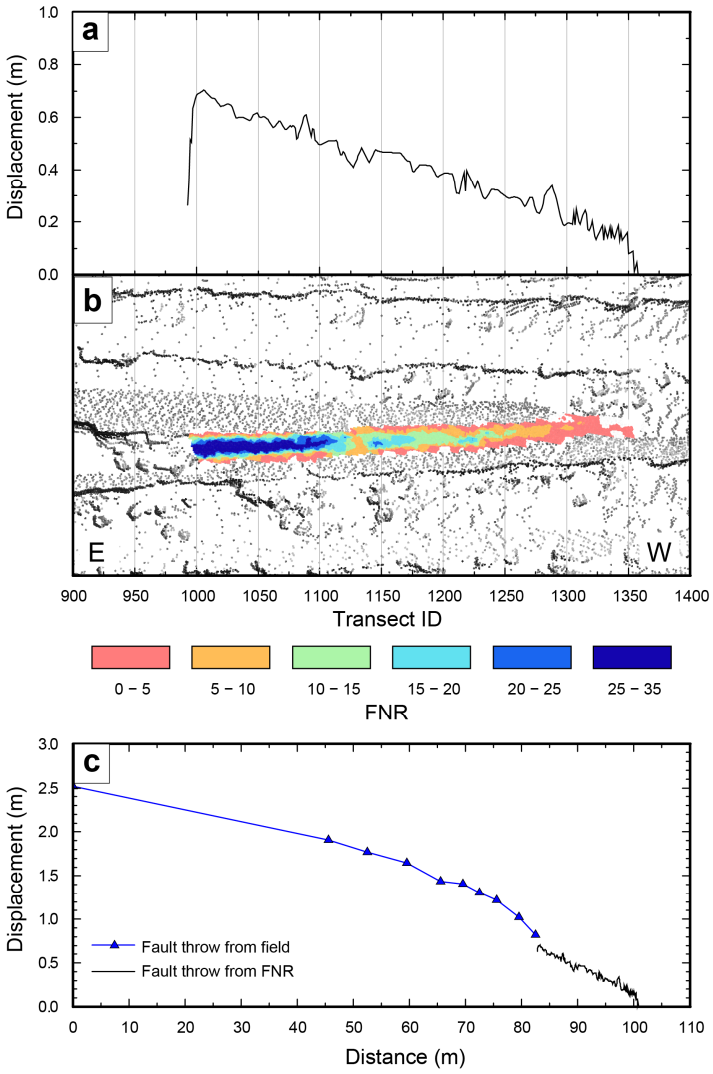

Fig. 5.12. (a) Displacement distance plot across the monocline in (**Fig. 5.11**). Displacement decreases steadily towards the west. The west end of the monocline is covered by sand. (b) Distribution of FNR at the tip of the fault, from which (a) is calculated. Point data is from the TLS of the Kilve foreshore, from which detailed distributions of FNR is calculated. (c) A d-x plot with fault throw recorded from the field and displacement measured across the monocline (a and b). Despite the change from fault to monocline, displacement decreases continuously towards the west.

5.3.1.3 Measuring fault length by remote sensing

Using the criteria developed in outcrop data (Section 5.3.1.1), fault tips can be composed of segmented fault strands and/or continuous deformation structures, such as monoclines. The fault tip is therefore defined as the point where the summed displacements across all fault-related structures in a fault-array decrease to zero. In seismic data the unique distribution of deformation at a fault tip is masked by its inherent resolution limits (Steen et al., 1998; Townsend et al., 1998). However, the developed criteria can still be applied to seismic data and fault tips can be located at

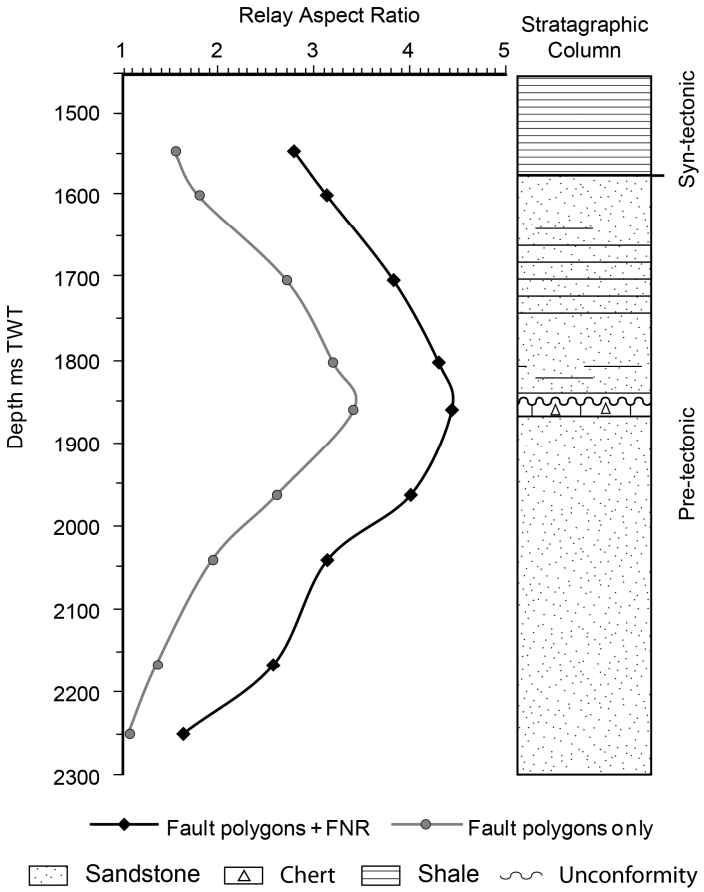

Fig. 5.13. AR plotted against depth for a single relay zone (IMF R1) from the IMF 3D seismic dataset. For the light grey profile relay overlap and separation is measured using only discontinuous fault offsets, i.e. breaks in the seismic signal. The dark grey profile includes the area of FNR around the mapped faults in measurements of AR. The geometry of the relay zone is depicted in (**Fig. 3.9**). The difference in measured AR between the two profiles is approximately 1.1 for each horizon. The largest ARs are found towards the centre of the relay zone and the upper section of the relay zone (above 170 ms) has elevated ARs compared to the lower section of the relay (below 2000 ms).

the point where the total d-x profile, for areas of fault-related deformation, decreases to zero. In comparison, in the literature, the locations of fault tips in seismic data are determined by simply extrapolating throw profiles to zero (Nicol et al., 1996). Our method for locating fault tips improves on this previous technique for two main reasons. Firstly, displacements are directly measure to zero, which captures potential along-strike variations in lateral displacements and displacement gradients. And secondly, FNR can occur along the entire length of the fault and in all previous chapters it has been demonstrated that FNR is a coherent part of the fault-array and should be added to the throw profile to get a new, more representative, total d-x profile. Therefore, simply extrapolating throw profiles to zero would underestimate the length of faults.

In chapter 3 it was shown that the mapped fault tip lines of faults F1 and F2 pass laterally into the areas of high FNR (**Fig. 3.10**). However, unlike in outcrop data these monoclines might in fact be low offset faults (**Fig. 3.1**). In the Inner Moray Firth (IMF) example we see that by adding FNR to fault length the AR of the relay zone increases on average by 1.1 at all depths (**Fig. 5.13**).

5.3.2 Measuring fault separation

Relay zone separation is defined as the distance between two overlapping fault segments measured from the centre of the relay zone (**Fig. 5.1**). There are two main sources of error in this measurement; correctly identifying the centre of the relay zone, and correctly locating the primary fault surface within a potentially wide zone of fault-related deformation. The centre of a relay zone is dependent on its length. Therefore, errors in establishing the fault overlap length will alter the location at which separation is recorded (**Fig. 5.1**). Once the overlap length is ascertained fault separation can be measured. This leaves errors associated with correctly identifying the location of the primary fault surface (i.e. the fault on which takes up the majority of displacement).

5.3.2.1 Identifying the location of the fault within a damage zone

Faults are often surrounded by a zone of deformation which can consist of lower offset faults and fractures, which is termed a damage zone (Chester et al., 1993). In chapters 2, 3, and 4 it is demonstrated that FNR surrounding mapped faults are areas of fault-related deformation and are equated to damage zones. The width of FNR (i.e. damage zone) varies along-strike and down-dip of a fault (See figures in chapters 3 to 4). The region of FNR around a fault can also be asymmetrically distributed between the hanging wall and footwall (**Fig. 2.13**, **Fig. 2.15**, and **Fig. 2.29**). The main fault trace, within a region of wide FNR, is identified as the laterally continuous structure on which the majority of the offset is accommodated. In outcrop this is often the fault scarp and its location can be directly identified, if exposure permits, and relay zone separation is measured to the centre of the mapped fault polygon (**Fig. 5.1**d). In contrast, in seismic data the exact position of the fault scarp is masked by limited lateral resolution, which is the lateral distance between two features below which they cannot be distinguished.

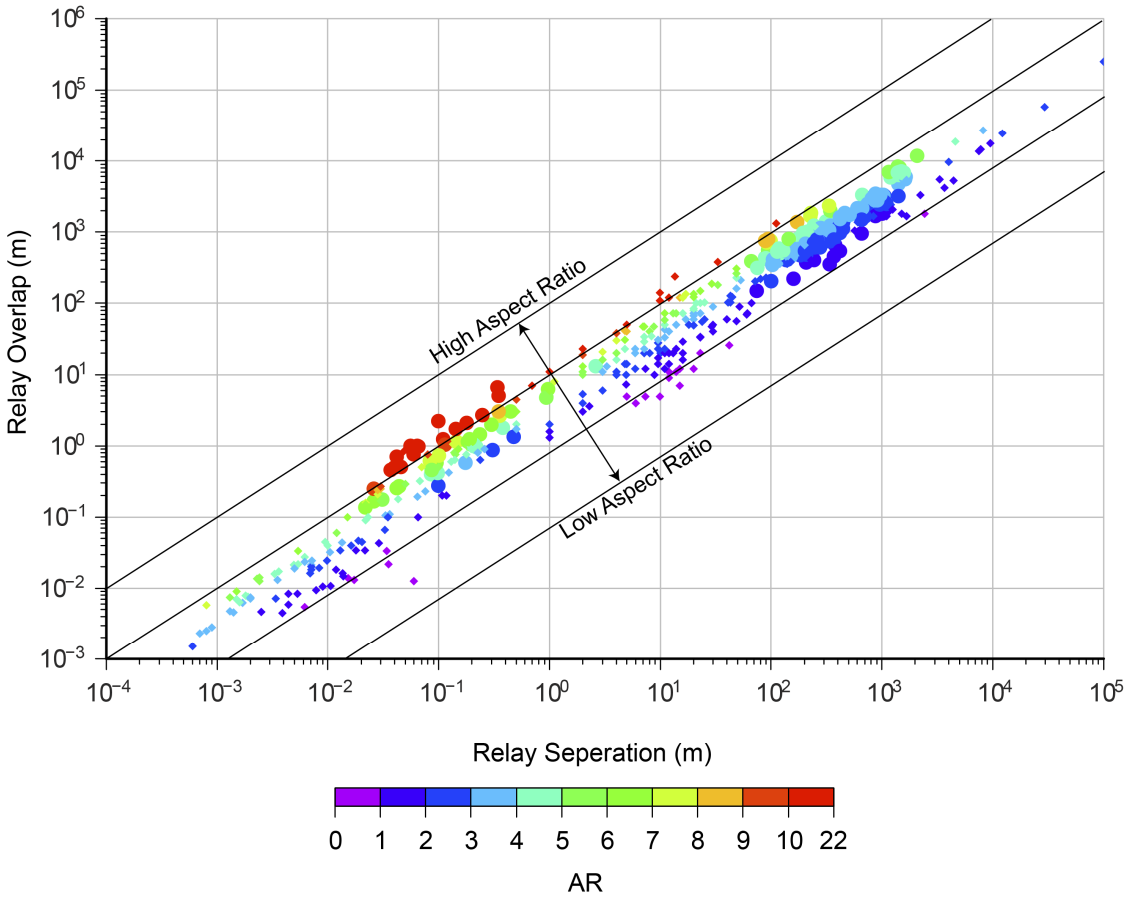

Fig. 5.14. Log log plot of relay overlap verses separation for data collected in this study (circles) and from literatures sources (diamonds). Relay ramp measurements collected in this study (circles) show higher AR (reds) at outcrop-scales (i.e. relay ramp separations < 10 m) compared to data collected from seismic datasets (i.e. relay ramps with separations > 100 m). In general, over nearly 9 orders of magnitude there is approximately an equal amount of scatter of measurements about a single power-law trend. Literature sources used in this plot are recorded in appendix 5: Relay table 2.

The lateral resolution of seismic data depends on the width of the Fresnel zone, which is dependent on the wave-length of the seismic signal and the depth of the structure being imaged (Brown, 2004). The lateral resolution thus decreases with depth. For the 3D seismic datasets used in this study, structures separated by a few tens of meters cannot be individually imaged, at depth less than 2.5 seconds TWT. Therefore the imaged locations of faults in seismic data are only ever approximations of their locations, unless directly correlated by well data.

Unique to this study is the widespread use of FNR to locate fault traces and associated fault-related deformation (i.e. damage zone). In relay zones that consist of bounding faults identified solely by FNR the fault separation is measured to the centre of the laterally continuous band of FNR with the largest measured displacement i.e. the

interpreted fault trace (**Fig. 5.1**e). However, these bands of FNR can range in width from 50 to 300 m (See figures in chapters 3 and 4). Therefore, the location of the main fault trace may not be in the centre of the FNR bands, because fault zones can be asymmetric. Measurements of fault separation could therefore be under or over estimated by an amount up to half of the width of the FNR band (**Fig. 5.1**f). At present, there are no ways to ascertain the unique distribution of faults below the resolution of seismic data and therefore these errors cannot be mitigated.

5.3.3 Relay zone AR measurements

Relay zone AR measurements from all locations and literature sources (**Fig. 5.4**) are plotted in (**Fig. 5.14**); see digital appendix 5: Relay tables 1 and 2 for details on data sources. For all the measurements, where possible, the previously discussed errors were minimised.

A general observation from data collected during this study is that the inclusion of continuous deformation (FNR) in the measurements of fault separation and overlap length has caused a shift in the best fit trend line towards greater overlap lengths, for at least 4 orders of magnitude, by a factor of 1.46 (**Fig. 5.15**). Fault separation measurements for some relay zones also changed when FNR was included. For, an increase in overlap length changed the point at which relay separation was measured (**Fig. 5.1**). From the uniform shift in the trend line in (**Fig. 5.15**) it is inferred that at all scales fault length is consistently under-sampled by a similar factor if fault-related deformations, i.e. FNR/damage zone, are not included. Including FNR counteracts this under sampling and for a relay zone with a separation of 0.5 m (outcrop-scales) overlap length increases by 1.7 m and for a separation of 500 m (seismic-scales) overlap length increases by 554.2 m (**Fig. 5.15**). Therefore, relay overlap lengths and thus relay AR, based on data collected from this study, will be larger than those of previous published studies who do not include the fault-related deformations in their measurements of fault overlap length. For instance, all relay zones collected during this study, with separations above 200 m have a mean AR of 3.3, in comparison, the mean AR for literature sources was 2.0 (See digital appendix 5: Relay tables 1 and 2).

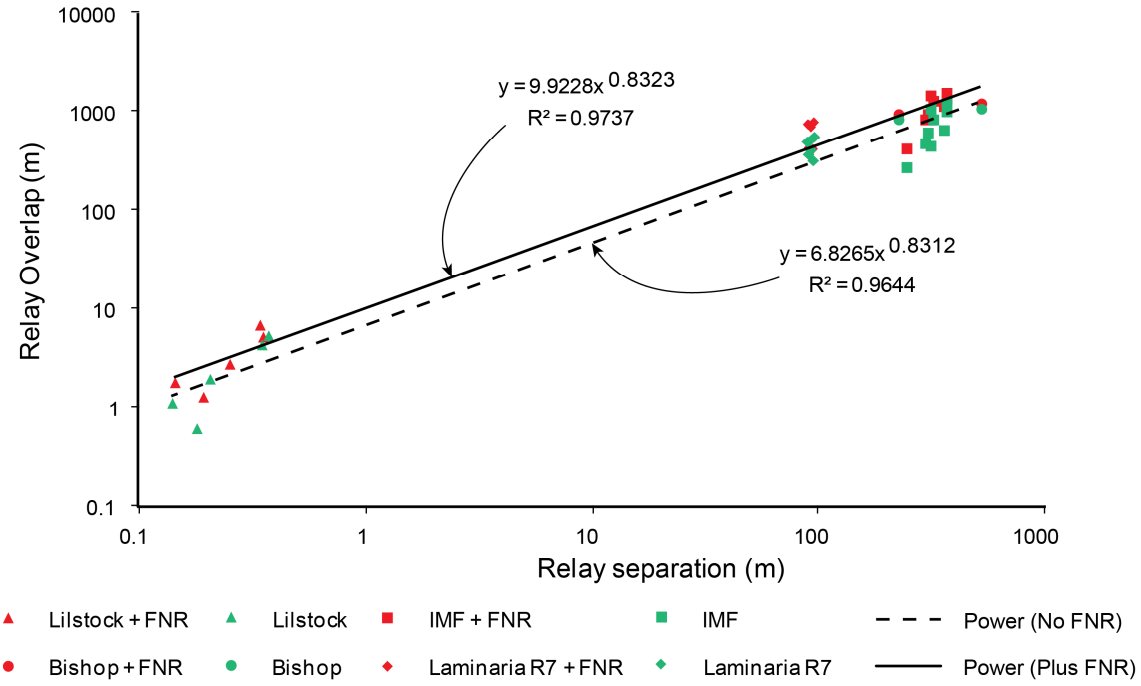

Fig. 5.15. A measurement of relay zone overlap and separation before and after FNR was included. Red points include FNR and green points, which are from the same relay zones, do not include FNR data. Relay zones from a range of scales are plotted, which were measured from both seismic and outcrop datasets. Including FNR primarily increases relay overlap length. While relay separation does change this is only due to the modified overlap length, which alters the location at which separation is measured. Including FNR increases AR measurements by a near constant factor over three orders of magnitude.

Another general observation from data collected during this study (**Fig. 5.14**: circles) is that relay zones at outcrop-scales have higher than average AR when compared to seismic-scales relays and other outcrop-scales relays from literature sources (diamonds). Possible geological controls that may account for this observed trend are identified in the next section (5.4).

5.4 Geological trends within the data

Once errors associated with measuring relay zones have been accounted for any remaining trends within the raw dataset should be a result of geological processes and mechanisms. The raw dataset comprises all recorded measurements of relay zones from this study (**Fig. 5.4**: stars), and literature sources (**Fig. 5.4**: squares).

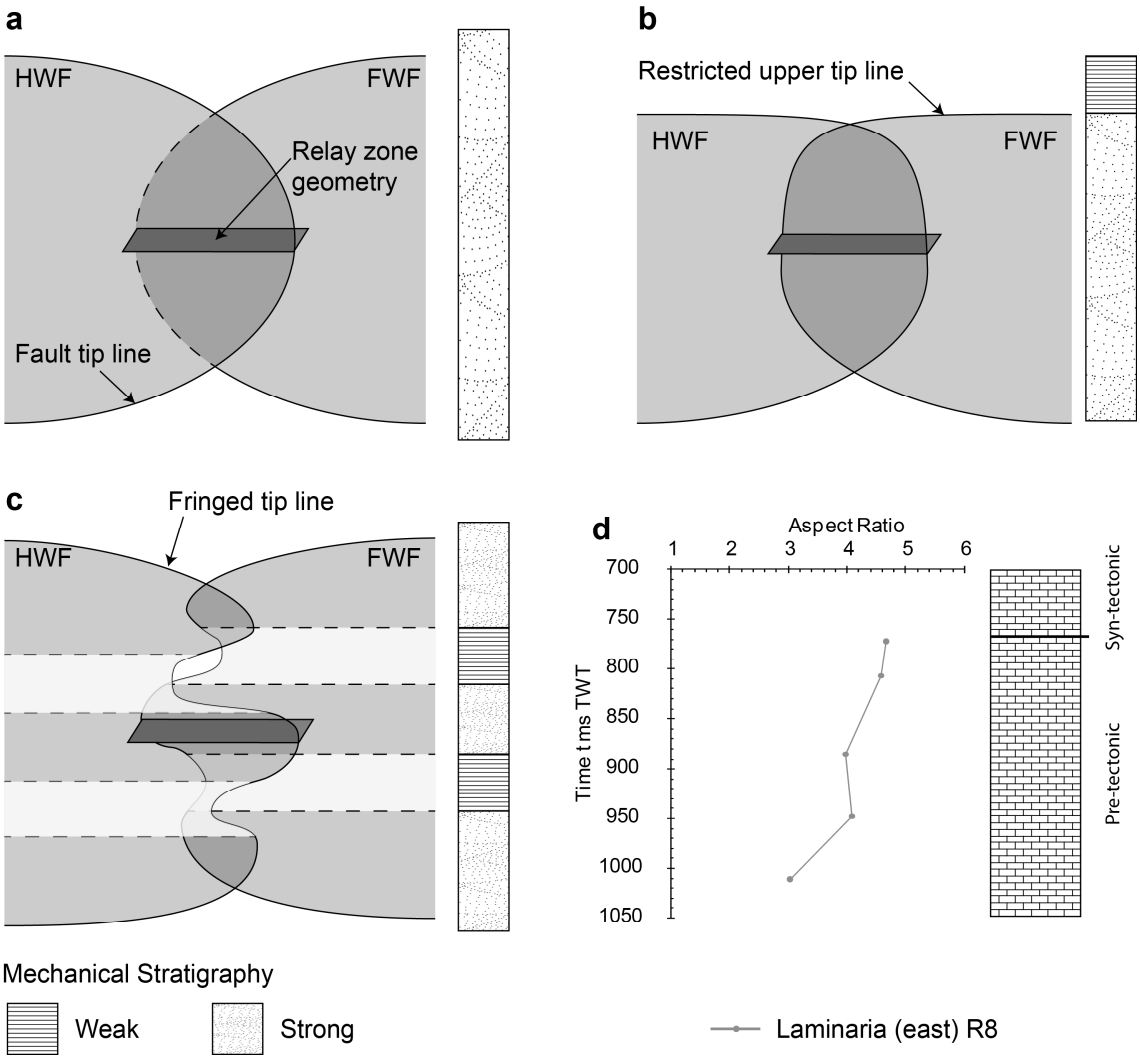

Fig. 5.16. Schematic illustrations of the interaction between fault tip lines and mechanical layers within relay zones. (a) A relay zone comprising two faults with ideal elliptical fault tip line hosted within a homogenous sequence. (b) A relay zone in which the upper tip line is modified by a weak mechanical layer, such as shale. (c) A relay zone with alternating strong and weak layers. Fault propagate more favourably in the strong layers compared to weak layers leading to fringed tip lines (Schöpfer et al., 2006). Even though the AR at the centre of the relay zones in (b) and (c) are similar to (a) the geometry of the relay zone are markedly different. (d) An example of a restricted upper tip line (b), the upper fault tip interacts with the free surface and produces a flat-topped fault (Nicol et al., 1996) and thus have elevated ARs in the upper sections of the relay zone.

5.4.1 Lithological and stratigraphical controls on fault relay zone geometries

The mechanical properties of the host rock, in which a fault propagates, control the shape of the fault. Mechanical strong (brittle) layers, like sandstones and limestone, favour fault propagation, while mechanically weak (ductile) layers, such as shales, hinder fault propagation (**Fig. 5.16**) (Peacock and Sanderson, 1992; Wilkins and Gross, 2002; Schöpfer et al., 2006; Ferrill and Morris, 2008).

Upper fault tip lines can become pinned below the free surface, mechanically weak lithological layers, and growth strata (**Fig. 5.16**b) (Nicol et al., 1996; Benedicto et al., 2003). This produces faults with sub-horizontal upper tip lines, termed flat-topped faults (**Fig. 5.16**b), instead of upward retreating tip lines (**Fig. 5.16**a), which would be expected in idealised elliptical isolated faults. This alteration of the bounding fault tip lines will affect the 3D shape of the relay zone and thus the distribution of AR with depth (**Fig. 5.16**d). In (**Fig. 5.16**d) the upper tip lines of the bounding faults have interacted with the free surface producing a relay zone that resembles (**Fig. 5.16**b). The upper section of the relay zone has an elevated AR (4.6) compared to the lower sections of the relay zone (3), which has an unrestricted tip line. Changes in relay AR for (**Fig. 5.16**d) are primarily produced by variations in overlap length, which ranges from 790 m to 1125 m whereas fault separation only varies by 69 m over the entire relay zone. Despite the modified tip line geometries of (**Fig. 5.16**d) the maximum recorded AR does not exceed 4.6, which is similar to published mean AR for relay zones observed at all scales (Aydin and Schultz, 1990; Huggins et al., 1995; Acocella et al., 2000; Soliva and Benedicto, 2004). Therefore, the strata in which a relay zone is a primary control on the shapes of bounding faults and thus the relative distributions of relay AR with depth.

A situation where the mechanical stratigraphy can directly modify the fault interaction model of Gupta and Scholz, (2000), and thus the mean relay AR, is inferred to occur when faults are confined within a mechanical layer. For, mechanically confined faults, such as Lamberton (**Fig. 5.9**) and Kilve (**Fig. 5.6**), have low displacement/length ratios, which modifies the size of the stress field (Ackermann et al., 2001; Benedicto et al., 2003). For further details on this modification to the fault interaction model see section 5.5.1.

The range of relay ARs recoded from any one lithology type can span the observed scatter in the raw data and different lithology types plot in the same regions (**Fig. 5.17**). From the lack of a correlation between lithology types it is inferred that the lithology of the host rock in which a fault forms is not the primary control on relay zone aspect ratio. The interaction between the bounding faults, through their stress fields (**Fig. 5.3**), is inferred to be the primary control of relay zone geometries. However, it is noted

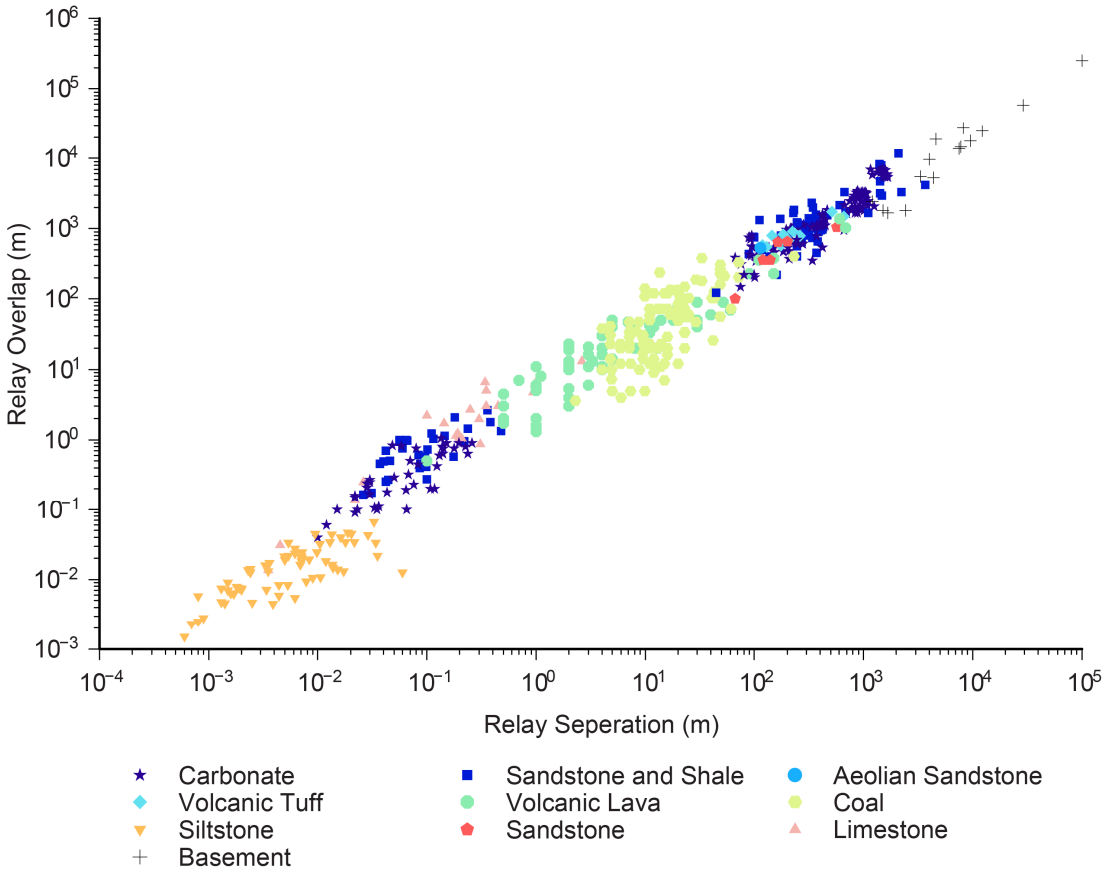

Fig. 5.17. Relay measurements are coloured for lithology type. No clear trend exists between the lithology and relay zone geometries. Details on the data sources can be found in appendix 5: Relay tables 1 and 2.

that yield strength of the host rock is an input in the fault interaction model (**Eq. 1**), and thus, should affect relay zone geometries. However, no clear trend exists between lithologies with similar yield strength (**Fig. 5.17**). This could be due to the likely spread of yield strengths encountered in heterogeneous sequences, which would mask any potential trend at this coarse scale of observation (i.e. over nine orders of magnitude) (**Fig. 5.17**). At finer scales, such as individual outcrops, heterogeneous yield strengths at the propagating fault tip are inferred to have an effect on the AR of relay zones, see section 5.5.2 for details on this inferred modification to the fault interaction model.

5.4.2 The evolution of relay zone geometries

5.4.2.1 A "classic" relay zone

Faults and relay zones are inherently 3D structures. However, AR is a 2D measurement. To capture their 3D geometric variations the AR are recorded systematically at different depths within relay zones (**Fig. 5.18**). To study the geometry of relay zones we start by describing the geometries of a "*classic*" relay zone. A "*classic"* relay zone, which is a relay zone similar to idealised models of relay zones (**Fig. 5.16**a), and in map view, similar to idealised relay ramps (**Fig. 5.10**), is presented in (**Fig. 5.13**). IMF R1 is comprised of two overlapping semi-planar fault segments. The upper and lower fault tip lines on the bounding faults retreat upwards and downwards respectively. In detail, the upper fault tip lines interact with a growth sequence (**Fig. 5.13**) and thus have elevated ARs in the upper section of the relay zone compared to the lower section, such as in (**Fig. 5.16**: b and d). In general, measured AR changes systematically with depth resulting in a low-high-low vertical AR profile (**Fig. 5.13**). Relay zone IMF R1 is characterised by moderately uniform fault separation, with depth, and a wide range in overlap length (**Fig. 5.18**b: IMF R1), which is a result of the upward retreating tip lines on the bounding faults.

The low-high-low AR profile for the IMF R1 relay zone is indicative of variable stages of relay ramp evolution within a single relay zone (**Fig. 5.18**: IMF R1). In the relay zone, the most "*mature*" relay ramp geometries, with relatively large AR (4.43), are located on the horizons with the highest displacement (**Fig. 3.9**: H6 right), near the centre of the relay zone (**Fig. 3.5**). "*Immature"* relay ramps (AR = 1.64) are located on low displacement horizons near the upper and lower fault tip (**Fig. 3.9**). Lateral displacement gradients also increase towards the centre of the relay zone where AR are highest (i.e. most *mature*). High lateral displacement gradients are indicative of faults that are laterally pinned from propagating along-strike at relay zones (Huggins et al., 1995).

Relay zones, like relay ramps (**Fig. 5.2**), are dynamic structures and change shape as the bounding faults increase in displacement and the tip lines expand. We now aim to

identify key stages in the evolution of relay zone geometries, from detailed 3D seismic interpretations.

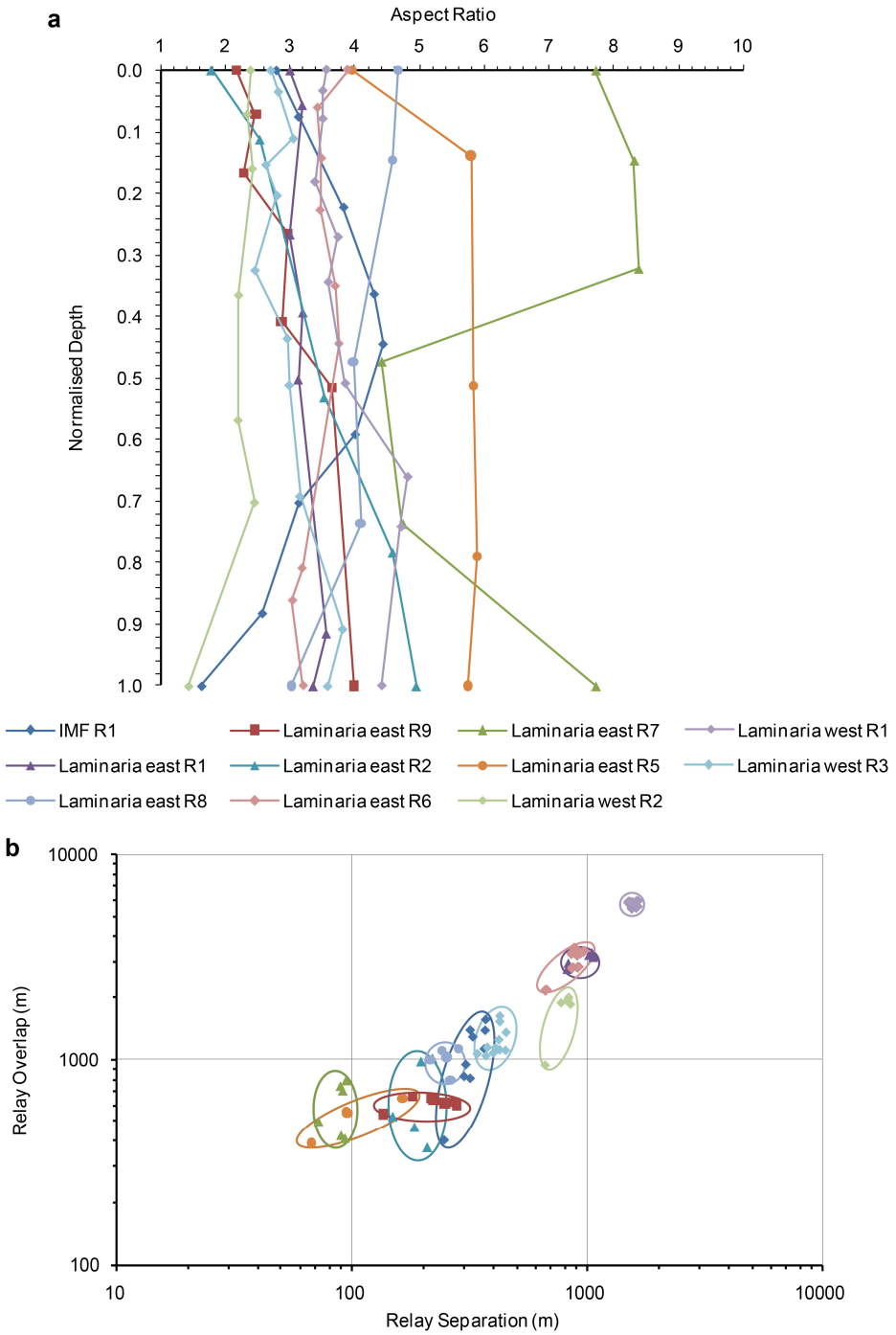

Fig. 5.18. (a) Relay AR against depth for eleven individual relay zones. Depths are normalised to the maximum vertical height of the relay zone. Details on each location can be found in appendix 5: Relay table. 1. Four main relay geometries are recognised; low-high-low AR profiles (i.e. IMF R1), uniform AR with depth (i.e. Laminaria east R1), low-high AR profiles (i.e. Laminaria east R9), and high-low AR (i.e. **Fig. 5.16**d: Laminaria east R8). Laminaria east R7 is an exception and is related to its fault linkage evolution. (b) A log-log plot of overlap verses separation coloured for individual relay zones and circled to highlight the spread of data. Three trends are recognised: sub-vertical distributions (i.e. Laminaria east R2), point distributions (i.e. Laminaria east R8), and horizontal distributions (i.e. Laminaria east R9).

5.4.2.2 The evolution of relay zone geometries

The evolution of relay ramp geometries, in map view, have been well studied (Peacock and Sanderson, 1991, 1994; Huggins et al., 1995; Ferrill and Morris, 2001; Peacock, 2002), however the 3D evolution of relay zone geometries are comparatively

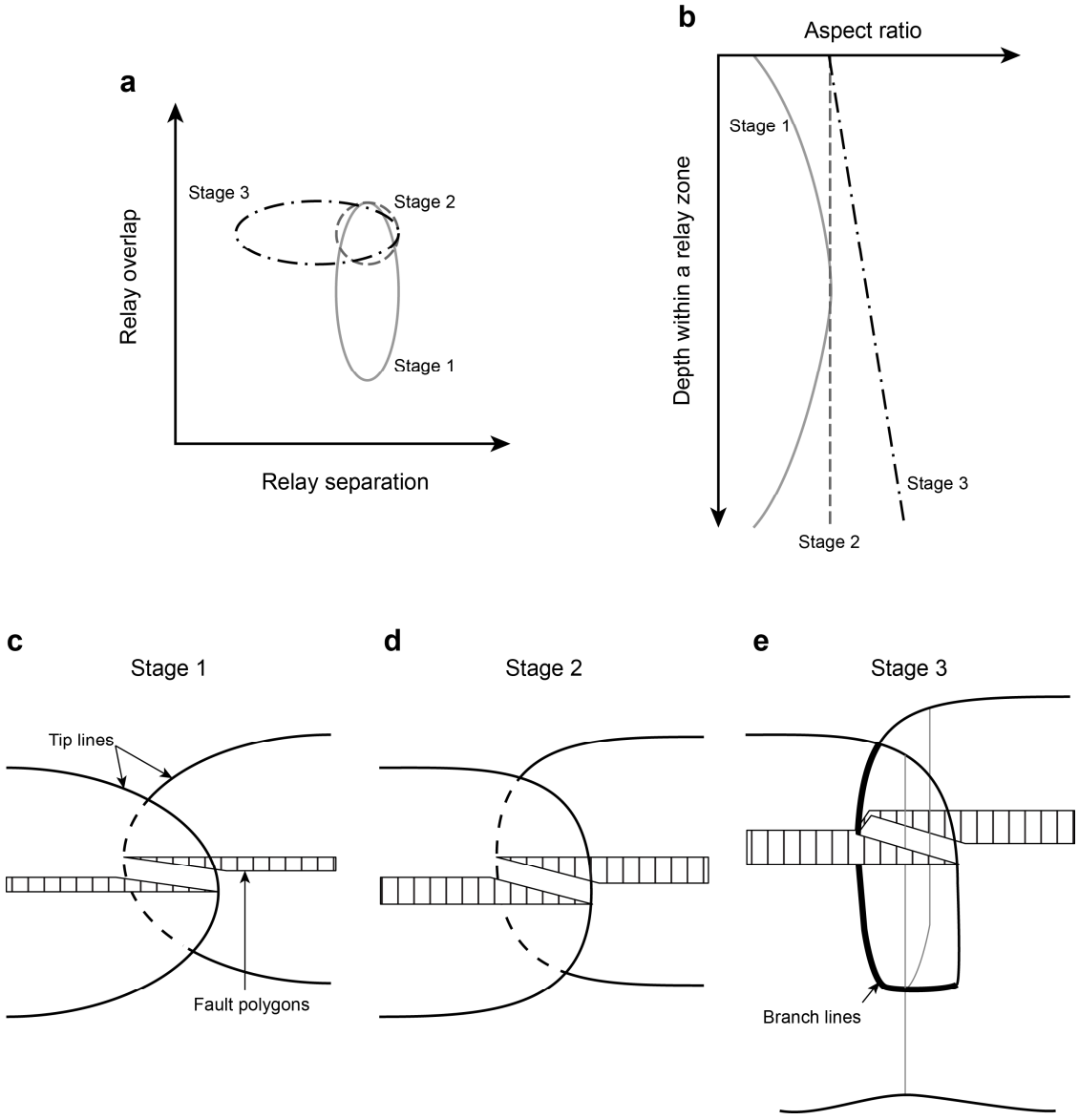

Fig. 5.19. The three stages in the geometric evolution of a relay zone, identified from (**Fig. 5.18**). (a) The schematic changes in overlap and separation for each relay zone, circled. Stage 1, the relay zone has a large spread in overlap length compared to separation. Stage 2, separation remains the same as in stage 1, but overlap length at all levels within the relay zone are now similar. Stage 3, overlap length remains similar to stage 2, whereas separation now decreases within the relay zone. (b) AR plotted against depth for each relay zone. (c-e) 3D schematic models of the geometry of the relay zones at the three stages in their evolution. (c) Stage 1, the relay zone is bounded by faults with upward/downward retreating tip lines which results in a high degree of scatter in overlap length, but not separation. Separation is set by the original location of the bounding faults. (d) Stage 2, the bounding faults are laterally pinned by the adjacent fault and develop sub-vertical tip lines. (e) Stage 3, breaching of a relay zone occurs when faults propagate towards each other and link, which results in the narrowing of fault separation.

understudied. Existing studies of relay zone geometries are based on 3D seismic data (Walsh et al., 1999) and serial cross-sections through outcrops (Kristensen et al., 2008). However, these studies are based on vertical cross-sections through relay zones, whereas in this study both vertical seismic-sections and FNR maps are used to interpret the detailed 3D geometries of relay zones. Eleven relay zones were interpreted using 3D seismic data from the IMF (See chapter 3) and Laminaria (See chapter 4) (**Fig. 5.18**).

Three main relay zone geometries are recognised in (**Fig. 5.18**a); low-high-low AR profiles (i.e. IMF R1), uniform AR profiles with depth (i.e. Laminaria east R1), and low-high AR profiles (i.e. Laminaria east R9). In (**Fig. 5.18**b) the variation in fault separation and overlap are plotted for each relay zone and again three end member trends are identified; sub-vertical distributions (i.e. Laminaria east R2), point distributions (i.e. Laminaria east R1), and horizontal distributions (i.e. Laminaria east R9). High-low AR profiles are also present in (**Fig. 5.18**a) but are not as common as the profiles mentioned above. High-low AR profiles relate to the strong interaction of the upper tip line with an overlying mechanical layer (**Fig. 5.16**), and are discussed in section 5.4.1. For clarity, the three main trends identified in (**Fig. 5.18**) are represented schematically in (**Fig. 5.19**), which are inferred to correspond to the different stages in the geometric evolution of an initially un-linked relay zone.

Stage 1, the tip lines on the overlapping bounding fault retreat upwards and downwards and appear elliptical in strike projection (**Fig. 5.19**c). The maximum overlap length is towards the centre of the relay zone where displacements on the bounding faults are the highest. Fault separation varies little with depth and equals the original separation distance of the overlapping fault segments (**Fig. 5.19**a). Changes in overlap length are the primary control of the observed variation in AR through the relay zone. The characteristic change in relay zone AR with depth, within a single relay zone, goes from low ARs near the upper tip lines to the maximum AR around the centre of the relay zone and then returns back to low ARs near the lower tip lines (**Fig. 5.19**b). Stage 2, the tip lines on the overlapping faults are sub-vertical within the relay zone (**Fig. 5.19**b). Overlap length and separation remain approximately constant with depth and like stage one, relay zone separation is equal to that of the original separation distance

of the overlapping fault segments (**Fig. 5.19**a). For Laminaria east R1, the AR of the relay zone remain similar with depth (**Fig. 5.19**b) and the shape of the relay zone is approximated to a rectangular box. Finally, stage 3, linked relay zones can have a combination of tip line geometries depending on the location and extent of fault linkage, for example (see figures in chapter 4). In relay zones that display down-dip fault linkage along slip-normal branch lines (BL) the separation distance decreases with depth, as fault propagate towards each other (**Fig. 5.19**e). This results in an increase in relay zone AR with depth towards the BL, if fault overlap length remains the same, such as in Laminaria east R9 (**Fig. 5.19**: a and b). Relay zones with chaotic variations in AR with depth can develop when levels within the relay zone continue to increase in overlap length after linkage has occurred on other horizons (**Fig. 5.18**: Laminaria east R7, i.e. **Fig. 4.15**). For more details on Laminaria east R7, see chapter 4. Such relay zone geometries are uncommon (**Fig. 5.18**) and are an exception to the three stages of relay zone evolution outline previously (**Fig. 5.19**).

It is proposed that the geometric evolution of most relay zones will progress from stage one to stage three with the accumulation of displacement on the bounding faults (Peacock and Sanderson, 1994) (**Fig. 5.19**). This evolutionary progression is governed by the interaction between the stress fields of the overlapping faults (Gupta and Scholz, 2000) and develops as follows. (Stage 1) Unrestricted, elliptical, fault tip lines overlap to form a relay zone (**Fig. 5.19**c), resulting in a large spread in fault overlap at different depths within the relay zone (**Fig. 5.19**a). The high displacement horizons have the longest overlap. (Stage 2) Continued propagation of the overlapping faults will result in horizons becoming laterally pinned, at all levels, by the critical stress drop contour of the nearby fault (**Fig. 5.19**d). This results in relatively uniform overlap and separation distances for the entire relay zone (**Fig. 5.19**a), and thus, moderately constant AR with depth (**Fig. 5.19**b). When horizons within the relay zone become laterally pinned relay ramp rotations and lateral displacement gradients, on the overlapping faults, increases. (Stage 3) The next stage is characterised by the onset of fault linkage (**Fig. 5.19**e), which produces narrow separation distances as fault propagate towards each other, thus increasing AR near BL and/or BP (**Fig. 5.19**a and b). The exact location at which faults begin to link varies between different relay zones and fault linkage can also

initiate at multiple points within a single relay zone (See chapter 4 for further details on fault linkage evolution). Therefore, the final geometry of a relay zone (i.e. stage 3) will depend on the linkage evolution. It is noted that not all relay zones will develop the sub-horizontal distribution of overlap/separation measurements, as in (**Fig. 5.19**a: stage 3). For, not all relay zones will develop slip-normal BL.

The proposed geometric progression is based on a relay zone consisting initially of two non-linked fault segments (**Fig. 5.19**b). However, fault propagation within a heterogeneous layered sequence will inevitably lead to irregular lobed shaped tip lines (Huggins et al., 1995; Marchal et al., 2003; Schöpfer et al., 2006), which become out-of-plane with one another (Childs et al., 1996b) and overlap to form a relay zone. The geometric evolution of relay zones formed by the bifurcation of fault tip lines has already been document by (Childs et al., 1995; Huggins et al., 1995; Childs et al., 1997; Kristensen et al., 2008). In these types of relay zones bounding faults are linked at depth throughout the growth of the relay zone. Therefore, both fault overlap and fault separation change at all stages in their evolution. In comparison, in the previous outlined evolutionary model (**Fig. 5.19**) fault separation remains constant until stage three when fault linkage initiated and the bounding faults begun to propagate towards each other.

5.4.3 Refined relay zone AR dataset

At all scales there is approximately an order of magnitude spread in both relay zone separation and overlap (**Fig. 5.20**). Up to half of the observed spread is proposed to have originated from the evolution of relay ramps from *immature* to *mature* AR, within individual relay zones (**Fig. 5.19**). Therefore, to refine the raw dataset and remove scatter relating to the evolution of relay zones a single AR was taken to define a relay zone. In relay zones where the 3D geometry was constrained, i.e. in 3D seismic data, the characteristic AR, for both linked and un-linked relay zones, was selected from the horizon where the displacement on the bounding faults was greatest (i.e. the most

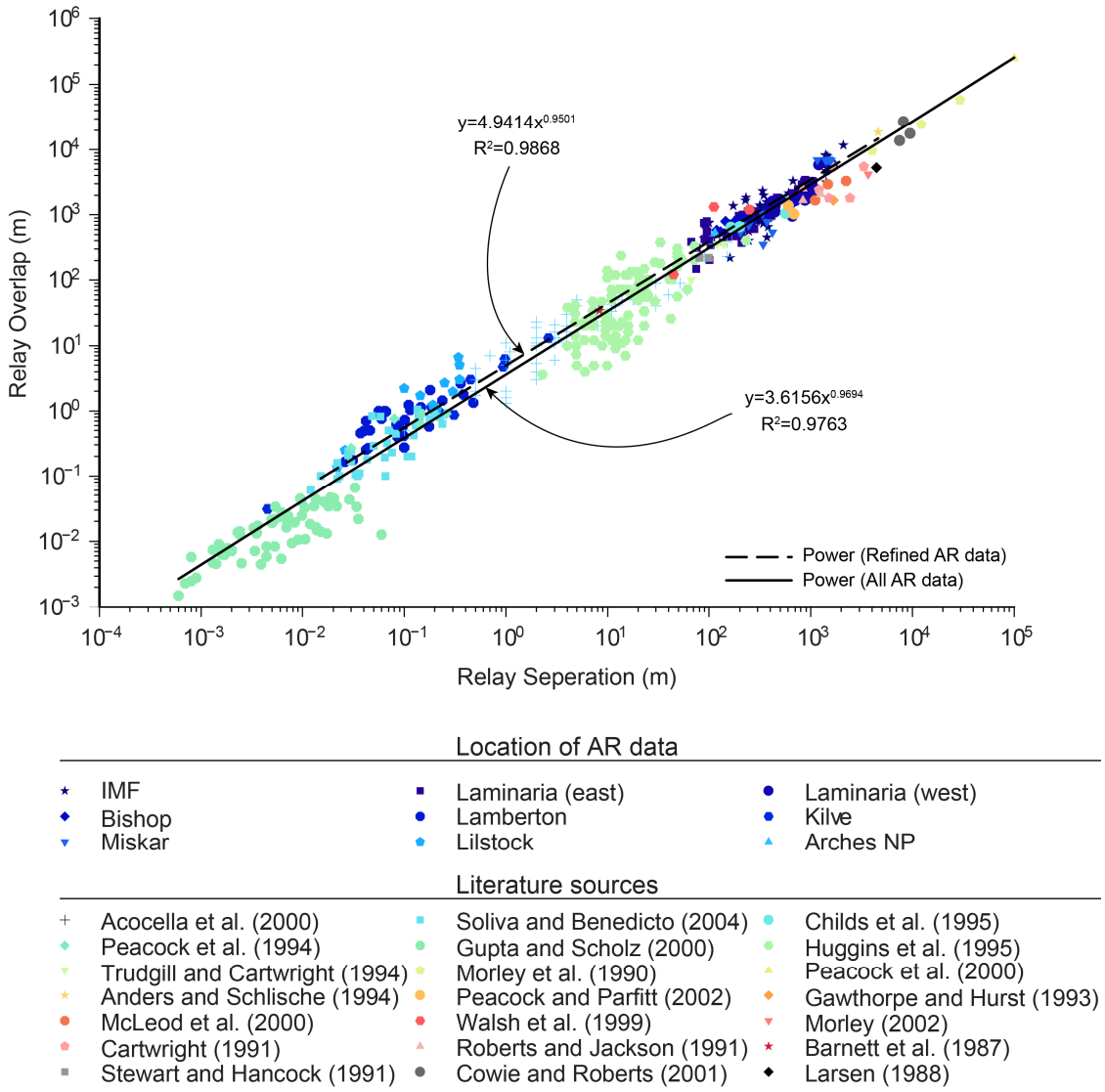

Fig. 5.20. A log-log plot of overlap verses separation for all AR measurements, coloured for their data source. For comparison, the power-law trend line for all the AR data is plotted alongside the trend line for the refined dataset (**Fig. 5.21**).

mature section of the relay zone), which in most relay zones was near its centre. In relay zones with no 3D constraints, i.e. outcrop data, only linked relay ramps are selected to represent the most mature level within a relay zone. For, once a relay ramp is linked the lateral propagation of the bounding fault is retarded and stops completely when the relay zone becomes fully breached (Imber et al., 2004). Whereas, open relay ramps may represent immature sections of a relay zone and are thus not included in the refined dataset. These assumption will add some scatter to outcrop-scales of the refined dataset (i.e. relay zones with separation < ~100 m), for even within fully breached relay zone AR can vary (See **Fig. 4.15** and sections therein). Therefore to strengthen the sample set at outcrop-scales and to ensure the population is accurately represented, relay measurements from literature sources, which meet the selection criteria, i.e. linked and breached relay ramps, are also included in (**Fig. 5.21**) (See digital appendix 5: Relay table: 1 for details of literature sources used).

Two methods exist within the literature to calculate the representative AR for a sample set, Acocella at al., (2000) used the mean of the sample set, and (Soliva and Benedicto, (2004) took the gradient of the linear best fit line. The refined dataset is compared to the raw dataset and both statistical methods are used to describe them (**Fig. 5.21**). Both methods indicate that the refined dataset has larger representative AR (mean = 5.5 and best fit gradient = 4.1), than the raw dataset (mean = 4.2 and best fit gradient = 2.5) (**Fig. 5.21**). This is expected, for *mature* relay zones, i.e. breached or linked relay zones, make up the refined dataset, which in general have higher AR than *immature* relay zones. Soliva and Benedicto, (2004) noted linked relays to have an AR of 4.5 and breached an AR of 6, compared to an AR of 2.9 for open relay ramps. However, high AR do not directly indicate *mature* relay zones (Soliva and Benedicto, 2004). Willemse, (1997) also notes relatively large AR (~4) in the centre of fault-arrays, where summed displacement is high, compared to relay ramps at the tips of the fault-array.

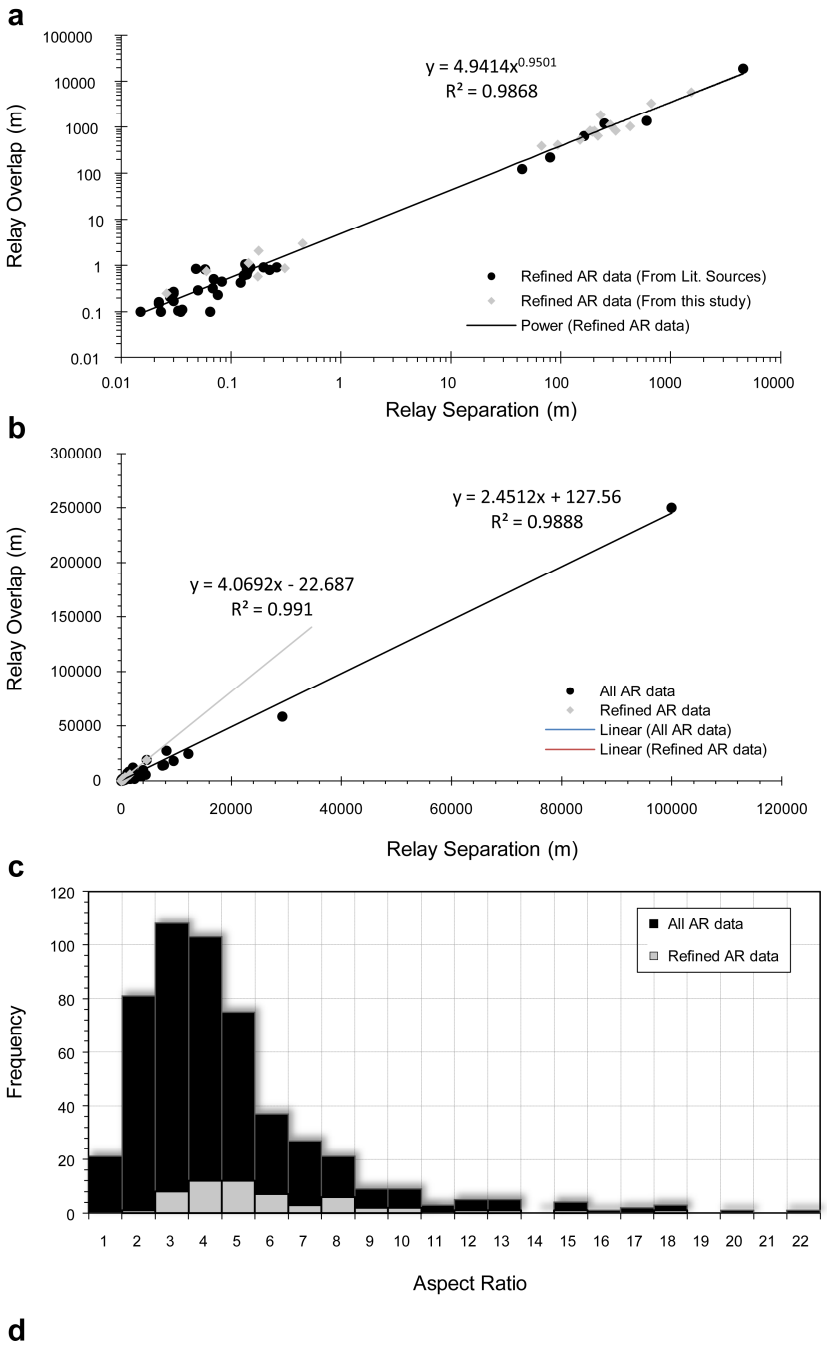

	Refined AR data	All AR data
Mean	5.5	4.2
Median	4.6	3.4
Standard Deviation	3.1	3.0
Skewness	1.7	2.2
Minimum	1.5	0.2
Maximum	17.3	22.0

Fig. 5.21. (a) A log-log plot of the refined dataset, which only includes measurements from the most *mature* sections of relay zone; see text for details on the selection criteria. To expand the refined dataset literature sources that meet the selection criteria are also included (blue circles) to data from this study (red diamonds). (b) Linear plot of the refined dataset (a) and all AR measurement (**Fig. 5.20**). (c) A histogram comparing the refined AR data to all the AR data. (d) A table of the summary statistics for both datasets. Both are skewed towards high AR and have similar standard deviations. The mean AR for the refined AR data is greater than that of all the AR data.

The power-law exponent for the refined dataset is 0.95, which is similar to that for the raw dataset, i.e. all recorded measurements from all locations (**Fig. 5.4**), at 0.97 (**Fig. 5.20**). A compiled dataset of published relay AR measurements by Soliva and Benedicto, (2004) has a power-law exponent of 0.97, which is similar to both the refined and raw datasets. The similarity between the power-law trends suggests that the raw dataset captures a representative sample of relay zone geometries and secondly, a large proportion of the observed scatter in (**Fig. 5.20**) can be attributed to the evolution of individual relay zones (**Fig. 5.18** and **Fig. 5.19**), which is removed in the refined dataset. The strong power-law trend for the refined dataset (R^2=0.99) suggests a single control that shapes relay zone AR over at least nine orders of magnitude, which is inferred to be summarised by Gupta and Scholz, (2000) fault interaction model.

Published mean overlap/separation ratios, from studies of relay zones, are 4.9 (Acocella et al., 2000), 4.7 (Aydin and Schultz, 1990), approximately 5 (Soliva and Benedicto, 2004), and approximately 4 (Huggins et al., 1995). These correspond to the mean AR for the raw dataset at 4.2, which includes published measurements (**Fig. 5.21**d). Individual locations can however have elevated AR when compared to the mean for the entire dataset. Kilve (including Lilstock) and Lamberton, which are both outcrop derived datasets, have mean AR of 8.60 with a s.d. of 5.1 and 8.64 with a s.d. of 4.5, respectively, and the majority of data points from these outcrops plot above the best fit power-law trend line (**Fig. 5.20**). The concentration of relay zone geometries towards high AR could indicate outcrop-specific geological factors that enable relay zones to obtain higher than average AR. Two potential outcrop specific modifications to Gupta and Scholz, (2000) model of fault interaction are presented in section 5.5, which attempt to explain the elevated mean AR from Kilve and Lamberton.

5.5 Evolutionary models for large AR relay zones

5.5.1 Fault growth in mechanically confined sequences

The faults at Lamberton are mechanically confined within the competent sandstone beds and are vertically restricted by a thick shale layer (**Fig. 5.9**). Likewise, in Kilve faults initiate in mechanically strong limestone beds and are initially confined by interbedded shales. Faults do not remain confined and with increased displacements faults can propagate through mechanical boundaries (**Fig. 5.6**). Faults confined within mechanical layers have low displacement-length ratios when compared to unrestricted faults (Nicol et al., 1996; Benedicto et al., 2003). Unlike Lamberton, faults at Kilve are also closely associated with pre-existing veins, which are sub-parallel to the strike of the faults and the fault tips are often hosted within the calcite veins (**Fig. 5.10**). This is proposed to affect the propagation of fault tips at Kilve and thus the AR of relay zones, see section 5.5.2 for details.

Dip-slip faults within mechanically confined sequences are free to propagate laterally but are restricted vertically. This results in long faults with relatively low displacements (**Fig. 5.8**) (Benedicto et al., 2003). The horizontal distance of the perturbed stress field relates to displacement, with larger displacement faults producing wider stress drop regions (Gupta and Scholz, 2000). Faults that are mechanically confined therefore have relatively small stress drop regions for their length. In addition, despite increases in fault length the critical stress contour remains in the same location, for displacement remains low (Soliva et al., 2006). Therefore, fault with separation distances (**Fig. 5.22**b: S*) greater than the horizontal extent of the critical stress drop contour (**Fig. 5.22**b: D*) are able to overlap un-hindered by nearby faults as they accommodate extension. When mechanically confined faults propagate vertically through the confining layer, the stress fields begin to enlarge (i.e. D* increases), as displacement can now increase (**Fig. 5.22**c). Eventually the stress field will grow to a stage where the critical stress drop contour will intersect with the overlapping fault tip (**Fig. 5.3**), which stops further overlap and initiates the development of a relay ramp (**Fig. 5.22**d). Measured AR for relay ramps formed by this method are greater than those expected for faults of similar lengths within non-layered sequences. For, while D* is less than S* faults can

overlap freely and thus develop greater than average AR. For reference, at each stage in the evolution of mechanically confined faults the faults are inferred to be geometrically coherent, as is inferred for un-restricted faults (Walsh and Watterson, 1991).

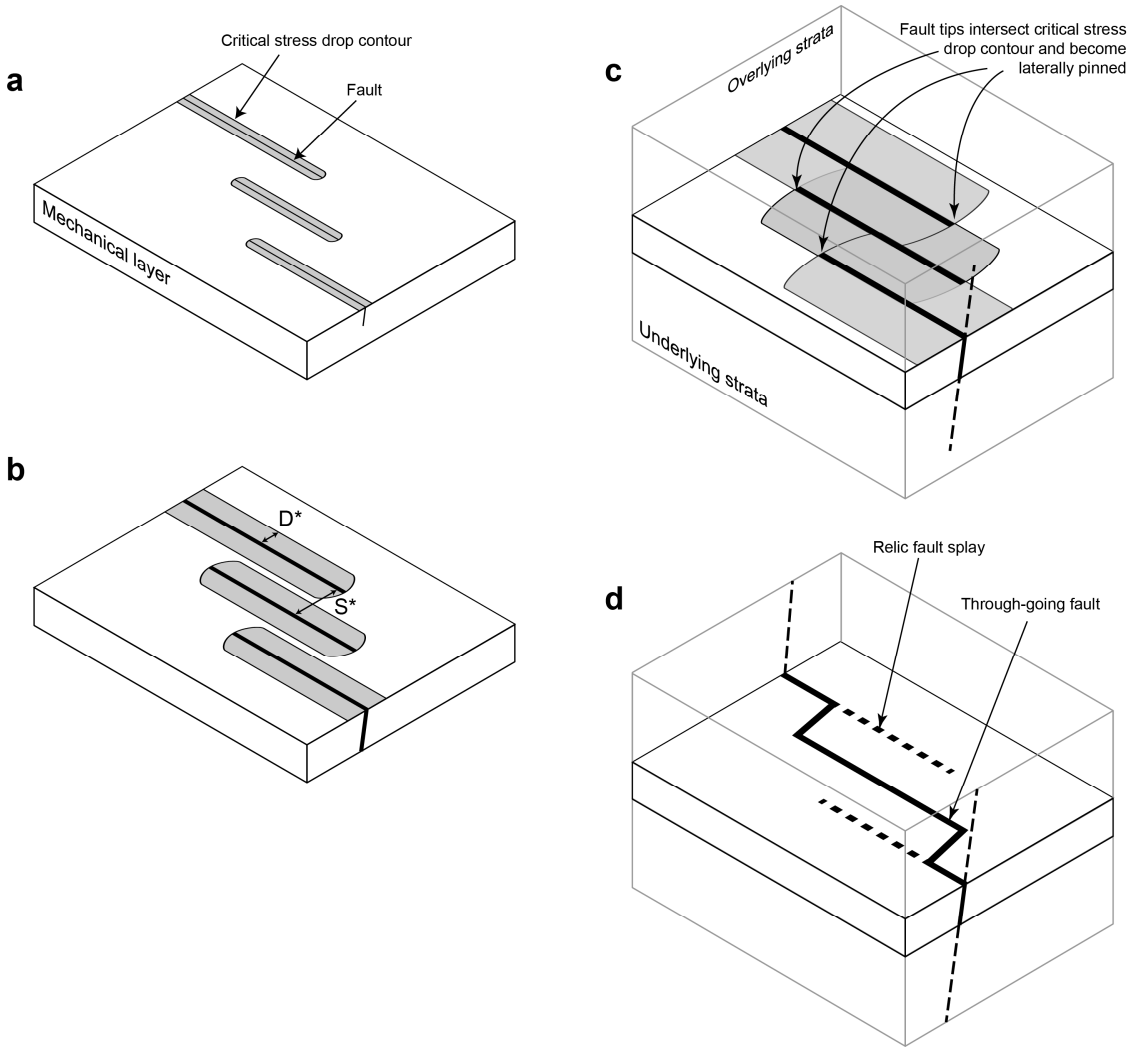

Fig. 5.22. A modification to Gupta and Scholz, (2000) fault interaction model based on observations from Lamberton and Kilve. The evolutionary model includes the affect of a fault that is initially confined within a mechanical layer. (a) Fault form within a strong mechanical layer. (b) The faults are confined within the mechanical layer and develop low displacement-length ratios, with relatively small stress fields when compared to unconfined faults with similar lengths. D* is the horizontal extent of the critical stress drop contour from the fault trace and S* is the separation distance between two overlapping faults. (c) Faults begin to propagate through the mechanical layer into surrounding strata. The stress fields begin to grow with the increases in fault displacement. At a certain point the critical stress drop contour will interact with the nearby fault tip stopping further overlap. (d) Fault linkage occurs and a through going fault is formed when D* equal S*. Large AR are produced by accumulating large overlap lengths in stage (b) prior to the expansion of the stress fields in (c). Figure style after (Soliva et al., 2006: their Fig. 14).

The concept behind this proposed evolutionary model is supported by Soliva et al., (2008) who observed elevated AR for a fault relay ramp that had an abnormally low

displacement footwall bounding fault. The low displacement bounding fault was caused by down-dip fault linkage at depth, which restricted fault movement on the rear segment due to a reduction in fault dip near the slip-normal BL. The cause of the restricted displacement differs from that inferred from Lamberton and Kilve, but the underlying relationship between reduced displacement and increased fault overlap length is the same, which adds weight to the proposed evolutionary model (**Fig. 5.22**).

5.5.2 Pre-existing structures and fault growth

At Kilve the close association of veins with the fault tips could also be a possible factor that facilitates large mean AR. For, the Gupta and Scholz, (2000) model of fault interaction assumes homogeneous and intact rock ahead of a fault tip. The presence of vein material at fault tips would therefore change the yield strength in (**Eq. 2**), which is rewritten as:

$$\sigma_{p(F1)} = \sigma_{yv} + \Delta\sigma_{(F2)} \qquad \textbf{(Eq. 2)}$$

Where σ_{yv} is the yield strength of the vein material. This is however a simplification of the geometric relationship observed in (**Fig. 5.10** and **Fig. 5.23**b) as substituting σ_y with σ_{yv} changes the entire yield strength of the modelled horizon. A better approximation would be to model a horizon with multiple material properties separated by mechanical boundaries, however this is beyond the scope of this study and would be a suitable topic for future studies. Nevertheless, in general, (**Eq. 2**) is inferred to model the fault interaction at Kilve. For, the propagating fault tip is enclosed within the vein material (**Fig. 5.23**) and as such the propagation equation (Eq. 2) is valid. In Kilve veins are composed of calcite, which is inferred to have lower yield strengths than the carbonate beds, for no yield strength measurements are known to exist for calcite veins. However, veins are noted to be relatively weak structures compared to the intact host rock and are often precursors to faults (Peacock and Sanderson, 1994; Crider and Peacock, 2004). At Kilve veins would also act as mechanical heterogeneities at the fault tip, which are favourably orientated for reactivation as faults.

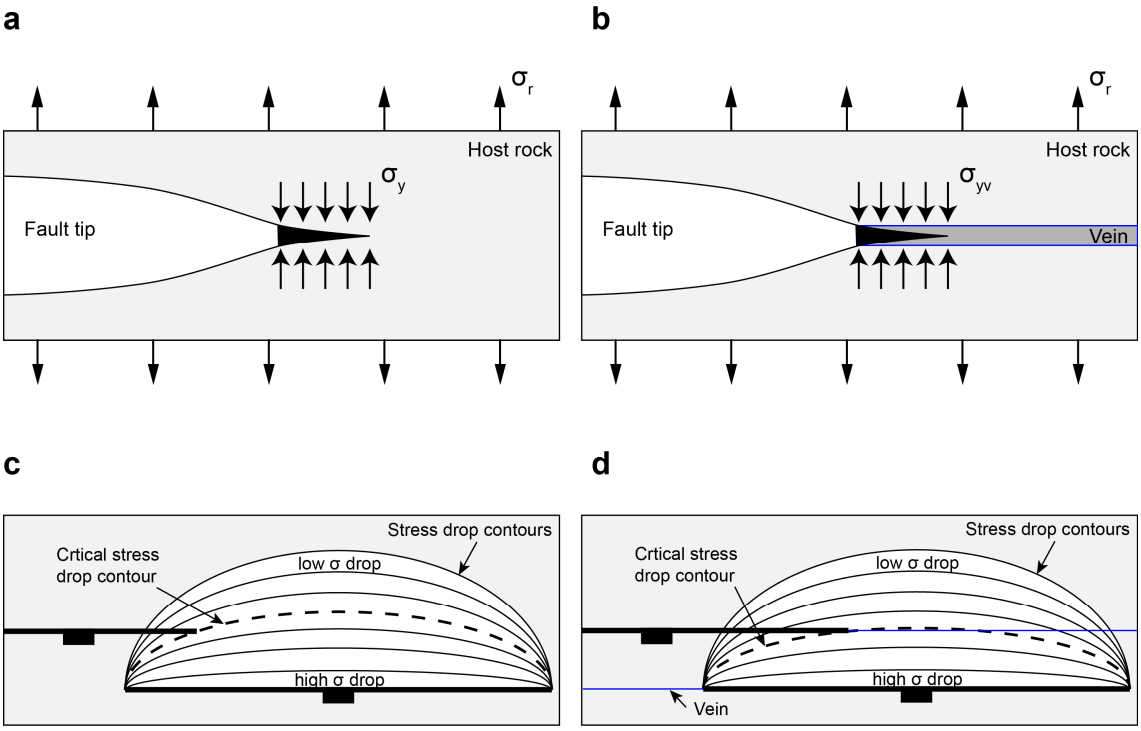

Fig. 5.23. A modification to (Gupta and Scholz, 2000) fault interaction model based on observations from Kilve. (a) A propagating fault tip as described in (Cowie and Scholz 1992), see Eq. 1. For a fault to propagate stresses at the fault tip must overcome the yield strength of the host rock. σ_r = regional applied extensional stress and σ_y = yield strength at the fault tip which acts as a cohesive stress. (b) A modification to (a), a vein is included at the fault tip, which changes the yield strength at the tip, see Eq. 2. The vein walls are also mechanical boundaries aligned parallel to the propagation direction of the fault tip. (c) A schematic illustration of (Gupta and Scholz, 2000) fault interaction model (**Fig. 5.3**), whereby fault F1 is limited from propagating laterally at the critical stress drop contour, the location of which is dependent on the yield strength (Eq. 1). (d) Lowering the yield strength at the fault tip increases the value of the critical stress drop contour thus allowing F1 to propagate into higher stress drop regions near the centre of F2.

In Kilve fault tips hosted within pre-existing veins will be able to propagate to greater overlap lengths, for a given fault separations, thus increasing relay AR. Because, the peak stress ($\sigma_{p(F1)}$) required to propagate the fault, within the stress drop region of a nearby fault, will be reduced due to the reduction in yield strength (**Eq. 2**). Therefore, overlapping faults in Kilve, associated with vein at their tips, will be limited at a greater stress drop value (i.e. closer to the centre of the nearby fault), thus allowing continued fault propagation altering the location at which the overlapping fault tip is laterally pinned by the critical stress drop contour (**Fig. 5.23**d). In addition, stresses could potentially be concentrated by the mechanical boundary between the vein and the host rock (**Fig. 5.23**b: blue lines). If so, this would focus stresses within the vein facilitating fault propagation along the course of the pre-existing structure, as is observed in Kilve which have tramline fault overlaps that follow the pre-existing veins,

which result in tabular relay ramps (**Fig. 5.10**). (Burchardt, 2008) models sill emplacement and demonstrates that stress can be restricted from crossing mechanical boundaries and are thus focused within mechanical layers. Further studies are required to modify the (Burchardt, 2008) model to make it more applicable to fault tip propagation rather than sill emplacement and test the inference that stress can be focussed within veins facilitating fault propagation.

The two proposed modifications to (Gupta and Scholz, 2000) model of fault interaction (**Fig. 5.22** and **Fig. 5.23**) are only inferred to exist in locations that have similar controls to Kilve and Lamberton, i.e. outcrops with mechanical layering and pre-existing veins at fault tips. Therefore, the scales over which these controls operate will be defined by the presence of the controlling factor, such as mechanical thickness, which has implications for calculating scaling relationships. For, if the controls on AR are scale-specific, such as at Kilve, centimetre-scale relay zones may not be comparable to meter-/kilometre-scale relays from the same location, see section 6.2.2.2 for further discussion on this point.

5.6 Conclusions

1. Including continuous deformation along-strike of fault tips in outcrop and seismic datasets increases the measured overlap length and thus relay zone AR. Irrespective of the sampling method the addition of continuous deformation at fault tips increases overlap length by a factor of 1.46 over at least four orders of magnitude.
2. The idealised elliptical tip line shape of relay-bounding faults can be modified by the mechanical stratigraphy of the host-rock, which alters the 3D geometry of relay zones.
3. The 3D geometry of relay zones evolves over time. Three basic stages are identified for initially un-linked overlapping faults; (1), Fault separation is set by initial segment location and overlap varies with depth. (2), Fault separation remains constant and fault overlap becomes more uniform throughout the

relay zone. (3), Fault overlap is limited at all horizons and as faults begin to link the separation distance decreases near the BL.

4. The overlaps and separations of relay-bounding faults display a single power-law scaling trend over 9 orders of magnitude of $y=3.6156x^{0.97}$ $R^2=0.98$ and a mean AR of 4.2, which are similar to published datasets which have power-law exponents of 0.97 and the mean AR that range from 4 to 5.

5. At all observed scales there exists an order of magnitude scatter in measurements of relay zone AR. Approximately half of this scatter can be attributed to the spread of AR that can be measured from individual relay zones. This scatter was removed by selecting a single representative AR for a relay zone, when its 3D geometry was known, that defined its most *mature* (i.e. most evolved) section. For 2D datasets linked relay ramps were taken to represent the most *mature* section of the relay zone. The refined dataset has a power-law scaling trend of $y=4.9414x^{0.95}$ $R^2=0.99$ and a mean AR of 5.5, which is greater than that of the original dataset at 4.2. For, in general, AR increases as the relay zone evolves and low AR measurements (i.e. *immature* relay) were filtered out of the refined dataset.

6. The strong power-law trend for relay zone AR ($R^2=0.99$) suggests that a single mechanism is the control on the geometry of relay zones over at least 9 orders of magnitude, which is inferred to be Gupta and Scholz, (2000) model of fault interaction.

7. Two outcrops, Kilve and Lamberton, display mean AR of 8.60 and 8.64 respectively, which are greater than both the mean AR for the refined dataset (5.5) and all recorded relay zones (4.2). This suggests that outcrop specific controls exist that modify the Gupta and Scholz, (2000) model of fault interaction and facilitate the development of relay zones with above average AR.

    a. Faults at Lamberton and Kilve are confined within a mechanical layer and as a result have low displacement/length ratios. While faults are confined within the mechanical layer displacement remains fairly

constant despite increases in fault length. When faults eventually break through the confining layer i.e. shale beds, fault displacement can increase and therefore the size of the stress field also increases. Therefore faults that could previously overlap unhindered become laterally pinned by the increased size of the stress drop regions on nearby faults. Relay ramps with pre-existing overlap length will have elevated AR compared to faults with normal displacement/length ratios.

b. For Kilve, pre-existing calcite veins ahead of propagating fault tips are inferred to lower the yield strength at the fault tip, which in turn lowers the peak stress required to propagate the fault tip. This allows a fault tip to propagate further into the stress drop region of the nearby fault compared to faults within material with stronger yield strengths. In addition, the vein hosted fault tip is enclosed by mechanical boundary between the host rock and vein walls, which could concentrate stress within the pre-existing veins enhancing fault propagation, thus facilitating elevated overlap lengths and thus above average AR.

8. Outcrop-specific controls make comparing relay zone geometries between different locations and scales difficult. The spatial extent and/or scale range over which outcrop-specific controls operate need to be established before relay zones can be accurately compared between different locations.

Chapter 6. Discussion

6.1 Isolated vs. Coherent growth models

Throughout this thesis the vertical displacements from both continuous and discontinuous deformation were measured from the entire fault-array, which included the relay ramps and the mutual hanging wall and footwall. This approach made it possible to capture the majority of fault-related deformation within a study area. Consequently, the more complete total displacement-distance plots, created using the FNR method (Chapter 2), can be used to correctly distinguish between competing growth models (i.e. **Fig. 1.5**; a displacement deficit at a relay zones = isolated growth model, and a total d-x profile that resembles a single isolated fault profile = coherent growth model) (see also Walsh et al., 2003b).

The fault-arrays studied in this thesis formed due to a single extension direction and, over the scale of observation, the along-strike variation in extension is assumed to be negligible (for details on the tectonic settings for each area see the relevant chapters). For brevity, the boundary condition for all the fault-arrays in this thesis can be approximated to those of a rift setting, whereby extension occurs across approximately linear boundaries, and faults within the extensional terrain are orientated parallel to the margins; the along-strike variations in displacement at the margins are minimal; and faults form in response to a single extension direction, orientated perpendicular to the average fault strike.

The magnitude of extension at the boundaries of rift zones does vary, such as in the East Africa rift, which decreases in extension towards the south, where it eventually terminates (Ebinger, 1989; Morley, 1999; Karner et al., 2000). At the crustal scale sampling extension can be difficult and variations in extension may result from only sampling displacements from large bounding faults and not the surrounding continuous/ductile deformation. Whereas, in sandbox style models, which are used to model rift evolution and fault growth, the extension at the boundaries is known and is constant (McClay et al., 2002; Marchal et al., 2003; Hus et al., 2005). Therefore, if

these types of models are correct approximations of rift settings, faults and regions of continuous deformation within a rift are inferred to equal the extension applied at the margins.

Based on results from the thesis, (**Fig. 6.1**) summarises the inferred fault growth and interaction model of faults from rift-like settings. At all stages in the evolution of the fault-array the internal deformation balances the applied extension at the margins, which is uniform along-strike (see figure caption for details on each stage). (**Fig. 6.1**b) is the key stage for contrasting competing fault growth models (Cartwright et al., 1996; Walsh et al., 2003b). To balance extension at the boundaries a region of continuous deformation must exist between the two faults (i.e. a zone of elastic-strain, minor fault/fractures, and/or ductile thinning). The isolated growth model does not invoke such a region of discontinuous deformation and as such the extension within the rift would not equal the applied extension at the margins. Therefore, the isolated growth model does not explicitly describe fault growth mechanisms in rift-like settings. Consequently, the proposed presence of the isolated fault growth models, in rift-like settings (Cartwright et al., 1996), probably relates to the under-sampling of continuous deformation and/or minor faults surrounding the measured fault segments, although without revisiting the original interpretations it is hard to prove this conclusively. In contrast, the coherent fault growth model allows apparently isolated faults to be connected, or soft-linked (**Fig. 1.3**), via a region of continuous deformation, which can consist of faults and fractures below the resolution of the study (Walsh and Watterson, 1991).

Fig. 6.1. (Next page) A graphic example of how faults interact. At all stages (a-e) the internal deformation balances the applied uniform extension at the margins, arrows. (a) At low extensions the crust is elastically strained. (b) With continued extension, represented by the changes in arrow length, faults begin to nucleate and some of the elastic-strain is converted into permanent strains, i.e. minor faults and fractures, which are initially distributed, assuming no pre-existing heterogeneities. (c) The faults propagate laterally and displacement is localised on to them. Around each fault a local stress field is produced and the dashed line represents the location of the critical stress drop contour (Gupta and Scholz, 2000). Deformation (strain) accumulated in previous steps remain. (d) and (e) are two possible scenarios, in (d) faults continue to increase in displacement and as such the size of the stress drop region expands. At the point where the propagating fault tips intersect the critical stress drop contour the faults are laterally pinned and a relay zone develops with typical AR of ~4.2. (e) Faults are restricted from accumulating displacement, i.e. mechanically confined faults (Soliva et al., 2005), therefore, to balance extension at the margins lateral fault propagation increases and new faults form (Ackermann et al., 2001; Soliva et al., 2006). In addition, low displacement-length (D-L) ratios results in comparatively small stress drop regions on nearby faults, and faults do not become laterally pinned, as in (d). See chapter 5 for further details on (d) and (e).

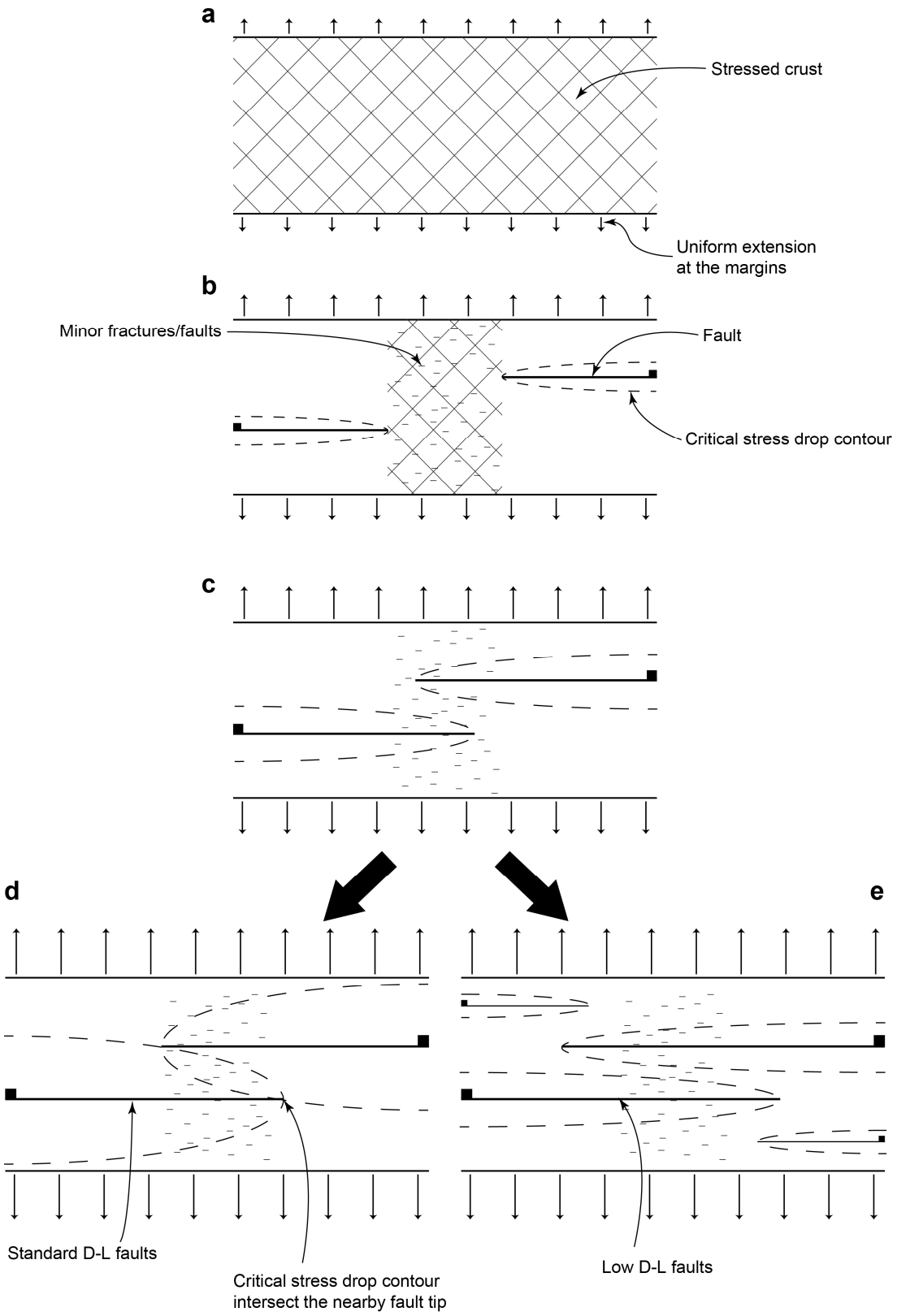
a
Stressed crust
Uniform extension
at the margins
b
Minor fractures/faults
Fault
Critical stress drop contour
c
d
e
Standard D-L faults
Critical stress drop contour
intersect the nearby fault tip
Low D-L faults

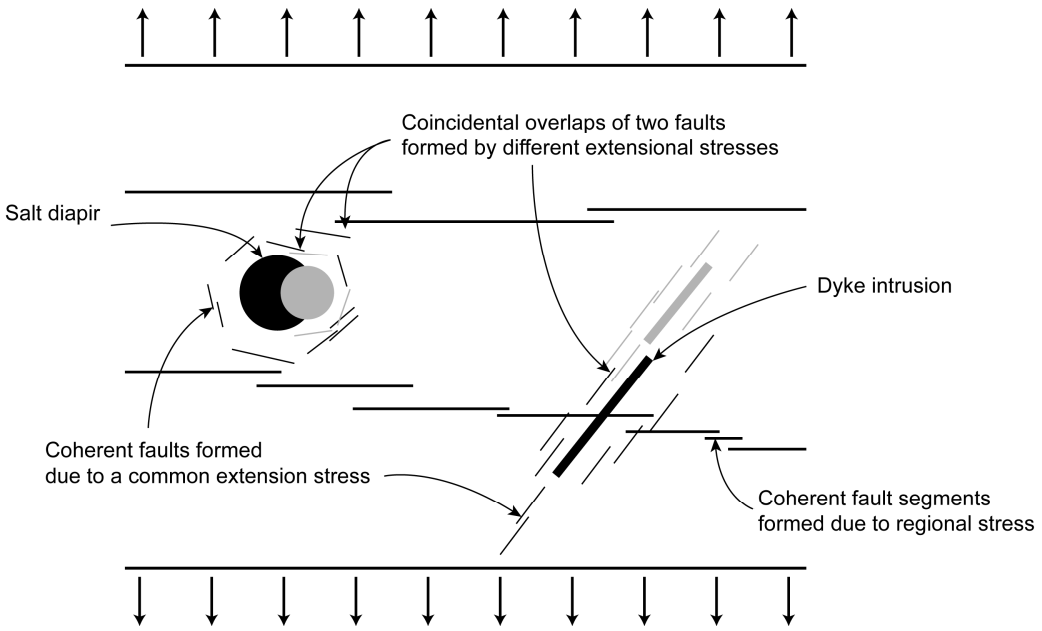

Fig. 6.2. Arrows on the boundaries indicate the amount of extension applied. Faults that form parallel to the margins (thick lines) are all proposed to be geometrically coherent and conform to the coherent growth model. Faults formed around local intrusions (thin lines) form due to episodic periods of extension that vary in both space and time are not expected to produce coherent d-x profiles when summed with faults formed by regional extension (thick lines). In detail, faults formed by a single intrusion are inferred to have coherent d-x profiles, while faults formed by different pulses of intrusion (black features equal the first pulse and grey second pulse) overlap by coincidence i.e. the isolated growth model.

Faults can however form in tectonic settings that cannot be approximated to rifts. For instance, salt diapirs, igneous intrusion (i.e. intrusions), and mountain/delta collapse (i.e. body forces) can give rise to magnitudes and directions of extension that vary in both space and time (Davison et al., 1993; Davison et al., 1996; Rowan et al., 1999; Tentler, 2005). Faults formed by different driving forces are not necessarily expected to behave as a coherent fault-array, for the boundary conditions are not the same. Therefore, total d-x profiles that include faults formed due to different extensional mechanisms (e.g. **Fig. 6.2**: salt movement, thin lines, and regional extension, thick lines) are not likely to resemble those of an idealised isolated fault (**Fig. 1.3**). Instead, faults would overlap by coincidence, even if they do resemble the basic map view geometries of coherent fault-arrays (i.e. overlap and separation of relay zones) (Dutton and Trudgill, 2009).

In detail, *individual* faults formed by each pulse of extension, for example around salt diapirs, are inferred to follow coherent growth models, as these faults form synchronously due to a single extension direction. However, with the continued

emplacement of the diapir the extensional stresses have the potential to change orientation, resulting in different fault families with variable strikes (Davison et al., 1993; Davison et al., 1996; Rowan et al., 1999). Subsequent faults therefore overprint each other and are not inferred to behave as geometrically coherent structures (**Fig. 6.2**). For, the driving mechanisms behind the individual faults are not the same. Therefore, relay zones in such settings can form by the coincidental overlap of originally coherent fault segments. Published examples of fault-arrays formed by salt and magma movement, and which potentially comply with the isolated fault growth model are described by (Stewart et al., 1996; Tentler, 2005; Dutton and Trudgill, 2009).

Determining which growth model dominates in a region is important, as it impacts on how one perceives fault growth and interaction and thus how fault-arrays are interpreted. In summary, how faults grow and interact is closely associated to tectonic setting and the distribution and timing of extension. As such, the coherent fault model is inferred to dominate in settings such as rifts and passive margins. And, the isolated fault model is inferred to operate in areas around the intrusion of buoyant materials. The above-mentioned tectonic settings can all occur in the same geographic location, thus complicating the distinction between the different growth models. However, within a single tectonic setting, such as around salt intrusions, the type of fault growth mechanism can change with scale, because isolated fault systems are likely to comprise one or more coherent segments.

6.2 Applications

6.2.1 Seismic hazard

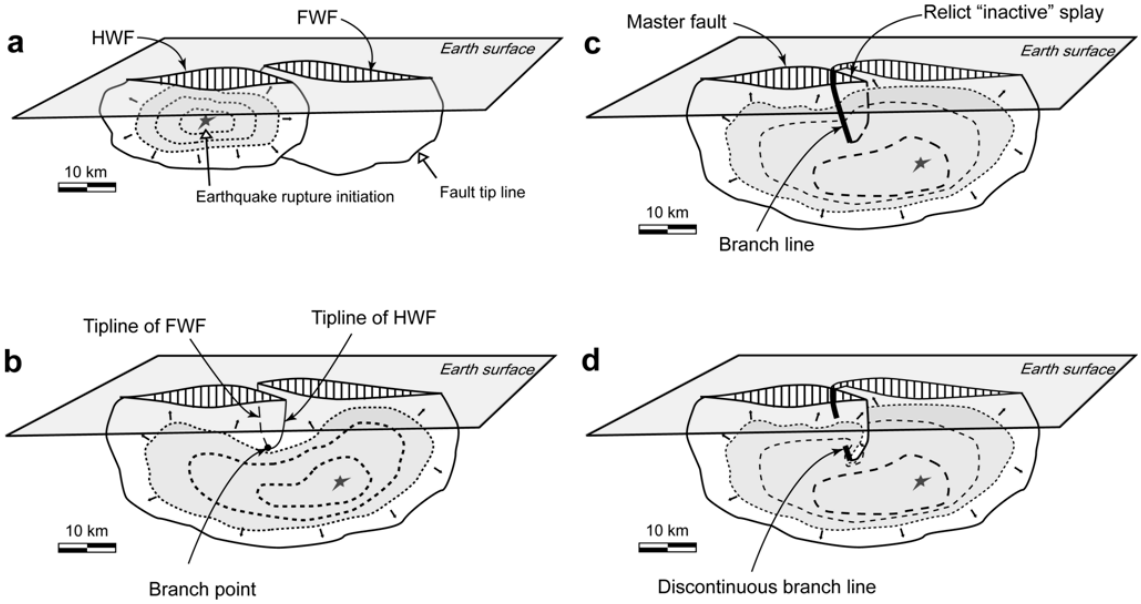

Fig. 6.3. Comparison between (a) separated fault segments and (b) fault segments linked below the Earth's surface (i.e. down-dip linked fault segments). Hypothetical earthquake rupture surface is represented on each case of fault segmentation. (b) Note that the area of the rupture surface in the case of branched fault segments can be twice that for separated fault segments (a). From (Soliva et al., 2008). Comparison between (c) fully breached relay ramp and (d) partially breached relay ramp. In (c) and (d) both are linked at the earth surface. In (c) the master fault is the only structure to host a rupture and the relict splay moves passively in the hanging wall. In (d) both the HWF and FWF bounding faults can slip in the relay zone.

The size of an earthquake is measured in terms of the moment magnitude (Mw) and is dependent on the size of the fault (i.e. rupture length), the average slip, and the rigidity of the faulted material (Wells and Coppersmith, 1994). Therefore, the larger the fault, the larger the potential earthquake (Schwartz and Coppersmith, 1984; Wesnousky, 1986; Machette et al., 1991; Sieh et al., 1993; Amato et al., 1998; Ferrill et al., 1999; Gupta and Scholz, 2000; Soliva et al., 2008), which is why understanding fault linkage geometries in 3D is vital to assessing the size of potential earthquakes. For example, on the Yucca Mountain fault, which is segmented at the earth surface, the individual segments are predicted to have a potential earthquake size of up to Mw 6.6, whereas if linked at depth the combined length of the Yucca Mountain fault segments could produce an earthquake as large as Mw 6.9 (Ferrill et al., 1999).

In this thesis the interpretation of 3D seismic and field data showed that faults can link simultaneously at multiple points along overlapping fault tip lines, resulting in segmented branch lines (**Fig. 4.11** and **Fig. 4.15**). Therefore, a relay zone that is open at the earth's surface might be linked along a slip-aligned BL at depth, thus increasing the size of the potential rupture plane and the resultant earthquakes (**Fig. 6.3**) (Soliva et al., 2008). Where 3D sub-surface data are not available, the shape of a d-x profile from an outcrop example of an open relay ramp can be used to predict whether a relay zone is breached along a slip-aligned BL in the subsurface (**Fig. 4.19**). This inference is similar to that of Soliva et al., (2008) who infers slip-normal fault linkage from the displacement distributions on overlapping faults. These two models combined can potentially be used to predict the locations of a linked relay zones in the subsurface.

Slip-normal fault linkage can enhance fault surface curvature normal to the continued slip direction and in some cases can produce restraining bends in the through going slip surface, such as in (**Fig. 4.15** and **Fig. 4.16**). While the asperity remains the relay zone is not fully breached and both boundary faults can continue to accommodate displacement (**Fig. 4.5**). Assuming that the faults are seismogenic and continued displacement results from seismic slip events, even an apparently breached relay ramp, in map view, can slip seismically on both boundary faults, i.e. what would be termed the master fault and relict splay (**Fig. 6.3** and **Fig. 1.1**). Traditionally, relict splays are seen as inactive structures which are carried passively in either the footwall or hanging wall, and thus do not slip seismically (**Fig. 1.1**). The inference that a relay ramp can be breached at the surface but continue to slip on both boundary faults has implication for seismic hazard mapping, and for instance, building structures on top of what might have been perceived as a relict "inactive" splay (**Fig. 6.3**).

6.2.2 Hydrocarbon industry

6.2.2.1 Fluid flow

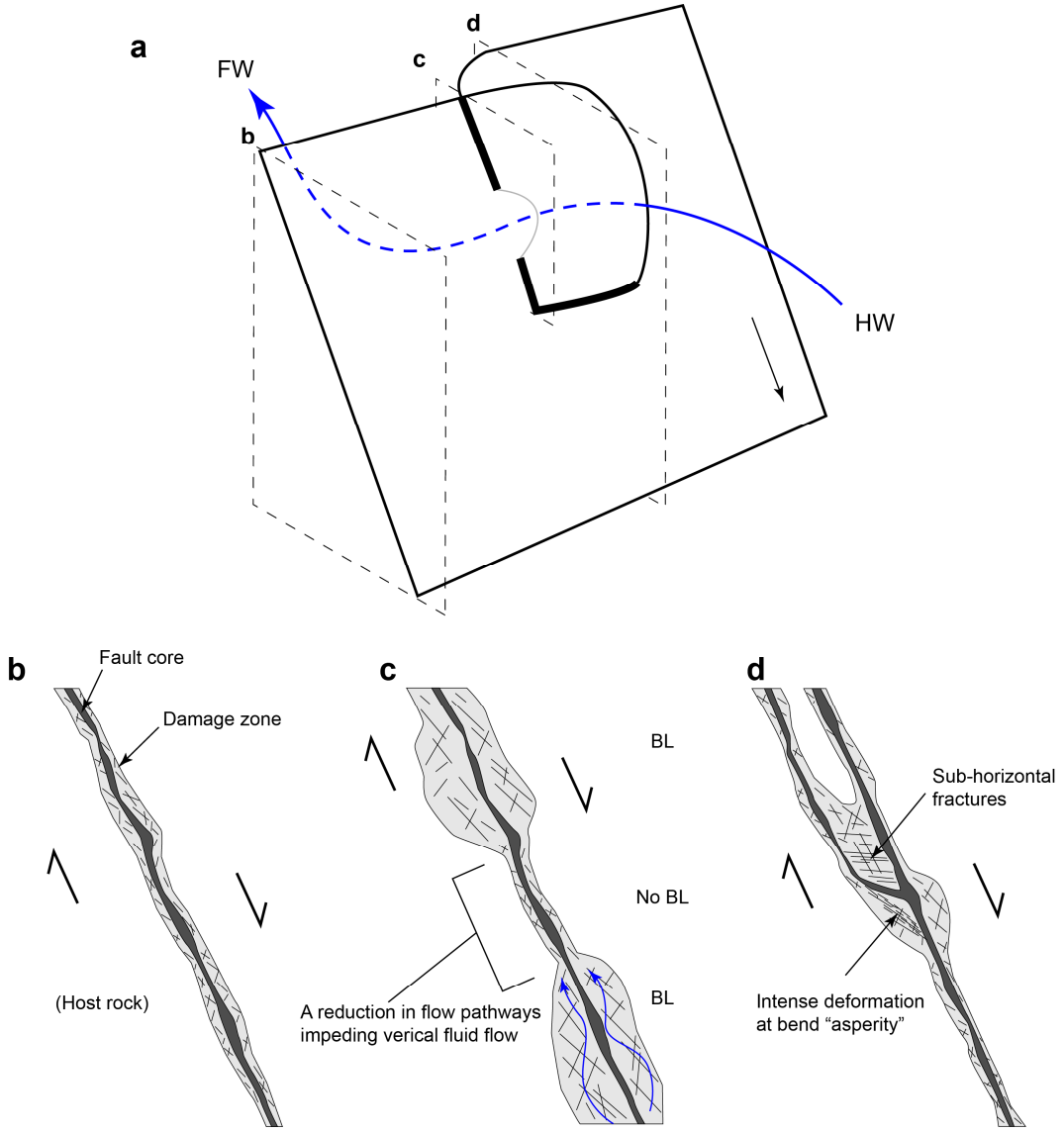

Fig. 6.4. (a) Schematic representation of a partially breached relay ramp with a discontinuous branch line (thick black line). Fault tip lines obscured by fault surfaces in the foreground are coloured grey. Black arrow indicates the slip direction. The cross-sections locations (b-d) are annotated. The gap in the BL allows fluids to flow freely between the hanging wall and footwall, blue line. (b) A fault surface consists of an anastomosing fault core and a damage zone of variable thickness (Caine et al., 1996). (c) A close-up cross-section along a slip-aligned branch line. The damage zone is wider in areas of fault linkage. The BL is discontinuous, which results in a segmented vertical flow pathway. Down-dip fault linkage in (d) results in a restraining bend, as in (**Fig. 4.16**), and increased deformation in the mutual footwall. Within the ramp local strain incompatibilities result in sub-horizontal fracturing in the base of the relay ramp.

Fault zones can be both fluid conduits and fluid barriers depending on the proportion of fault core to damage zone, where the fault core acts as a barrier and the damage zone a pathway for fluids (See appendix 1: **Fig. A1** and **Table A1**) (Caine et al., 1996).

Fracture and fault densities (i.e. damage zones) around branch lines (BL) are higher than those adjacent to planar sections of the fault surface (Davatzes et al., 2005; Fossen et al., 2005; Bonson et al., 2007), because any mismatch in slip between the two fault surfaces causes strain incompatibilities, which are maintained by increased fracturing and faulting (Bonson et al., 2007). Therefore, branch lines can be either fluid conduits, facilitating the communication of fluid between different stratigraphic horizons, or fluid flow barriers, forming fault bounded traps in the subsurface (Ferrill and Morris, 2001). The controls on the transmissibility of a BL are the same as for a fault and depend of the permeability of the fault core (e.g. shale content, degree of cementation, cataclasis) (Yielding et al., 1997), the juxtaposition of reservoir units (Caine et al., 1996; Knipe et al., 1998; Jolley et al., 2007; Freeman et al., 2010), and the thickness of the fault zone (Manzocchi et al., 1999). As presented in chapter 4, BL can be discontinuous. Therefore, the control a BL has on fluid flow will also be variable, which will affect the sealing potential of fault bounded traps (**Fig. 6.4**a), and the vertical distances over which permeable damage zones extend i.e. the zones of enhanced fracturing associated with fault linkage (**Fig. 6.4**c).

In Lilstock it was shown that the mechanical layering controlled the timing of fault linkage (**Fig. 4.12**). Fault linkage in the mechanically strong layers i.e. limestone, occurred prior to linkage in the weaker shale beds. This pattern of fault linkage is inferred to relate to variable propagation rates within mechanical layered sequences (Schöpfer et al., 2006). In general, reservoir units (i.e. sandstone and limestone) are more competent than the seals (i.e. shales and salt), and therefore fault linkage could preferentially occur in reservoir units before a seal is breached by a through going fault. This may affect fault seal predictions across low-offset faults.

Volumetric strains increase towards the base of fault-bounded ramps to accommodate the rotation of overlying beds (**Fig. 4.21**). The structures developed to achieve volumetric strains will differ depending on lithology, but for reservoir units, which are normally competent, beds are more likely to deform in a brittle manner and thus increase the fracture and fault density in the base of confined relay ramps (**Fig. 6.4**d). As shown in the Moab relay ramp (**Fig. 4.16**), brittle structures develop normal to the local compressive stress directions within the ramp, which are approximately sub-

horizontal in the case of dip-slip faults. These are at high angle to the majority of shear surfaces, which form due to regional stress (**Fig. 6.4**b-c). The presence of sub-horizontal fractures, or dissolution surfaces in limestone, could greatly affect the vertical permeability within the base of fault bounded relay ramps i.e. ramps that have slip-normal fault linkage (**Fig. 1.4**).

6.2.2.2 Relating outcrops analogues to seismic-scales

The AR of relay zones follows power-law scaling relationship over at least 9 orders of magnitude which imply they are self-similar over this scale range (**Fig. 5.20**) (Turcotte, 1989; Acocella et al., 2000; Soliva and Benedicto, 2004). For instance, if the scale bars were removed the relay zones from Lilstock (**Fig. 2.12**), Bishop (**Fig. 2.29**), Arches NP (**Fig. 2.15**), IMF (**Fig. 3.9**), and Laminaria (**Fig. 4.9**) there would be no noticeable difference in relay geometries. Therefore, the self-similarity of relays zones allow outcrop analogue observations to be applied to larger scales, which can aid in the interpretation of seismic-scale fault-arrays.

However, outcrop-specific departures from the mean geometry of a relay zone (AR = 4.2) can occur when faults are confined within mechanically layered sequences, which produce higher than average ARs (8.6) (**Fig. 5.22** and **Fig. 6.1**e). This scale-dependant modification to relay zone geometries needs to be considered when comparing observations between different scales in mechanically layered sequences, for the mean AR of a relay zone will not be the same (**Fig. 6.5**). For instance, shown schematically in (**Fig. 6.5**), the mean relay zone AR for faults confined within a mechanical layer, of finite thickness (**Fig. 6.5**: red oval), will be greater than a relay zone from the same location which is no longer layer bound (**Fig. 6.5**: green oval). The scale-dependant behaviour of relay zone geometries can be incorporated into reservoir models, were lithological layering and thus mechanical stratigraphy is recorded. For instance, the geometry of discrete fracture networks can be made to vary depending on changes in mechanical layering within a reservoir.

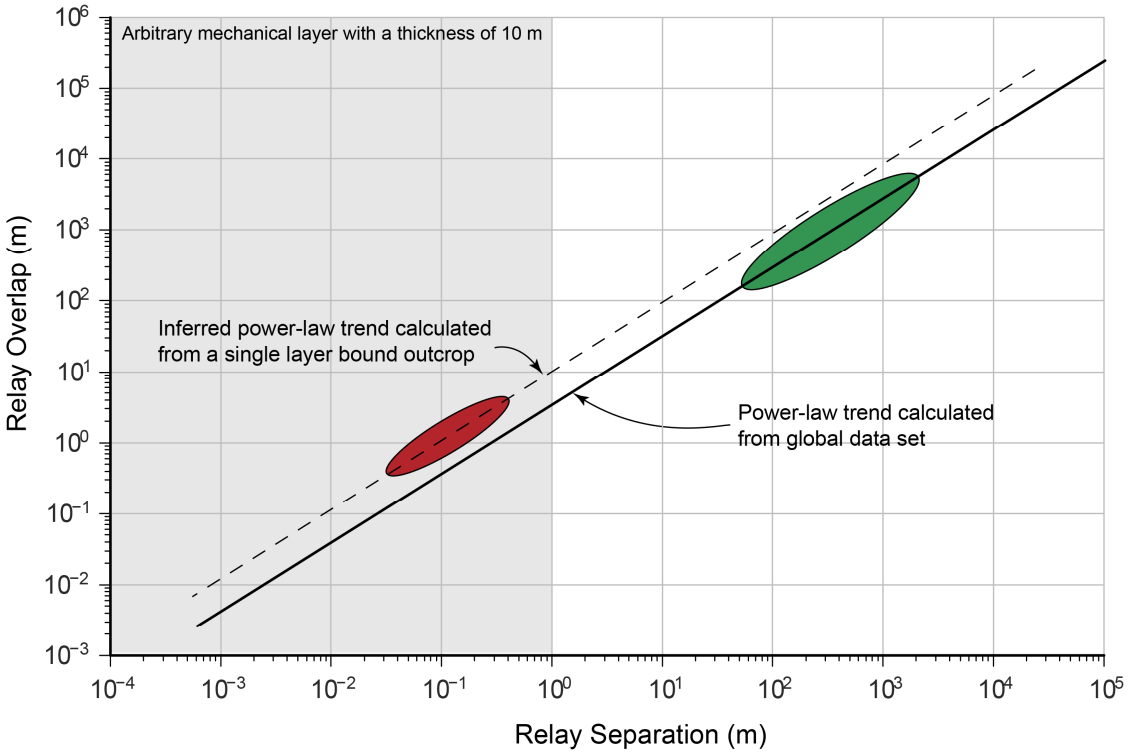

Fig. 6.5. The affect of outcrop-specific scaling factors. The light grey area of the plot relates to the thickness of an arbitrary mechanical layer 10 m thick. Faults confined within a mechanical layer develop longer overlap length for a given separation distance (**Fig. 6.1**e), see chapter 5 for details and figures therein. Relays, from the same location, that are no longer confined by the mechanical layer, propagate and interact as predicted by the fault interaction model of (Gupta and Scholz, 2000) and relay AR resemble the global average of 4.2 (**Fig. 6.1**). Inferred scaling relationships (dashed line) calculated from only mechanically confined relay zones (red region), such as at Kilve and Lamberton, will not necessarily reflect the geometries of relay zones at larger scales (green region). The global power-law scaling trend from chapter 5 is plotted for reference.

6.3 Future work

The inference that geometric coherence is more likely in certain tectonic settings (i.e. rifts) needs investigating in greater detail, for studies undertaken in this thesis were limited to similar tectonic settings. Fault-arrays from multiple tectonic settings with varying extension mechanisms need to be studied and compared. Such tectonic settings should include the forceful intrusion of buoyant materials, such as salt or magma. Understanding how faults grow, be it by the isolated fault growth model or the coherent fault growth model, is fundamental to our understanding of how materials deform. The fault normal rotation (FNR) method, developed during the thesis, could be used to identify which growth model prevails in different tectonic settings.

As touched upon during the method (Chapter 2), Elastic Dislocation (ED) models, such as that incorporated in FaultED, can be used to check the observed FNR strain predictions and in doing so also give weight to the theoretical equations that underpin the ED models. Further tests are required to strengthen the link between FNR and ED modelling. To do this, case studies should be chosen which do not have large mechanical contrast or growth strata, and where fault geometries are clearly imaged in 3D seismic data. In addition, outcrop studies should be used to see whether elastic dislocation models can predict known locations of fault-related strains. Possible case studies could be from Laminaria and Lilstock, respectively.

And finally, as mentioned in chapter 5 fault propagation models should incorporate pre-existing heterogeneities at the fault tips, such as veins or fractures (**Fig. 5.23**). For current models of fault propagation and linkage occur within homogenous mediums (Cowie and Scholz, 1992; Gupta and Scholz, 2000), which is not always a good approximation of natural fault networks (**Fig. 5.10**).

Chapter 7. Conclusions

1. The fault normal rotation (FNR) surface attribute utility developed during this thesis enables the quantitative analysis of the location and intensity of continuous fault-related deformation from centimetre to kilometre-scales.

2. In each chapter, the fault-arrays are shown to be geometrically coherent and thus are likely to have been kinematically coherent throughout their evolution. In addition, without the inclusion of the vertical displacements from areas of FNR (i.e. fault normal rotation, or continuous deformation) the fault-arrays could easily have been miss-interpreted as a series of overlapping, isolated faults.

3. In rift-like settings the internal deformation, which can be continuous (i.e. folds/monoclines) or discontinuous (i.e. faults), must sum to equal the extension at the margins. As a result, faults that are physically separated from each other must be soft-linked to balance the applied extension. Therefore, in rift-like settings, the coherent fault model (Walsh et al., 2003b) more accurately describes fault growth and interactions than the isolated fault growth model (Cartwright et al., 1996).

4. In non-rift-like settings, such as around salt diapirs, the episodic and variable extension results in pulses of fault growth. For individual fault families form synchronously from a single pulse of extension and are inferred to be coherent, whereas when faults formed from different pulses of extension overlap they do so by coincidence and thus conform to the isolated fault growth model.

5. From outcrop and seismic studies, fault linkage within relay zones does not exclusively evolve from a branch point but can link simultaneously at multiple points along overlapping fault tip lines. As a result, branch lines can be segmented.

6. The segmented nature of the BL will lead to segmented fluid flow pathways, which exploit the well-developed damage zones around BL.

7. Fault linkage evolution controls the amount and location of ramp rotation within a relay zone. For, on horizons where the relay ramp is intact, the ramp will accommodate shear strain, whereas on horizons where the relay ramp is breached, strains are localised onto a through going fault. Volumetric strains are required to accommodate strain incompatibilities created between horizons with different ramp rotations.

8. Relay zones that have slip-normal fault linkage enclose the base of relay zones with fault surfaces. Continued rotation of the overlying ramps causes high compressive stresses to develop leading to enhanced volumetric strains within the base of the relay zone.

9. Slip-normal fault linkage can enhance fault curvature normal to the slip direction. Fault curvature at BL can act as an asperity impeding slip on the through going fault. Until these asperities are removed, apparently breached relay zones can continue to evolve.

10. Displacement distributions within open relay ramps at the earth's surface can be used to infer fault linkage at depth, which can be used to determining the potential size of a rupture plane and the likely size of an earthquake. Relay zones are 3D structures and therefore their 3D geometry needs to be considered when determining the potential seismic hazard for a fault-array.

11. The overlaps and separations of relay-bounding faults display a single power-law scaling trend over 9 orders of magnitude of $y=3.6156x^{0.97}$ $R^2=0.98$ and a mean AR of 4.2, which is similar to published datasets that display power-law exponents of 0.97 and a mean AR that ranges from 4 to 5. The strong power-law trend for relay zone AR suggests that a single mechanism is the control on the geometry of relay zones, which is summarised by Gupta and Scholz, (2000) model of fault interaction.

12. Two outcrops, Kilve and Lamberton, display mean AR of 8.60 and 8.64 respectively, which are greater than the mean AR for all recorded relay zones (4.2). This suggests that outcrop specific controls exist that modify the Gupta

and Scholz, (2000) model of fault interaction and facilitate the development of relay zones with above average AR.

a. Faults at Lamberton and Kilve are confined within a mechanical layer and as a result have low displacement/length ratios. While faults are confined, the horizontal extent of the stress drop region is small when compared to unrestricted faults. Therefore, for the same separation distance mechanically confined faults can overlap unhindered compared to unrestricted faults of the same length, while still remaining geometrically coherent. When faults eventually break through the confining layers i.e. the surrounding shale beds, fault displacement can increase and therefore the size of the stress field also increases. Faults that could previously overlap unhindered now become laterally pinned by the critical stress drop contour and fault begin to coalesce forming relay ramps with larger overlap lengths and thus higher than average AR.

b. For Kilve, pre-existing calcite veins ahead of propagating fault tips are inferred to lower the yield strength at the fault tip, which in turn lowers the peak stress required to propagate the fault tip. This allows a fault tip to propagate further into the stress drop region of the nearby fault compared to faults within material with stronger yield strengths. In addition, the vein hosted fault tip is enclosed by mechanical boundaries between the host rock and vein walls, which could concentrate stress within the pre-existing veins enhancing fault propagation, thus facilitating elevated overlap lengths and thus above average AR.

13. Outcrop specific and therefore scale-dependant modifications to the AR of relay zones, such as in Lamberton and Kilve, can complicate the scaling of relay geometries. For, the mean AR of a relay zone will vary at different scales depending on whether the specific control, such as mechanically confined faults, exist at that scale.

Appendices

Table of content

Appendix 1. Extra literature material

Supporting figures from the literature are included for reference. Where appropriate the figures are modified to emphasise the relevant points. For details of each figure/table, and it source publication, see the figure captions.

In summary this appendix contains extra material relating to:

- The classification of fault zones and fluid pathways.
- The shapes of “ideal” fault surfaces.
- The displacement fields around normal faults.

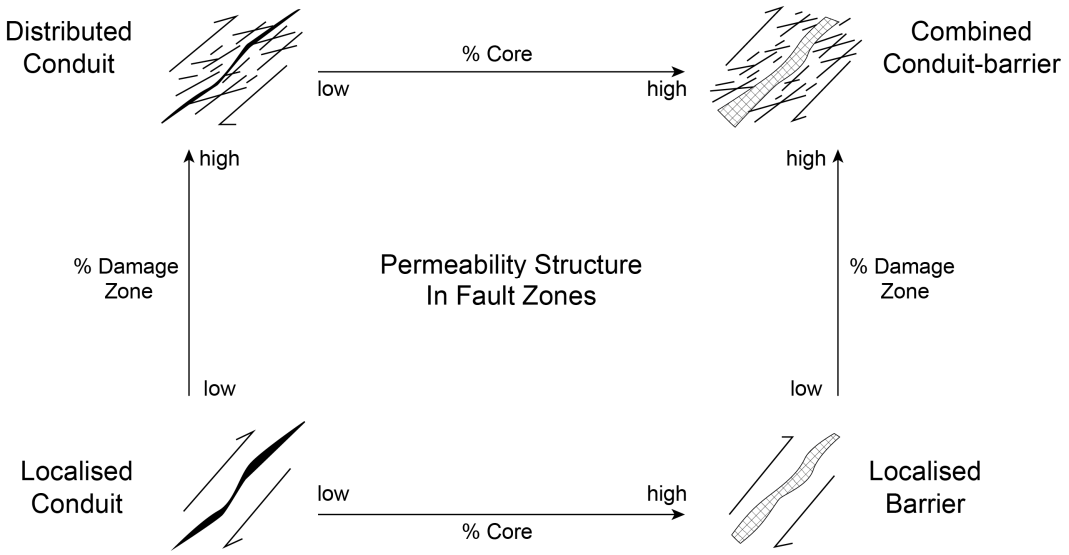

Fig. A1. Conceptual scheme for fault-related fluid flow. From (Caine et al., 1996).

Permeability structure	Architectural style	Fault core	Damage zone	Examples	Applicable flow model
Localised conduit	Localised slip along a single curviplanar surface or along discretely segmented planes.	Absent to poorly developed.	Absent to poorly developed.	Small faults in Shawangunk Mountains of eastern New York.	Discrete fracture modelled as conduits with parallel walls.
Distributed conduit	Distributed slip accommodated along distributed surfaces and fractures.	Absent to poorly developed as narrow, discrete and discontinuous bands.	Well-developed discrete slip surfaces and associated fracture networks.	Modern accretionary prisms.	Equivalent porous medium.
Localised barrier	Localised slip accommodated within cataclastic zone.	Well-developed fault core cataclasites.	Absent to poorly developed.	Deformation bands in sandstones.	Aquitard (fault core) within a highly permeable aquifer (protolith).
Combined conduit-barrier	Deformation accommodated within a localised cataclastic zone and distributed zone of subsidiary structures.	Well-developed fault core cataclasites.	Well-developed discrete slip surface and associated fracture network.	Dixie Valley normal fault, Nevada.	Aquitard (fault core) sandwiched between two aquifers (damage zones).

Table A1. Fault zone architectural styles and permeability structure (Caine et al., 1996: and references therein).

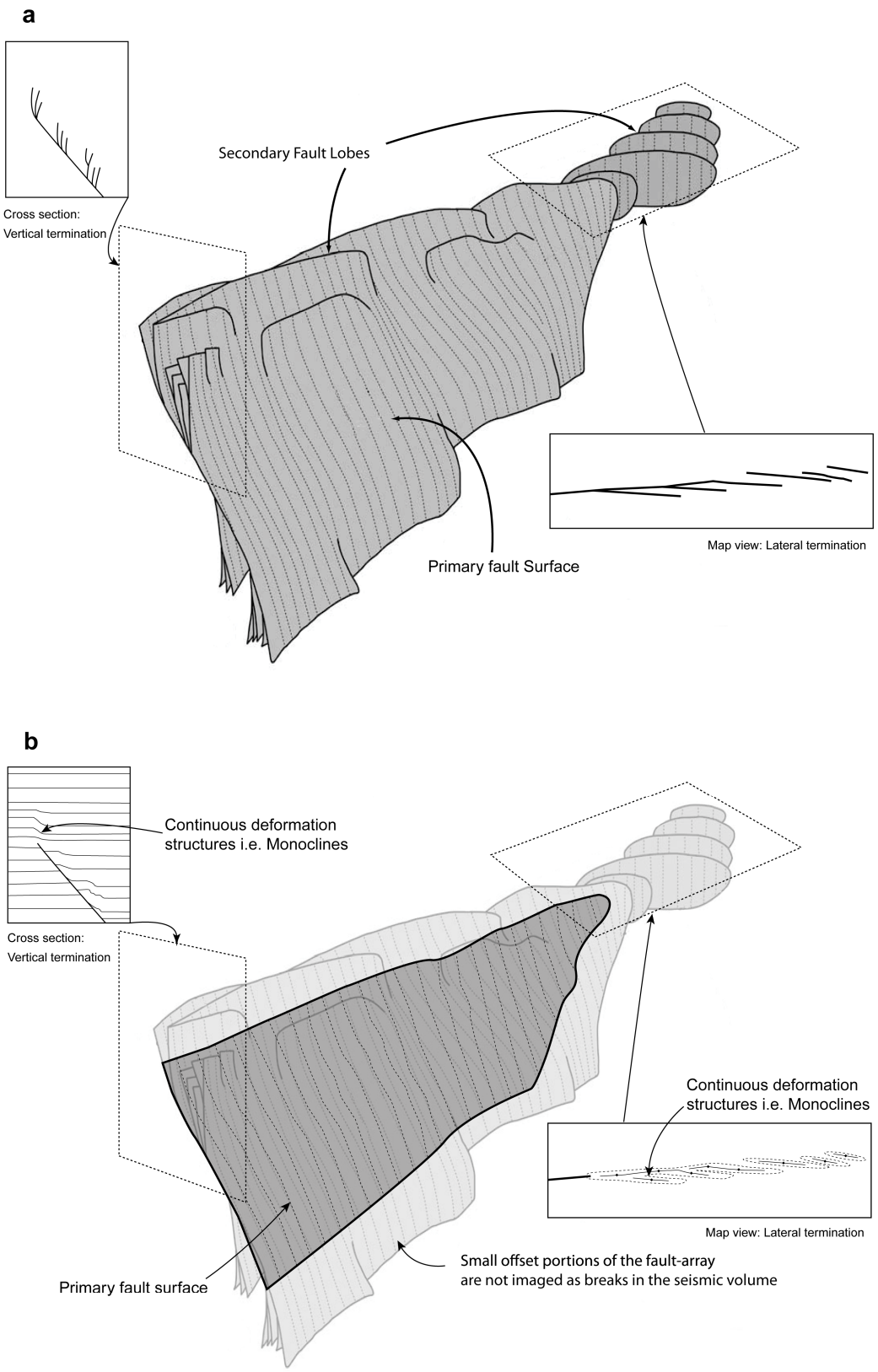

Fig. A2. Simplified 3D geometry of normal faults. (a) The half-plane of a normal fault composed of a primary fault surface and secondary fault lobes, which are either physically linked to the primary surface or soft-linked via a relay ramp. (b) Is a schematic illustration of the mappable section of (a) imaged in seismic data. Low offset structures are not visualised as breaks in the seismic but are imaged as continuous rotations of the seismic horizons, such as monoclines. Modified from (Marchal et al., 2003).

Appendix 2. FNR Method

To expand on material presented in the methodology sections of this thesis, extra details are given, which can aid in the replication of my results.

In summary this appendix contains material on:

- Workflows untaken to create surfaces and extract fault normal rotation (FNR) data.
- Details on how I gridded the raw FNR point data.
- Examples of how FNR data can be plotted for analysis.

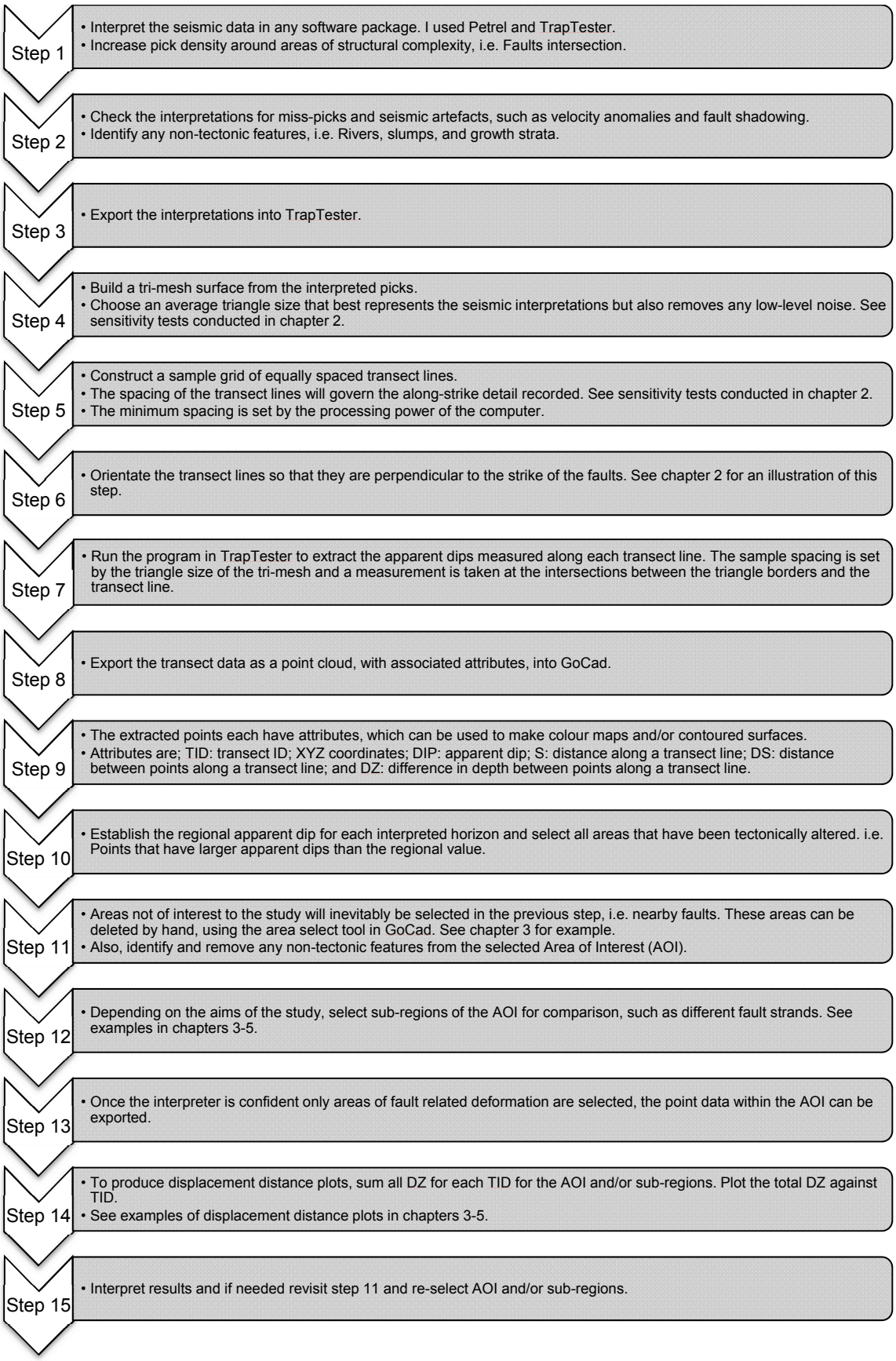

Fig. A3. Workflow for building and a digital surface from seismic data and extracting FNR data for interpretation.

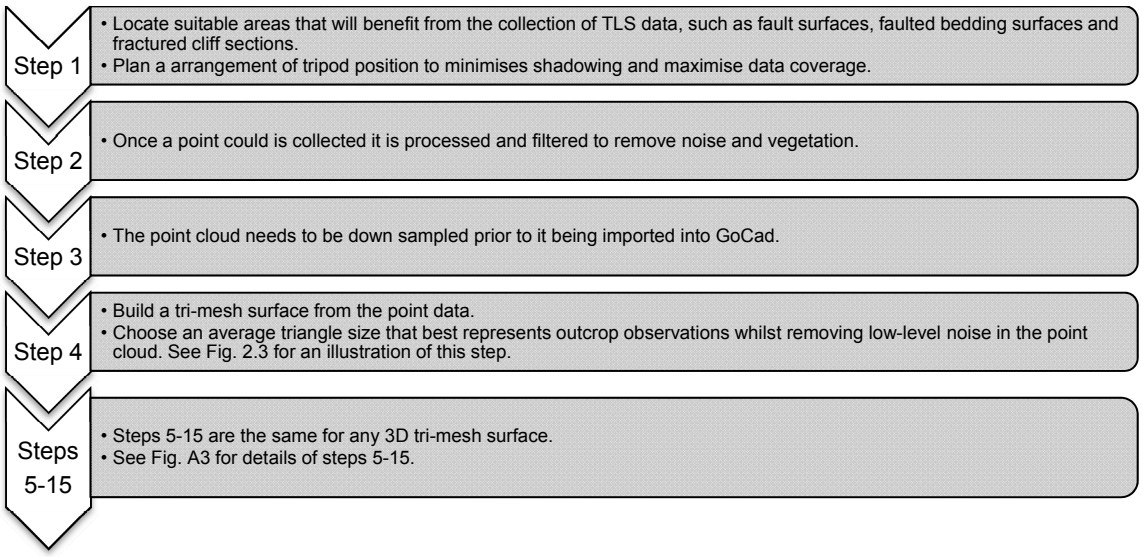

Fig. A4. Workflow for building a digital surface from outcrop data for interpretation using the new FNR method.

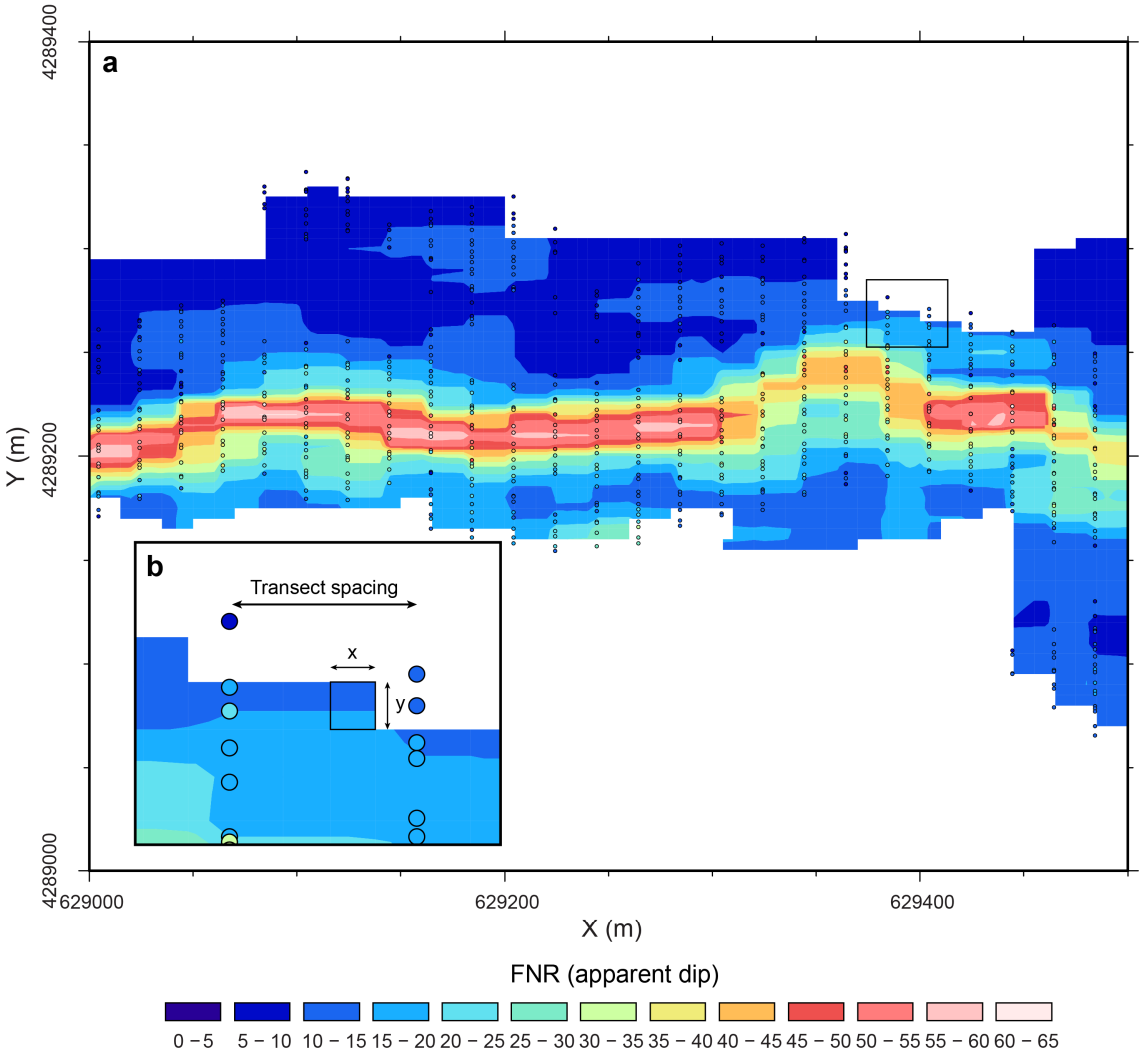

Fig. A5. Overview of how FNR point data is gridded. (a) A section of the Arches relay ramp, presented in chapter 2 (method). The raw FNR data points are circled and coloured for the recorded value. The arrangement of the raw point data reflects the dimensions of the sampling grid and points are aligned into parallel transects. To create a continuous FNR map the point data is gridded, which aids in highlighting trends within the point data. (b) The point data was gridded using a nearest-neighbour gridding algorithm in the open source software package GMT (Generic Mapping Tool). An equally sized grid dimension was chosen, which was less than the transect line spacing, so that along-strike variations in FNR were captured. A limitation in the gridding algorithm is that data on extremities of the area of interest do not always meet the gridding criteria and are not gridded. In datasets where this is a problem the raw point data is overlaid for clarity.

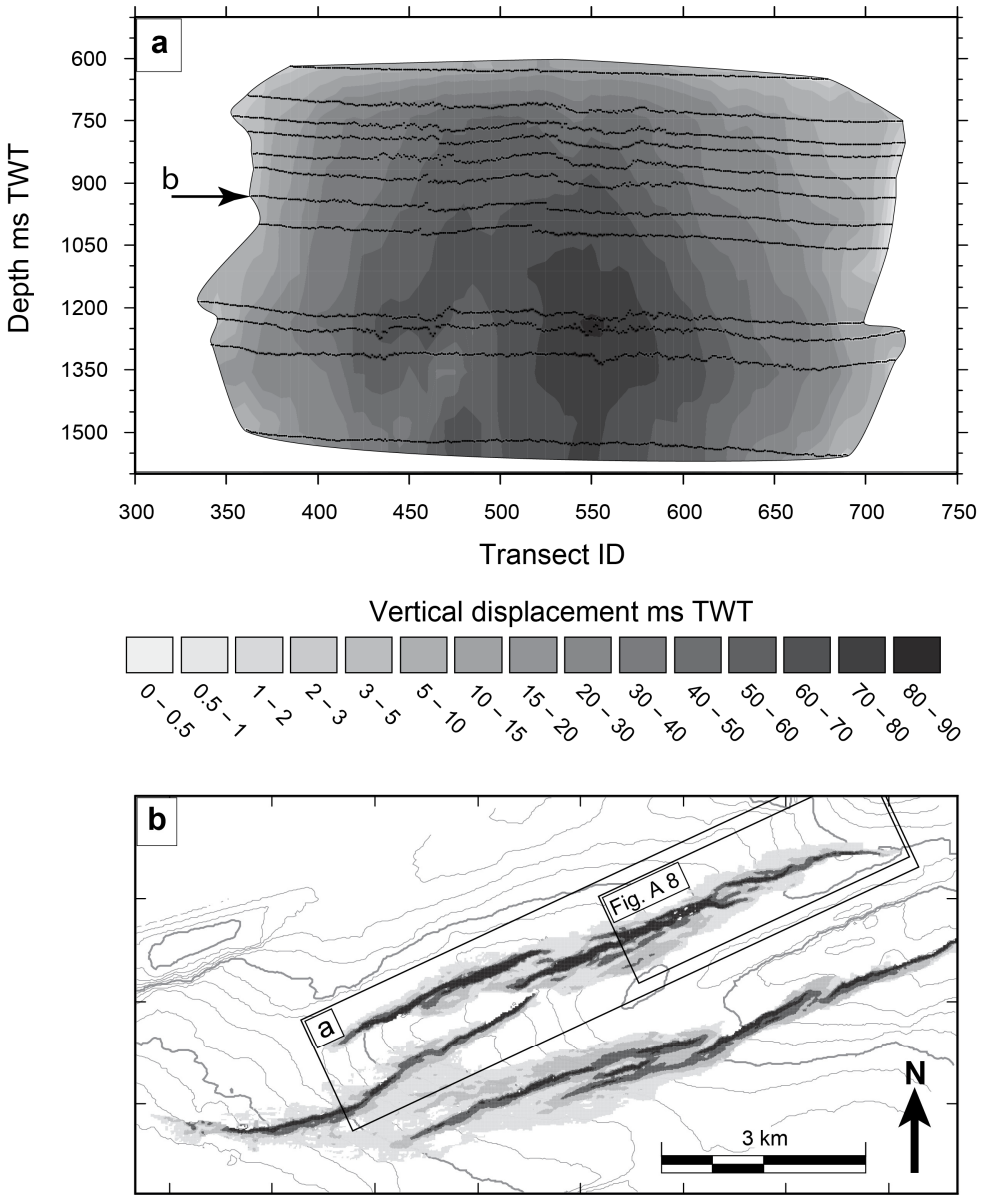

Fig. A6. An example of a pseudo fault surface plot contoured for displacement from the Laminaria High 3D seismic survey. (a) A pseudo fault surface viewed in strike projection, black dots indicate the locations of the raw data points from which the contours are made. The displacements are from the entire fault-array in (b), and include both continuous and discontinuous displacements from all the mapped horizons. Therefore, the edges of the pseudo fault surface do not refer to the mapped location of a fault tip but are the locations at which any form of deformation stops. The distribution of displacement is highest in the centre and decreases towards the pseudo tip line, which is similar to throw distributions on isolated faults. (b) Map view plot of horizon H8. Arrow in (a). The contours are for time depth and are in ms TWT. The grey scale shading represents the distribution of FNR and is plotted for reference. For a detailed view of FNR distributions in Laminaria, see figures in chapter 4.

Fig. A7. (Next page) Examples of detailed pseudo fault surfaces contoured for displacement from the Laminaria High 3D seismic survey, box in (**Fig. A6**). In this figure the displacements from different regions of the fault-array (f), are plotted individually (a-e). (a) Vertical displacements from the footwall. (b) Vertical displacements (throw) from fault Fa-3. (c) Vertical displacements (throw) from fault Fa-2. (d) Vertical displacements from the relay ramp. (e) Vertical displacements from the footwall. Each panel (a-e) is spatially aligned. In general, the displacement distributions for the two faults (b and c) resemble that of the entire fault-array (**Fig. A6**a). However, the distribution of deformation in the footwall, hanging wall and ramp varies with depth and along-strike. This type of diagram could be used to map the changes in distribution of fault-related deformation around mapped fault surfaces.

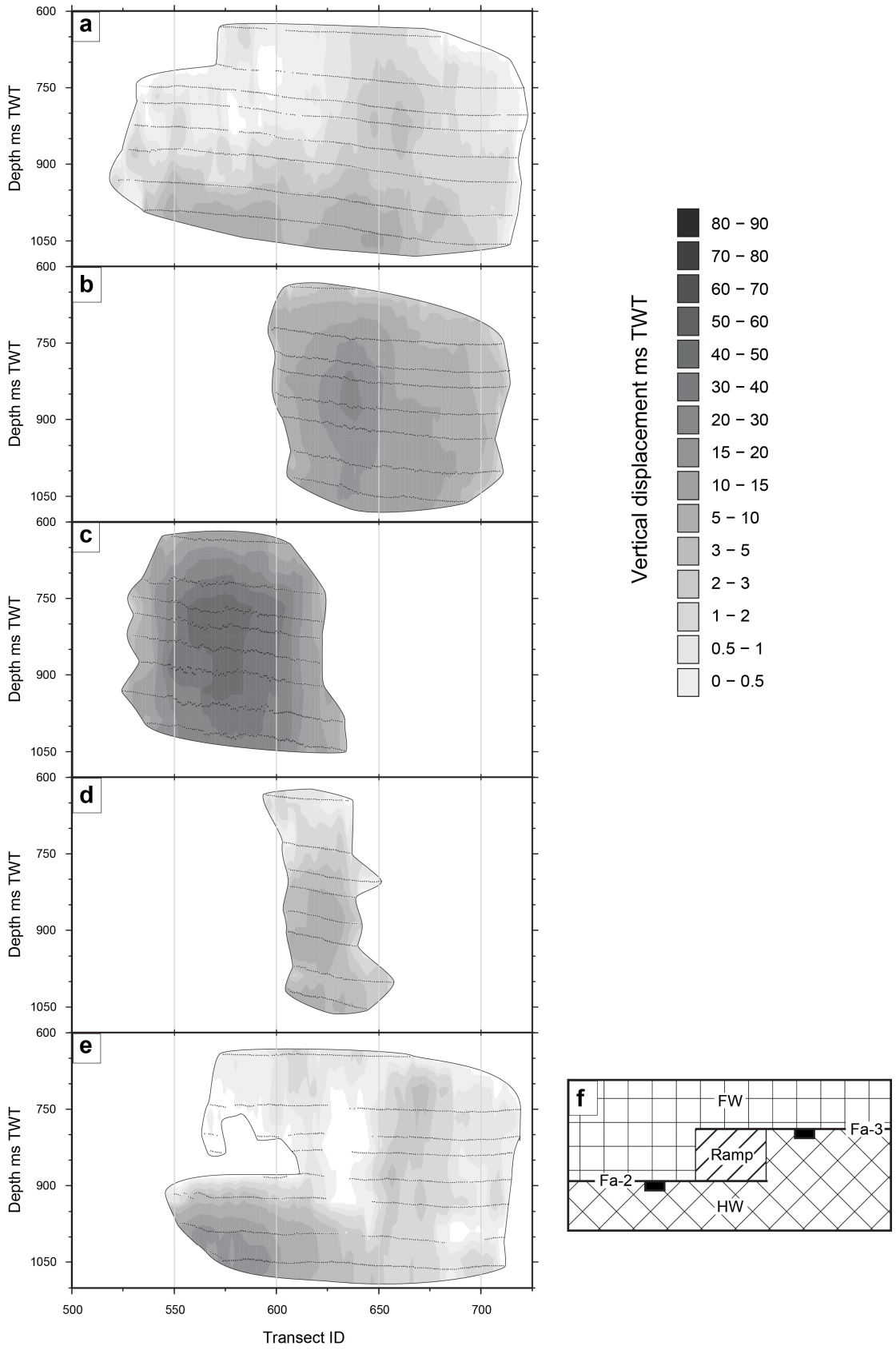
a
b
c
d
e
f
Depth ms TWT
600
750
900
1050
500
550
600
650
700
Transect ID
Vertical displacement ms TWT
80 – 90
70 – 80
60 – 70
50 – 60
40 – 50
30 – 40
20 – 30
15 – 20
10 – 15
5 – 10
3 – 5
2 – 3
1 – 2
0.5 – 1
0 – 0.5
FW
Fa-3
Ramp
Fa-2
HW

Appendix 3. Location maps and field photos

For reference extra location maps and field photos are included, where needed.

In summary this appendix contains:

- Time depth map of the entire Laminaria High 3D Seismic Survey.
- Location and overview map of the Moab relay ramp.
- Field photos of the Moab relay ramp.
- Location maps and stratigraphic columns for Kilve, Lilstock and Lamberton field areas.

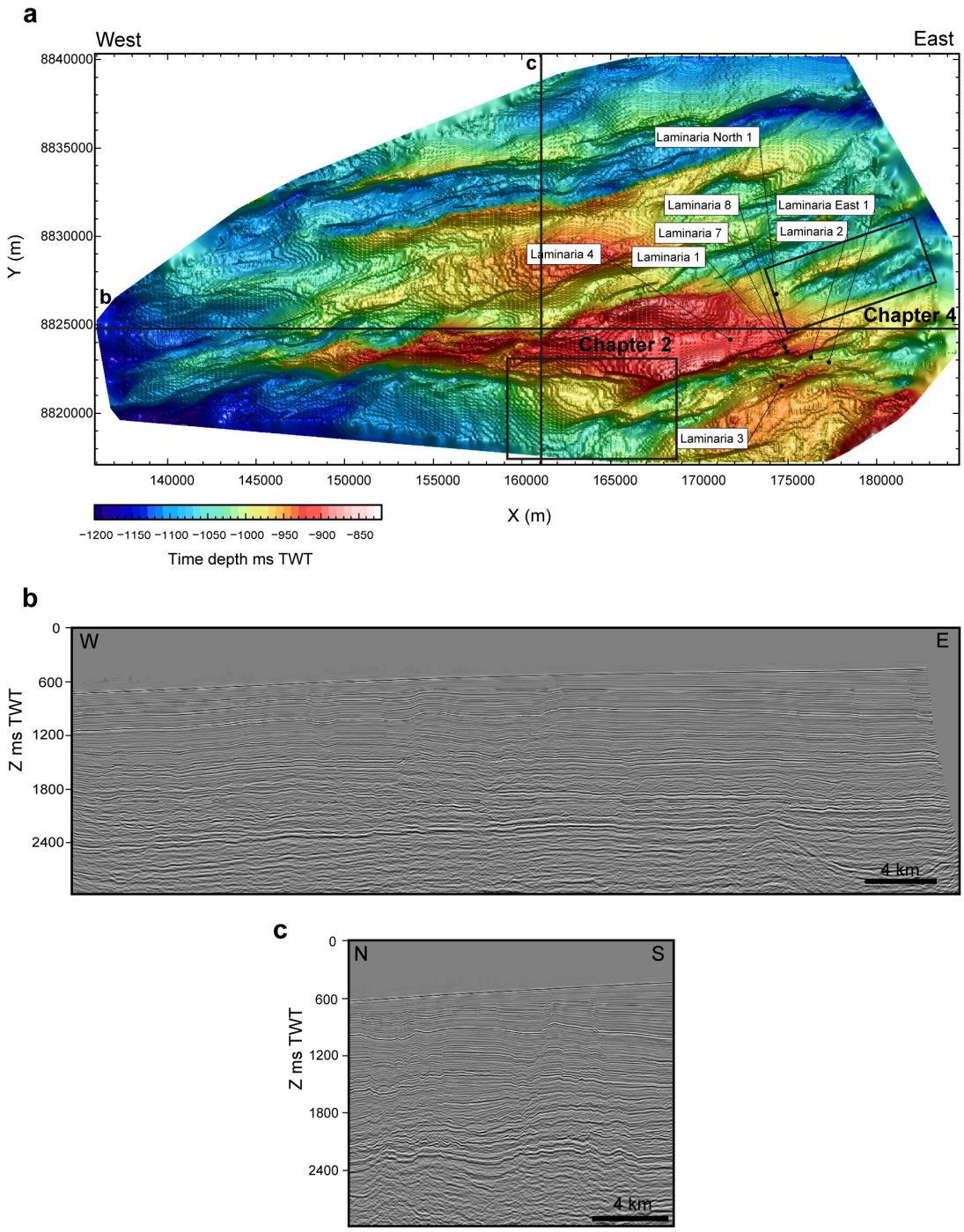

Fig. A8. Time structure map and seismic sections for the Laminaria High 3D seismic survey. (a) A seismic time depth horizon of horizon H9, for the entire lateral extent of the seismic survey. The locations of detailed studies are boxed and all well locations are annotated. Faults trend roughly E-W and form a series of graben and horst structures. (b) An un-interpreted regional cross-line and (c) inline.

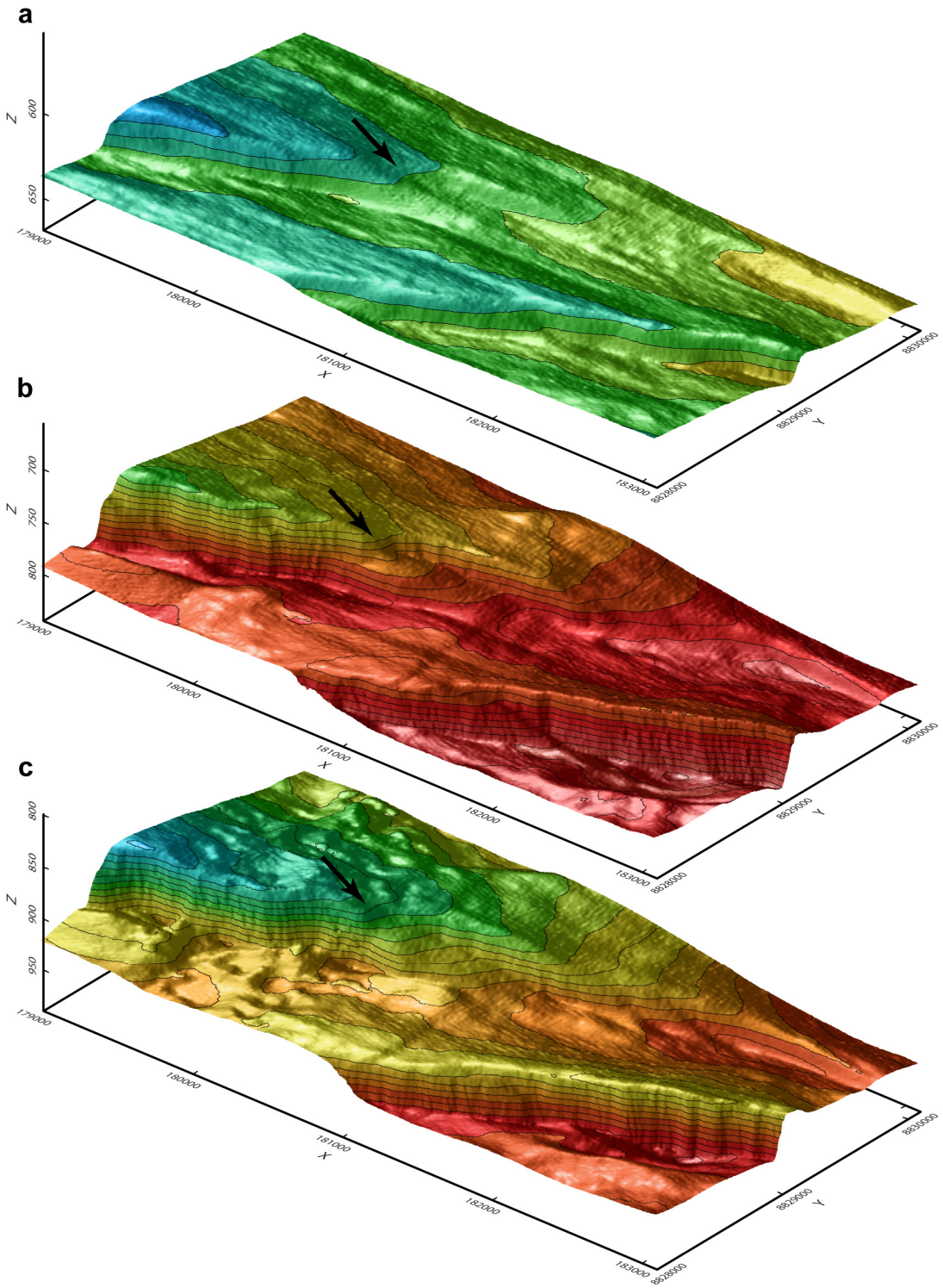

(Figure continues on next page)

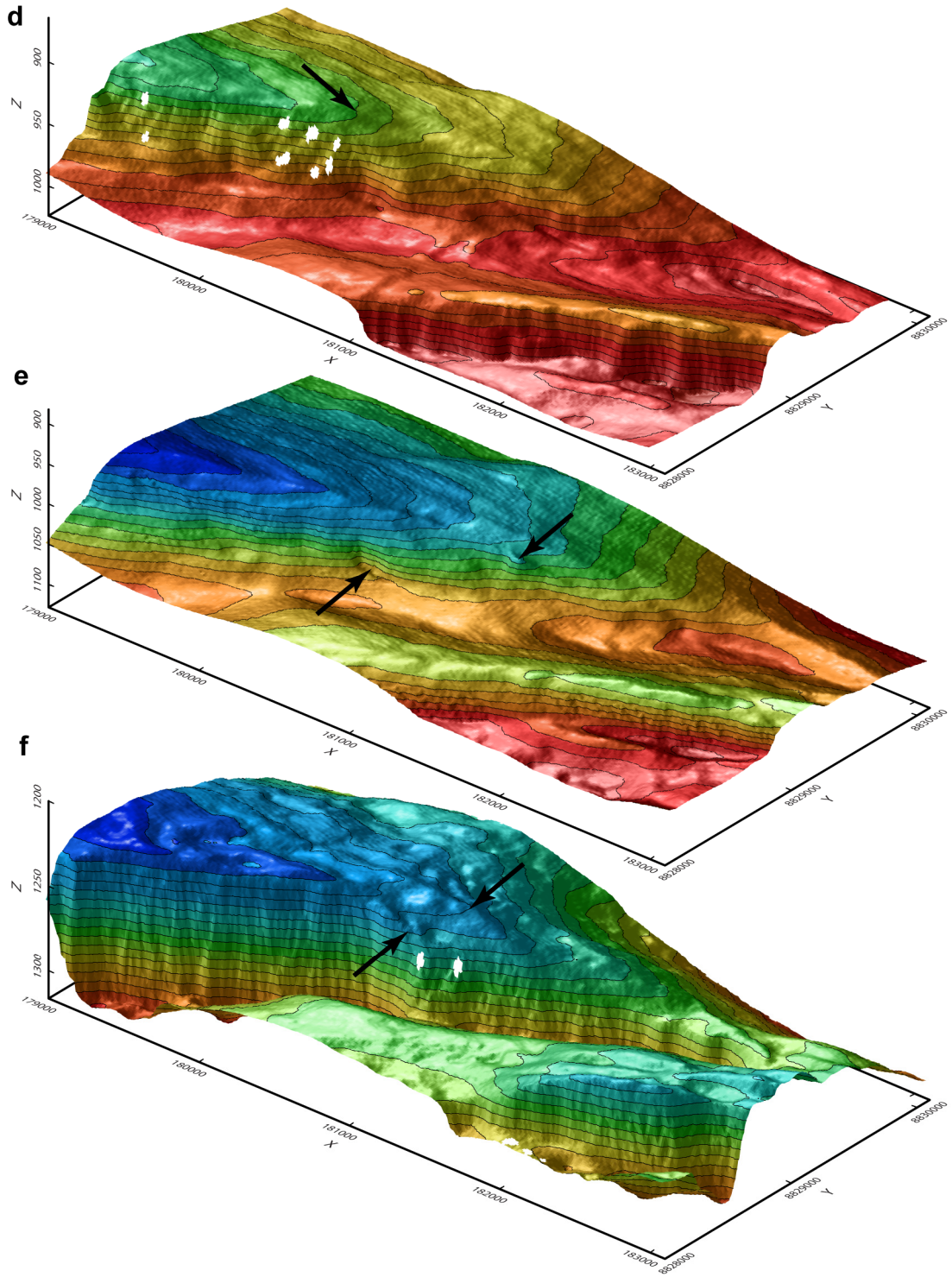

Fig. A9. 3D views of horizons (a) H2, (b) H4, (c) H7, (d) H8, (e) H9, and (f) H12 from Laminaria R2. Arrows in (a-d) indicate the location of the cross-ramp fault linking the overlapping fault segments F4 (FWF) and F3 (HWF). Arrows in (e-f) indicate the location of the two bounding faults F4 and F3. Note that in (e) there is no fault scarp linking the two overlapping faults. In (f) the along-strike bend in the main fault (F3) is associated with a minor fault in the FW.

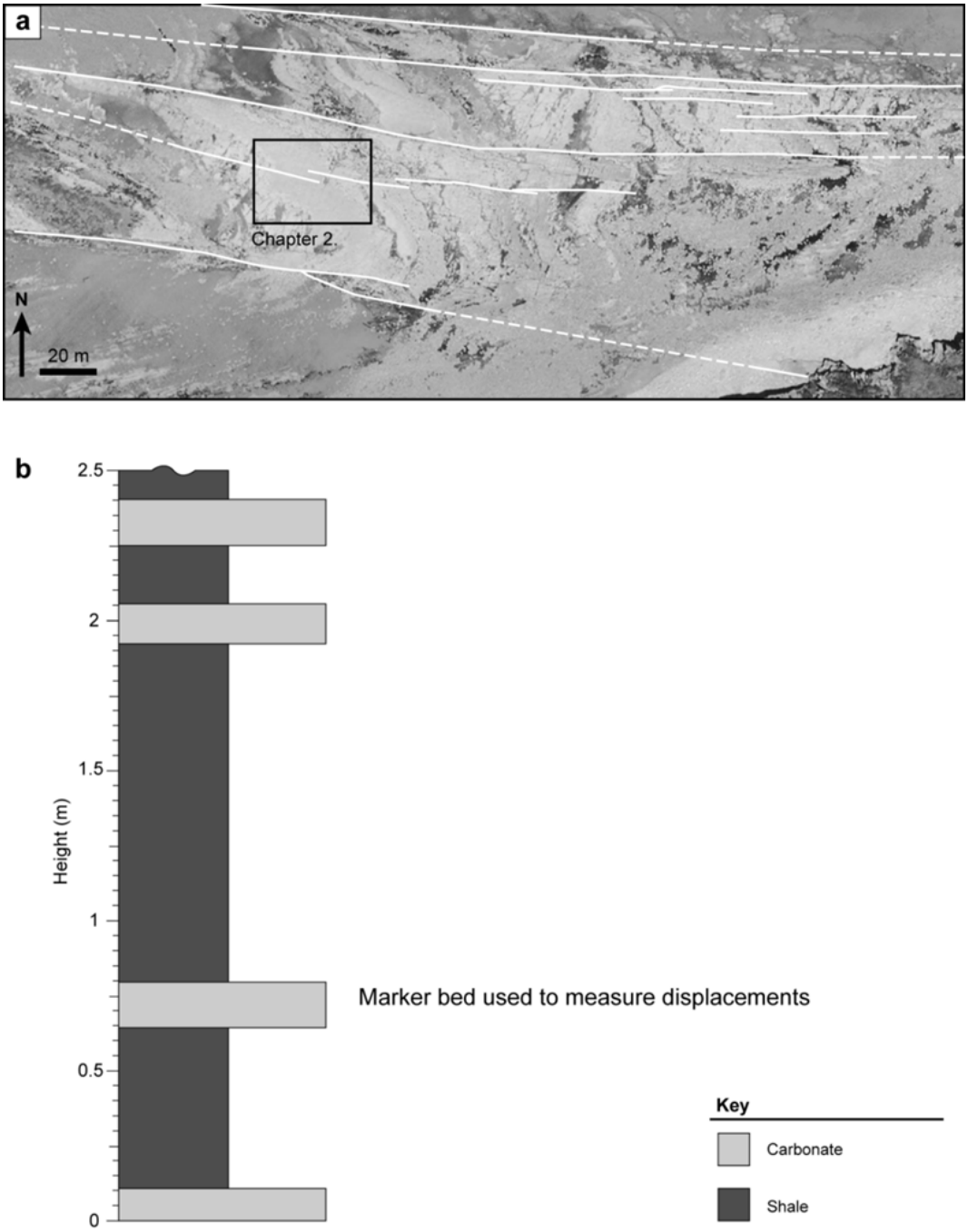

Fig. A10. Location map and stratigraphic log for Lilstock, UK. (a) Aerial photo of the wave-cut-platform near Lilstock, Somerset, UK. The main fault segments are annotated and they trend approximately E-W. The relay zone presented in chapter 2 is boxed. Image from Google Earth. (b) A stratigraphic log depicting the mechanical stratigraphy around the marker bed from which displacements where calculated in chapter 2.

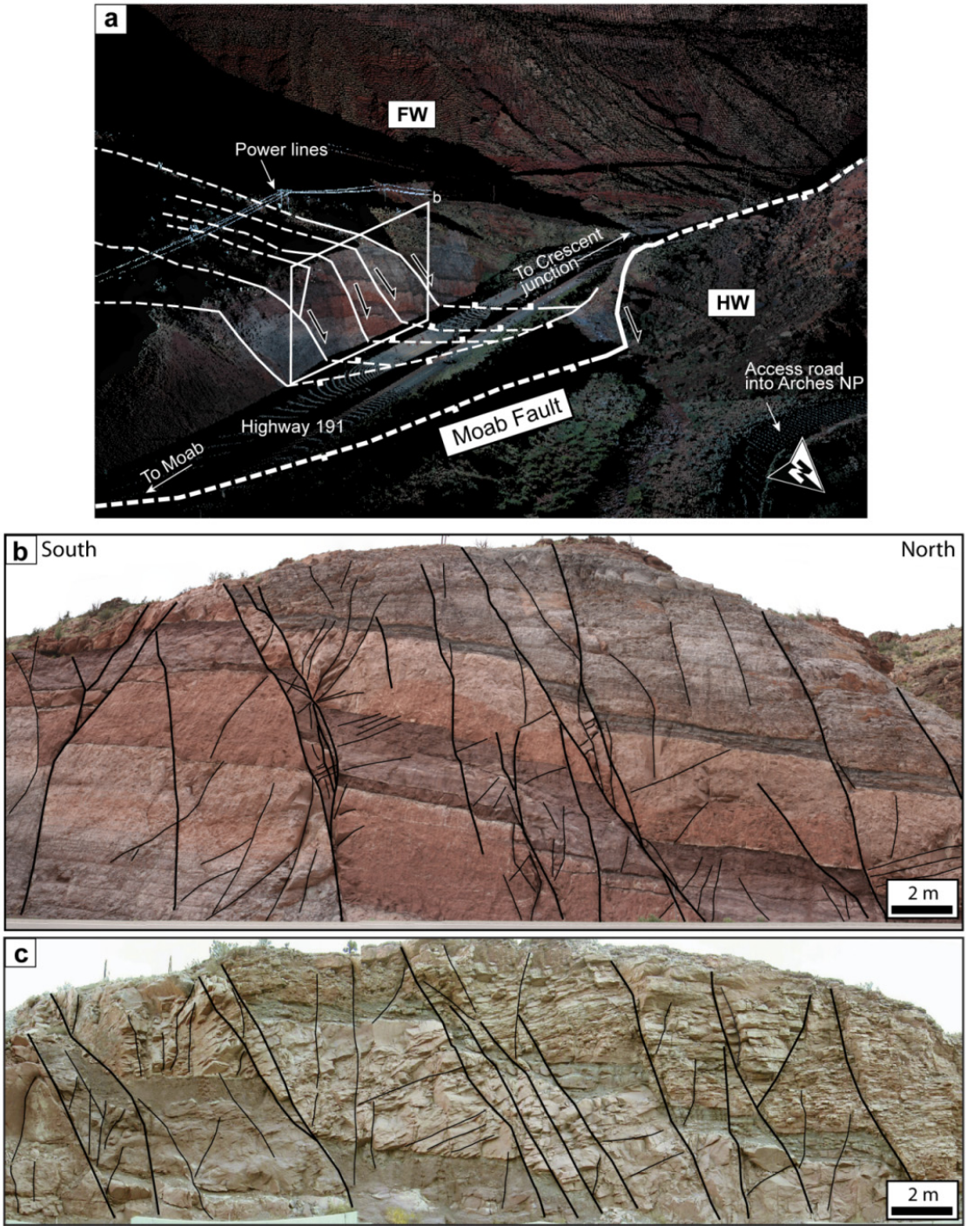

Fig. A11. Moab Location map and overview images of the Moab relay zone. (a) Perspective image of the coloured point cloud collected using a terrestrial laser scanner. The outcrop is located on a vertical road cutting opposite the entrance to Arches National Park. The faults studied trend NNW-SSE and splay off the main Moab fault, which trends NW-SE. The faults in the HW are inferred to form synchronously with the main Moab fault and are located at an along-strike bend in the Moab fault. (b) A photo of the outcrop surface. The main faults and fractures are annotated. Photo taken in 2010. (c) A previous section through the outcrop prior to the expansion of highway 191. The main faults and fractures are annotated. Taken in 2003 by Russell K. Davies of Rock Deformation Research USA Inc.

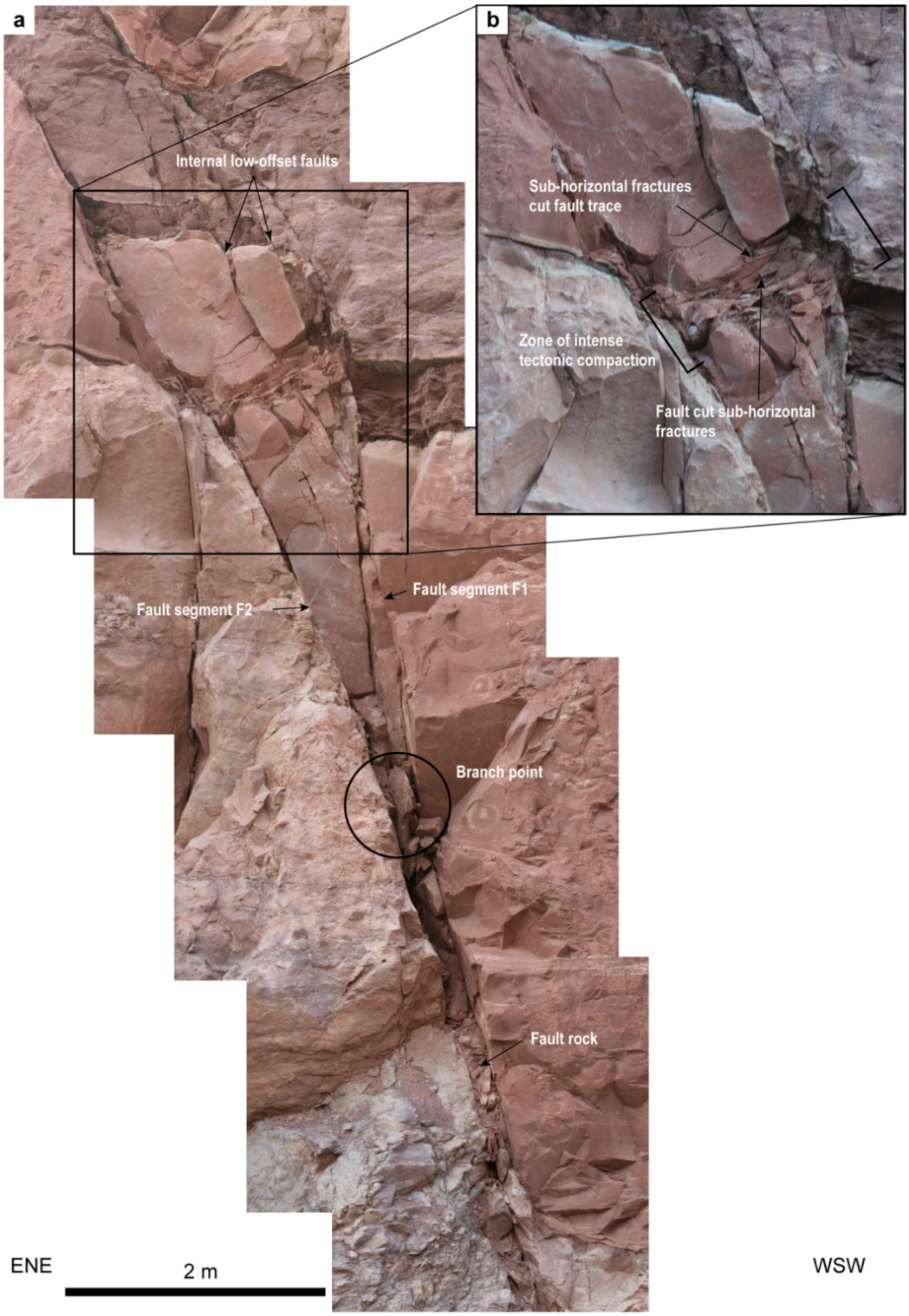

Fig. A12. (a) Photo mosaic of the Moab relay zone. Fault segments F1 and F2 link down-dip at a branch point (circled). Within the ramp low-offset faults cut the ramp and cut back sequentially into the ramp. (b) Close up photo of the internal ramp deformation. A zone of tectonic compaction crosses the ramp. The sub-horizontal fractures formed synchronously with the internal faults, as they both cross-cut each other.

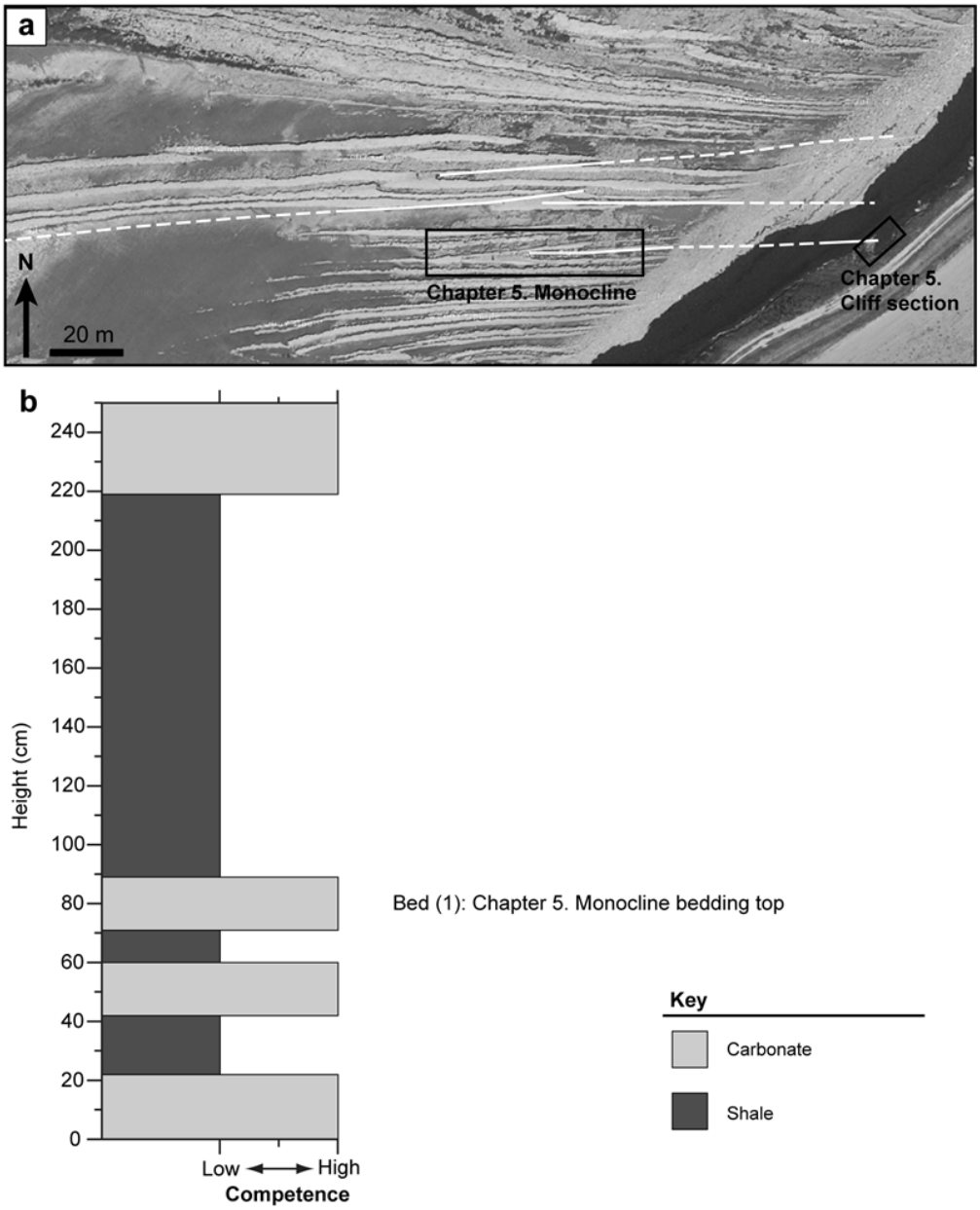

Fig. A13. Location map and stratigraphic log for Kilve, UK. (a) Aerial photo of the wave-cut-platform from near Kilve, Somerset, UK. The location of the detailed studied locations is boxed. The main fault segments are annotated and trend E-W. Image from Google Earth. (b) Stratigraphic log for the beds around those depicted in chapter 5. The stratigraphic log illustrates the variable mechanical stratigraphy between the carbonate and shale beds.

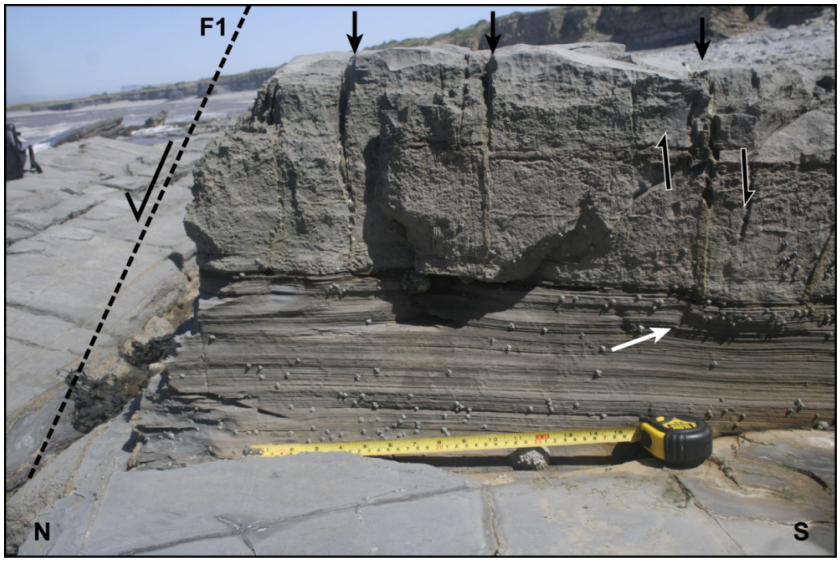

Fig. A14. A field photo from Lilstock. Veins are annotated with arrows (black) and are only present in the carbonate beds and they do not penetrate, or offset, the laminated shale bed below. A vein with approximately 1 cm of offset is annotated with a white arrow. This structure causes the warping of the underlying shale bed but is still confined within the carbonate bed, i.e. the fault is confined within a mechanical layer. A fault with 64 cm of offset is located on the edge of the photo and is annotated F1.

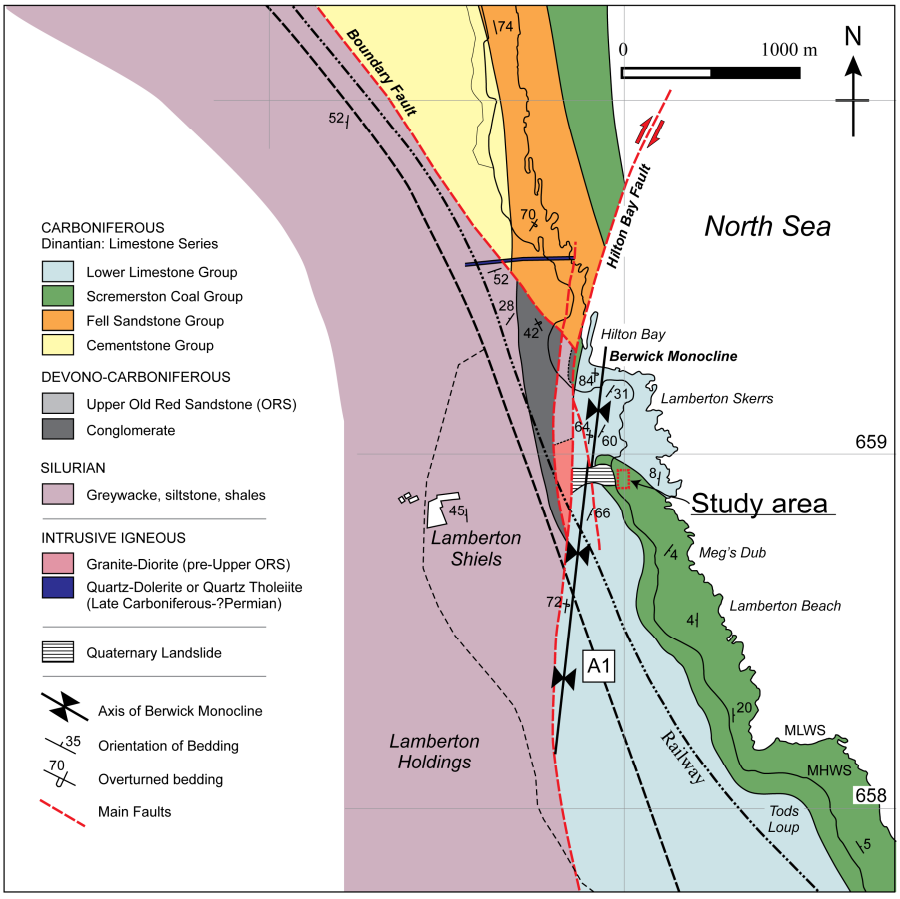

Fig. A15. Location map for the study area at Lamberton.

Appendix 4. Equation sheet

This appendix outlines the fault interaction model of Gupta and Scholz (2000), which is inferred in the thesis to control the geometry of relay zones. For context information on the Dugdale model is also given.

7.1 The "Fault interaction model" of Gupta and Scholz (2000)

A brief summary of the main points of the fault interaction model:

1) Uses the Dugdale model as a starting point (see section 7.2). i.e. a crack deforms plastically whereas the region ahead of the crack tip deforms elastically.
2) When a fault propagates into a stress drop region of a nearby fault the stresses at the fault tip need to balance both the yield stress of the rock and the shear stress drop produced by the nearby fault (see section 7.3).
3) At a critical stress drop contour the propagating fault tip is laterally pinned, as it is no longer able to balance the induced stress drop caused by the nearby fault (**Fig. A16**).
4) A relay ramp is developed between the laterally pinned faults, causing the rotation of the ramp until the yield strength of the ramp is overcome and the faults coalesce.
5) Incorporates the changes in displacement along-strike of a fault into the calculation of stress drop, i.e. net displacement on a fault not just individual ruptures.
6) The stress fields around a fault is calculated by determining the deflections of a horizontal surface by a vertical screw dislocation and converting shear strains into shear stresses.

7.2 A summary of the Dugdale model

As summarised by (Cowie and Scholz, 1992), the main points of the Dugdale model (Dugdale, 1960) that are relevant for this thesis are:

1) The peak stress at the tip of the crack just equals σ_y (yield strength).
2) The material beyond the tip of the crack deforms elastically.
3) The size of the inelastic zone, i.e. the length over which a crack extends, decreases as the yield strength, σ_y, of the material containing the crack increases. Conversely, if the applied remote extensional stress remains constant, as σ_y decreases the length of the crack (fault) will increase.

7.3 Propagation criterion

The propagation criterion applies to a mode III fault tip. For fault F1 to continue propagating into the stress drop region of fault F2 (**Fig. A16**), the stress concentration at the crack tip must increase to balance the stress drop, which is expressed as:

$$\sigma_{p(F1)} = \sigma_y + \Delta\sigma_{(F2)} \qquad \textbf{(Eq. A1)}$$

Where $\sigma_{p(F1)}$ is the peak stress at the tip of F1, σ_y is the material yield strength, and $\Delta\sigma_{(F2)}$ is the shear stress drop produced by fault F2 at the tip of F1 (**Fig. A16**). In an isolated fault the peak stress equals the yield stress, as the Dugdale model requires.

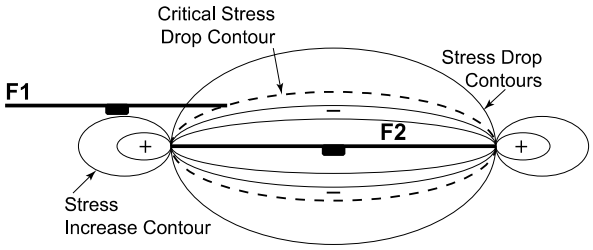

Fig. A16. Map view of the stress field around fault F2 and its interaction with the propagating tip of F1. The stress field for F2 is modelled as if an isolated fault, which is taken to be a first order approximation of the stress field for the relay zone. Each fault is surrounded by a region of stress drop and stress increase near the tips. Taken from (Gupta and Scholz 2000).

7.3.1 Summary of equation (Eq. A1)

The peak stress at the tip of F1 must balance both the yield stress and the induced stress drop, caused by F2. To propagate the fault within a stress drop region the peak stress must thus increase. This can be achieved by increasing the displacement gradients at the fault tips (Gupta and Scholz, 2000). The yield stress is an intrinsic property of the material being deformed and can be obtained from rock deformation experiments. Calculating the stress drop is a more involved process and is outlined in the next section.

7.4 Determining the stress drop around F2

Gupta and Scholz (2000) simplify a fault to a vertical screw dislocation and the horizon to a flat surface after (Contreras et al., 1997). A realistic fault surface is approximately

elliptical and displacement varies with depth, however the fault surface is approximated to a rectangle with constant displacement with depth (**Fig. A17**).

(**Eq. A1**) is a modification of (Contreras et al., 1997) which incorporates changes in displacement along-strike and depth:

$$w(x,y) = \frac{-u(x)}{\pi}\left(arctan\left(\frac{H}{y}\right)\right) \qquad \textbf{(Eq. A2)}$$

There w is the solution for the deflection of a horizontal surface due to a vertical screw dislocation (**Fig. A17**b). The x-axis runs along fault strike, the y-axis is perpendicular to the fault plane, u(x) is the characteristic displacement distribution for the fault population being studied (**Fig. A17**a) and H is the dislocation depth.

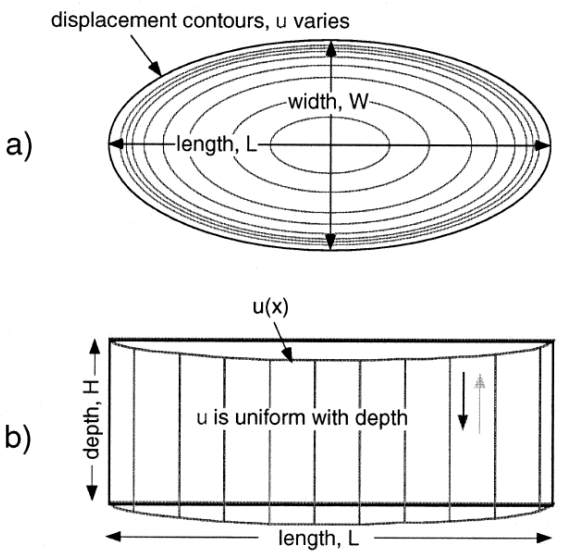

Fig. A17. (a) A realistic fault plane has an elliptical tip line and displacement varies from displacement maximum near the centre to zero at the tip line. (b) Dislocation geometry: We use a rectangular dislocation and uniform displacement with depth, equal to the surface displacement, u(x), to approximate the displacement field. We must scale H properly to obtain a reasonable approximation to the actual displacement field. From (Gupta and Scholz 2000).

7.4.1 Determining the depth of a dislocation

The depth of the dislocation:

$$H = C_2 L \qquad \textbf{(Eq. A3)}$$

Where C_2 is a constant that depends on the slip distribution and shape of the fault plane, and L is the length of the fault (**Fig. A17**).

In the case of the Solite Quarry, which is the worked example given by Gupta and Scholz (2000), an average height, h_{avg}, of a fault is taken to be L/8. However, because displacement, u(x), is assumed to be constant with depth this will produce too broad a surface displacement field. This is compensated by assuming a fault of half its actual depth, i.e. H ≈ L/16, hence C_2=1/16, in the case of the Solite Quarry.

7.4.2 Converting a deflected surface in to a shear strain

Partial derivative of deflection, w, with respect to y to obtain the shear strain:

$$\varepsilon_{zy} = \frac{1}{2}\left(\frac{\partial w}{\partial y} + \frac{\partial v}{\partial z}\right) = \frac{u(x)H}{2\pi y^2}\left(1 + \left(\frac{H}{y}\right)^2\right)^{-1} \quad \textbf{(Eq. A4)}$$

Gupta and Scholz (2000) neglected the contribution to shear strain from $\frac{\partial v}{\partial z}$, the change in displacement in the y-direction with depth, because it is small relative to the change in deflection, w. ε_{zy} is the shear strain along the zy plane, i.e. normal to fault strike (**Fig. A17**b).

7.4.3 Converting shear strain around a fault to shear stress drop

The shear strain calculated in (**Eq. A4**) is multiplied by the shear modulus μ to obtain the shear stress drop around a fault with a characteristic displacement distribution:

$$\Delta\sigma = \mu\varepsilon_{zy} \quad \textbf{(Eq. A5)}$$

Appendix 5. Digital appendices

The files for the digital appendix can be located in the attached CD at the rear of the hardbound thesis or appended to the digital pdf file.

The digital appendix contains:

- **Relayzone_tables.xlsx**
  - This spreadsheet contains all recorded relay zone measurements and includes information on data location, Horizon name, Relay ID., Separation (m), Overlap (m), AR, Rock Type(s), Fault Linkage type, Data Type, and Data Source.
- **Arches_DB_table.xlsx**
  - This spreadsheet contains information collected from the Arches relay ramp, Utah. The location and width of deformation bands are recorded along a single transect line orientated north-south.
- **Poster_FNR_vs_ED.pdf**
  - Poster presented at Petex conference 2010 outlining the comparison between the two methods FNR and ED.
- **Reprints of published papers**
  - **JSG_2010**
  - **CSEG Recorder_2010**

Chapter 8. References

Ackermann, R.V., Schlische, R.W., 1997. Anticlustering of small normal faults around larger faults. *Geology* 25 (12), 1127-1130.

Ackermann, R.V., Schlische, R.W., Withjack, M.O., 2001. The geometric and statistical evolution of normal fault systems: an experimental study of the effects of mechanical layer thickness on scaling laws. *Journal of Structural Geology* 23 (11), 1803-1819.

Acocella, V., Gudmundsson, A., Funiciello, R., 2000. Interaction and linkage of extension fractures and normal faults: examples from the rift zone of Iceland. *Journal of Structural Geology* 22 (9), 1233-1246.

Amato, A., Azzara, R., Chiarabba, C., Cimini, G.B., Cocco, M., Di Bona, M., Margheriti, L., Mazza, S., Mele, F., Selvaggi, G., Basili, A., Boschi, E., Courboulex, F., Deschamps, A., Gaffet, S., Bittarelli, G., Chiaraluce, L., Piccinini, D., Ripepe, M., 1998. The 1997 Umbria-Marche, Italy, Earthquake Sequence: A first look at the main shocks and aftershocks. *Geophys. Res. Lett.* 25 (15), 2861-2864.

Aydin, A., Schultz, R.A., 1990. Effect of mechanical interaction on the development of strike-slip faults with echelon patterns. *Journal of Structural Geology* 12 (1), 123-129.

Barnett, J., Mortimer, J., Rippon, J., Walsh, J., Watterson, J., 1987. Displacement geometry in the volume containing a single normal fault. *AAPG Bulletin* 71 (8), 925-937.

Bellian, J.A., Kerans, C., Jennette, D.C., 2005. Digital Outcrop Models: Applications of Terrestrial Scanning Lidar Technology in Stratigraphic Modeling. *Journal of Sedimentary Research* 75 (2), 166-176.

Benedicto, A., Schultz, R.A., Soliva, R., 2003. Layer thickness and the shape of faults. *Geophys. Res. Lett.* 30 (20), 2076.

Bonson, C.G., Childs, C., Walsh, J.J., Schopfer, M.P.J., Carboni, V., 2007. Geometric and kinematic controls on the internal structure of a large normal fault in massive limestones; the Maghlaq Fault, Malta. *Journal of Structural Geology* 29 (2), 336-354.

Brooks, M., Trayner, P.M., Trimble, T.J., 1988. Mesozoic reactivation of Variscan thrusting in the Bristol Channel area, UK. *Journal of the Geological Society* 145 (3), 439-444.

Brown, A.R., 2004. Interpretation of three-dimensional seismic data, 6th ed. *AAPG*.

Burchardt, S., 2008. New insights into the mechanics of sill emplacement provided by field observations of the Njardvik Sill, Northeast Iceland. *Journal of Volcanology and Geothermal Research* 173 (3-4), 280-288.

Caine, J.S., Evans, J.P., Forster, C.B., 1996. Fault zone architecture and permeability structure. *Geology* 24 (11), 1025-1028.

Cartwright, J., Bouroullec, R., James, D., Johnson, H., 1998. Polycyclic motion history of some Gulf Coast growth faults from high-resolution displacement analysis. *Geology* 26 (9), 819-822.

Cartwright, J., Mansfield, C., Trudgill, B., 1996. The growth of normal faults by segment linkage, In: Buchanan, P.G., Nieuwland, D.A. (Eds.), Modern developments in structural interpretation. *Geological Society, London, Special Publications* pp. 163-177.

Cartwright, J.A., Mansfield, C.S., 1998. Lateral displacement variation and lateral tip geometry of normal faults in the Canyonlands National Park, Utah. *Journal of Structural Geology* 20 (1), 3-19.

Cartwright, J.A., Trudgill, B.D., Mansfield, C.S., 1995. Fault growth by segment linkage: an explanation for scatter in maximum displacement and trace length data from the Canyonlands Grabens of SE Utah. *Journal of Structural Geology* 17 (9), 1319-1326.

Chester, F.M., Evans, J.P., Biegel, R.L., 1993. Internal Structure and Weakening Mechanisms of the San Andreas Fault. *J. Geophys. Res.* 98 (B1), 771-786.

Childs, C., Manzocchi, T., Walsh, J.J., Bonson, C.G., Nicol, A., Schöpfer, M.P.J., 2009. A geometric model of fault zone and fault rock thickness variations. *Journal of Structural Geology* 31 (2), 117-127.

Childs, C., Nicol, A., Walsh, J.J., Watterson, J., 1996a. Growth of vertically segmented normal faults. *Journal of Structural Geology* 18 (12), 1389-1397.

Childs, C., Nicol, A., Walsh, J.J., Watterson, J., 2003. The growth and propagation of synsedimentary faults. *Journal of Structural Geology* 25 (4), 633-648.

Childs, C., Walsh, J.J., Watterson, J., 1997. Complexity in fault zone structure and implications for fault seal prediction, In: P. Møller-Pedersen, D., A.G. Koestler, D. (Eds.), Norwegian Petroleum Society Special Publications. *Elsevier*, pp. 61-72.

Childs, C., Watterson, J., Walsh, J.J., 1995. Fault overlap zones within developing normal fault systems. *Journal of the Geological Society of London* 152 (3), 535-549.

Childs, C., Watterson, J., Walsh, J.J., 1996b. A model for the structure and development of fault zones. *Journal of the Geological Society of London* 153 (3), 337-340.

Contreras, J., Scholz, C.H., King, G.C.P., 1997. A model of rift basin evolution constrained by first-order stratigraphic observations. *J. Geophys. Res.* 102 (B4), 7673-7690.

Corfield, S., Sharp, I.R., 2000. Structural style and stratigraphic architecture of fault propagation folding in extensional settings: a seismic example from the Smørbukk area, Halten Terrace, Mid-Norway. *Basin Research* 12 (3-4), 329-341.

Cowie, P.A., Scholz, C.H., 1992. Physical explanation for the displacement-length relationship of faults using a post-yield fracture mechanics model. *Journal of Structural Geology* 14 (10), 1133-1148.

Cowie, P.A., Shipton, Z.K., 1998. Fault tip displacement gradients and process zone dimensions. *Journal of Structural Geology* 20 (8), 983-997.

Crider, J., Pollard, D., 1998a. Fault linkage: Three-dimensional mechanical interaction between echelon normal faults. *Journal of Geophysical Research* 103 (B10), 24373-24391.

Crider, J.G., Peacock, D.C.P., 2004. Initiation of brittle faults in the upper crust: a review of field observations. *Journal of Structural Geology* 26 (4), 691-707.

Crider, J.G., Pollard, D.D., 1998b. Fault linkage: Three-dimensional mechanical interaction between echelon normal faults. *Journal of Geophysical Research B: Solid Earth* 103 (B10), 24,373-324,391.

Davatzes, N.C., Eichhubl, P., Aydin, A., 2005. Structural evolution of fault zones in sandstone by multiple deformation mechanisms: Moab fault, southeast Utah. *Geological Society of America Bulletin* 117 (1-2), 135-148.

Davison, I., Bosence, D., Alsop, G.I., Al-Aawah, M.H., 1996. Deformation and sedimentation around active Miocene salt diapirs on the Tihama Plain,

northwest Yemen. *Geological Society, London, Special Publications* 100 (1), 23-39.

Davison, I., Insley, M., Harper, M., Weston, P., Blundell, D., McClay, K., Quallington, A., 1993. Physical modelling of overburden deformation around salt diapirs. *Tectonophysics* 228 (3-4), 255-274.

Dawers, N.H., Anders, M.H., 1995. Displacement-length scaling and fault linkage. *Journal of Structural Geology* 17 (5), 607-614.

Dawers, N.H., Anders, M.H., Scholz, C.H., 1993. Growth of normal faults: Displacement-length scaling. *Geology* 21 (12), 1107-1110.

De Ruig, M., Trupp, M., Bishop, D., Kuek, D., Castillo, D., 2000. Fault architecture and the mechanics of fault reactivation in the Nancar Trough/Laminaria area of the Timor Sea, northern Australia. *APPEA Journal* 40174–193.

Dee, S., Yielding, G., Freeman, B., Healy, D., Kusznir, N., Grant, N., Ellis, P., 2007. Elastic dislocation modelling for prediction of small-scale fault and fracture network characteristics. *Geological Society London Special Publications* 270 (1), 139.

Doelling, H.H., 1988. Geology of Salt Valley Anticline and Arches National Park, Grand County, Utah, In: Doelling, H.H., Oviatt, C.G., Huntoon, P.W. (Eds.), Salt Deformation in the Paradox Region. *Geological and Mineral Survey Bulletin*, Salt Lake City, Utah, pp. 1-60.

Doelling, H.H., 2001. Geologic map of the Moab and eastern part of the San Rafael Desert 30' x 60' quadrangles, Grand and Emery Counties, Utah, and Mesa County, Colorado., Utah Geological Survey, Map 180.

Doelling, H.H., Ross, M.L., Mulvey, W.E., 2002. Geologic map of the Moab 7.5' quadrangle Grand County, Utah. *Utah Geological Survey* Map 181.

Dugdale, D.S., 1960. Yielding of steel sheets containing slits. *Journal of the Mechanics and Physics of Solids* 8 (2), 100-104.

Dutton, D.M., Trudgill, B.D., 2009. Four-dimensional analysis of the Sembo relay system, offshore Angola; implications for fault growth in salt-detached settings. *AAPG Bulletin* 93 (6), 763-794.

Ebinger, C.J., 1989. Tectonic development of the western branch of the East African rift system. *Geological Society of America Bulletin* 101 (7), 885-903.

Favreau, P., Wolf, S., 2009. Theoretical and numerical stress analysis at edges of interacting faults: application to quasi-static fault propagation modelling. *Geophysical Journal International* 179 (2), 733-750.

Ferrill, D.A., Morris, A.P., 2001. Displacement gradient and deformation in normal fault systems. *Journal of Structural Geology* 23 (4), 619-638.

Ferrill, D.A., Morris, A.P., 2008. Fault zone deformation controlled by carbonate mechanical stratigraphy, Balcones fault system, Texas. *AAPG Bulletin* 92 (3), 359-380.

Ferrill, D.A., Morris, A.P., Smart, K.J., 2007. Stratigraphic control on extensional fault propagation folding: Big Brushy Canyon monocline, Sierra Del Carmen, Texas, In: Jolley, S., Barr, D., Walsh, J.J., Knipe, R.J. (Eds.), Structurally complex reservoirs. *Geological Society, London, Special Publications*, pp. 203-217.

Ferrill, D.A., Stamatakos, J.A., Sims, D., 1999. Normal fault corrugation: implications for growth and seismicity of active normal faults. *Journal of Structural Geology* 21 (8-9), 1027-1038.

Finch, E., Hardy, S., Gawthorpe, R., 2004. Discrete-element modelling of extensional fault-propagation folding above rigid basement fault blocks. *Basin Research* 16 (4), 489-506.

Ford, M., Le Carlier de Veslud, C., Bourgeois, O., 2007. Kinematic and geometric analysis of fault-related folds in a rift setting: The Dannemarie basin, Upper Rhine Graben, France. *Journal of Structural Geology* 29 (11), 1811-1830.

Fossen, H., Johansen, T.E.S., Hesthammer, J., Rotevatn, A., 2005. Fault interaction in porous sandstone and implications for reservoir management examples from southern Utah. *AAPG Bulletin* 89 (12), 1593-1606.

Fossen, H., Schultz, R.A., Shipton, Z.K., Mair, K., 2007. Deformation bands in sandstone: a review. *Journal of the Geological Society* 164 (4), 755-769.

Freeman, S.R., Harris, S.D., Knipe, R.J., 2010. Cross-fault sealing, baffling and fluid flow in 3D geological models: tools for analysis, visualization and interpretation. *Geological Society, London, Special Publications* 347 (1), 257-282.

Garden, I.R., Guscott, S.C., Burley, S.D., Foxford, K.A., Walsh, J.J., Marshall, J., 2001. An exhumed palaeo-hydrocarbon migration fairway in a faulted carrier system, Entrada Sandstone of SE Utah, USA. *Geofluids* 1 (3), 195-213.

Gawthorpe, R.L., Jackson, C.A.L., Young, M.J., Sharp, I.R., Moustafa, A.R., Leppard, C.W., 2003. Normal fault growth, displacement localisation and the evolution of normal fault populations: the Hammam Faraun fault block, Suez rift, Egypt. *Journal of Structural Geology* 25 (6), 883-895.

Gillespie, P.A., Walsh, J.J., Watterson, J., 1992. Limitations of dimension and displacement data from single faults and the consequences for data analysis and interpretation. *Journal of Structural Geology* 14 (10), 1157-1172.

Gupta, A., Scholz, C.H., 1998. Utility of elastic models in predicting fault displacement fields. *J. Geophys. Res.* 103 (B1), 823-834.

Gupta, A., Scholz, C.H., 2000. A model of normal fault interaction based on observations and theory. *Journal of Structural Geology* 22 (7), 865-879.

Huggins, P., Watterson, J., Walsh, J.J., Childs, C., 1995. Relay zone geometry and displacement transfer between normal faults recorded in coal-mine plans. *Journal of Structural Geology* 17 (12), 1741-1755.

Hus, R., Acocella, V., Funiciello, R., De Batist, M., 2005. Sandbox models of relay ramp structure and evolution. *Journal of Structural Geology* 27 (3), 459-473.

Hus, R., De Batist, M., Klerkx, J., Matton, C., 2006. Fault linkage in continental rifts: structure and evolution of a large relay ramp in Zavarotny; Lake Baikal (Russia). *Journal of Structural Geology* 28 (7), 1338-1351.

Imber, J., Tuckwell, G.W., Childs, C., Walsh, J.J., Manzocchi, T., Heath, A.E., Bonson, C.G., Strand, J., 2004. Three-dimensional distinct element modelling of relay growth and breaching along normal faults. *Journal of Structural Geology* 26 (10), 1897-1911.

Izett, G.A., Obradovich, J.D., 1994. 40Ar/39Ar age constraints for the Jaramillo Normal Subchron and the Matuyama-Brunhes geomagnetic boundary. *J. Geophys. Res.* 99 (B2), 2925-2934.

Jackson, C.A.L., Gawthorpe, R.L., Sharp, I.R., 2006. Style and sequence of deformation during extensional fault-propagation folding: examples from the Hammam Faraun and El-Qaa fault blocks, Suez Rift, Egypt. *Journal of Structural Geology* 28 (3), 519-535.

Jackson, J., 1999. Fault death: a perspective from actively deforming regions. *Journal of Structural Geology* 21 (8-9), 1003-1010.

Jolley, S., Barr, D., Walsh, J., Knipe, R., 2007. Structurally complex reservoirs: an introduction. *Geological Society London Special Publications* 292 (1), 1.

Jones, R.R., Kokkalas, S., McCaffrey, K.J.W., 2009. Quantitative analysis and visualization of nonplanar fault surfaces using terrestrial laser scanning (LIDAR)—The Arkitsa fault, central Greece, as a case study. *Geosphere* 5 (6), 465-482.

Jones, R.R., Mccaffrey, K.J.W., Imber, J., Wightman, R., Smith, S.A.F., Holdsworth, R.E., Clegg, P., De Paola, N., Healy, D., Wilson, R.W., 2008. Calibration and validation of reservoir models: the importance of high resolution, quantitative outcrop analogues. *Geological Society, London, Special Publications* 309 (1), 87-98.

Jones, R.R., Pringle, J.K., McCaffrey, K.J.W., Imber, J., Wightman, R.H., Guo, J., Long, J.J., In press. Extending Digital Outcrop Geology into the Subsurface. *SEPM Special Publication*.

Karner, G.D., Byamungu, B.R., Ebinger, C.J., Kampunzu, A.B., Mukasa, R.K., Nyakaana, J., Rubondo, E.N.T., Upcott, N.M., 2000. Distribution of crustal extension and regional basin architecture of the Albertine rift system, East Africa. *Marine and Petroleum Geology* 17 (10), 1131-1150.

Kim, Y.-S., Sanderson, D.J., 2005. The relationship between displacement and length of faults: a review. *Earth-Science Reviews* 68 (3-4), 317-334.

Knipe, R.J., Jones, G., Fisher, Q.J., 1998. Faulting, fault sealing and fluid flow in hydrocarbon reservoirs: an introduction, In: Jones, G., Fisher, Q.J., Knipe, R.J. (Eds.), Faulting, fault sealing and fluid flow in hydrocarbon reservoirs. *Geological Society, London, Special Publications*, pp. vii-xxi.

Kristensen, M.B., Childs, C.J., Korstgård, J.A., 2008. The 3D geometry of small-scale relay zones between normal faults in soft sediments. *Journal of Structural Geology* 30 (2), 257-272.

Long, J.J., Imber, J., 2010. Geometrically coherent continuous deformation in the volume surrounding a seismically imaged normal fault-array. *Journal of Structural Geology* 32 (2), 222-234.

Machette, M.N., Personius, S.F., Nelson, A.R., Schwartz, D.P., Lund, W.R., 1991. The Wasatch fault zone, utah--segmentation and history of Holocene earthquakes. *Journal of Structural Geology* 13 (2), 137-149.

Maerten, L., Gillespie, P., Pollard, D., 2002. Effects of local stress perturbation on secondary fault development. *Journal of Structural Geology* 24 (1), 145-153.

Maerten, L., Maerten, F., 2006. Chronologic modeling of faulted and fractured reservoirs using geomechanically based restoration: Technique and industry applications. *AAPG Bulletin* 90 (8), 1201-1226.

Maerten, L., Willemse, E.J.M., Pollard, D.D., Rawnsley, K., 1999. Slip distributions on intersecting normal faults. *Journal of Structural Geology* 21 (3), 259-272.

Manzocchi, T., Walsh, J.J., Nell, P., Yielding, G., 1999. Fault transmissibility multipliers for flow simulation models. *Petroleum Geoscience* 553-63.

Marchal, D., Guiraud, M., Rives, T., 2003. Geometric and morphologic evolution of normal fault planes and traces from 2D to 4D data. *Journal of Structural Geology* 25 (1), 135-158.

Marchal, D., Guiraud, M., Rives, T., van den Driessche, J., 1998. Space and time propagation processes of normal faults, In: Jones, G., Fisher, Q.J., Knipe, R.J. (Eds.), Faulting, fault sealing and fluid flow in hydrocarbon reservoirs. *Geological Society, London, Special Publications*, pp. 51-70.

Marsh, N., Imber, J., Holdsworth, R., Brockbank, P., Ringrose, P., 2009. The structural evolution of the Halten Terrace, offshore Mid-Norway: extensional fault growth and strain localisation in a multi-layer brittle–ductile system, Basin Research.

McCaffrey, K.J.W., Jones, R.R., Holdsworth, R.E., Wilson, R.W., Clegg, P., Imber, J., Holliman, N., Trinks, I., 2005. Unlocking the spatial dimension: digital technologies and the future of geoscience fieldwork. *Journal of the Geological Society* 162 (6), 927-938.

McClay, K.R., Dooley, T., Whitehouse, P., Mills, M., 2002. 4-D evolution of rift systems: Insights from scaled physical models. *AAPG Bulletin* 86 (6), 935-959.

McGrath, A.G., Davison, I., 1995. Damage zone geometry around fault tips. *Journal of Structural Geology* 17 (7), 1011-1024.

Morley, C.K., 1999. Patterns of displacement along large normal faults; implications for basin evolution and fault propagation, based on examples from East Africa. *AAPG Bulletin* 83 (4), 613-634.

Needham, D., Yielding, G., Freeman, D., 1996. Analysis of fault geometry and displacement patterns, In: Buchanan, P.G., Nieuwland, D.A. (Eds.), Modern

Developments in Structural Interpretation,Validation and Modelling. *Geological Society London Special Publications*, pp. 189-200.

Nicol, A., Walsh, J.J., Watterson, J., Underhill, J.R., 1997. Displacement rates of normal faults. *Nature* 390 (6656), 157-159.

Nicol, A., Watterson, J., Walsh, J.J., Childs, C., 1996. The shapes, major axis orientations and displacement patterns of fault surfaces. *Journal of Structural Geology* 18 (2-3), 235-248.

Nuccio, V.F., Condon, S.M., 1996. Burial and thermal history of the Paradox Basin, Utah and Colorado, and petroleum potential of the Middle Pennsylvanian Paradox Basin, Reston, Virginia. *U.S. Geological Survey Bulletin* 2000-OO1-O41.

Peacock, D.C.P., 2002. Propagation, interaction and linkage in normal fault systems. *Earth-Science Reviews* 58 (1-2), 121-142.

Peacock, D.C.P., 2003. Scaling of transfer zones in the British Isles. *Journal of Structural Geology* 25 (10), 1561-1567.

Peacock, D.C.P., Sanderson, D.J., 1991. Displacements, segment linkage and relay ramps in normal fault zones. *Journal of Structural Geology* 13 (6), 721-733.

Peacock, D.C.P., Sanderson, D.J., 1992. Effects of layering and anisotropy on fault geometry. *Journal of the Geological Society* 149 (5), 793-802.

Peacock, D.C.P., Sanderson, D.J., 1994. Geometry and development of relay ramps in normal fault systems. *AAPG Bulletin* 78 (2), 147-165.

Pedersen, S., Skov, T., Randen, T., Sønneland, L., 2005. Automatic Fault Extraction Using Artificial Ants, In: Iske, A., Randen, T. (Eds.), Mathematical Methods and Modelling in Hydrocarbon Exploration and Production. *Springer Berlin Heidelberg*, pp. 107-116.

Pinter, N., 1995. Faulting on the Volcanic Tableland, Owens Valley, California. *The Journal of Geology* 103 (1), 73-83.

Rotevatn, A., Fossen, H., Hesthammer, J., Aas, T.E., Howell, J.A., 2007. Are relay ramps conduits for fluid flow? Structural analysis of a relay ramp in Arches National Park, Utah, In: Lonergan, L., Jolly, R.J.H., Rawnsley, K., Sanderson, D.J. (Eds.), Fractured Reservoirs. *Geological Society of London, Special Publications*, London, pp. 55-71.

Rowan, M.G., Jackson, M.P.A., Trudgill, B.D., 1999. Salt-related fault families and fault welds in the northern Gulf of Mexico. *AAPG Bulletin* 83 (9), 1454-1484.

Schlische, R.W., Young, S.S., Ackermann, R.V., Gupta, A., 1996. Geometry and scaling relations of a population of very small rift-related normal faults. *Geology* 24 (8), 683-686.

Schöpfer, M.P.J., Childs, C., Walsh, J.J., 2006. Localisation of normal faults in multilayer sequences. *Journal of Structural Geology* 28 (5), 816-833.

Schwartz, D.P., Coppersmith, K.J., 1984. Fault Behavior and Characteristic Earthquakes: Examples From the Wasatch and San Andreas Fault Zones. *J. Geophys. Res.* 89 (B7), 5681-5698.

Segall, P., Pollard, D.D., 1980. Mechanics of Discontinuous Faults. *J. Geophys. Res.* 85 (B8), 4337-4350.

Sharp, I., Gawthorpe, R., Underhill, J., Gupta, S., 2000. Fault-propagation folding in extensional settings: Examples of structural style and synrift sedimentary response from the Suez rift, Sinai, Egypt. *Bulletin of the Geological Society of America* 112 (12), 1877-1899.

Shiells, K.A.G., 1964. The geological structure of northeast Northumberland. *Transactions of the Royal Society of Edinburgh* 65449-484.

Shipton, Z.K., Cowie, P.A., 2001. Damage zone and slip-surface evolution over µm to km scales in high-porosity Navajo sandstone, Utah. *Journal of Structural Geology* 23 (12), 1825-1844.

Sieh, K., Jones, L., Hauksson, E., Hudnut, K., Eberhart-Phillips, D., Heaton, T., Hough, S., Hutton, K., Kanamori, H., Lilje, A., Lindvall, S., McGill, S.F., Mori, J., Rubin, C., Spotila, J.A., Stock, J., Thio, H.K., Treiman, J., Wernicke, B., Zachariasen, J., 1993. Near-Field Investigations of the Landers Earthquake Sequence, April to July 1992. *Science* 260 (5105), 171-176.

Soliva, R., Benedicto, A., 2004. A linkage criterion for segmented normal faults. *Journal of Structural Geology* 26 (12), 2251-2267.

Soliva, R., Benedicto, A., Maerten, L., 2006. Spacing and linkage of confined normal faults: Importance of mechanical thickness. *Journal of Geophysical Research* 111 (B1).

Soliva, R., Benedicto, A., Schultz, R.A., Maerten, L., Micarelli, L., 2008. Displacement and interaction of normal fault segments branched at depth: Implications for fault growth and potential earthquake rupture size. *Journal of Structural Geology* 30 (10), 1288-1299.

Soliva, R., Schultz, R.A., Benedicto, A., 2005. Three-dimensional displacement-length scaling and maximum dimension of normal faults in layered rocks. *Geophys. Res. Lett.* 32 (16), L16302.

Steen, O., Sverdrup, E., Hanssen, T.H., 1998. Predicting the distribution of small faults in a hydrocarbon reservoir by combining outcrop, seismic and well data, In: Jones, G., Fisher, Q.J., Knipe, R.J. (Eds.), Faulting, fault sealing and fluid flow in hydrocarbon reservoirs. *Geological Society Special Publication*, London, pp. 27-50.

Stevens, V., 1991. The Beatrice Field, Block 11/30a, UK North Sea. *Geological Society, London, Memoirs* 14 (1), 245-252.

Stewart, S.A., Harvey, M.J., Otto, S.C., Weston, P.J., 1996. Influence of salt on fault geometry: examples from the UK salt basins. *Geological Society, London, Special Publications* 100 (1), 175-202.

Tentler, T., 2005. Propagation of brittle failure triggered by magma in Iceland. *Tectonophysics* 406 (1-2), 17-38.

Thomson, K., Underhill, J.R., 1993. Controls on the development and evolution of structural styles in the Inner Moray Firth Basin, In: Parker, J.R. (Ed.), Petroleum Geology of Northwest Europe: Proceedings of the 4th Conference. *The Geological Society, London*, pp. 1167-1178.

Townsend, C., Firth, I., Westerman, R., Kirkevollen, L., Harde, M., Andersen, T., 1998. Small seismic-scale fault identification and mapping, In: Jones, G., Fisher, Q.J., Knipe, R.J. (Eds.), Faulting, fault sealing and fluid flow in hydrocarbon reservoirs. *Geological Society, London, Special Publications*, pp. 1-25.

Trudgill, B., Cartwright, J., 1994. Relay-ramp forms and normal-fault linkages, Canyonlands National Park, Utah. *Geological Society of America Bulletin* 106 (9), 1143.

Turcotte, D.L., 1989. Fractals in geology and geophysics. *Pure and Applied Geophysics* 131 (1), 171-196.

Underhill, J.R., 1991a. Controls on Late Jurassic seismic sequences, Inner Moray Firth, UK North Sea; a critical test of a key segment of Exxon's original global cycle chart. *Basin Research* 3 (2), 79-98.

Underhill, J.R., 1991b. Implications of Mesozoic-Recent basin development in the western Inner Moray Firth, UK. *Marine and Petroleum Geology* 8 (3), 359-369.

Vermilye, J.M., Scholz, C.H., 1998. The process zone: A microstructural view of fault growth. *J. Geophys. Res.* 103 (B6), 12223-12237.

Walsh, J., Childs, C., Imber, J., Manzocchi, T., Watterson, J., Nell, P., 2003a. Strain localisation and population changes during fault system growth within the Inner Moray Firth, Northern North Sea. *Journal of Structural Geology* 25 (2), 307-315.

Walsh, J.J., Bailey, W.R., Childs, C., Nicol, A., Bonson, C.G., 2003b. Formation of segmented normal faults; a 3-D perspective. *Journal of Structural Geology* 25 (8), 1251-1262.

Walsh, J.J., Nicol, A., Childs, C., 2002. An alternative model for the growth of faults. *Journal of Structural Geology* 24 (11), 1669-1675.

Walsh, J.J., Watterson, J., 1988. Analysis of the relationship between displacements and dimensions of faults. *Journal of Structural Geology* 10 (3), 239-247.

Walsh, J.J., Watterson, J., 1989. Displacement gradients on fault surfaces. *Journal of Structural Geology* 11 (3), 307-316.

Walsh, J.J., Watterson, J., 1991. Geometric and kinematic coherence and scale effects in normal fault systems, In: Roberts, A.M., Yielding, G., Freeman, B. (Eds.), The geometry of normal faults. *Geological Society, London, Special Publications*, pp. 193-203.

Walsh, J.J., Watterson, J., Bailey, W.R., Childs, C., 1999. Fault relays, bends and branch-lines. *Journal of Structural Geology* 21 (8-9), 1019-1026.

Walsh, J.J., Watterson, J., Childs, C., Nicol, A., 1996. Ductile strain effects in the analysis of seismic interpretations of normal fault systems, In: Buchanan, P.G., Nieuwland, D.A. (Eds.), Modern developments in structural interpretation, validation and modelling. *Geological Society Special Publications*, pp. 27-40.

Wells, D.L., Coppersmith, K.J., 1994. New empirical relationships among magnitude, rupture length, rupture width, rupture area, and surface displacement. *Bulletin of the Seismological Society of America* 84 (4), 974-1002.

Wesnousky, S.G., 1986. Earthquakes, Quaternary Faults, and Seismic Hazard in California. *J. Geophys. Res.* 91 (B12), 12587-12631.

White, I.R., Crider, J.G., 2006. Extensional fault-propagation folds: mechanical models and observations from the Modoc Plateau, northeastern California. *Journal of Structural Geology* 28 (7), 1352-1370.

Whittam, D.B., Norvick, M.S., McIntyre, C.L., 1996. Mesozoic and Cainozoic tectonostratigraphy of western ZOCA and adjacent areas. *APPEA Journal* 36 (1), 209-231.

Wightman, R.H., Imber, J., Jones, R.R., 2007. Quantifying fault zone thicknesses and fault rock distribution in Coal Measures sequences using terrestrial laser scan data, Geological Society of America, 2007 annual meeting *Geological Society of America (GSA), Boulder, CO, United States*, Denver, CO United States, p. 50.

Wilkins, S.J., Gross, M.R., 2002. Normal fault growth in layered rocks at Split Mountain, Utah: influence of mechanical stratigraphy on dip linkage, fault restriction and fault scaling. *Journal of Structural Geology* 24 (9), 1413-1429.

Willemse, E.J.M., 1997. Segmented normal faults: Correspondence between three-dimensional mechanical models and field data. *J. Geophys. Res.* 102 (B1), 675-692.

Willemse, E.J.M., Pollard, D.D., Aydin, A., 1996. Three-dimensional analyses of slip distributions on normal fault arrays with consequences for fault scaling. *Journal of Structural Geology* 18 (2-3), 295-309.

Withjack, M., Callaway, S., 2000. Active normal faulting beneath a salt layer: an experimental study of deformation patterns in the cover sequence. *AAPG Bulletin* 84 (5), 627-651.

Withjack, M., Olson, J., Peterson, E., 1990. Experimental models of extensional forced folds. *AAPG Bulletin* 74 (7), 1038-1054.

Yielding, G., Freeman, B., Needham, D.T., 1997. Quantitative fault seal prediction. *Journal Name: AAPG Bulletin; Journal Volume: 81; Journal Issue: 6; Other Information: PBD: Jun 1997*Medium: X; Size: pp. 897-917.